



**UNIVERSIDAD NACIONAL AUTÓNOMA DE MÉXICO
PROGRAMA DE POSGRADO EN ASTROFÍSICA**

Instituto de Radioastronomía y Astrofísica

EVOLUCIÓN DE DISCOS DE ACRECIÓN EN CÚMULOS ESTELARES JÓVENES

PARA OPTAR PARA EL GRADO DE
DOCTOR EN CIENCIAS (ASTROFÍSICA)

PRESENTA
KARINA MAUCÓ

TUTOR
DR. JAVIER BALLESTEROS PAREDES, INSTITUTO DE RADIOASTRONOMÍA Y
ASTROFÍSICA

CO-TUTOR
DR. JESÚS HERNÁNDEZ, INSTITUTO DE ASTRONOMÍA (IAUNAM-E)

MÉXICO, D.F. JULIO 2018
CD.MX.



Universidad Nacional
Autónoma de México

Dirección General de Bibliotecas de la UNAM

Biblioteca Central



UNAM – Dirección General de Bibliotecas
Tesis Digitales
Restricciones de uso

DERECHOS RESERVADOS ©
PROHIBIDA SU REPRODUCCIÓN TOTAL O PARCIAL

Todo el material contenido en esta tesis esta protegido por la Ley Federal del Derecho de Autor (LFDA) de los Estados Unidos Mexicanos (México).

El uso de imágenes, fragmentos de videos, y demás material que sea objeto de protección de los derechos de autor, será exclusivamente para fines educativos e informativos y deberá citar la fuente donde la obtuvo mencionando el autor o autores. Cualquier uso distinto como el lucro, reproducción, edición o modificación, será perseguido y sancionado por el respectivo titular de los Derechos de Autor.

Contents

1	Introduction	2
2	Disk Structure	8
2.1	α -disks	8
2.2	Irradiated Accretion Disks Models	9
3	Dust in Protoplanetary Disks	14
3.1	Spectral Energy Distribution	14
3.2	Classification of YSOs	17
3.3	Color-color Diagrams	20
3.4	Dust settling	20
3.5	Dust processing and composition	25
3.5.1	Polycyclic Aromatic Hydrocarbons (PAH)	29
3.6	Disk Geometry and SED Shape	30
3.6.1	Transitional and Pre-transitional Disks	30
3.6.2	Photoevaporation in Disks	32
3.6.3	Orion Proplyds	35
4	The Orion OB1 Association	37
4.0.1	The σ Ori cluster	40
5	Peer-Reviewed Articles	42
5.1	Article 1	42
5.1.1	Abstract	42
5.2	Article 2	64
5.2.1	Abstract	64
5.3	Article 3	80
5.3.1	Abstract	80
6	Conclusions	97

Chapter 1

Introduction

Over the years the study of Young Stellar Objects (YSOs) has been of crucial interest to understanding the early stages of star formation. It is believed that stars form from the collapse of dense cores in large molecular clouds complexes. Because of angular momentum conservation, the collapse of rotating cloud cores leads to the formation of stars surrounded by disks (Andre et al., 2000; Ward-Thompson et al., 2005; Hartmann, 2009a). Therefore, circumstellar disks are both the natural byproducts of star formation and the structures from which eventually rocky and giant planets form. Thus, it is clear that we need to understand the physical processes that control their evolution. For this, we need both theoretical developments and observational constraints to determine how the solid material in protoplanetary disks evolves from interstellar medium (ISM)-like conditions to planetesimals and planets. Many factors are at play and observations are essential to constrain the evolutionary processes taking place in the disks.

It is believed that disks evolve because they are accreting mass onto the star and because the dust grains tend to settle towards the midplane where they collide and grow (Hartmann, 1998, 2009a). The material in the disk is subject to irradiation from the stellar radiation and by the high energy fields from the accretion shock on the stellar surface, from the stellar active regions, and from the environment, if the star is immersed in the radiation field of nearby OB stars in a stellar cluster (D'Alessio et al., 2001, 2006a; Adams et al., 2004; Anderson et al., 2013). These high energy fields heat the gas, eventually contributing to its dissipation, while the solids grow to planetesimal and planet sizes. These planets also dissipate the disk material around them through accretion.

In order to have a better understanding of the evolution of protoplane-

tary disks, the study of different populations of young stars within a wide range of ages (1 – 10 Myr) is needed. Previous studies using Spitzer data of different star-forming regions with ages between 1 and 10 Myr, show a decrease of disk fraction around K & M stars as a function of age of the clusters (Hernández et al., 2007b). The decrease of disk frequency is reflected as a clear drop in the mid-IR emission of the disks, indicating that only 20% of the stars retain their original disks by 5 Myr (Hernández et al., 2007a). It is therefore essential to observe disks in the crucial age range between 2 and 10 Myr in which the agents driving the evolution of protoplanetary disks are most active. It is worth noting, that Downes et al. (2015) have shown that disks around very low mass stars and brown dwarf can survive for longer periods of time, so the decrease of disk fraction seem to be mass-dependent. This effect has to be taken into account when studying late-type stars. The decrease of the IR excess can be explained by grain growth and by settling of dust to the disk midplane, reducing the flaring of the disk, and thus, its emitting flux. This interpretation is confirmed by the analysis made by D’Alessio et al. (2006a) using irradiated accretion disk models.

Once the dust has settled, large bodies formed in the disk will interact with its local environment creating more complex radial structures like inner clearings or gaps. Many studies have now revealed stars with inner disks devoid of optically thick material –the so-called transitional disks (TD)– and with spectral energy distributions (SEDs) characterized by small or negligible near-infrared excesses but significant emission in the mid-infrared and beyond (Strom et al., 1989; Skrutskie et al., 1990; Calvet et al., 2002; Espaillat et al., 2007, 2008a, 2014). This morphology has been interpreted as cavities in the inner regions and has been confirmed through (sub)millimeter interferometric imaging and, recently, by spatially resolved images (e.g., Hughes et al., 2009; Brown et al., 2009; Andrews et al., 2009; Isella et al., 2010; Andrews et al., 2011a,b; van Dishoeck et al., 2015; Carrasco-González et al., 2016), especially those taken with the Very Large Telescope (VLT)/SPHERE and the Atacama Large Millimeter/submillimeter Array (ALMA) (ALMA Partnership et al., 2015; Nomura et al., 2016; Schwarz et al., 2016; Andrews et al., 2016; van Boekel et al., 2017). A subset of these disks, commonly called pre-transitional disks (PTD), show similar features but with substantial near-infrared excesses over the stellar photosphere. This excess has been explained by an optically thick disk located close to the star, separated from the outer disk by a gap (Espaillat et al., 2008a, 2010, 2011).

Great advances in the understanding of the structure and evolution of protoplanetary disks have been achieved in the last decade with observations

provided by the Spitzer and Herschel space missions and the sub/millimeter interferometers. Studies using data from Spitzer have provided a description of the state of gas and dust within the first AU from the central object. In the ~ 5 -10 Myr old (de Zeeuw et al., 1999) Upper-Scorpius (US) group Dahm and Carpenter (2009) examined, among others, 7 late-type disk-bearing (K+M) members using the Infrared Spectrograph (IRS). They found a lack of sub-micron dust grains in the inner regions of the disks and that the strength of silicate emission is spectral-type dependent. In a disk census performed by Luhman and Mamajek (2012) with Spitzer and WISE photometry they found that late-type members have a higher inner disk fraction than early-types. The ~ 10 Myr old (Uchida et al., 2004) TW Hydrae (TW Hya) association has also been the target for different disk evolution studies. Uchida et al. (2004) analyzed two objects with IR excesses on their IRS spectra. They found signs of significant grain growth and dust processing and also evidence of dust clearing in the inner (~ 4 AU) disks, possibly due to the presence of orbiting planets. Similar studies performed in other regions like Ophiucus (McClure et al., 2010, ~ 1 Myrs), Taurus (Furlan et al., 2006, 1-2 Myrs), and Chamaeleon I (Manoj et al., 2011, ~ 2 Myrs), using IRS spectra to analyze the strength and shape of the $10 \mu\text{m}$ and $20 \mu\text{m}$ silicate features, have shown that disks in these regions are highly settled and exhibit signs of significant dust processing. The fact that all these young regions share the same degree of dust evolution despite their different ages, suggests that age does not seem to be the dominant factor in determining the evolutionary stage of disks (at least within the first ~ 10 AU from the central object), but rather the initial conditions of the cloud core and the local ambient from which the stars were formed. For instance, stars in clustered environments may dissipate their disks faster because of interactions with other stars or with external, high energy radiation fields from massive stars.

Many works done using the Photodetector Array Camera & Spectrometer (PACS) instrument on board Herschel have improved the understanding about disk evolution since disk fluxes, at the wavelength range probed by Herschel, are strongly dependent on the evolutionary stage of the dust around young stars. For instance, the Wide-field Infrared Survey Explorer (WISE, Wright et al., 2010) covered wavelengths from $3.6 \mu\text{m}$ to $22 \mu\text{m}$, and Spitzer was most sensitive from $3.6 \mu\text{m}$ to $24 \mu\text{m}$, with limited sensitivity at $70 \mu\text{m}$. Therefore, studies of dust depletion have mostly been limited to the inner disk regions (e.g., McClure et al., 2010; Sargent et al., 2009; Luhman et al., 2010; Manoj et al., 2011). With Herschel we now have a window into longer wavelengths important for disk studies, since allows the improve characterization of evolutionary effects, like dust settling. Additionally, the

smaller beam size and higher spatial resolution of PACS compared with *Spitzer*/MIPS results in a lower rate of confusion with background sources making it easier for Herschel to detect faint sources. The main idea of the studies using PACS data has been the description of disks structures as well as the estimation of gas and dust masses in different star-forming regions (e.g., Riviere-Marichalar et al., 2013; Mathews et al., 2013; Olofsson et al., 2013). For instance, Howard et al. (2013) modeled PACS detections in Taurus, and found that the region probed by their observations constitutes the first 5 to 50 AU of their disks. Thi et al. (2010) constrained the gas and dust mass of TW Hya by looking at the fine-structure lines of [OI] and [CII] and continuum emission of ^{12}CO 3–2 and ^{13}CO 3–2. They found a gas mass of $(0.5 - 5) \times 10^{-3} M_{\odot}$ and a dust mass ($a_{\text{max}} < 1$ mm) of $1.9 \times 10^{-4} M_{\odot}$. Riviere-Marichalar et al. (2013) studied the IR properties of 14 members of the TW Hya Association and obtained dust masses in the range from $\sim 0.15 M_{\oplus}$ to $\sim 63 M_{\oplus}$. Mathews et al. (2013) observed K & M stars in US at 70, 100 and 160 μm founding clear sings of dust settling as well as low dust masses and low number of gas line detections and concluded that by the age of US, giant planet formation is essentially complete. Manoj et al. (2013) presented FIR spectra for 21 protostars in the Orion molecular clouds for which CO emission lines were analyzed, they concluded that the emission is dominated by sub-thermally excited, shock-heated gas at high temperatures and low densities at radii greater than several 100 – 1000 AU.

Sub-mm and mm wavelength surveys are specially suitable for probing the bulk of dust and gas material in protoplanetary disks, since at these wavelengths the emission from the disk is mostly optically thin. On this regard, the enhanced sensitivity of the Atacama Large Millimeter/sub-millimeter Array (ALMA) is by far the most sensitive telescope available today that can best probes both gas and dust for large samples of protoplanetary disks in the entire age range expected for disks lifetime. Through these ALMA surveys (Pascucci et al., 2016; Manara et al., 2016; Ansdell et al., 2016; Barenfeld et al., 2016; Ansdell et al., 2017), it has been possible to confirm that the average dust mass in protoplanetary disks does decrease with age, which indicates that during the first few Myr significant evolution is expected on these systems and thus, giant planet formation occurs early on in the life of the disks.

However, most disk studies have concentrated on populations $\lesssim 2$ Myr (i.e., Taurus, the Orion Nebula Cluster), and much less information exists for older populations, especially around 10 Myr. The main reason is that already at ages ~ 4 Myr the parent molecular clouds have largely dissipated, such that these somewhat older stars are harder to identify among

the general field population. It is not surprising that many of the $\sim 4 - 10$ Myr old groups have been discovered in the last ~ 20 years. The TW Hya association (Webb et al., 1999) and the η Cha cluster (Mamajek et al., 1999) are among the nearest 10 Myr old groups, but contain only around 20 stars. The Scorpius-Centaurus OB association, with ages $\sim 5 - 20$ Myr (e.g. Preibisch and Mamajek, 2008; Pecaut and Mamajek, 2016) is the closest OB association (~ 130 pc). Among its various sub-groups, the US group, likely the youngest, is also the one that has been most studied, with ~ 800 members reported by Luhman and Mamajek (2012), though spectroscopic confirmation of many low-mass members is still ongoing (Pecaut and Mamajek, 2016). US has an age which is still debated, in the range $4 - 10$ Myr (Preibisch and Mamajek, 2008; Pecaut and Mamajek, 2016). ALMA submm studies in US have reported dust properties and disk sizes in samples of ~ 100 disk systems (Carpenter et al., 2006, 2009; Barenfeld et al., 2016, 2017).

As one of the closest region with active low and high-mass star formation ($d \sim 400$ pc), the Orion OB1 association contains large samples of young stars, spanning ages from the protostellar stage up to “older” PMS stars, and sharing a common origin (Bally, 2008; Briceño, 2008; Briceño et al., 2018). Moreover, Orion has populous clusters of stars at various ages, which alleviates the problem of the highly uncertain PMS ages, harder to constrain for isolated stars. Even if the absolute ages for each cluster are uncertain, the relative progression of ages among the various stellar aggregates is better understood. At the young end of optically visible PMS stars, the ~ 1 Myr old Trapezium cluster contains $\gtrsim 2000$ stars (Muench et al., 2008), and the ~ 3 Myr σ Ori cluster has over 300 confirmed members (Hernández et al., 2014). The latter is an excellent laboratory for studies of disk evolution for two reasons: first, the large number of stars still harboring disks allows us to obtain results with statistical significance and second, given its intermediate age, one can expect the first traces of disk evolution to become apparent. At the “old” end of the PMS age spectrum, the ~ 10 Myr old 25 Ori cluster (Briceño et al., 2007) has ~ 360 members, which have been characterized spectroscopically and photometrically in a consistent and uniform way (Briceño et al., 2005; Briceño, 2008; Briceño et al., 2018; Downes et al., 2014, 2015; Hernández et al., 2007a, 2014; Suárez et al., 2017). For these reasons the Orion OB1 association highlights as one of the best regions to study disk evolution from protostars and embedded clusters in the molecular clouds, to $5 - 10$ Myr old stellar populations in the wide, low-extinction, off-cloud regions.

In the present work we report Herschel Space Telescope $70 \mu\text{m}$ and 160

μm observations of TTS in the σ Ori cluster and in four fields in the Orion OB1 association, targeting a subset of the stellar population in the $\sim 3 - 10$ Myr age range. Combining the Herschel data with optical V, R, I, near infrared J, H, K photometry, as well as mid-IR data from Spitzer/WISE, we assemble spectral energy distributions for several disk-bearing sources, that we then fit with detailed irradiated accretion disk models to infer the structure, characteristics and evolutionary state of these disks aiming to provide new insights about planet formation and disk dissipation.

Chapter 2

Disk Structure

2.1 α -disks

Matter in disks covers a wide range of temperatures and densities. This is seen by analysis of IR observations along with the predictions of simple viscous models, the so-called α -disks. The viscosity ν on these models is given by

$$\nu = \alpha c_s H_p \quad (2.1)$$

where c_s is the sound speed, H_p is the vertical pressure scale height, and α is a free parameter (typically between 0.1 and 0.001) describing the viscous turbulence on the disk. In these models, there is no motion in the vertical direction and the Keplerian rotation, which is supersonic at all radii, dominates the gas motions. The dust is assumed to be in thermal balance with the gas for simplicity. The radial drift toward the star is subsonic, with velocity of the order of ν/R . In steady state, the mass accretion rate \dot{M} is

$$\dot{M} \sim 2\pi \Sigma R v_R \quad (2.2)$$

where Σ and v_R are the surface density and the accretion velocity at R respectively.

Viscous dissipation heats the disk. This heating is lost in form of radiation, so the disk luminosity is directly proportional to the mass-accretion rate. Viscous α -disks are geometrically thin, e.g. $H_p/R \sim c_s/v_K$, where v_K represents the Keplerian rotation velocity at R , so most of the disk mass is concentrated on the midplane. If hydrostatic equilibrium in the vertical direction is assumed, then the density distribution is $\propto \exp(-z^2/2H_p^2)$. If

the heating caused by the central star is neglected, the profile of the surface radial temperature produced by viscous dissipation is $T \propto R^{-3/4}$; so these disks are hotter at the midplane than on the surface, producing only absorption spectral features as in a plane-parallel stellar atmosphere.

2.2 Irradiated Accretion Disks Models

Even though it is believed that disks around YSOs are accreting material onto the central object, the standard accretion disks models cannot explain the observed SEDs which are flatter than the predicted trend of $\lambda F_\lambda \propto \lambda^{-3/4}$ (Kenyon and Hartmann, 1987). In general, viscosity is not the only source of heating. The disk surface and, as an indirect consequence, the whole disk will be heated by radiation from the central star. Normally, the stellar luminosity, L_* , is higher than the accretion luminosity, L_{acc} , assuming an average mass-accretion rate of $10^{-8} M_\odot \text{ yr}^{-1}$ for low-mass stars (Hartmann, 2009b) and typical stellar parameters, $L_{\text{acc}} \sim 0.1 L_\odot \approx 0.1 L_*$. Therefore, disk models must take into account the stellar irradiation as an important heating agent.

In fact, this is often the dominant effect in observed disks, where the stellar radiation is reprocessed by its interaction with disk material producing an excess emission on IR wavelengths (Adams et al., 1987). In this situation, disks are heated from the outside. The temperature at the midplane is lower than at the surface, producing gas and dust spectral features in emission rather than in absorption, as would be the case if the disk heating were dominated by accretion energy dissipated in the midplane.

For a flat disk, the irradiation flux can be estimated as:

$$F_{\text{irr}} \sim I_* \Omega_* \cos \theta_0 \sim \frac{I_* \pi R_*^2 h_*}{R^2 R} \sim \frac{2I_*}{3} \left(\frac{R_*}{R} \right)^3, \quad (2.3)$$

where θ_0 is the angle between the line connecting a point on the stellar surface at a height $h_* \sim \frac{2R_*}{3\pi}$ above the disk midplane, and a point on the disk surface at distance R and the vector normal to this surface. Here the stellar radiation, I_* , have been approximated as impinging on the disk surface in a single beam with solid angle Ω_* . If we take $F_{\text{irr}} \sim \sigma T^4$, then the temperature is $T \propto R^{-3/4}$, which results in SEDs that cannot explain the observations. An important aspect to take into account is that in irradiated disks, the amount of reprocessed radiation depends on the disk geometry, i.e., on the geometrical shape of the disk.

Kenyon and Hartmann (1987) proposed that disks around CTTSs are not flat but flared, so they can capture more stellar radiation than a flat

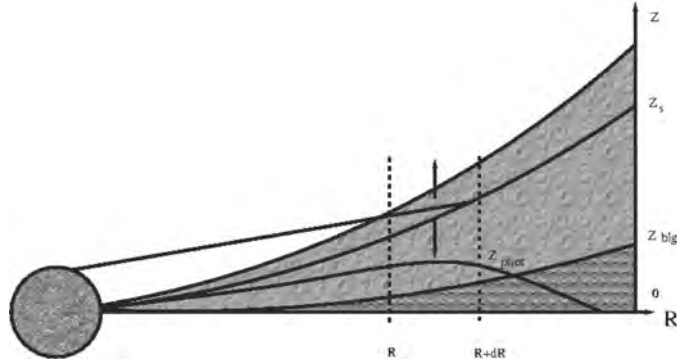


Figure 2.1: Schematic diagram of the disk geometry. Stellar radiation is intercepted by the surface $z_s(R)$. The layer above z_s is heated by direct stellar radiation, and the emission of this layer heats deeper disk regions. The disk photosphere, z_{phot} , is the height where the Rosseland mean optical depth is $2/3$. The outer disk can be optically thin to its own radiation, in which case it is not possible to define z_{phot} at those radii (taken from D’Alessio et al. (2006b)).

disk, since the fraction of solid angle covered by the disk increases with radius (note that flat in this context implies a constant ratio of scale height to radius). This situation is illustrated schematically in Figure 2.1. Disk heating (at most radii) is dominated by the absorption of light from the central star, because of the larger dust opacities at short wavelengths, the radiation is then absorbed in the upper, low-density layers of the disk. The irradiation surface $z_s(R)$ is defined such that the mean optical depth integrated along the radial direction to the star is unity. The absorbed stellar light is then re-radiated at longer wavelengths, and about half of this emission gets into deeper layers of the disk (Calvet et al., 1991; D’Alessio et al., 1998). The amount of stellar flux entering the disk at a given radius is approximately proportional to μ_0 , defined as the cosine of the angle between the radial direction and the local normal to the irradiation surface. Thus, the shape of $z_s(R)$, determines the amount of energy entering the disk, and thus, the main heating at most radii.

For a geometrically thin disk affected by the central gravitational potential well of its host star, the equation of hydrostatic equilibrium in the vertical direction is as following

$$\frac{1}{\rho} \frac{dp}{dz} = -\frac{GM_* z}{R^3}, \quad (2.4)$$

where $\rho(z, R)$ and $p(z, R)$ are the mass density and pressure at height z and radius R , respectively. If the disk is isothermal in the vertical direction, then $p = \rho c_s^2$, where c_s is the sound speed with a value of $c_s = (kT/m)^{1/2}$, which is independent of z , and m indicates the mean mass of the gas particles. With this approximation the mass density is

$$\rho(z, R) = \rho_m e^{-\frac{z^2}{2H^2}}, \quad (2.5)$$

where $\rho_m(R)$ is the density at the disk midplane and H is the gas scale height, given by

$$H = \frac{c_s}{(GM_*/R^3)^{1/2}} = \frac{c_s}{\Omega_K} \propto T^{1/2} R^{3/2}. \quad (2.6)$$

Now, from this equation one can see that if the temperature decreases with distance more slowly than R^{-3} , then the gas scale height will grow outwardly on the radial direction. If additionally, the height of the disk surface is proportional to H , then the disk is flared (curved). In this case $T \sim R^{-3/7}$, the disk will absorb more stellar flux and will have a larger IR excess, resulting in a much flatter SED than the one predicted from viscous disk modeling or flat irradiated disks.

Since the stellar emission, absorbed by dust particles on the disk, has a wavelength of $\sim 1 \mu m$, and the emission re-radiated by the disk falls in the NIR, MIR and mm regions of the electromagnetic spectrum, the radiation field can be separated, for simplicity, in two frequency ranges. One is given by the stellar energy distribution and hence related to the effective temperature of the central star, T_{eff} , called the *stellar* range. The other is related to the disk local temperature and dominated by the local emissivity, known as the *disk* range. As the stellar flux penetrates the disk, only a fraction $d\tau_*/\mu_0$ is absorbed at each z , where τ_* represents the mean optical depth at the stellar range. The main opacity source in disks around CTTS is dust grains, that get to survive in most of the disk thanks to the low temperature present, except in the vicinity of the central star. This energy is then re-radiated at the wavelengths describing the local temperature, i.e. the disk range, so the direct incident stellar flux decreases with height. Additionally, since dust opacity increases as λ decreases, the hotter the star (and thus the shorter the wavelength of its emission) the larger the opacity at the stellar range, as a result more energy is captured and a higher disk heating is produced.

The peculiar shape of the temperature profile has significant observational implications. First, features formed in the disk atmosphere (optically

thin upper layers) like those from silicates, will appear in emission (Calvet et al., 1992; Furlan et al., 2006; McClure et al., 2010), even if the disk is optically thick, because the temperature decreases toward the midplane being higher at the surface. Second, molecular features formed in the upper layers, as the CO near infrared (Carr, 1995; Carr et al., 2001; Najita et al., 2003, 2008) and water lines (Clarke and Pringle, 1993), will also appear in emission. It is worth mentioning that the high temperatures of the upper layers imply that molecules can exist in the disk in gas form, even when the temperatures at the midplane are too low and molecules settle onto grain surfaces (Alexander and Armitage, 2007; Akeson et al., 2005).

The disk surface density can be calculated in a self-consistent way based on the equations of an irradiated accretion disk. For a geometrically thin accretion disk with a constant mass-accretion rate \dot{M} , the surface-density distribution is equal to

$$\Sigma = \frac{\dot{M}}{3\pi\nu} \left[1 - \left(\frac{R_*}{R} \right)^{1/2} \right], \quad (2.7)$$

given by the conservation of the angular momentum flux. In the parametric α prescription (§2.1) and using equation 1.2 and 1.7, the viscosity can be written as $\nu = \alpha c_s^2 / \Omega_K$, with $c_s \propto T^{1/2} \propto R^{-1/4}$ and $\Omega_K \propto M_*^{1/2} R^{-3/2}$, such that at large radii the surface density of the disk will be

$$\Sigma \sim 4 \left(\frac{\dot{M}}{10^{-8} M_\odot \text{yr}^{-1}} \right) \left(\frac{\alpha}{0.01} \right)^{-1} \left(\frac{T_{100\text{AU}}}{10\text{K}} \right)^{-1} \left(\frac{R}{100\text{AU}} \right)^{-1} \left(\frac{M_*}{1M_\odot} \right)^{-1/2}, \quad (2.8)$$

in units of gr cm^{-2} . The dependence of disk surface density with radius, $\Sigma \propto R^{-1}$, for irradiated accretion disks is much flatter than $\Sigma \propto R^{-1.5}$ usually assumed, and it has been confirmed by observations (Alexander et al., 2006a).

Assuming this dependence at all radii, the disk mass would be given by

$$\frac{M_d}{M_\odot} = 0.03 \left(\frac{\dot{M}}{10^{-8} M_\odot \text{yr}^{-1}} \right) \left(\frac{R_d}{100\text{AU}} \right) \left(\frac{\alpha}{0.01} \right)^{-1} \left(\frac{T_{100\text{AU}}}{10\text{K}} \right)^{-1} \left(\frac{M_*}{1M_\odot} \right)^{1/2}, \quad (2.9)$$

where R_d is the disk outer radius. This is consistent with values determined from dust emission at millimeter wavelengths as well as with the mass-accretion rates obtained from the inner disk properties. Note that for a

known \dot{M} , the temperature at the outer disk radii (T_{Rd}) is fixed by stellar irradiation, then, M_d and α are complementary parameters and sizes can be estimated from observations.

Chapter 3

Dust in Protoplanetary Disks

To characterize dust in protoplanetary disks, one must focus on the study of the infrared excess emission observed in these disks, since this emission comes from the absorption of stellar radiation by optically thick dust which is then reprocessed, as a product of its interaction with matter, and reemitted at longer wavelengths. For this reason several observations of disks have been made, specially with *Spitzer* and *Herschel*, over a large range of ages and environments. One powerful tool we can use to study protoplanetary disks is the spectral energy distribution.

3.1 Spectral Energy Distribution

Thermal emission of dust in the disk is detected at long, infrared and millimeter wavelengths, where it dominates the spectral energy distribution. A SED is a graph of the energy (flux) emitted by an object as a function of wavelength or frequency. Figure 3.1 shows typical blackbody curves. It shows that the amount of energy emitted by the object at all wavelengths varies with the temperature of the object. Hotter objects emit more light at shorter wavelengths than cooler objects; therefore the hotter the object, the more the peak wavelength is shifted toward the left of the graph. Stars are not perfect blackbodies, specially at short wavelengths, but their emission is very similar to blackbodies. Any emission from dust around the stars (disks) will show up as an excess emission at IR wavelengths, since dust is being heated by the star reprocessing the stellar light toward longer wavelengths.

In disks, the dust temperature distribution is a function that depends on several factors, for example the disk geometry, the radiation from the star, and of course, the opacity of the dust particles. For black body grains, the

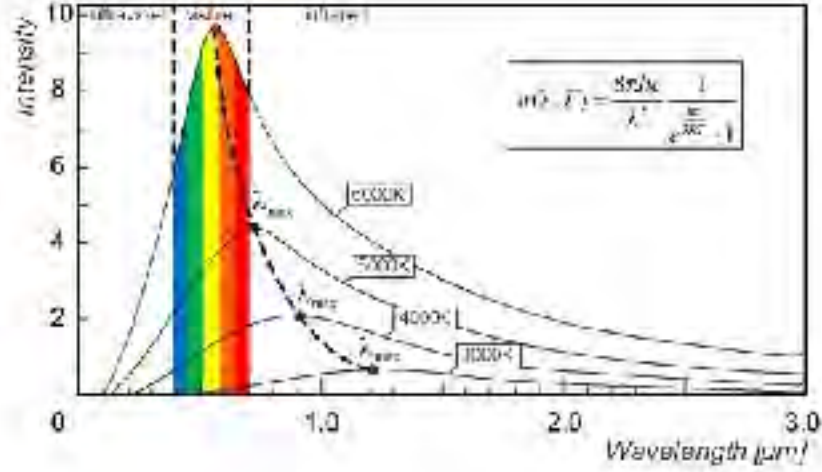


Figure 3.1: Blackbody curves for different temperatures.

dust temperature distribution as a function of distance from the central star is $T(r) \propto r^{-1/2}$. This result is obtained assuming optically thin dust at all wavelengths and a dust opacity $\kappa_{\nu}^{\text{abs}}$ proportional to ν^p , with $p = 0$. The spectral slope of the SED can then be derived, if one adopt a dust density gradient of the form $n(r) \propto r^{-m}$, as follows:

$$F_{\nu} \propto \nu^{3+p-0.5(3-m)(4+p)} \quad (3.1)$$

The optically thin approximation does not apply to the disk mid-plane, where most of the total mass of the disk resides, but it gives a suitable first order estimate of the temperature gradient of the disk upper layers, which are responsible for the emission in the 10-100 μm wavelength range in the SED. Since IR emission in disk is the result of the stellar light being absorbed and re-emitted by dust grains into longer wavelengths, usually three wavelength regimes can be seen on the SED: 1 – 10 μm , 10 – 100 μm , and the sub-mm - mm wavelength range (Figure 3.2), and each regime corresponds to different physical regions on the disk.

In the innermost part of the disk temperatures are so high (~ 1500 K) that dust cannot survive, and therefore, close to the star, there is a dust-free cavity and the stellar radiation can directly illuminate the disk edge. The emission from this region dominates the 1 – 10 μm wavelength range. The hottest dust located in this inner disk edge represents only a very small fraction ($\sim 10^{-6}$) of the total dust mass.

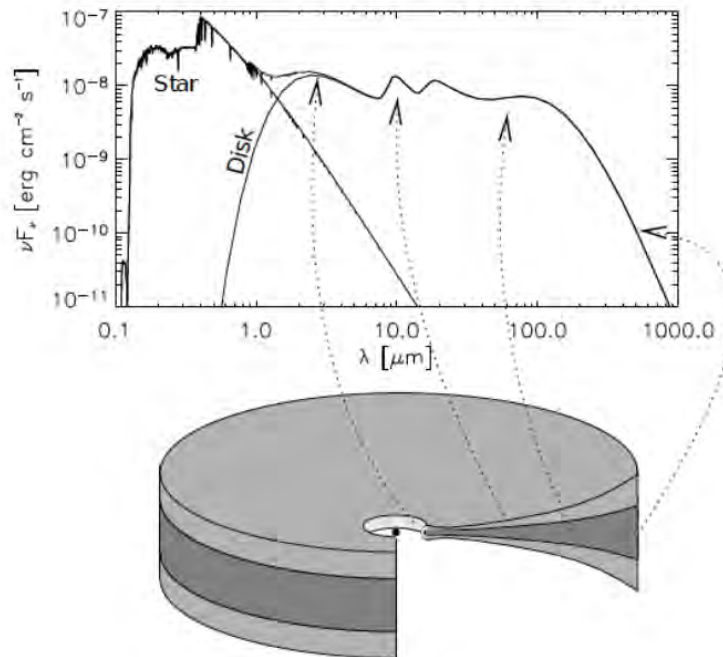


Figure 3.2: Schematic spectral energy distribution of a protoplanetary disk. The optical spectrum is dominated by the stellar photosphere, while at IR and longer wavelengths the disk dominates. Shown is the region from which different parts of the disk spectrum are emitted. Taken from Dullemond et al. (2007).

The warm dust, with temperatures between 100 – 500 K, dominates in the 10 – 100 μm range and is located in the disk surface layers from a couple to a few tens of AU from the star. At this wavelength range many vibrational resonances of different dust species are seen in emission (if the disk is not viewed edge-on). This allows us to study the mineralogy and composition of this warm dust. Interestingly, these characteristic signatures seen on the SED are produced by small (1 μm) grains. Giving that, at these distances, settling timescales for dust particles are shorter than the disk lifetime, it is believed that turbulent mixing from the disk mid-plane is responsible for the maintenance of this small dust in the disk upper layers. It is important to keep in mind, that the dependence of the properties of the grain population with time in the disk is a function of dust growth, mixing and destruction. This warm dust typically represents 10% of the disk mass.

Finally, the sub-mm wavelength range is dominated by cold dust in the mid-plane of the disk. Here is where most of the disk total mass (90%) resides. If one considers the emission from the disk to be optically thin, estimates of disk mass can be made from sub-mm fluxes, assuming a certain dust temperature and a power-law dependence of the frequency with the opacity of the grains, $\kappa(\nu) \propto \nu^\beta$. Then, the observed flux will have the form $F_\nu \propto \nu^\alpha$, with $\alpha = 2 + \beta$. α is usually called the spectral index, while β is known as the opacity spectral index. Protoplanetary disks have $2 < \alpha < 3$, while $\beta_{\text{disk}} \approx 1$, according to studies of numerous stars at different star-forming regions (Calvet et al., 2002; Testi et al., 2003; Natta et al., 2004; Andrews and Williams, 2005). For comparison, optically thin interstellar-like dust would have $\alpha = 2 + \beta_{\text{ISM}} \approx 3.8 \pm 0.2$. Therefore, one can have a proxy of the grain size distribution by looking at these spectral indices at mm wavelengths (e.g. Testi et al., 2003; Draine, 2006), assuming the Rayleigh-Jeans approximation for the source function, which in this case is just the Planck function. The values of α found in protoplanetary disks imply the presence of “black body” grains with a wavelength independent opacity, such that the emission is dominated by large grains, typically larger than ≈ 1 mm. Since dust settling timescales are short near the star, i.e. grain growth is expected to be faster in the inner disk than outside, the millimeter spectral index in protoplanetary disks should increase outwards. This effect has been observed in a few cases (Pérez et al., 2012; Testi et al., 2014; Carrasco-González et al., 2016; Tsukagoshi et al., 2016).

Figure 3.3 shows a predicted SED, using irradiated accretion disk models described in §2.2, indicating the contribution from the star (photosphere), constructed from the observed colors of Kenyon and Hartmann (1995), and the contribution from the disk. The emission from the disk model is generally divided in two components. A first component, responsible for the near-IR (NIR) excess, produced by the inner edge of the disk and usually called the disk “wall”. On it, disk temperatures are high enough to sublimate dust particles, leaving behind it a region filled with only gas. The second component, is the emission from the disk itself and covers a wide range of wavelengths as described above. The predicted SED was constructed assuming a $M_* = 0.5 M_\odot$ and a disk radius of $R_d = 350$ AU.

3.2 Classification of YSOs

YSOs, with masses $< 8 M_\odot$, are typically classified according to their mass as:

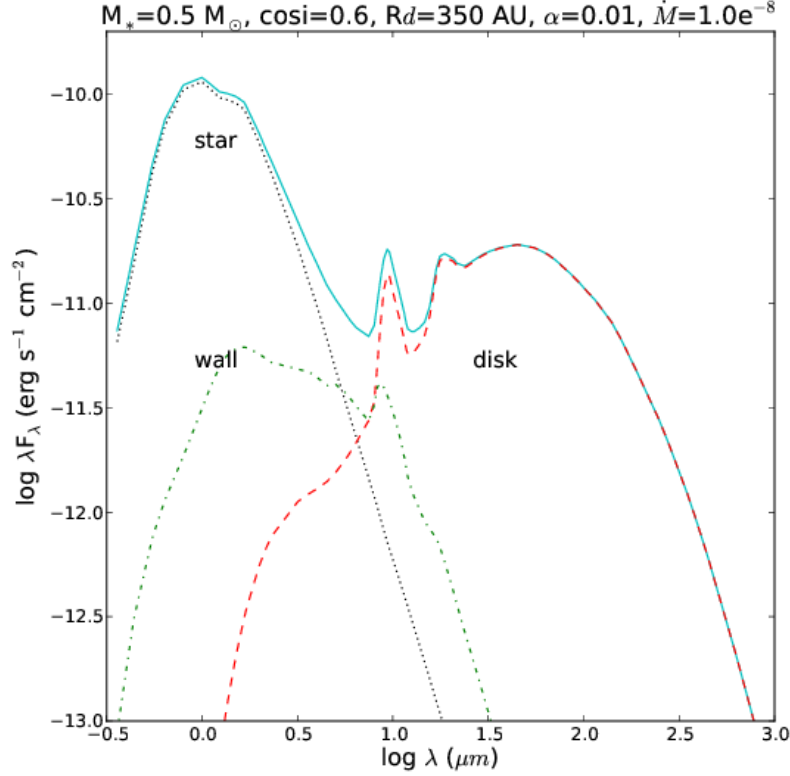


Figure 3.3: Theoretical SED indicating the contribution of the star (photosphere), the wall and the disk.

- **Herbig Ae/Be stars (HAeBe)**, A and B stars with emission lines (Herbig, 1962), with masses $2 M_\odot < M_* < 8 M_\odot$ (Hernández et al., 2005; Williams and Cieza, 2011).
- **T Tauri stars (TTs)**, characterized by late-type spectra with strong emission lines (Herbig, 1962), with masses $0.08 M_\odot < M_* < 1 M_\odot$. These are also divided, based on the strength of their emission lines, into (Hartmann, 2009b):
 - **Classical TTs (CTTs)**, with an equivalent width of $H\alpha$ larger than 10 \AA . These stars also show strong excesses in line and continua above the intrinsically photospheric fluxes and are

thought to be accreting mass from a disk. Intermediate mass TTS (IMTTS) are CTTS with spectral types F & G.

- **Weak-line TTSs (WTTSs)**, with $H\alpha$ equivalent widths lower than 10 \AA , although some studies indicate that the $H\alpha$ equivalent width separating both classes depends on spectral type. These stars are believed not to be accreting mass from a disk.
- **Young brown dwarfs (YBDs)**, substellar objects with masses $M_* < 0.08 M_\odot$ that will never reach a central temperature high enough to burn hydrogen.

Now, based on observational criteria, there are different classification schemes related to the IR excess emission observed in these objects (Lada et al., 2006; Hernández et al., 2007b; Furlan et al., 2009). Since this emission comes mostly from the disk, and over time the disk gets colder and emits less, the shape of the SED will change depending on the evolutionary stage of a given disk population. Therefore, the slope of the SED has been widely used to classify YSOs in the 2.0 to 25 μm infrared range (Lada et al., 2006; Hernández et al., 2007b), defined as:

$$n = \frac{\log(\lambda_1 F_{\lambda_1}) - \log(\lambda_2 F_{\lambda_2})}{\log(\lambda_1) - \log(\lambda_2)} \quad (3.2)$$

where λ_i and F_{λ_i} are the wavelength and the observed flux at that particular wavelength, respectively. This classification is based on the following groups:

- **Class I**, with positive slope ($n > 1$). Commonly called protostars: those that are still embedded in an optical thick envelope releasing the excess emission.
- **Class II**, with negative slope ($-2.56 \lesssim n < 0$). Characterized by having accreting circumstellar disks and, in the low mass regimen ($\leq 1M_\odot$), related to classical T Tauri stars (CTTS).
- **Class III**, with photospheric slopes ($n < -2.56$). Those who are believed to have dissipated almost all their inner disk material and, in the low mass regimen, associated with weak T Tauri stars (WTTS).

This classification is believed to be an evolutionary continuum sequence of the disks lifetime.

The accretion-based classification of CTTSs and WTTSs have to be taken carefully. Although most CTTSs are Class II, some WTTSs may

show emission from remnant disks; also, some stars with clear signs of being accreting may show no excess in the $1 - 10 \mu m$ range and thus could not be classified as Class II. Another aspect of CTTSs and WTTSs is the presence of emission lines in their spectra, but in CTTSs the lines are much broader and generally stronger.

3.3 Color-color Diagrams

A powerful tool that provides useful information about the nature of YSOs are the color-color diagrams. Previous studies (Lada and Adams, 1992) have shown that each type of YSO tends to occupy a certain well defined region on these diagrams.

On these plots, in particular the J-H versus H-K (JHK) color-color diagram, stars with intrinsic excess emission, heavily reddened stars, and stars with unreddened photospheric colors can be distinguished from each other. Stars with IR excess fall to the right of the band defined by the projection of the giant and dwarf sequences along the direction of interstellar reddening (Figure 3.4), known as the reddening band. The extinction vector is defined by a standard reddening law (Rieke and Lebofsky, 1985).

In the near IR, CTTSs show characteristic excesses. In particular, in the JHK color-color diagram, most CTTSs fall in a well-defined region, “the CTTS locus” (Meyer et al., 1997), shown as a straight line at Figure 3.4 and at the left panel of Figure 3.5, which is defined by large H-K colors indicative of dramatic intrinsic extinction due to the presence of circumstellar material, while WTTSs have colors consistent with dwarf stars.

In color-color diagrams constructed with combinations of the four bands of the Infrared Array Camera (IRAC) instrument, at 3.6, 4.5, 5.8, and 8 μm , and the Multiband Imaging Photometer (MIPS) 24 μm band, most CTTSs fall in a region well separated from the WTTSs. The right panel of Figure 3.5 shows one of these diagrams. The WTTSs have colors ~ 0 , while most CTTSs populate a distinct region of the [3.6][4.5] versus [5.8][8.0] diagram, which corresponds to the emission expected from optically thick disks (Allen et al., 2004; Hartmann et al., 2005; Muench et al., 2007).

3.4 Dust settling

Based on previous studies in different star-forming regions followed with *Spitzer*, a clear exponential decay is observed between the fraction of stars with disks and age of different stellar populations (Hernández et al., 2007b).

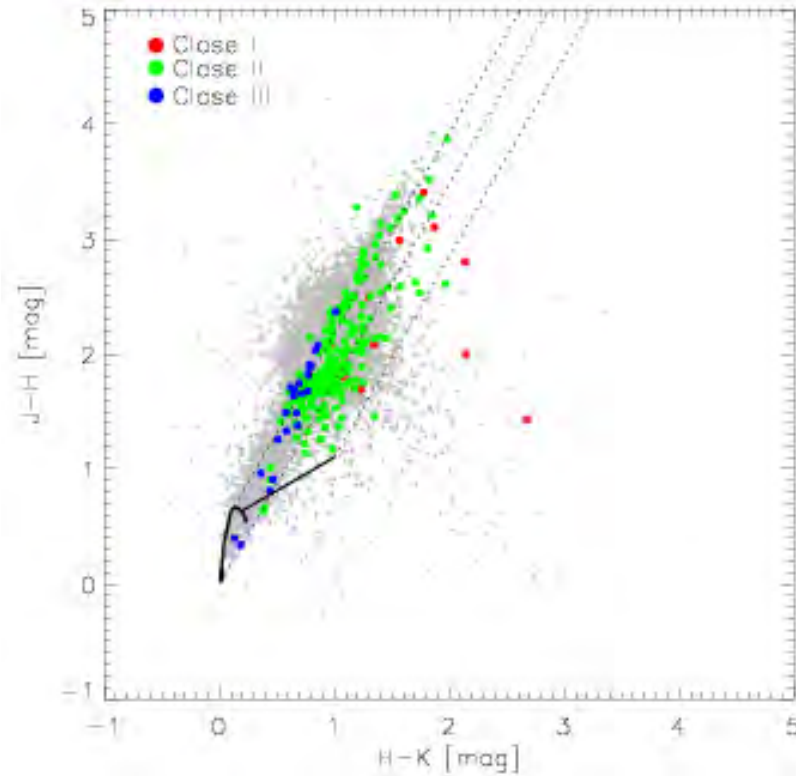


Figure 3.4: JHK color-color diagram of YSOs in the DR17 cluster located in the Cygnus X star-forming region. The different YSOs classes seem to populate different regions of the diagram. Class I sources (red circles) have the most intrinsic IR excesses, class II sources (green circles) are characterized by modest values of extinction, while class III sources (blue circles) have no IR excess. Grey circles indicate the rest of the samples of the catalog that did not meet the color cuts criteria used for the classification. The solid curve line represents the unreddened main sequence while the straight solid line the locus of the CTTSs (Meyer et al., 1997). Dashed lines are parallel to the reddening vector, where the two leftmost lines define the reddening band for normal stellar photospheres.

Figure 3.6 shows the disk frequency in late-type stars as a function of age of the populations, which include clusters and associations. The disk frequency

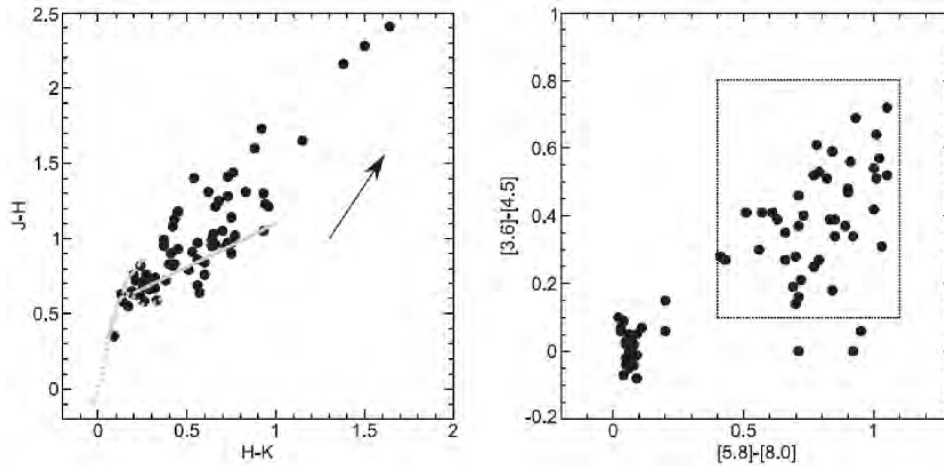


Figure 3.5: Left panel: Taurus stars in the J-H versus H-K diagram. The dwarf sequence and the CTTS locus (solid gray line) are shown. Observations have not been corrected for reddening. Right panel: Taurus stars in the IRAC [3.6][4.5] versus [5.8][8] diagram. The dotted square indicates the region covered by colors of irradiated accretion-disk models. Data from Hartmann et al. (2005) as adapted from Calvet and D’Alessio (2011).

is measured by the ratio of stars with near-IR excess (either JHK or in the Spitzer/IRAC bands) to the total number of stars, so it is actually a measure of the presence of the inner disk of the stars. It seems that by 5 Myr about $\sim 80\%$ of the inner disks have dissipated. An important point to kept in mind is that the disk frequency is also mass dependent. Disks around intermediate-mass stars seem to evolve faster than for later types (Hernández et al., 2005, 2007b).

Besides the decay of disk frequency, it has also been observed that the excess emission itself decreases with age (Hernández et al., 2007b). The top panel of Figure 3.7 shows how the median SED slopes of [3.6]-[8.0] IRAC bands for several stellar groups decrease with age.

The decreasing of IR excess can be explained by grain growth and by settling of dust to the disk midplane that cause a reduction of the flaring of the disk and, by consequence, a decrease in its emitting flux. This interpretation is confirmed by analysis made by D’Alessio et al. (2006a) with irradiated accretion disk models. On these models the settling process is simulated by introducing the ϵ parameter, which represents the dust-to-gas mass ratio at the disk atmosphere compared to that of the ISM; so a depletion of small

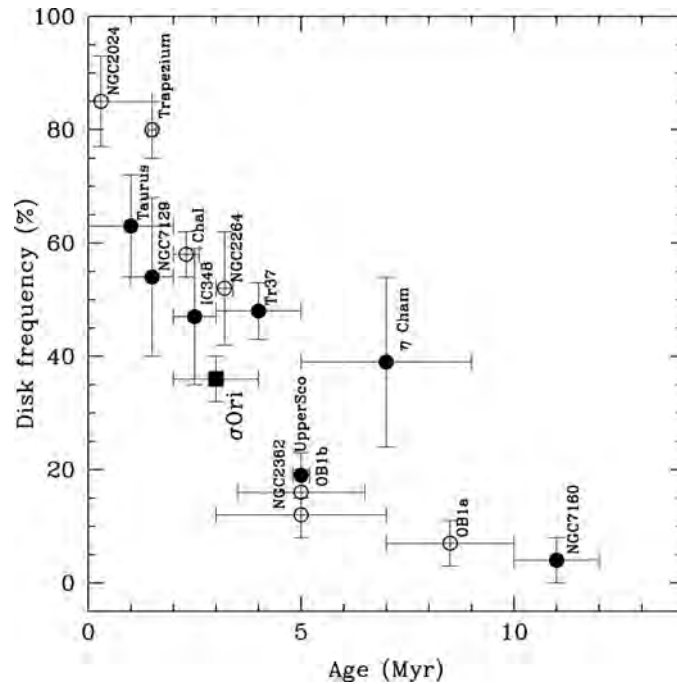


Figure 3.6: Fraction of stars with near-infrared disk emission as a function of the age of the stellar group. Open circles represent the disk frequency for stars in the TTS mass range derived using JHKL observations, while filled symbols represent the disk frequency calculated for stars in the TTS mass range using IRAC data. Taken from Hernández et al. (2007b).

grains in the upper layer of the disks (and thus more abundance of larger grains in the midplane) will be reflected as a small (less than one) value of ϵ as expected in evolved disks, while a value of one indicates no evolution. An example of this is seen in Figure 3.8 that shows how different degrees of dust settling affect the IR excess emission of disk models, and therefore also changing their SED slopes. Comparisons of predicted median SEDs slope of models with different inclination angles, with those obtained from observations of stellar groups with different ages (bottom panel of Figure 3.7) have confirmed the correlation between the drop of the IR excess and dust settling (Hernández et al., 2007b; D’Alessio et al., 2006a).

So combining the SED slope n , that contains information about the shape of the SED at a certain wavelength range, with information from irradiated accretion disks models, one can estimate the degree of settling

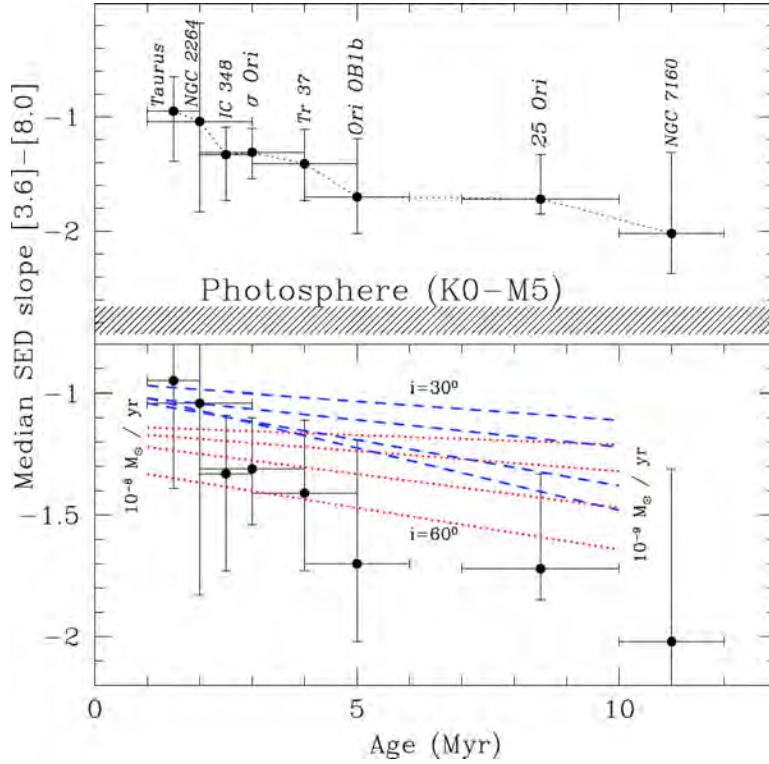


Figure 3.7: Top: Median SED slope in the IRAC spectral range vs. stellar ages of different stellar groups. The dashed region indicates the photospheric levels. Note how the infrared disk emission seems to decrease with the age of the stellar groups. Bottom: a comparison with predicted values from D’Alessio et al. (2006a). Two sets of models are displayed showing different orientation of the disks, 30° (dashed lines) and 60° (dotted lines). Different lines describe different degree of settling ($\epsilon = 1, 0.1, 0.01, \text{ and } 0.001$) showing flatter slopes for models with less degree of settling. Taken from Hernández et al. (2007a)

in circumstellar disks (D’Alessio et al., 2006a; Calvet et al., 2005). It is worth mentioning that for nearby objects where high-resolution imaging is possible, Pinte et al. (2016) showed that using ALMA resolved-images of HL Tau at different wavelengths, combined with a radiative transfer model that was able to account for the observed gaps, bright rings and radial changes of the emissivity index, estimations of dust settling, viscosity coefficients and gas-to-dust ratios can be made.

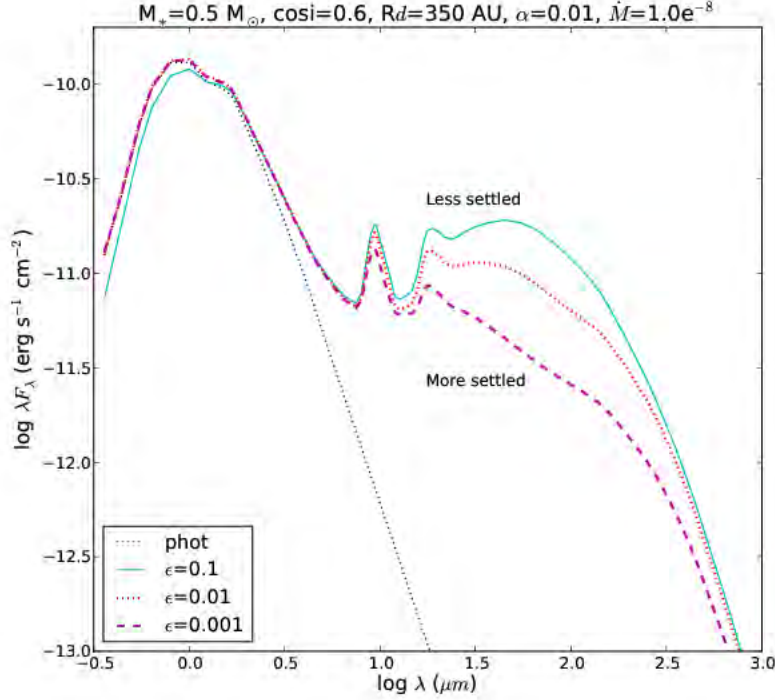


Figure 3.8: SEDs of models with different degree of settling as indicated by the dust-to-gas mass ratio ϵ , where a value of $\epsilon = 1$ indicates ISM-like dust (no evolution), while lower values represent an increase in the degree of dust settling. A typical photosphere (dotted line) is also shown.

3.5 Dust processing and composition

Even though dust grains constitute only 1% of the total mass in circumstellar disks, they dominate their opacity; so knowing the radiation properties of dust is of crucial interest in order to determine the temperature and density structure of these disks.

It is believed that over time, the initial ISM-like dust population evolves to large bodies that settle to the disk midplane providing the raw material for planets. Dust also plays an important role in disk chemistry, since the formation of molecules takes place on the grain surfaces. If the temperatures are high enough, these molecules will be present on the disks in gas form, and then, can be observed with submillimeter and millimeter telescopes.

Infrared spectroscopy have been widely used to characterize dust in protoplanetary disks. Thanks to telescopes, like ISO and *Spitzer Space Telescope*, a wide amount of data have been acquired in order to study the mineralogy of disks around young stars, putting several constraints on the type of dust particles (amorphous/crystalline) present on disks and in the chemical composition of their grains, addressing questions such as radial distribution and mixing processes.

In accretion disks the initial dust composition is assumed to be similar to the molecular cloud core from which the stars were formed, as the infalling material comes from the ISM. This initial composition changes during the passage of the accretion-shock front, created when material from the molecular cloud is accreted onto the disk, where the oxygen could convert into water or could merge with silicon atoms to form quartz (SiO_2). The most abundant dust species are those composed of silicates and carbonates, e.g., compounds of O, Si, C, Fe and Mg (Dorschner et al., 1995).

Different processes are expected to occur in protoplanetary disks, whose appearance depends on the radial distance from the central star. These processes can lead to a significant dust processing on circumstellar disks: at the disk inner regions, processes like thermal annealing, ion irradiation by stellar flares, destruction of carbonaceous dust by oxidation, X-ray and UV irradiation play an important role. At the outer disk, processes like solid phase reactions and molecular ices formation can occur.

The ISM-like dust consists primordially of amorphous silicates and carbonates. This is corroborated by observations at $10 \mu\text{m}$ with ISO that have proven that 98 % (by mass) of the silicates in the ISM have an amorphous structure (Kemper et al., 2004). Since crystalline grains are not present in the ISM, the cold crystals must have been produced in the disk. This can be done through transport of grains from the inner disk to the outer disk. This transport can be either through radial mixing in the disk mid-plane, or transport of grains entrained in a disk wind/outflow (Gail, 2001, 2002). An alternative to transport of grains from the inner to the outer disk are local processes that heat up grains to temperatures above the glass temperature, such as lightning or shock waves induced by planet-disk interactions (Bouwman et al., 2008, 2010; Juhász et al., 2010; Mulders et al., 2011).

There has also been demonstrations of dust crystallization in protoplanetary disks with infrared spectroscopy studies of HAeBe stars, T Tauri stars and brown dwarfs (Malfait et al., 1998; Bouwman et al., 2001; Acke and van den Ancker, 2004; Forrest et al., 2004; van Boekel et al., 2005; Kessler-Silacci et al., 2006; Sicilia-Aguilar et al., 2007; Watson et al., 2009; McClure et al., 2010; Furlan et al., 2009; Juhász et al., 2010; Manoj et al., 2011; Mulders

et al., 2011). Since crystallization of amorphous silicates can only occur at high temperatures, these observations suggest a temperature greater than ~ 500 K for the amorphous material to become crystals.

In the context of protoplanetary disks, the mineral structures that have been extensively discussed are Mg-Fe olivines and pyroxenes, which form forsterite (Mg_2SiO_4) and enstatite (MgSiO_3) crystals, respectively. These silicate particles show a wide variety of IR features, characteristic of their chemical structure and composition. In Figure 3.9 the spectra around $10 \mu\text{m}$ of three TTSs in Taurus are shown. The first one consists of pristine, ISM-like dust (IP Tau/magenta line) peaking at $9.6 \mu\text{m}$. The second one (CX Tau/blue line) exhibits a smooth and flatter $10 \mu\text{m}$ silicate feature, indicative of grain growth. The third one (IS Tau/green line) shows strong crystalline features of enstatite and forsterite as a result of dust processing.

An important aspect to be kept in mind is that the silicate features observed in emission arise in the optically thin disk atmosphere, since the midplane region is optically thick, and thus, featureless. So with IR spectroscopy we can only trace a small part of the whole disk material. The shape of the spectral feature depends on the properties of the dust grains (size, shape, chemical composition, material structure, etc.) and in the dust temperature. Besides, the features will be influenced by disk geometry, since the outer regions of flared disks will significantly contribute to the spectrum at $10 \mu\text{m}$, while for flat disks the inner disk edge is more dominant.

The most important processes that are believed to turn pristine, interstellar dust grains into minerals are:

- Evaporation and re-condensation of the original grains at temperatures and densities such that chemical-equilibrium products are produced (Grossman 1972; Gail 2001, 2004). These conditions are satisfied only in regions close to the central star ($T > 1200$ K).
- Annealing of grains through viscous heating of the disk by accretion processes such as the expected at $r \lesssim 1$ AU at temperatures below the grains sublimation points (800-1200 K) (e.g., Gail, 2001, 2002; Nuth et al., 2000; Bockelée-Morvan et al., 2002) or as a product of spiral density wave shocks over the central 10 AU originated by fluid-mechanical instabilities (e.g., Harker and Desch, 2002).
- Local heating of dust and gas by shock waves driven by tidal interactions of a giant planet with the disk material (e.g., Bouwman et al., 2010; Mulders et al., 2011; Juhász et al., 2010). In this case warm ~ 400 -500 K crystalline silicates are produced.

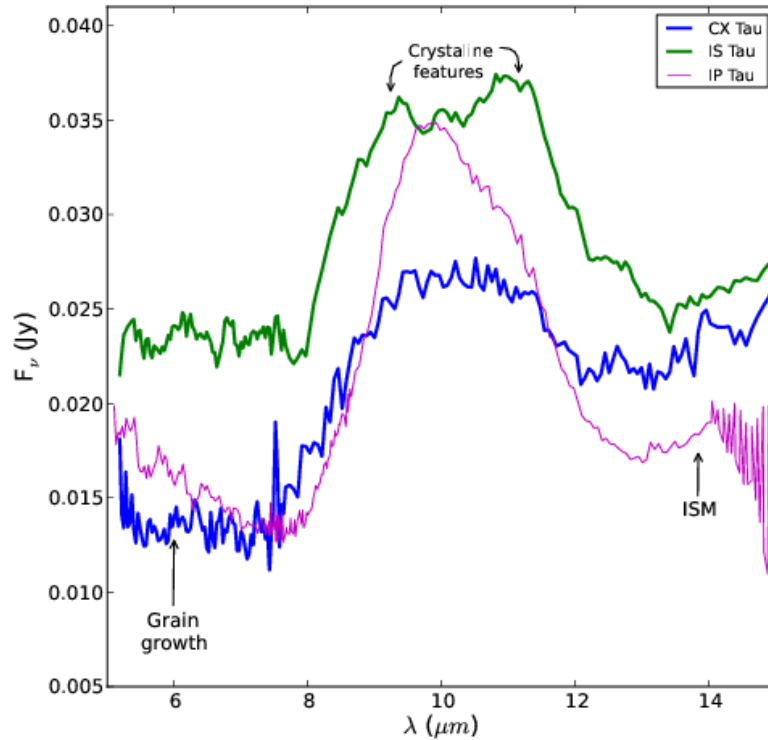


Figure 3.9: $10 \mu m$ silicate features of T Tauri stars: IP Tau (magenta line) characteristic of submicron ISM-like dust, of CX Tau (blue line) which shows signs of significantly grain growth and of IS Tau (green line) which exhibits crystals features as a result of dust processing.

In Figure 3.10 the IRS spectrum of IS Tau is shown along with the positions of the strongest mineral features expected in submicron dust grains. As can be noted in the figure, the spectrum of IS Tau exhibits several crystalline features similar to those present on the comet Hale-Bopp (Crovisier et al., 1997, 2000) also shown in the figure, indicating that dust in IS Tau has been processed in a very similar way to that of comets (Watson et al., 2009).

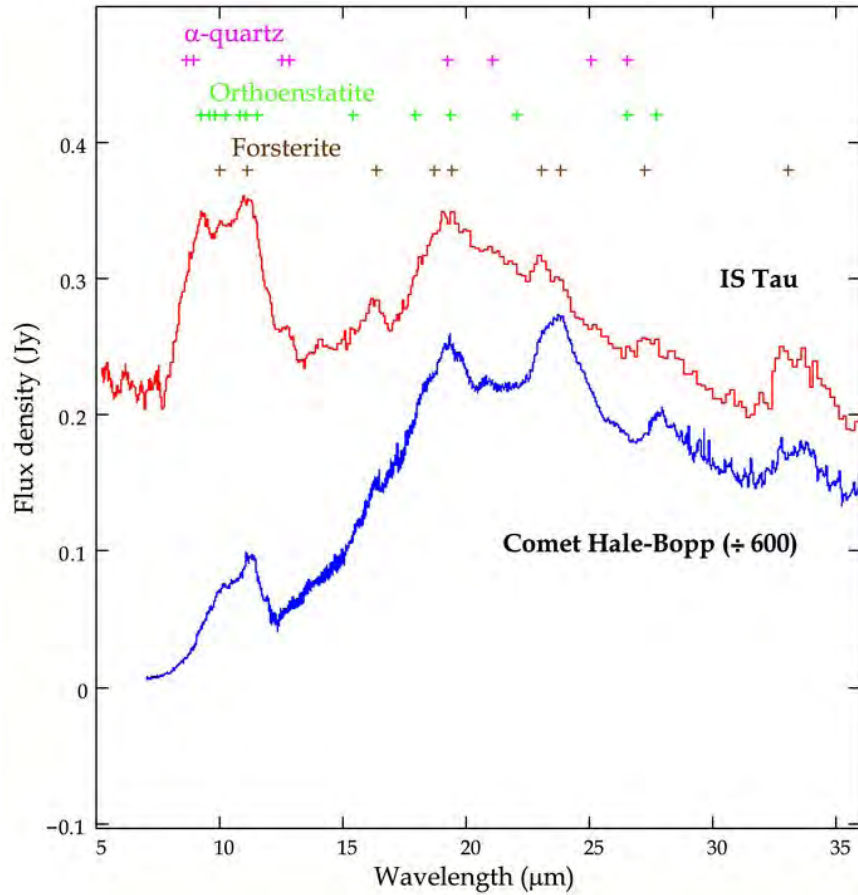


Figure 3.10: *Spitzer*-IRS spectrum of IS Tau. At the top are also indicated the positions of the strongest mineral features expected in submicron dust grains, calculated from optical constants for α quartz (Wenrich and Christensen, 1996), orthoenstatite (Jaeger et al., 1998), and forsterite (Fabian et al., 2001). At bottom, for comparison, is an ISO SWS spectrum of comet Hale-Bopp (Crovisier et al., 1997, 2000). Taken from Watson et al. (2009).

3.5.1 Polycyclic Aromatic Hydrocarbons (PAH)

Analysis of MIR spectra around TTS and Herbig Ae/Be stars have shown clear PAH features among their spectral emission features (e.g., Geers et al., 2006; Acke and van den Ancker, 2004; Habart et al., 2004), however PAH detections around TTS are more scarce. The detection of PAH emission is an indicator that carbonaceous material subsists in protoplanetary disks

(Henning and Meeus, 2011). The main features can be seen at 3.3, 6.2, 7.7, 8.6, 11.3 and 12.7 μm . One limitation of the study of PAH features in TTS is the proper identification of PAH lines in the presence of strong silicate features, specially around 10 μm . It is believed that the UV radiation from the central star excites the PAH molecules, so PAHs can be useful in probing the strength of the UV radiation field. Moreover, given the high opacity of these molecules in the UV, the presence of PAH in the innermost part of disks can significantly affect the amount of UV radiation that will finally reach the outer regions. Therefore, PAH are an important agent in setting the temperature and chemical composition in disks. Since PAH emission can be produced close as well as far away from the star (Ressler and Barsony, 2003; Maaskant et al., 2014), the study of these features also give us a measure of the amount of flaring of the disks (Habart et al., 2006; Lagage et al., 2006). For all these reasons, studies of PAHs emission in protoplanetary disks and its correlations with stellar properties is essential to understand the diverse characteristics observed on these systems.

3.6 Disk Geometry and SED Shape

As stated in section 3.1, the SED describes the emission of dust in the disk, and naturally, this emission will depend on the geometry of the system. Since the SED is constructed with unresolved (photometric/spectroscopic) data, depending on the adopted properties for the dust, a range of disk geometries might fit the observed SED, and as a consequence, SED fitting suffers from some degeneracies. Even though, direct imaging is the best way to constraint the geometry of the disk, SEDs do contain very useful information that we can access without paying the high cost of deep, resolve observations, specially for star-forming regions like Orion, which are not as nearby as Taurus and Ophiuchus, for example. Figure 3.11 shows some examples of disk geometries along with their SED for comparison. As shown on the figure, the shape of the SED can give us a good idea of the disk structure and thus, studies of disk evolution using this methodology are also possible.

3.6.1 Transitional and Pre-transitional Disks

As shown on Figure 3.11, a lack of NIR excess is an indicator of dust depletion in the innermost regions of the disk. The hottest dust on these systems is observed to be cooler than the dust sublimation temperature of silicates, and therefore, an inner hole exists.

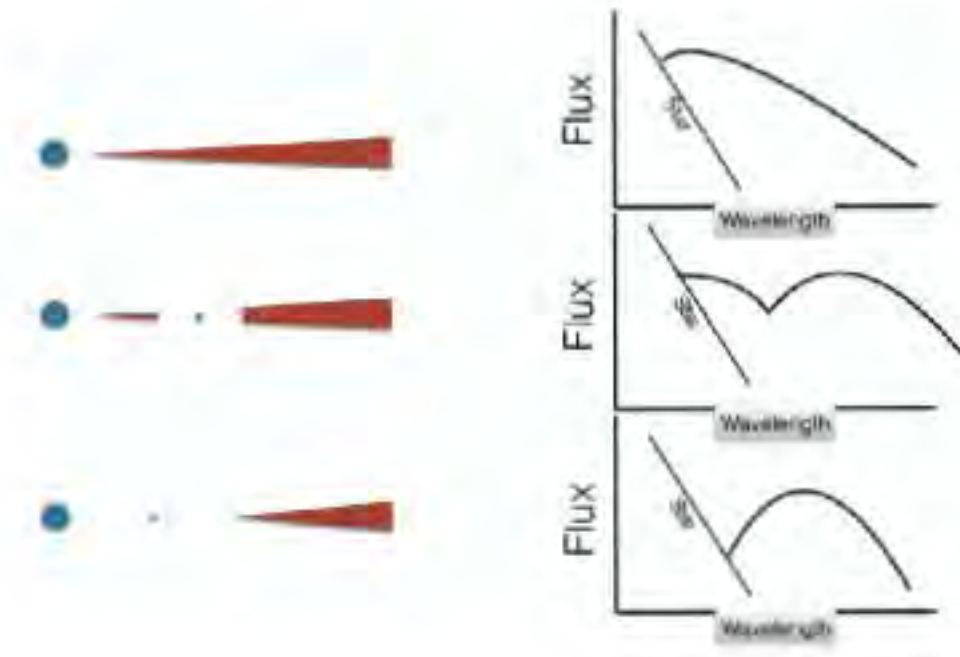


Figure 3.11: Disk geometries and their schematic SED shapes. From top to bottom: a full continuous disk, a disk with a gap formed by a young planet, and a disk with a hole and an outer disk. The disk gap causes a dip in the SED at the wavelength at which the removed grains would have emitted given their distance to the central star. The disk with large inner hole shows no NIR excess. Taken from Waters (2015).

These disks are classified as transitional disks (TD). The SED of these objects are characterized by small or negligible near-IR excesses but substantial emission in the mid-IR and beyond. A subset of these disks, commonly called pre-transitional disks (PTD), show similar features but with significant near-infrared excesses over the stellar photosphere. This excess has been explained by an optically thick disk located close to the star, separated from the outer disk by a gap (Espaillat et al., 2008a, 2010, 2011). Figure 3.12 shows a schematic picture of a TD and a PTD (top) along with the SED of LkCa 15 a PTD and of GM Aur a TD (bottom) for comparison.

Transitional and pre-transitional disks are thought to be at an important phase of disk evolution. The distinct SEDs of these sources have puzzled researchers over the years. For instance, dust clearing mechanisms in

TD/PTD are still under debate. Observations made with the *Spitzer Space Telescope* (Werner et al., 2004) have been widely used to identify TD/PTD and to characterize their IR emission. Moreover, *Spitzer* IRS spectra have also provided unprecedented details regarding disk cavities and dust properties within them. Extensive modeling of several TD/PTD around T Tauri stars (TTS) has been made (Calvet et al., 2002, 2005; Uchida et al., 2004; D’Alessio et al., 2005; Espaillat et al., 2007, 2008b, 2010; McClure et al., 2010, 2012, 2013). Some mechanisms have been proposed to explain the substantial dust clearing observed on these disks, e.g. grain growth, photoevaporation and interaction with embedded planets or stellar companions (Espaillat et al., 2014). Many researchers have proposed planet formation as the most likely mechanism, since models of planet-disk interaction have resulted in cleared disk regions (e.g., Paardekooper and Mellema, 2004; Zhu et al., 2011; Dodson-Robinson and Salyk, 2011; Dipierro and Laibe, 2017; Dong et al., 2017). Additionally, thanks to new generation-high angular resolution instruments, observational evidence implying the presence of (proto)planets has increased over the years (e.g., Huélamo et al., 2011; Kraus et al., 2011; Pinilla et al., 2015; Follette et al., 2015; Sallum et al., 2015, 2016; de Juan Ovelar et al., 2016; Andrews et al., 2016).

3.6.2 Photoevaporation in Disks

Besides an orbiting planet, truncation of the inner disk may result from the dissipation of gas being heated by high-energy radiation fields coming from the host star (Hollenbach et al., 2000; Alexander et al., 2006b; Clarke, 2007; Dullemond et al., 2007). The high energy photons, which radiate at UV, FUV and X rays wavelengths, can effectively heat the disk upper layer producing outflows induced by thermal pressure. The mass-loss rate is low, of order $10^{-10} M_{\odot}/\text{yr}$, compared to the mass accretion rate through the disk. However, with the decrease of mass accretion over time, the mass-loss produced by stellar winds gets more significant. At some point the disk will not be able to sustain material inside its gravitational radius and the disk will evaporate from the *inside-out*. This may causes the disk to quickly dissipates, shortening its lifetime (Alexander et al., 2014). Some models including viscous evolution with photoevaporative winds have been proposed in order to describe disk dispersal in this scenario (Clarke et al., 2001; Clarke, 2007; Alexander et al., 2006b; Dullemond et al., 2007).

The truncation of the *outer* parts of the disks, on the other hand, may be the result of environmental effects. In dense environments containing OB stars, far-ultraviolet radiation fields from massive stars can externally

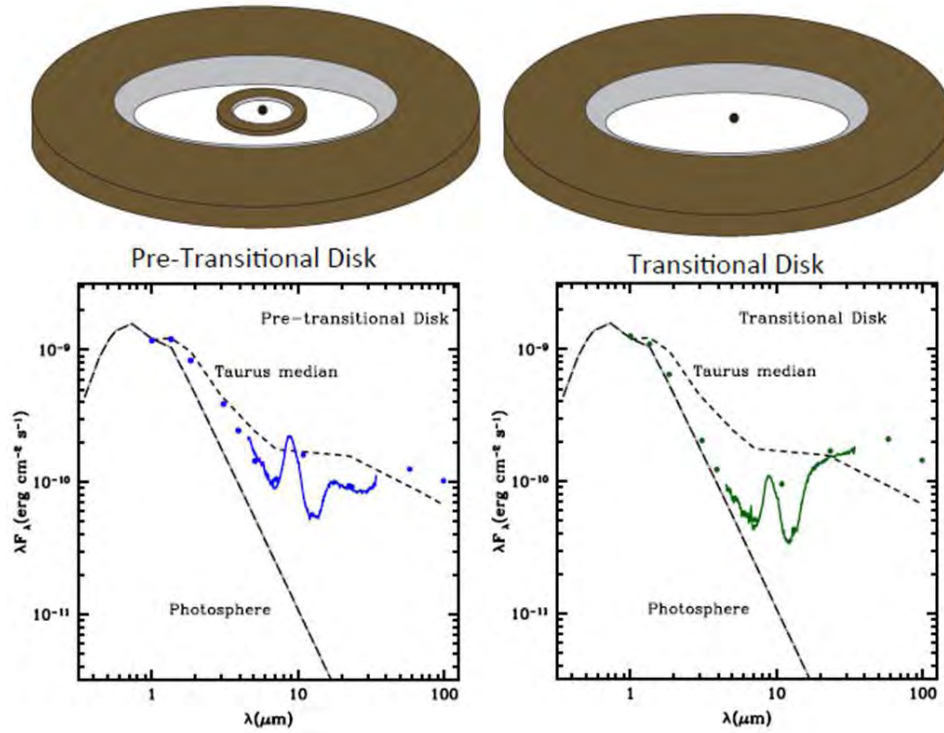


Figure 3.12: Top: Schematic of pre-transitional (left), and transitional (right) disk structure. Pre-transitional disks (PTDs) have an inner disk wall (light gray) and inner disk (dark brown) followed by a disk gap. Then the outer disk wall (light gray) and outer disk (dark brown). The transitional disk (TD) has an inner disk hole followed by an outer disk wall (light gray) and outer disk (dark brown). Bottom: SEDs of a PTD (left, LkCa 15; Espaillat et al. 2007) and a TD (right, GM Aur; Calvet et al. 2005). Both stars are late-type (K) and the fluxes have been corrected for reddening and scaled to the stellar photosphere (long dashed line) for comparison. Relative to the Taurus median (short dashed line; DAlessio et al. 1999), a PTD has a mid-IR deficit ($5 - 20 \mu\text{m}$, ignoring the $10 \mu\text{m}$ silicate emission feature), but comparable emission in the near-IR ($1 - 5 \mu\text{m}$) and at longer wavelengths, and a TD has a deficit of emission in the near-IR and mid-IR with comparable emission at longer wavelengths. As adapted from Espaillat et al. (2014).

illuminate the disks. The disk evaporates from *outside-in*, with a mass-loss

rate that decreases with time as the disk dissipates (Hollenbach et al., 2000; Anderson et al., 2013). Expected mass loss rates in externally-illuminated disks can be substantial (Adams et al., 2004; Facchini et al., 2016). Viscous evolution models including external photoevaporation (Clarke, 2007; Anderson et al., 2013; Kalyaan et al., 2015) have shown the strong impact that this dissipation mechanism can produce in the disk structure and, consequently, also in its lifetime. Externally-illuminated disks, known as proplyds, have been well characterized in the Orion Nebula Cluster (hereafter ONC; O’deH and Wen, 1994; Johnstone et al., 1998; Henney and O’DeH, 1999; Störzer and Hollenbach, 1999; García-Arredondo et al., 2001; Smith et al., 2005; Williams et al., 2005; Eisner et al., 2008; Mann et al., 2014) where the radiation from the Trapezium stars photoevaporates the disks. Evidence of outer photoevaporation in other star-forming regions has also been found (Rigliaco et al., 2009, 2013; Natta et al., 2014).

Observational evidence of mass loss on disks is supplied by the presence of forbidden lines of atomic and low-ionization species which present at least two different components (Hartigan et al., 1995). One is emitted by gas moving at high velocity (HVC), which is clearly identified with the jets that have been imaged and carefully studied in several objects (e.g, Carrasco-González et al., 2010, 2011; Carrasco-Gonzalez et al., 2011; Carrasco-González et al., 2012b,a, 2013; Galván-Madrid et al., 2017; Meaburn et al., 2000; Rodríguez et al., 2008; Rodríguez, 2011; Rodríguez et al., 2012, 2014, 2016). The other component is originated by a much slower moving gas (LVC). The LVC is detected in most Class II objects, and its origin is still unknown. It could be emitted at the base of a magnetically driven disk wind, as suggested by Hartigan et al. (1995) based on the OI lines, but it can also be a tracer of a photoevaporative disk wind, as shown by Pascucci and Sterzik (2009) using the LVC of the [NeII] mid-IR emission lines. Rigliaco et al. (2013) have shown that the LVC OI lines could also have multiple components, with one component tracing gas in keplerian rotation, and another component tracing a photoevaporative wind. The most common forbidden lines used to characterize photoevaporative winds are the lines of [SII] at $\lambda 6717$ and $\lambda 6732$ which ratio ($[SII] 6732/6717$) is used to estimate the density of the wind, the lines of [OI] at $\lambda 5770$ and $\lambda 6300$ which ratio ($[OI]5770/6300$) is used to obtain the temperature of the outflow and lines of [NII] which are expected in highly ionized gas, as in HII regions or in the bow shocks at the head of jets, and are weaker than the other forbidden lines in the partially neutral wind/jets of TTS. In Figure 3.13 we show the forbidden lines of [NII] and [SII] for the source SO587 in the σ Ori cluster reported by Rigliaco et al. (2009).

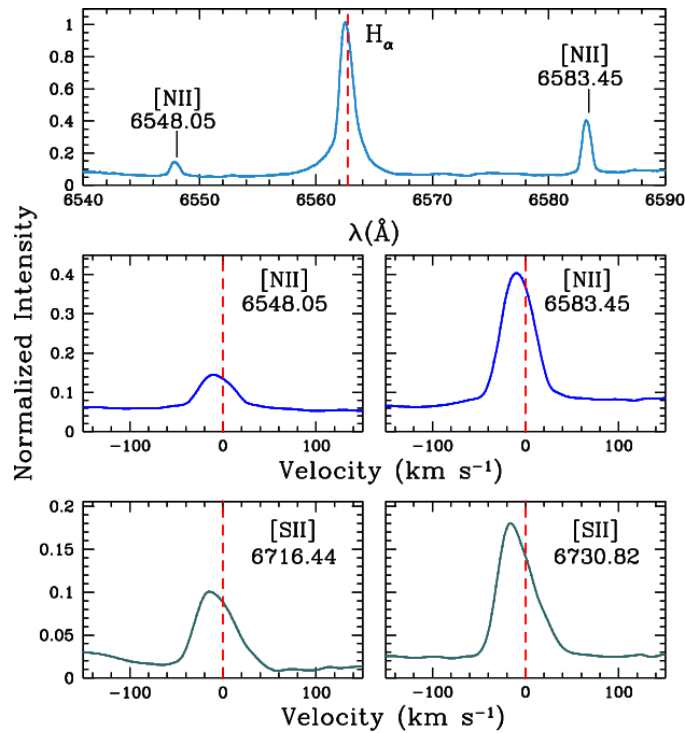


Figure 3.13: The top panel shows the spectrum in the H_{α} region, with H_{α} and the two $[\text{NII}]\lambda 6548.05$ and $[\text{NII}]\lambda 6583.45$ lines. Middle panel: $[\text{NII}]\lambda 6548.05$ and $[\text{NII}]\lambda 6583.45$ line profiles as function of the velocity shift with respect to the stellar velocity (vertical dashed line). Bottom panel: same for $[\text{SII}]\lambda 6716.64$ and $[\text{SII}]\lambda 6730.82$, as label. Taken from Rigliaco et al. (2009).

3.6.3 Orion Proplyds

In Orion, photoevaporative flows are manifest as proplyds, cometary-shaped ionization fronts that are associated with a number of stars in the inner regions of the ONC. The radiation from the four massive Trapezium stars, most notably θ^1 Ori C, a $40 M_{\odot}$ O star, externally illuminate the disks residing within ~ 2 pc from the cluster center. In the standard, and highly successful, models for proplyds, the FUV radiation field in Orion creates a layer of warm outflowing gas, fed by the disk, into which ionizing photons can only penetrate to within a couple of disk radii of the central star (Johnstone et al., 1998; Störzner and Hollenbach, 1999). The mass-loss rate deduced from these models, independently confirmed by spectroscopic measurements

(Henney and O'Dell, 1999), is high ($\sim 10^{-7} M_{\odot}/\text{yr}$) thus raising the issue of the longevity of circumstellar disks in this environment. Most of the well-studied Orion proplyds are caught in this first, short evolutionary phase when the mass-loss rate is very high. The optical spectrum of these objects is characterized by forbidden lines of ionized species, such as [SII] and [NII], that are formed in the outer part of the outflow, which is ionized, heated, and shocked by the radiation and wind of θ^1 C Ori (García-Arredondo et al., 2001).

Chapter 4

The Orion OB1 Association

The Orion OB1 association (Ori OB1) shows a well-defined age sequence, that suggests a large-scale triggered star formation scenario (Briceño et al., 2005; Briceño et al., 2007; Briceño et al., 2018). Ori OB1 contains a variety of stellar groups with very different properties.

As noted in Figure 4.1 the Ori OB1 association is divided into two sub-associations, Ori OB1a and 1b, which differ in age. Ori OB1b, has an estimated age between ~ 2 and ~ 7 Myr (Warren and Hesser, 1978; Brown et al., 1994; Briceño et al., 2005) and contains the σ Ori cluster along with subgroups in the process of dispersing their natal gas (Hernández et al., 2014). Ori OB1a on the other hand, contains more evolved populations with an age of $\sim 7 - 10$ Myr (Briceño et al., 2005; Briceño et al., 2007; Briceño et al., 2018) and it is where the 25 Ori cluster is located. This is one of the reason why the Orion star-forming region is an excellent laboratory to study the formation and evolution of stars and protoplanetary disks in the entire range of stellar masses, since it contains clusters young enough to have a high disk frequency with a large diversity of protoplanetary disks, and at the same time, clusters old enough to find dusty disk systems. This allows to estimate timescales of physical processes like dust settling, grain growth, planet formation and disk dissipation.

We targeted a set of 165 TTS distributed in four fields (Figure 4.2), two in the Orion OB1b subassociation and two in the Orion OB1a region (Briceño et al., 2005). These stars have been confirmed as members of the OB association based on their K and M spectral types, $H\alpha$ emission, and the presence of Li I ($\lambda 6707\text{\AA}$) in absorption (Briceño et al., 2005).

The two fields in the Ori OB1a region are roughly centered on the 25 Ori cluster (Briceño et al., 2007) and the HR1833 stellar aggregate (Briceño,

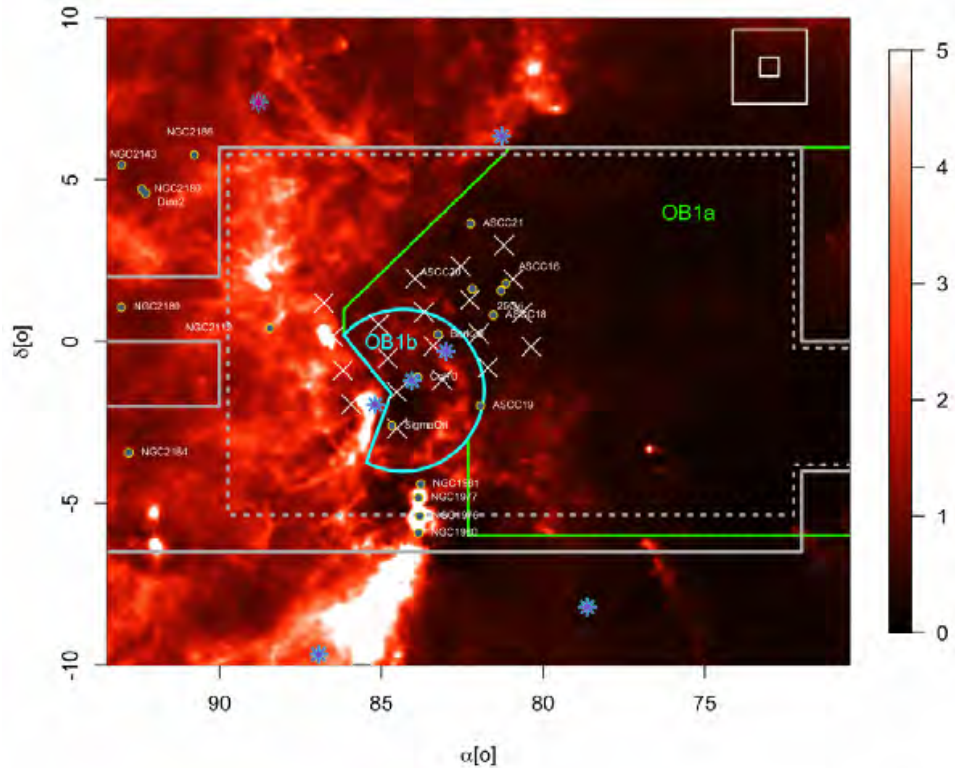


Figure 4.1: The star-forming region of Orion. The color scale indicates the average A_V extinction of Schlegel et al. (1998). The circles indicate clusters and nebulae. The green and blue lines enclose the sub-regions OB1a and OB1b, respectively. In the upper right, the white squares show the spatial coverage of the field of view (FOV) of the 1 m Jürgen Stock Telescope and the Quest-I camera and the 4 m telescope and the MOSA camera of KPNO (small box). The white polygons show the spatial coverage of the Quest-I photometric survey of individual sweeps (continuous) and summed sweeps (dotted) reduced and analyzed at Downes et al. (2011). The Xs indicate the centers of the VISTA survey fields. The asterisks represent the brightest stars in the Orion direction. Other important regions such as λ Orionis located further north, and regions of molecular clouds located further east, are not included in this plot. Taken from Downes et al. (2011).

2008), and combined encompass 118 confirmed TTS. The two Ori OB1b fields contain 47 confirmed TTS. The spectral types for the young stars in both regions are similar, and span the range K4 to M5, which at the ages of

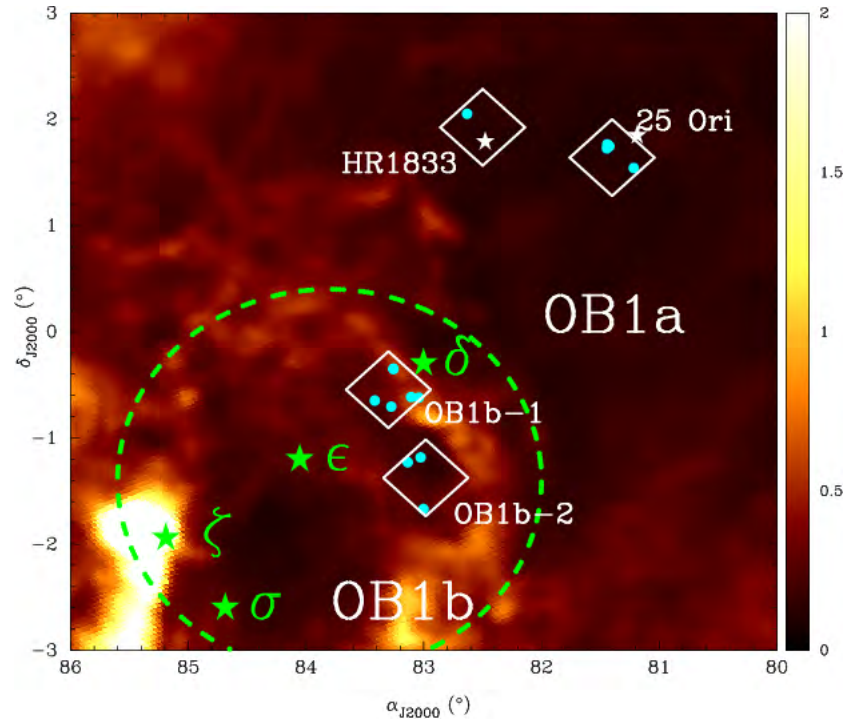


Figure 4.2: Location of the four *Herschel* PACS fields in the Orion OB1 association, overlaid on the extinction map from Schlegel et al. (1998). The Orion OB1b region encompasses the three Orion belt stars, and is delimited by the large dashed lined circle (Briceño et al., 2005); the OB1a region is located west and north of OB1b, and includes the 25 Ori cluster and the HR 1833 stellar aggregate. The TTS detected at $70 \mu\text{m}$ in the PACS fields are shown as cyan dots. Our *Herschel* fields are all in regions of low extinction with $A_V \lesssim 1$ mag. Taken from Maucó et al. (2018).

our stars corresponds to masses $0.12 \lesssim M/M_{\odot} \lesssim 1.2$ (Baraffe et al., 1998).

4.0.1 The σ Ori cluster

Low-mass members of the σ Ori cluster were first reported by Walter et al. (1997) who found over 80 X-ray sources and spectroscopically identified more than 100 low-mass, pre-main-sequence (PMS) members lying within 1° from the star σ Ori, which is a massive quintuplet system (Caballero, 2014). The brightest stars of the system, the σ Ori Aa, Ab (O9.5, B0.5) pair and σ Ori B (\sim B0-B2) with a total mass of $\sim 44 M_{\odot}$ (Simón-Díaz et al., 2015), forms a large, low-density HII region and the bright photo-dissociation region known as the Horsehead nebula (Habart et al., 2005; Abergel et al., 2003). The σ Ori cluster, the Horsehead nebula and the distribution of the massive multiple system at the center of the cluster are shown in Figure 4.3.

With an estimated age of ~ 3 Myr and at a distance of ~ 385 pc (Caballero, 2008), the σ Ori cluster is of particular interest because at its intermediate age, one might expect the signs of disk evolution to become apparent. Moreover, is an excellent laboratory to study protoplanetary disks since is relatively close and populous (with a third of its members having disks), so studies of primordial disks with statistically significant are possible. For instance, in a spectroscopic study of the cluster Hernández et al. (2014) estimated spectral types for more than 300 σ Ori members, estimating radial velocities and accretion indicators for a subset of stars in the sample.

As part of the Orion OB1 variability survey, that have discovered hundreds of low mass stars in the Orion OB1 subassociations with ages between ~ 4 and 10 Myrs (Briceño et al., 2001, 2005, 2007; Briceño, 2008), we have observed a sample of 37 TTS, mostly class II sources, belonging to the σ Ori cluster with *Spitzer*/IRAC and MIPS (Hernández et al., 2007b) and *Herschel*/PACS. Since the emission of dust at 70 and 160 μm (PACS bands) comes from the outer, colder regions of the disk, the effects of evolutionary processes, like dust settling and grain growth, are going to be more apparent at these wavelengths. For this reason, the PACS photometry obtained for these disks served as a crucial input in the current study of their evolution. The following results are based on these unique data.



Figure 4.3: Zooming into the core of the σ Ori cluster, from the Orion constellation (left) to the σ Ori Aa, Ab, B triple system (top right). The Horsehead nebula is also shown (bottom). Image credits: Gabriel Pérez (SMM, IAC), Sergio Simón-Díaz (IAC/ULL), and Jose A. Caballero (CAB/INTA). Taken from <https://www.youtube.com/watch?v=t42YdyfkizI>, based on the study from Simón-Díaz et al. (2015).

Chapter 5

Peer-Reviewed Articles

5.1 Article 1

5.1.1 Abstract

Presentamos nuevas observaciones de Herschel utilizando el fotómetro y espectrómetro de PACS a 70 y 160 μm de 32 estrellas T Tauri en el cúmulo de σ Ori. La mayoría de nuestros objetos son estrellas K y M con grandes excesos a 24 μm . Usamos modelos de discos irradiados de D'Alessio et al. (2006a) para comparar sus distribuciones espectrales de energía con los datos observacionales. Nuestras conclusiones fueron las siguientes: (i) Los discos observados son consistentes con sistemas de discos irradiados. (ii) La mayoría de nuestros objetos (60 %) pueden ser explicados mediante una disminución de polvo en las capas superiores del disco. (iii) Del mismo modo, 61% de nuestros objetos pueden ser modelados con discos de grandes dimensiones ($R_d \geq 100$ AU). (iv) Las masas de nuestros discos oscilan entre 0.03 y 39 M_{Jup} , donde 35% de los objetos tienen masas de disco menores a 1 M_{Jup} . A pesar de que estos valores son límites inferiores, no conseguimos discos masivos ($> 0.05 M_{\odot}$) como los encontrados en Tauro, por ejemplo. (v) Si suponemos una distribución uniforme de objetos alrededor de las estrellas más brillantes en el centro del cúmulo, encontramos que el 80% de nuestros discos están expuestos a radiación UV externa de $300 \leq G_0 \leq 1000$, la que puede ser suficientemente fuerte para fotoevaporar las partes más externas de los discos cercanos. (vi) Dentro de los primeros 0.6 pc de distancia a σ Ori encontramos emisión de líneas prohibidas de [N II] en el espectro de uno de nuestros discos más grandes (SO662), más no detectamos ninguna emisión en la muestra de discos pequeños. Ésto sugiere que este objeto puede ser un ejemplo de un disco siendo fotoevaporado.

A *HERSCHEL* VIEW OF PROTOPLANETARY DISKS IN THE σ ORI CLUSTER

KARINA MAUCÓ¹, JESÚS HERNÁNDEZ^{2,8}, NURIA CALVET³, JAVIER BALLESTEROS-PAREDES¹, CÉSAR BRICEÑO⁴, MELISSA MCCLURE⁵,
 PAOLA D'ALESSIO¹, KASSANDRA ANDERSON⁶, AND BABAR ALI⁷

¹Instituto de Radioastronomía y Astrofísica (IRyA), Universidad Nacional Autónoma de México (UNAM), Morelia 58089, Mexico; k.mauco@crya.unam.mx

²Centro de Investigación de Astronomía (CIDA), Mérida 5101-A, Venezuela

³University of Michigan, UMich, Ann Arbor, MI 48109, USA

⁴Observatorio Interamericano Cerro Tololo, AURA/CTIO, Chile

⁵The European Southern Observatory, ESO, Garching, Germany

⁶Cornell University, Ithaca, NY, USA

⁷Space Sciences Institute, Boulder, CO, USA

Received 2016 February 14; revised 2016 June 27; accepted 2016 June 29; published 2016 September 20

ABSTRACT

We present new *Herschel* observations using the Photodetector Array Camera and Spectrometer of 32 T Tauri stars in the young (~ 3 Myr) σ Ori cluster. Most of our objects are K and M stars with large excesses at $24\ \mu\text{m}$. We used irradiated accretion disk models of D'Alessio et al. to compare their spectral energy distributions with our observational data. We arrive at the following six conclusions. (i) The observed disks are consistent with irradiated accretion disk systems. (ii) Most of our objects (60%) can be explained by significant dust depletion from the upper disk layers. (iii) Similarly, 61% of our objects can be modeled with large disk sizes ($R_d \geq 100$ au). (iv) The masses of our disks range between 0.03 and $39 M_{\text{Jup}}$, where 35% of our objects have disk masses less than $1 M_{\text{Jup}}$. Although these are lower limits, high-mass ($>0.05 M_{\odot}$) disks, which are present in, e.g., Taurus, are missing. (v) By assuming a uniform distribution of objects around the brightest stars at the center of the cluster, we found that 80% of our disks are exposed to external FUV radiation of $300 \leq G_0 \leq 1000$, which can be strong enough to photoevaporate the outer edges of the closer disks. (vi) Within 0.6 pc from σ Ori we found forbidden emission lines of [N II] in the spectrum of one of our large disks (SO662), but no emission in any of our small ones. This suggests that this object may be an example of a photoevaporating disk.

Key words: infrared: stars – open clusters and associations: individual (σ Orionis Cluster) – protoplanetary disks – stars: formation – stars: pre-main sequence

1. INTRODUCTION

The collapse of rotating cloud cores leads to the formation of stars surrounded by disks because of the conservation of angular momentum. These disks evolve because they are accreting mass onto the star and because the dust grains tend to settle toward the midplane, where they collide and grow (e.g., Hartmann et al. 1998; Hartmann 2009). The material in the disk is subject to irradiation from the host star and from the high-energy fields produced in accretion shocks on the stellar surface, in the stellar active regions, and in the environment, if the star is immersed in the radiation field of nearby OB stars in a stellar cluster (D'Alessio et al. 2001, 2006; Adams et al. 2004; Anderson et al. 2013). These high-energy fields heat the gas, eventually leading to its dissipation, while the solids grow to planetesimal and planet sizes. Still, many open questions remain on how these processes happen and interact with each other.

Previous studies using *Spitzer* data on different star-forming regions with ages between 1 and 10 Myr show a decrease in disk fraction as a function of the age of the cluster (Hernández et al. 2007a, henceforward H07a). The decrease in disk fraction is reflected as a clear drop in the mid-IR excess, indicating that only 20% of the stars retain their original disks by 5 Myr (Hernández et al. 2007b). It is therefore essential to observe disks in the crucial age range between 2 and 10 Myr, in which the agents driving the evolution of protoplanetary disks are most active. The decrease in the IR excess can be explained by

grain growth and by settling of dust to the disk midplane, reducing the flaring of the disk and thus its emitting flux. This interpretation is confirmed by the analysis made by D'Alessio et al. (2006) using irradiated accretion disk models. These models simulate the settling process by introducing the parameter ϵ , which represents the dust-to-gas mass ratio of the disk atmosphere compared to that of the interstellar medium (ISM). In this sense, a depletion of small grains in the upper layer of the disks will be reflected as a small value of ϵ . Unevolved disks, on the other hand, will have ϵ values close to unity.

Once the dust has settled, large bodies present in the disk will interact with their local environment, creating more complex radial structures such as inner clearings or gaps. The most probable mechanism responsible for this effect is an orbiting companion, either stellar or planetary, that clears out the material in the inner disk (Calvet et al. 2002; Espaillat et al. 2014). This mechanism can explain some of the so-called transitional and pre-transitional disks (TDs and PTDs hereafter).

Also important is disk truncation via mass loss. Besides an orbiting planet, truncation of the *inner* disk may result from the dissipation of gas being heated by high-energy radiation fields coming from the host star (Hollenbach et al. 2000; Alexander et al. 2006; Clarke 2007; Dullemond et al. 2007). Evidence of mass loss in disks comes from forbidden emission lines of ionized species like [S II], [O I], [Ne II], and [N II]. The low-velocity component of these lines has been associated with photoevaporative winds that might be able to explain some of the TDs and PTDs observed (Pascucci & Sterzik 2009; Gorti

⁸ Visiting Scientist, IRyA, UNAM; Instituto de Astronomía, UNAM, Unidad Académica en Ensenada, Ensenada 22860, Mexico.

et al. 2011; van Loon & Oliveira 2003; Hodapp et al. 2009; Guarcello et al. 2010, 2014, 2016).

The truncation of the *outer* parts of the disks, on the other hand, may be the result of environmental effects, such as mass loss due to high-energy photons from nearby massive stars impinging on the surface of the disk and heating the less tightly bound material. Expected mass loss rates in externally illuminated disks can be substantial (Adams et al. 2004; Facchini et al. 2016), and when incorporated into viscous evolution models (Clarke 2007; Anderson et al. 2013; Kalyaan et al. 2015) they can have a strong impact on the disk structure’s and lifetime. Externally illuminated disks, known as proplyds, have been well characterized in the Orion Nebula Cluster (hereafter ONC; O’dell & Wen 1994; Johnstone et al. 1998; Henney & O’Dell 1999; Störzer & Hollenbach 1999; García-Arredondo et al. 2001; Smith et al. 2005; Williams et al. 2005; Eisner et al. 2008; Mann et al. 2014), where the radiation from the Trapezium stars photoevaporates the disks. Evidence of outer photoevaporation in other star-forming regions has also been found (Rigliaco et al. 2009, 2013; Natta et al. 2014).

Multiplicity can also produce truncated disks. The fraction of binary companions in young regions can be $\sim 30\%$ or larger, where close (<100 au) binaries can affect the evolution of protoplanetary and circumbinary disks by significantly reducing their lifetime (Daemgen et al. 2015). In the Taurus star-forming region the disk population affected by multiplicity consists of close binaries with separations <40 au (Kraus & Hillenbrand 2012).

In order to understand what physical processes cause the disks to evolve, many multiband observations of different regions within a wide range of ages and environments have been made. Many of these studies have used data from the *Spitzer Space Telescope* to describe the state of gas and dust within the first au from the central object. In the ~ 5 Myr old (de Zeeuw et al. 1999) Upper Scorpius OB association Dahm & Carpenter (2009) examined, among others, seven late-type disk-bearing (K+M) members using the Infrared Spectrograph (IRS). They found a lack of submicron dust grains in the inner regions of the disks and that the strength of silicate emission is dependent on spectral type. In a disk census performed by Luhman & Mamajek (2012) with *Spitzer* and *WISE* photometry they found that late-type members have a higher inner disk fraction than early types. The ~ 10 Myr old (Uchida et al. 2004) TW Hydrae (TW Hya) association has also been the target for different studies of disk evolution. Uchida et al. (2004) analyzed two objects with IR excesses on their IRS spectra. They found signs of significant grain growth and dust processing and also evidence of dust clearing in the inner (~ 4 au) disks, possibly due to the presence of orbiting planets. Similar studies performed in other regions like Ophiucus (McClure et al. 2010, ~ 1 Myr), Taurus (Furlan et al. 2006, 1–2 Myr), and Chamaeleon I (Manoj et al. 2011, ~ 2 Myr), using IRS spectra to analyze the strength and shape of the 10 and $20 \mu\text{m}$ silicate features, have shown that disks in these regions are highly settled and exhibit signs of significant dust processing.

In order to describe the distribution of gas and dust in circumstellar disks around young stars, many works have been done using the Photodetector Array Camera and Spectrometer (PACS) instrument on board the *Herschel Space Observatory*. The main idea of these studies has been the description of disk structures as well as the estimation of gas and dust masses in

different star-forming regions (Riviere-Marichalar et al. 2013: TW Hya association; Mathews et al. 2013: Upper Scorpius; Olofsson et al. 2013: Chamaeleon I). Additionally, Howard et al. (2013) modeled PACS detections in Taurus, and found that the region probed by their observations constitutes the inner part (5–50 au) of their disks.

The ~ 3 Myr old σ Ori cluster (H07a) is an excellent laboratory for studies of disk evolution for two reasons: first, the large number of stars still harboring disks allows us to obtain results with statistical significance, and second, given its intermediate age, one can expect the first traces of disk evolution to become apparent. We present here new *Herschel* PACS 70 and $160 \mu\text{m}$ photometry of 32 T Tauri stars (TTSs) in the cluster, with *B*, *V*, *R*, and *I* magnitudes, 2MASS, *Spitzer* IRAC and MIPS photometry from H07a, and spectral types from Hernández et al. (2014, H14 hereafter). Our main goal is to describe the state of the dust in our sample by analyzing the infrared properties of the stars and by modeling their spectral energy distributions (SEDs) with irradiated accretion disk models. In Section 2 we describe the observational data and a few details about the reduction process; in Section 3 we present the SEDs of our objects; in Section 4 we characterize our PACS sources; our results are shown in Section 5, where we characterize our PACS disks using spectral indices (Section 5.2) and model the SEDs of individual objects (Section 5.3); the discussion is presented in Section 6 and the conclusions are given in Section 7.

2. PACS OBSERVATIONS

Our *Herschel*/PACS imaging survey of the σ Ori cluster was obtained on 2012 March 14 as part of our *Herschel* program OT1_ncalvet_1. We used the “scan map” observational template with medium scan speed ($20'' \text{ s}^{-1}$) to map a square field $3'$ per side. Each scan line was $30'$ long, and we used 134 overlapping scan lines with a step size of $15''$. The field was observed twice with orthogonal scan directions in order to mitigate the low-frequency drift of the bolometer timelines. We aimed at reaching a 1σ point source sensitivity of 2.6 mJy at $70 \mu\text{m}$ and 6 mJy at $160 \mu\text{m}$.

Our observations were processed using the map-making software Scanmorphos, which was developed and described by Roussel (2013). We used the “FM6” version of the PACS calibration (Balog et al. 2014) and the data processed with version 9 of the *Herschel* Interactive Processing Environment (HIPE, Ott 2010) software (see Briceño et al. 2013, p. 2). The scales for the 70 and $160 \mu\text{m}$ maps are $1''/\text{pixel}$ and $2''/\text{pixel}$, respectively. Scanmorphos preserves astrophysical emission on all spatial scales, ranging from point sources to extended structures with scales just below the map size. We performed source detection on the 70 and $160 \mu\text{m}$ maps using the daofind task in the Image Reduction and Analysis Facility (IRAF). We extracted aperture photometry for the detected sources using *apphot* in IRAF. Following Fischer et al. (2013), for the $70 \mu\text{m}$ images we used an aperture radius of 9.6 arcsec, inner sky annulus radius of 9.6 arcsec, and sky annulus width of 9.6 arcsec; for the $160 \mu\text{m}$ images we used an aperture radius of 12.8 arcsec, inner sky annulus radius of 12.8 arcsec, and sky annulus width of 12.8 arcsec. The photometric error was determined as the sum in quadrature of the measurement error and the calibration error (see Briceño et al. 2013, p. 2). The detections were then cross-matched with the photometric candidates selected in H07a.

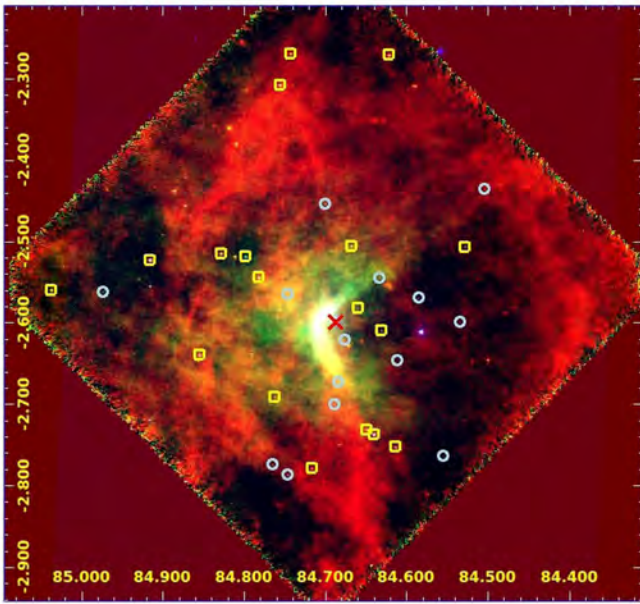


Figure 1. Three-color map (red: PACS 160 μm ; green: PACS 70 μm ; blue: MIPS 24 μm) of the σ Ori cluster showing the coverage of PACS observations (big square). Detections are shown as squares for objects detected at 70 and 160 μm and as circles for objects detected only at 70 μm (with 160 μm upper limits). The red cross indicates the position of the multiple-star system σ Ori.

The PACS field of view (FOV) is shown in Figure 1 as a three-color map using *Spitzer* MIPS 24 μm (H07a) and PACS bands. We detected 32 TTSs in the cluster at PACS 70 μm . Of these, 17 sources were also detected at 160 μm and the rest only as upper limits. Stars with 160 μm upper limits were defined using the 3σ criterion. The large range of values for these upper limits is due to the non-uniform background in the image. On Figure 1 squares indicate stars detected at 70 and 160 μm while circles represent stars detected only at 70 μm (with 160 μm upper limits). The lowest flux measured at 70 μm is equal to 9.4 ± 1.1 mJy. The multiple-star system σ Ori is shown by a red cross on the center of the field, where an arc-shaped nebulosity can be seen to the west side. This nebulosity consists of gas and dust that have been dragged away by the strong radiation of the massive stars on the system.

The σ Ori cluster has a dense core (see Figure 2) extending from the center to a radius of $20'$, in which most members are located, and a rarefied halo extending up to $30'$ (Caballero 2008a). Note that the dense core is almost entirely covered by the FOV of PACS, which covers a total of 142 TTS, of which 23% are detected at 70 μm . These detections have been reported as disk-bearing candidates with infrared excess at 24 μm (H07a). The disk fraction for members inside the dense core is 42% (H07a). Our PACS photometry is reported in Table 1.

Others PACS detections not considered in this work were: (1) eight sources with optical or 2MASS counterparts detected only at 160 μm ; all these sources are background candidates from optical-2MASS color-magnitude diagrams; (2) 13 sources detected at 70 μm (six of them were reported as non-members or galaxy candidates): SO406 and SO950 are galaxy candidates (galaxies based on the profile flag of UKIDSS), SO916 and SO596 are identified as background sources (H07a; H14), SO457 is a pulsating red giant (Caballero et al. 2010), SO668 is reported as an obscured QSO at $z = 0.2362$ (Caballero et al. 2008b), SO770 is highly contaminated by the

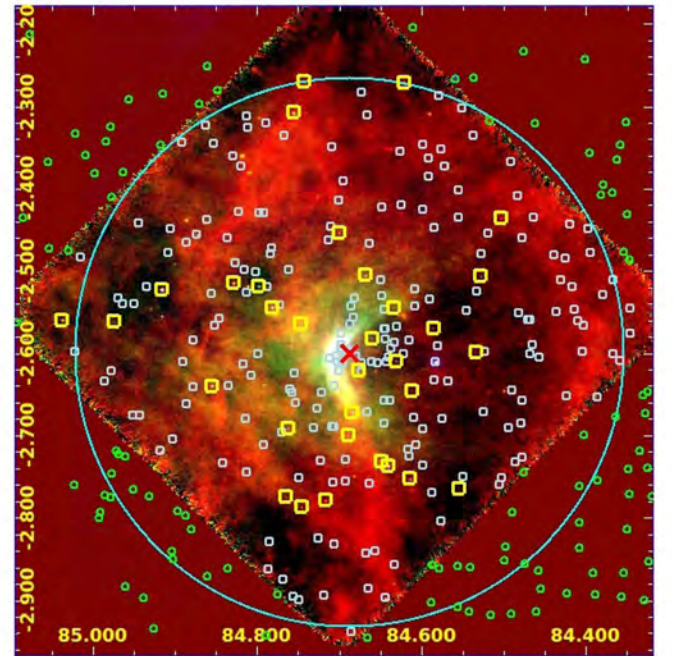


Figure 2. Three-color map (red: PACS 160 μm ; green: PACS 70 μm ; blue: MIPS 24 μm) of the σ Ori cluster showing undetected members that lie inside and outside the FOV of PACS (light blue squares and green circles respectively) and members with PACS detections (yellow boxes) reported by H14. The big circle encloses the dense core of σ Ori (extending from the center to a radius of $20'$). The majority of the members lie inside the FOV of PACS.

background (located on the arc-shaped nebulosity), SO848, SO1266, SO1154, and SO1182 have no spectral types reported by H14, SO1075 has no optical information, and SO1155 is located near the edge of the PACS coverage. The undetected classical T Tauri stars (CTTSs) have the smallest excesses at MIPS 24 μm (see Section 4.1, Figure 5).

3. SPECTRAL ENERGY DISTRIBUTION

The 32 sources detected by PACS in the σ Ori field have stellar counterparts that have been characterized by H14. Their spectral types, effective temperatures (using the calibrations of Pecaut & Mamajek 2013), and reddening corrections A_v are shown in Table 2.

We constructed the SEDs for all of our targets using optical B , V , R , and I magnitudes (when available), 2MASS, *Spitzer* IRAC and MIPS photometry taken from H07a, and adding photometry data from *Herschel* PACS at 70 and 160 μm , reported here. We have added submillimeter data from Williams et al. (2013) for four of our PACS sources: SO540, SO844, SO984, and SO1153. The SEDs of our objects are shown in Figure 3 (filled dots).

Figure 3 also shows the σ Ori median, normalized to the J band of each object, for stars with PACS detections (solid red line). The median values and the first and third quartiles are in Table 4. For reference we show the Taurus median estimated from photometric data only (dashed line) with quartiles. To estimate the photometric Taurus median we used J , H , and K 2MASS photometry from Hartmann et al. (2005), *Spitzer* IRAC and MIPS photometry from Luhman et al. (2010), and PACS 70, 100, and 160 μm photometry from Howard et al. (2013), with a total of 21 stars for the calculation, covering spectral types ranging from K3 to M4 (Table 5). This median

Table 1
PACS Photometry for Members of the σ Ori cluster

SO ID	2MASS ID	R.A. (J2000.0) (deg)	Decl. (J2000.0) (deg)	70 μ m (mJy)	160 μ m (mJy)
SO299	05380097-0226079	84.50404	-2.43553	16.8 \pm 1.3	<56.6
SO341	05380674-0230227	84.52808	-2.50631	42.0 \pm 1.6	31.9 \pm 2.7
SO362	05380826-0235562	84.53442	-2.59894	16.0 \pm 1.3	<16.1
SO396	05381315-0245509	84.55479	-2.76414	30.5 \pm 1.7	<38.8
SO462	05382050-0234089	84.58542	-2.56914	26.6 \pm 1.5	<9.8
SO514	05382684-0238460	84.61183	-2.64611	9.4 \pm 1.1	...
SO518	05382725-0245096	84.61354	-2.75267	71.8 \pm 2.3	48.1 \pm 4.9
SO540	05382915-0216156	84.62146	-2.271	207.0 \pm 5.7	243.4 \pm 11
SO562	05383141-0236338	84.63087	-2.60939	24.0 \pm 1.3	18.7 \pm 3.1
SO566	J053832.13-023243	84.63387	-2.54528	16.6 \pm 2.2	<26.7
SO583	05383368-0244141	84.64033	-2.73725	263.5 \pm 7.2	89.1 \pm 5.3
SO615	05383587-0243512	84.64946	-2.73089	47.0 \pm 1.9	93.0 \pm 6.5
SO638	05383848-0234550	84.66033	-2.58194	23.8 \pm 1.6	<8.2
SO662	05384027-0230185	84.66779	-2.50514	64.9 \pm 2.7	37.4 \pm 2.9
SO682	05384227-0237147	84.67612	-2.62075	28.6 \pm 2.9	<14.2
SO697	05384423-0240197	84.68429	-2.67214	21.0 \pm 1.9	<11.7
SO710	05384537-0241594	84.68904	-2.69983	10.5 \pm 1.4	<17.4
SO736	05384803-0227141	84.70012	-2.45392	26.8 \pm 1.5	<19.3
SO774	05385200-0246436	84.71667	-2.77878	50.8 \pm 1.7	49.3 \pm 3.7
SO818	05385831-0216101	84.74296	-2.26947	141.4 \pm 3.9	148.9 \pm 6.7
SO823	05385911-0247133	84.74629	-2.78703	40.9 \pm 1.8	<26.7
SO827	05385922-0233514	84.74675	-2.56428	31.9 \pm 1.5	<39.8
SO844	05390136-0218274	84.75567	-2.30761	219.6 \pm 6.0	196.6 \pm 10.4
SO859	05390297-0241272	84.76238	-2.69089	22.0 \pm 1.5	33.4 \pm 3.3
SO865	05390357-0246269	84.76488	-2.77414	25.8 \pm 1.4	<14.2
SO897	05390760-0232391	84.78167	-2.54419	121.7 \pm 3.6	75.8 \pm 7.4
SO927	05391151-0231065	84.79796	-2.51847	100.2 \pm 2.9	33.8 \pm 2.5
SO984	05391883-0230531	84.82846	-2.51475	138.8 \pm 3.9	179.1 \pm 8.1
SO1036	05392519-0238220	84.85496	-2.63944	107.3 \pm 3.2	73.5 \pm 4.5
SO1153	05393982-0231217	84.91592	-2.52269	482.9 \pm 12.8	448.6 \pm 19
SO1260	05395362-0233426	84.97342	-2.56183	12.2 \pm 1.1	<31.8
SO1361	05400889-0233336	85.03704	-2.55933	199.5 \pm 5.5	80.1 \pm 4.5

Note. Column 1: ID following [H07a](#); Column 2: 2MASS ID; Columns 3 and 4: R.A. and decl. from [H07a](#); Column 5: PACS 70 μ m flux; Column 6: PACS 160 μ m flux.

was corrected for extinction using the Mathis reddening law (Mathis 1990, $R = 3.1$) with A_V from Furlan et al. (2006). The dotted line represents the median SEDs of non-excess stars in the σ Ori cluster ([H07a](#)).

The photometry of the PACS sources was corrected for extinction using the Mathis reddening law (Mathis 1990, $R = 3.1$) with visual extinctions A_V from [H14](#). In Figure 3 each panel is labeled with the ID of the source and its classification, according to the IR excess it exhibits. We based the classification of stars with different IR excess emission on the value of the IRAC SED slope determined from [3.6]–[8.0] color ($n_{3.6-8.0}$), following [H07a](#). In this scheme, class II stars are defined as systems with $n_{3.6-8.0} > -1.8$ (e.g., SO1036, SO396, and SO562, where IRAC IR excesses are comparable to the median SED of Taurus); stars with IRAC IR excesses above the photosphere and with $n_{3.6-8.0} < -1.8$ are termed here as evolved (EV) disks (like SO638, where its IRAC IR excesses fall below both medians); and systems without any excess emission, below the photospheric limit, are called class III stars. Objects that are classified as class III stars or EV disks by their IRAC IR excess but that exhibit strong 24 μ m excesses are known as transitional disks, which is the case for SO299, SO818, and SO897.

4. PROPERTIES OF σ Ori SOURCES

4.1. Characterization of PACS Sources

As shown in Figure 2, 142 TTSS in σ Ori ([H07a](#)) fall in the PACS FOV but only 23% of them are detected. Here we compare the detections with the entire TTS population in the field, aiming to understand what makes them different.

The left panel of Figure 4 shows the PACS 70 μ m detections in the [3.6]–[4.5] versus [5.8]–[8.0] diagram, as well as all the σ Ori sources in the PACS field. Sources around [0, 0] are referred to as diskless stars while PACS detections are identified following the disk classification of [H07a](#). Note that most of the PACS-detected sources are inside the rectangle that encompasses the optically thick disk region (Hartmann et al. 2005; D’Alessio et al. 2006) and are considered as CTTSS. This is consistent with the shape of their SEDs and their similarities with the Taurus median (Figure 3). Excluding the TDs/PTDs and the two evolved disks in our sample, which have a decrease of IR excess in the IRAC bands and therefore will have lower colors than those predicted by optically thick disks, four sources fall outside the loci of CTTSS: SO823, SO462, SO774, and SO927. The source SO823 has a low [5.8]–[8.0] color. The others (SO462, SO774, and SO927) present higher [5.8]–[8.0] colors. The stars SO462 and SO774

Table 2
Properties of 32 PACS Sources in the σ Ori cluster

SO ID	Sp. Type	T_{eff} (K)	A_v (mag)	Disk Type	M_* (M_{\odot})	R_* (R_{\odot})	\dot{M} ($M_{\odot} \text{ yr}^{-1}$)	Age (Myr)	d_p (pc)
SO299	M2.5 \pm 1.0	3490.0	0.42	TD	0.341	1.192	1.27e-09	3.81	1.54
SO341	M0.0 \pm 0.5	3770.0	0.58	II	0.505	1.769	1.21e-09	2.04	1.15
SO362	M2.5 \pm 0.5	3490.0	0.57	II	0.348	1.641	1.04e-09	2.16	0.95
SO396	M1.5 \pm 0.5	3630.0	0.64	II	0.417	1.638	7.85e-09	2.21	1.32
SO462	M4.0 \pm 1.0	3160.0	2.94	II	0.231	2.083	1.22e-09	1.00	0.66
SO514	M3.5 \pm 1.0	3360.0	2.2	II	0.254	0.885	...	6.90	0.55
SO518	K6.0 \pm 1.0	4020.0	0.0	II	0.754	1.367	2.88e-09	6.50	1.06
SO540	K6.5 \pm 1.5	4020.0	0.53	II	0.728	1.662	...	2.99	2.11
SO562	M3.5 \pm 1.5	3360.0	0.07	II	0.294	1.616	2.68e-09	2.20	0.35
SO566	M5.0 \pm 1.0	2880.0	0.59	II	0.099	1.391	...	0.46	0.47
SO583	K4.5 \pm 1.5	4330.0	0.0	II	1.087	2.848	7.48e-09	1.03	0.90
SO615	K3.0 \pm 3.0	4550.0	1.98	EV	1.498	3.019	7.7e-10	1.46	0.85
SO638	K2.0 \pm 1.0	4760.0	1.03	EV	1.867	3.170	...	1.93	0.20
SO662	K7.0 \pm 1.0	3970.0	1.89	II	0.660	2.196	1.99e-09	1.62	0.60
SO682	M0.5 \pm 1.0	3770.0	0.67	II	0.505	1.785	2.3e-10	2.00	0.14
SO697	K6.0 \pm 0.5	4020.0	0.43	II	0.725	1.900	1.07e-09	2.42	0.45
SO710	M1.5 \pm 1.5	3630.0	0.59	II	0.417	1.677	1.02e-09	2.12	0.62
SO736	K6.0 \pm 0.5	4020.0	0.88	II	0.748	3.528	2.38e-09	0.69	0.92
SO774	K7.5 \pm 1.0	3970.0	0.12	II	0.674	1.730	1.21e-09	2.69	1.13
SO818	M0.0 \pm 0.5	3770.0	0.54	TD	0.509	1.346	3.4e-10	3.84	2.10
SO823	M2.0 \pm 1.5	3490.0	2.11	II	0.354	2.958	...	0.38	1.23
SO827	M2.5 \pm 1.0	3490.0	0.0	II	0.335	1.094	7.3e-10	4.98	0.44
SO844	M0.5 \pm 0.5	3770.0	0.42	II	0.506	1.754	4.38e-09	2.08	1.88
SO859	M2.5 \pm 0.5	3490.0	0.71	II	0.347	1.473	1.9e-09	2.51	0.74
SO865	M3.5 \pm 1.0	3360.0	0.0	II	0.280	1.180	7.2e-10	3.47	1.19
SO897	K6.5 \pm 1.5	4020.0	0.35	TD	0.725	1.945	1.78e-09	2.33	0.69
SO927	M0.0 \pm 1.0	3770.0	1.04	II	0.506	1.690	9.2e-10	2.24	0.86
SO984	K7.0 \pm 0.5	3970.0	0.74	II	0.665	1.983	2.83e-09	2.08	1.04
SO1036	K7.5 \pm 0.5	3970.0	0.92	II	0.662	2.124	8.13e-09	1.77	1.08
SO1153	K5.5 \pm 1.0	4140.0	0.15	I	0.875	1.402	4.19e-09	6.99	1.52
SO1260	M2.5 \pm 1.0	3490.0	0.71	II	0.343	1.223	2.03e-09	3.46	1.81
SO1361	K7.5 \pm 1.0	3970.0	0.53	II	0.670	1.843	...	2.42	2.21

Note. Column 1: ID following H07a; Column 2: spectral type from H14; Column 3: effective temperature; Column 4: extinction from H14; Column 5: disk type from H07a; Column 6: stellar mass, Column 7: stellar radius; Column 8: mass accretion rate; Column 9: age; Column 10: projected distance to the central σ Ori multiple system. Stellar masses, radii, and ages were derived as described in Section 4.2.

seem to have a slight decay in the first three IRAC bands (3.6, 4.5, 5.8 μm), which causes an apparent redder [5.8]–[8.0] color (note their high 8 μm fluxes resembling those of TDs/PTDs in our sample). The source SO927 has a peculiar SED with very large near-IR and mid-IR excesses.

The right panel in Figure 4 displays the K –[5.8] versus [8.0]–[24] SED slopes. The slope of the SED is defined as

$$n = \frac{\log(\lambda_1 F_{\lambda_1}) - \log(\lambda_2 F_{\lambda_2})}{\log(\lambda_1) - \log(\lambda_2)}, \quad (1)$$

where λ_i and F_{λ_i} are the wavelength and the observed flux at that particular wavelength, respectively. This parameter has been used to classify young stellar objects (Lada 1987, 2006; H07a). We also indicate the lower limit of primordial disks in Taurus (Luhman et al. 2010, dashed line). Photospheric limits are shown by dotted lines. H07a have classified the object SO540 as a class II star based on its slopes between 3.6 and 8.0 μm ; however, using the K –[5.8] and the [8]–[24] slopes indicates that it could be a TD candidate. Another interesting point to notice is the fact that one of our two evolved disks, the source SO615, appears just in the limit of primordial disks and has the lowest [8.0]–[24] color of the PACS sample. This may be the result of chromospheric

contamination, which is more significant in evolved stars with low mass accretion rates, where magnetic activity from the chromosphere of the star may produce an extra heating of dust, which is reflected at 5.8 μm (Ingleby et al. 2013).

Figure 5 shows the [24] versus K –[24] color–magnitude diagram of σ Ori members, highlighting our PACS disks. Also shown are the histograms of MIPS 24 μm (right) and of K –[24] color (top). As shown in the figure, our detections have the largest excesses at 24 μm , despite their similar near- and mid-IR colors to those of non-detections (Figure 4), with an average magnitude of 5.65 that corresponds to a flux of 67.27 mJy. The lowest 24 μm magnitude detected corresponds to the source SO514 with a value of 8.3 mag. Non-detections, on the other hand, present an average magnitude of 8.16. The source SO566 is a variable star with variability amplitude in the J band larger than 2.7 mag (H14), as can be seen in its non-contemporaneous SED in Figure 3; thus, its large K –[24] color is not real.

Figure 6 shows a histogram of spectral types for σ Ori members (H14). PACS 70 μm detections cover spectral types from K2.0 to M5.0. Objects with spectral types later than M5 are unlikely to be detected because the average flux at 70 μm would be below the detection limit by more than a factor of 2 (Section 2). On the other hand, disk-bearing stars with spectral types earlier than K0 have evolved disks with 24 μm

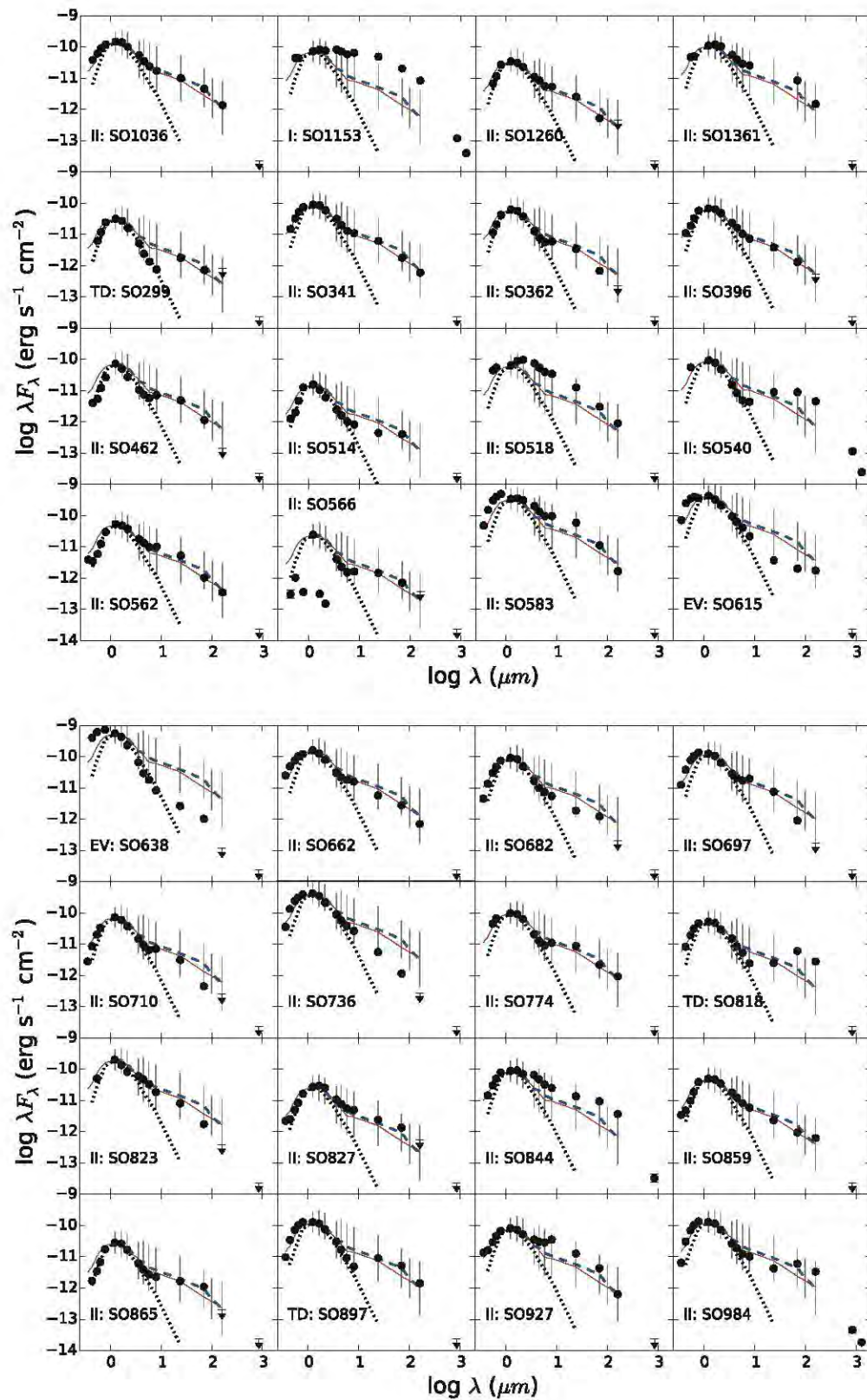


Figure 3. Extinction-corrected SEDs (filled dots) of PACS sources in the σ Ori cluster, following the Mathis reddening law according to the A_V reported in H14. Each panel is labeled with the ID of the source and its classification following H07a. The solid red line represents the σ Ori median of PACS sources normalized to the J band of each object (Table 4). Also shown is the Taurus photometric median (blue dashed line) with quartiles, estimated in this work (see text for details). The dotted line corresponds to the median photosphere-like fluxes in the σ Ori cluster (H07a). Error bars are included, but in most cases are smaller than the symbol. Downward arrows indicate upper limits.

Table 3
Properties of 74 Undetected Sources in the σ Ori Cluster

SO ID	Sp. Type	T_{eff} (K)	A_v (mag)	Disk Type	M_* (M_{\odot})	R_* (R_{\odot})	\dot{M} ($M_{\odot} \text{ yr}^{-1}$)	Age (Myr)
SO117	M3.0 \pm 0.5	3360	0.26	III	0.276	1.143	7.2E-11	3.85
SO165	M4.5 \pm 1.0	3160	0.16	III	0.163	0.817	4.1E-11	6.29
SO214	M2.0 \pm 0.5	3490	0.57	III	0.35	1.855	5.5E-10	1.77
SO219	M4.5 \pm 1.5	3160	1.29	III	0.144	0.578	8.0E-12	9.31
SO220	M3.0 \pm 0.5	3360	0.13	III	0.276	1.143	6.6E-11	3.85
SO247	M5.0 \pm 0.5	2880	0.0	II	0.075	1.063	3.45E-10	0.83
SO271	M5.0 \pm 1.0	2880	0.38	II	0.049	0.803	1.36E-10	4.49
SO283	M5.5 \pm 0.5	2880	0.0	III	0.085	1.205	1.83E-10	0.65
SO327	M4.5 \pm 2.0	3160	1.77	II	0.144	0.578	1.33E-10	9.31
SO397	M4.0 \pm 1.0	3160	0.0	II	0.218	1.529	1.057E-9	2.11
SO398	M5.5 \pm 1.0	2880	0.0	III	0.049	0.803	8.2E-11	4.49
SO426	M3.5 \pm 0.5	3360	0.6	III	0.254	0.885	4.2E-11	6.90
SO432	M5.0 \pm 0.5	2880	0.46	III	0.08	1.136	1.75E-10	0.74
SO435	M5.0 \pm 0.5	2880	0.0	II	0.09	1.27	2.79E-10	0.58
SO484	M4.0 \pm 0.5	3160	0.42	III	0.178	1.001	5.0E-11	4.53
SO485	M2.0 \pm 1.0	3490	1.83	II	0.324	0.947	8.58E-10	6.95
SO489	M4.5 \pm 0.5	3160	0.31	III	0.187	1.106	4.4E-11	3.66
SO490	M4.0 \pm 1.0	3160	1.14	II	0.191	1.156	2.073E-9	3.28
SO500	M4.5 \pm 2.0	3160	0.6	II	0.144	0.578	1.98E-10	9.31
SO520	M3.5 \pm 0.5	3360	0.3	II	0.284	1.217	4.8E-10	3.11
SO525	M3.0 \pm 1.0	3360	0.39	III	0.295	1.669	3.23E-10	2.10
SO539	M1.5 \pm 0.5	3630	0.63	III	0.414	1.264	1.45E-10	3.67
SO563	K7.5 \pm 0.5	3970	1.99	II	0.659	2.227	1.252E-9	1.56
SO572	K6.0 \pm 1.0	4020	0.91	III	0.726	1.867	3.03E-10	2.50
SO582	M2.5 \pm 0.5	3490	0.29	III	0.348	1.664	1.52E-10	2.11
SO587	M3.0 \pm 1.0	3360	0.71	II	0.297	1.912	1.084E-9	1.71
SO592	K7.0 \pm 1.0	3970	0.25	III	0.665	1.983	2.66E-10	2.08
SO598	M2.0 \pm 1.0	3490	2.19	II	0.346	1.312	9.2E-11	2.88
SO611	K7.0 \pm 1.0	3970	0.48	III	0.665	2.005	3.86E-10	2.03
SO616	K7.0 \pm 1.0	3970	0.2	III	0.665	1.983	4.86E-10	2.08
SO624	M4.5 \pm 0.5	3160	0.51	III	0.199	1.248	3.9E-11	2.84
SO628	M4.5 \pm 1.5	3160	0.24	III	0.206	1.334	7.7E-11	2.60
SO637	K6.0 \pm 1.0	4020	0.78	III	0.718	2.191	4.28E-10	1.84
SO646	M2.5 \pm 1.0	3490	1.08	II	0.343	1.223	7.29E-10	3.46
SO655	M3.5 \pm 0.5	3360	1.2	III	0.254	0.885	2.1E-11	6.90
SO658	M4.5 \pm 1.0	3160	0.18	III	0.168	0.883	6.0E-12	5.63
SO669	M0.0 \pm 1.0	3770	0.2	III	0.503	1.933	4.45E-10	1.66
SO687	M1.0 \pm 1.0	3630	0.0	II	0.417	1.619	9.42E-10	2.25
SO691	M1.5 \pm 1.5	3630	0.25	III	0.418	1.823	3.5E-10	1.81
SO696	K7.0 \pm 1.0	3970	0.7	III	0.654	2.51	1.141E-9	1.02
SO706	G5.0 \pm 2.5	5500	1.73	III	1.649	2.773	1.202E-9	6.65
SO721	M5.0 \pm 2.0	2880	0.0	III	0.085	1.205	1.73E-10	0.65
SO723	M4.0 \pm 1.5	3160	0.61	II	0.219	1.565	1.827E-9	2.03
SO726	M0.5 \pm 1.0	3770	0.03	II	0.506	1.69	1.359E-9	2.24
SO733	M1.0 \pm 0.5	3630	0.35	II	0.417	1.474	6.48E-10	2.60
SO740	M4.5 \pm 0.5	3160	0.0	III	0.227	1.857	1.77E-10	1.41
SO742	M1.5 \pm 1.5	3630	0.24	III	0.417	1.517	2.44E-10	2.49
SO747	M0.5 \pm 0.5	3770	0.59	III	0.501	2.109	4.54E-10	1.29
SO748	M3.5 \pm 0.5	3360	0.23	III	0.298	2.065	4.63E-10	1.49
SO757	M3.0 \pm 1.0	3360	0.25	III	0.286	1.252	7.0E-11	2.94
SO759	M3.5 \pm 1.0	3360	0.19	EV	0.291	1.415	1.0E-10	2.58
SO765	M3.0 \pm 1.0	3360	1.66	III	0.287	1.286	4.2E-11	2.86
SO785	M1.0 \pm 1.0	3630	0.75	III	0.417	1.538	2.31E-10	2.44
SO855	M4.0 \pm 1.0	3160	0.0	III	0.212	1.415	1.54E-10	2.39
SO866	M4.5 \pm 1.0	3160	0.15	II	0.163	0.817	6.3E-11	6.29
SO879	K6.5 \pm 1.0	4020	0.64	III	0.727	1.797	2.28E-10	2.66
SO896	M2.5 \pm 1.5	3490	0.75	III	0.341	1.192	1.8E-10	3.81
SO901	M4.0 \pm 1.0	3160	0.05	EV	0.157	0.746	9.0E-12	7.09
SO908	M3.0 \pm 1.0	3360	1.51	II	0.289	1.32	4.0E-10	2.79
SO914	M1.5 \pm 1.0	3630	0.44	III	0.412	1.212	6.3E-11	4.30
SO929	K7.0 \pm 1.0	3970	0.51	III	0.674	1.743	2.01E-10	2.66
SO940	M4.0 \pm 0.5	3160	0.55	III	0.183	1.055	6.0E-12	4.08
SO947	M1.5 \pm 1.0	3630	0.74	III	0.417	1.579	4.07E-10	2.34

Table 3
(Continued)

SO ID	Sp. Type	T_{eff} (K)	A_v (mag)	Disk Type	M_* (M_{\odot})	R_* (R_{\odot})	\dot{M} ($M_{\odot} \text{ yr}^{-1}$)	Age (Myr)
SO967	M4.0 ± 0.5	3160	0.0	II	0.183	1.055	6.3E-11	4.08
SO978	M1.5 ± 1.0	3630	0.44	III	0.405	1.073	2.2E-11	6.15
SO999	M4.0 ± 1.0	3160	1.05	III	0.183	1.055	1.0E-11	4.08
SO1000	M2.0 ± 1.0	3490	0.68	III	0.348	1.664	2.89E-10	2.11
SO1017	M2.0 ± 1.0	3490	0.6	III	0.341	1.192	1.6E-10	3.81
SO1027	M2.0 ± 0.5	3490	0.48	III	0.335	1.094	1.1E-10	4.98
SO1052	M1.5 ± 1.0	3630	0.67	III	0.396	0.876	3.5E-11	9.20
SO1133	K7.5 ± 1.0	3970	0.62	III	0.675	1.704	2.9E-10	2.76
SO1207	M5.0 ± 0.5	2880	0.0	III	0.099	1.391	2.21E-10	0.45
SO1250	K7.0 ± 1.5	3970	0.36	III	0.672	1.793	2.58E-10	2.53
SO1268	M4.5 ± 3.0	3160	1.72	TD	0.151	0.667	3.6E-11	8.07

Note. Columns description as in Table 2.

Table 4

Median SEDs and Quartiles of Disk-bearing Stars with PACS Detections in σ Ori

Wavelength (μm)	$\log \lambda F_{\lambda}$		
	Median	Lower	Upper
0.44	-10.84	-11.35	-10.42
0.55	-10.50	-11.04	-10.19
0.64	-10.33	-10.77	-10.03
0.79	-10.18	-10.56	-9.89
1.235	-10.07	-10.28	-9.89
1.662	-10.08	-10.32	-9.93
2.159	-10.25	-10.48	-10.10
3.6	-10.60	-10.84	-10.24
4.5	-10.78	-11.07	-10.44
5.8	-11.00	-11.25	-10.54
8.0	-11.04	-11.28	-10.70
24.0	-11.30	-11.59	-11.04
70.0	-11.81	-12.00	-11.32
160.0	-12.15	-12.45	-11.84

Table 5

Photometric Median SEDs and Quartiles of Disk-bearing Stars in Taurus

Wavelength (μm)	$\log \lambda F_{\lambda}$		
	Median	Lower	Upper
1.235	-9.07	-9.25	-8.92
1.662	-9.09	-9.34	-8.94
2.159	-9.20	-9.50	-9.08
3.6	-9.64	-9.94	-9.36
4.5	-9.70	-10.09	-9.38
5.8	-9.86	-10.21	-9.48
8.0	-9.95	-10.25	-9.54
24.0	-10.23	-10.61	-9.88
70.0	-10.54	-10.85	-10.25
100.0	-10.87	-11.04	-10.40
160.0	-11.18	-11.33	-10.47

excesses below the medians of Taurus and σ Ori, and therefore 70 μm fluxes below the detection limit, or are located out of the PACS FOV.

4.1.1. Statistics of Transitional and Pre-transitional Disks

Statistical studies conducted by Muzerolle et al. (2010) in star-forming regions with ages from ~ 1 to 10 Myr have shown

that the fraction of TDs expected in young regions ($\lesssim 1\text{--}2$ Myr) is less than 2%, while for older regions (> 3 Myr) this fraction can be from 7% to 17%. However, Kim et al. (2013) estimated the fraction of TDs in the Orion A star-forming region including PTDs and what they defined as WTDs—intermediate between TDs and PTDs and considered as systems with an optically thin inner disk separated by a gap from an optically thick outer disk—and found that the fraction of TDs for clusters with ages < 1 Myr can be quite high (11%–25% for NGC 1333, 21%–29% for ONC, and 21%–31% for L1641) and similar to or greater than the fraction of Muzerolle et al. (2010) for clusters with ages between 1 and 2 Myr. Applying the exact test for the success rate in a binomial experiment (R Statistical Software, Ihaka & Gentleman 1996), we find that the fraction of objects classified as TDs is 12.5%, with a 95% confidence interval of 0.035–0.290. The rather large uncertainty is due to the modest size of our sample; however, this result is consistent with the results of Muzerolle et al. (2010) for a region with an estimated age of ~ 3 Myr.

4.2. Stellar and Accretion Properties

We estimated stellar and accretion properties of all the σ Ori members reported in H07a and H14 that lie inside the PACS FOV, for which we have the necessary spectra and photometry. This information complements the spectroscopic census of σ Ori sources made by H14. To characterize the stellar properties of the sources we located them in the H–R diagram. For this, we estimated the luminosity of our sample using J and V photometry, visual extinctions A_v , and spectral types from H14. For stars of F0 or later, bolometric correction and effective temperatures were obtained from the standard table for 5–30 Myr old pre-main-sequence (PMS) stars from Pecaut & Mamajek (2013, Table 6). For stars earlier than F0 we used the standard table of main-sequence stars reported by Pecaut & Mamajek (2013, Table 5). Using these luminosities and effective temperatures we estimated stellar radii for σ Ori members. We adopted the Mathis reddening law (Mathis 1990, $R = 3.1$). We assumed a distance to the σ Ori cluster of 385 pc (Caballero 2008c).

The H–R diagram for σ Ori members inside the FOV of PACS is displayed in Figure 7. Objects detected with PACS are, in general, late-type PMS stars, as discussed in Section 4.1. Using the isochrones of Siess stellar models (Siess et al. 2000), we were able to calculate the age and mass of all our stars in the

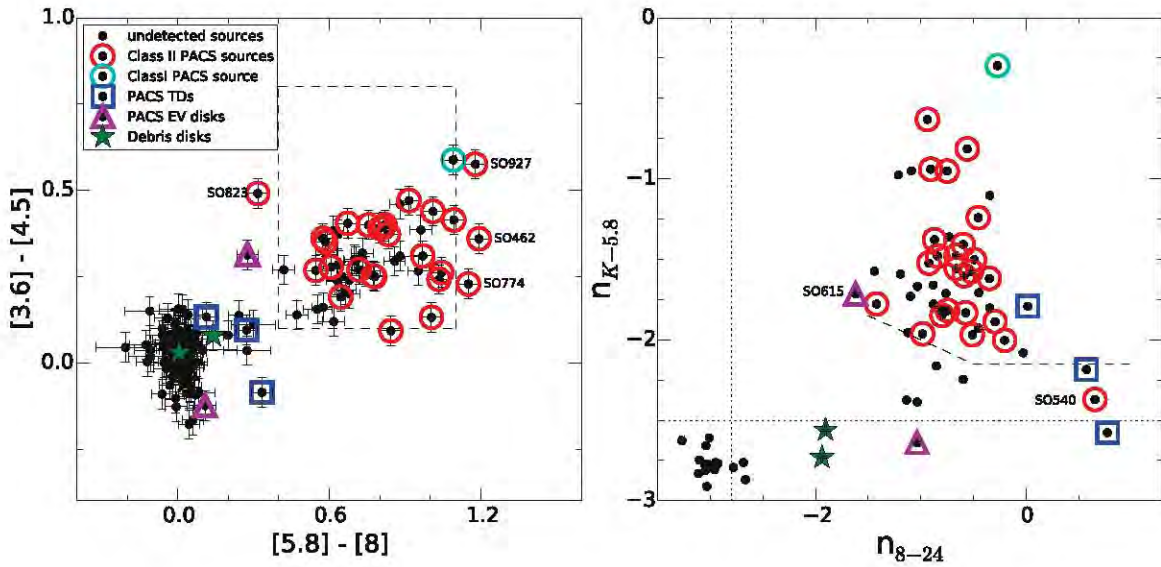


Figure 4. Left: IRAC color–color diagram of members of the σ Ori cluster reported by H07a (black dots). Different symbols are used to identify PACS detections: circles, squares, and triangles for class I/class II stars, TD and PTD disks, and evolved disks, respectively, as classified in H07a. Green stars indicate the colors of the two known debris disks (DD) in the cluster, which are not detected by PACS. The dashed box encloses the region of predicted colors for optically thick disks with different accretion rates and different inclinations (D’Alessio et al. 2006). The object SO823 is described as a slow accretor in H14. The source SO927 has large mid- and far-IR excesses, but is accreting just above the limit of Barrado y Navascués et al. (2003). Sources SO462 and SO774 present apparent redder [5.8]–[8.0] colors. Right: SED slopes for K –[5.8] and [8.0]–[24] colors of members of the σ Ori cluster reported by H07a. Objects detected at PACS are mostly systems with significant $24\ \mu\text{m}$ excesses. The dashed line represents the lower limit of primordial disks in Taurus (Luhman et al. 2010). Photospheric limits are indicated by dotted lines. Based on this diagram SO540 could be a transitional disk candidate instead of a class II star, and SO615 may be affected by chromospheric contamination, which would explain its flat $n_{K-5.8}$ slope (see text for details).

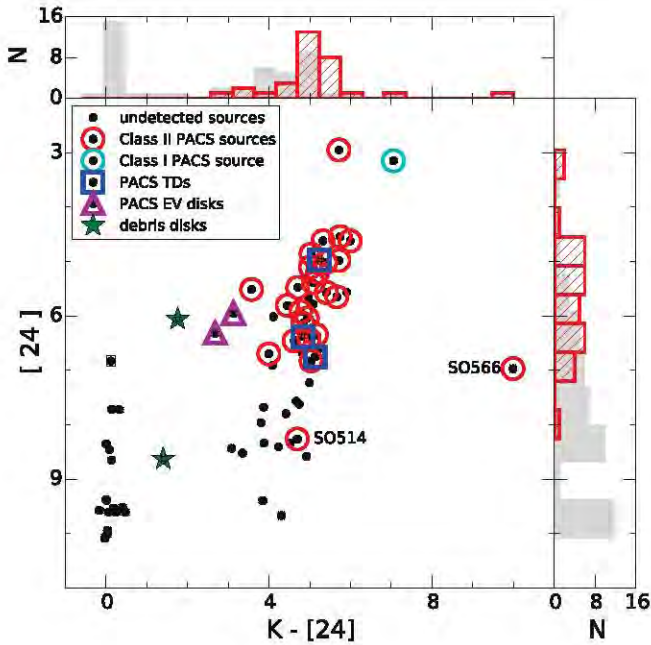


Figure 5. [24] vs. K –[24] color–magnitude diagram for members of the σ Ori cluster. Symbols are similar to Figure 4. Also shown are the histograms of MIPS $24\ \mu\text{m}$ (right) and K –[24] color (top) for detected (red dashed bars) and undetected (solid gray) sources. Note that PACS detections are stars with the largest excesses at $24\ \mu\text{m}$. The source SO566 is a variable star (see Figure 3), thus its large K –[24] color may not be real.

sample. Stellar properties are listed in Tables 2 and 3 for detected and undetected sources, respectively.

Mass accretion rates (\dot{M}) were estimated from the $H\alpha$ line luminosity (Muzerolle et al. 2003, 2005; Natta et al. 2004; Rigliaco et al. 2012; Ingleby et al. 2013). The $H\alpha$ luminosity was estimated by approximating the flux of the line ($F_{H\alpha}$) as

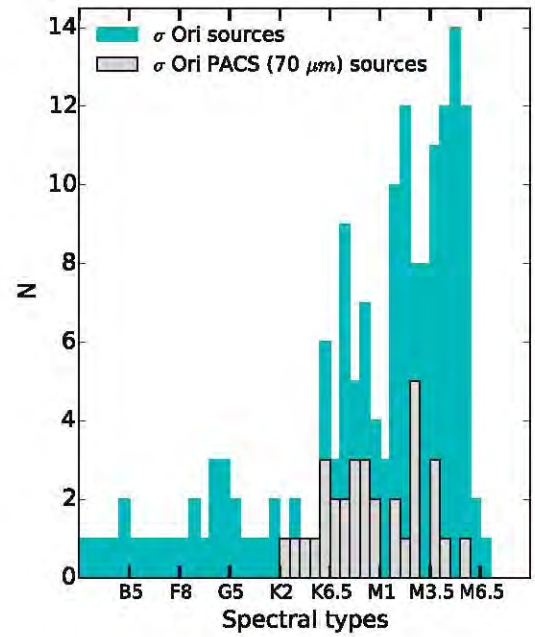


Figure 6. Histogram of spectral types reported by H14 for members of the σ Ori cluster. PACS detections are late-type stars with spectral types between K2.0 and M5.0.

$\text{EW}(H\alpha) \times F_{\text{cont}}$, where F_{cont} and $\text{EW}(H\alpha)$ are the continuum flux around the line and the equivalent width, respectively. We calculated F_{cont} from the R_c magnitude of each source reported in H07a corrected for extinction, and the equivalent widths $\text{EW}(H\alpha)$ from low-resolution spectra reported in H14. Once the line fluxes are estimated, the line luminosities are given by

$$L_{H\alpha} = 4\pi d^2 F_{H\alpha}, \quad (2)$$

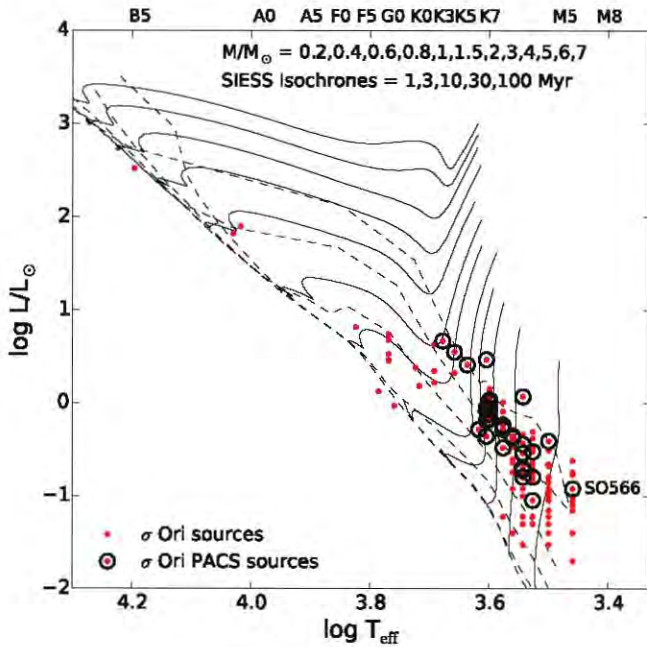


Figure 7. H–R diagram of σ Ori members reported in [H07a](#) and [H14](#) with the PACS sources marked. The object SO566 is a variable star (see [Figure 3](#)) so its position on the H–R diagram is uncertain. Solid lines are evolutionary tracks for $M/M_{\odot} = 0.2, 0.4, 0.6, 0.8, 1, 1.5, 2, 3, 4, 5, 6,$ and 7 from left to right. Dashed lines are isochrones of 1, 3, 10, 30, and 100 Myr. Evolutionary tracks and isochrones are from [Siess et al. \(2000\)](#).

where d is the distance to the σ Ori cluster.

In order to obtain the accretion luminosities we used the relation between the $H\alpha$ luminosity ($L_{H\alpha}$) and the accretion luminosity (L_{acc}) from [Ingleby et al. \(2013\)](#):

$$\log(L_{acc}) = 1.0(\pm 0.2)\log(L_{H\alpha}) + 1.3(\pm 0.7). \quad (3)$$

Finally, L_{acc} can be converted into \dot{M} using

$$\dot{M} = \frac{L_{acc}R_{*}}{GM_{*}}, \quad (4)$$

where M_{*} and R_{*} are the stellar mass and radius respectively. Three sources have no estimation of mass accretion rates since they do not have photometry in the R_c band (SO540, SO566, and SO638).

[Figure 8](#) shows a histogram of the mass accretion rates for the σ Ori cluster. PACS ($70 \mu\text{m}$) detections are plotted as gray bars and undetected sources as light blue bars. PACS detections exhibit $\dot{M} \leq 10^{-8} M_{\odot} \text{yr}^{-1}$. Note, however, that values of $\dot{M} < 10^{-9} M_{\odot} \text{yr}^{-1}$ are unreliable because of chromospheric contamination, as demonstrated by [Ingleby et al. \(2013\)](#), where an active chromosphere can mask all evidence of an accretion shock excess for the lowest accretors. Additionally, chromospheric activity adds uncertainty to the estimation of the luminosities of the lines associated with accretion for low-mass stars at later evolutionary stages ([Manara et al. 2013](#)). As noted in the figure, 23 undetected sources have $\dot{M} \geq 10^{-9} M_{\odot} \text{yr}^{-1}$; this is consistent with the discussion of [Figures 4 and 5](#) where the undetected CTTs in the PACS FOV are those with the lowest excesses at $24 \mu\text{m}$. Most of these sources are the less massive and intrinsically weaker CTTs in the cluster.

We compared our mass accretion rates with those reported by [Rigliaco et al. \(2011\)](#), who estimated \dot{M} from U -band excesses. In general, our mass accretion rates are higher than

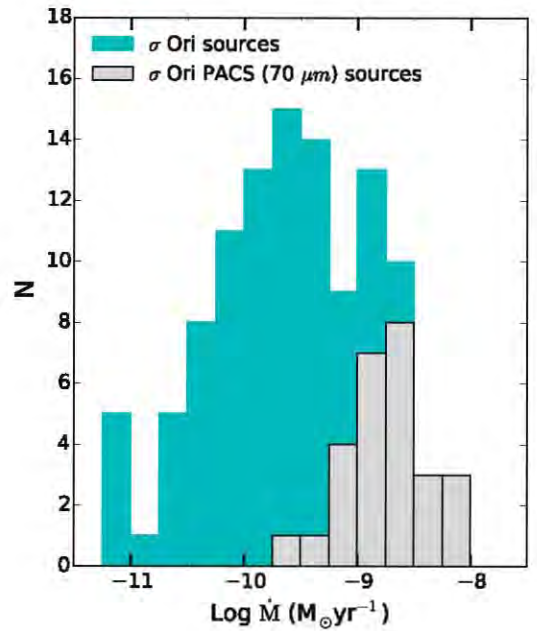


Figure 8. Accretion rates of σ Ori members. PACS ($70 \mu\text{m}$) detections are shown as gray bars while undetected members (inside the FOV of PACS) are plotted as light blue bars. PACS sources are consistent with accretion rates $\dot{M} \leq 10^{-8} M_{\odot} \text{yr}^{-1}$. Values of $\dot{M} < 10^{-9} M_{\odot} \text{yr}^{-1}$ are unreliable because of chromospheric contamination (see text for details).

[Rigliaco's](#). For the PACS sample we found that 10 out of 19 sources are consistent with the values reported by [Rigliaco et al. \(2011\)](#) within a factor of less than 3, while for the undetected sources we found that 10 out of 16 sources agree within the same factor. [Rigliaco et al. \(2011\)](#) neglected extinction, but [H07a](#) found extinctions up to 2.94 mag, which can be significant at the U band. This can explain some of the discrepancies between their values and ours. Another source of uncertainty is due to the fact that mass accretion rates determined from the U -band excess are not adequate for sources with $\dot{M} < 10^{-9} M_{\odot} \text{yr}^{-1}$ because of chromospheric contamination ([Ingleby et al. 2013](#)), which is the case for several of our undetected sources. Therefore, we also compared our mass accretion rates with those reported by [Rigliaco et al. \(2012\)](#), who estimated \dot{M} from the $H\alpha$ luminosities. Even though they also neglected extinction, accretion rates estimated from $H\alpha$ line luminosities are less affected by extinction than \dot{M} determined from U -band excesses. We found that, for the six sources we have in common, all but one (SO490) agree within a factor of $\lesssim 3$. [Gatti et al. \(2008\)](#) used near-IR hydrogen recombination lines ($\text{Pa}\gamma$) to measure mass accretion rates of 35 objects in σ Ori. If we compare our mass accretion rates with [Gatti's](#) we find that, for the 25 objects we have in common, all but three agree within a factor of ≤ 3 . The main uncertainties are due to the stellar mass adopted in each case, which in turn depends on the luminosity and the extinction of the sources, and on the spectral type.

All the accretion parameters of PACS sources are shown in [Table 2](#). Additionally, [Table 3](#) lists the accretion parameters for σ Ori members in the PACS FOV but without detections.

5. RESULTS

In this section we examine the emission of the disks around the PACS sources in σ Ori and interpret it in terms of irradiated

disk models including dust settling. We first make a global comparison of the spectral slopes in the PACS range with those predicted by irradiated disk models. We then model individual objects to provide a more detailed characterization of their disks. This detailed analysis of a fairly large number of disks in a young cluster, with estimated stellar and accretion parameters, will provide a census of disk properties useful for studies of the evolution of protoplanetary disks.

5.1. Disk Models

We follow the methods of D’Alessio et al. (2006) to calculate the structure and emission of accretion disk models. The main input parameters are the stellar properties (M_* , R_* , L_*), the mass accretion rate (\dot{M}), the viscosity parameter (α), the cosine of the inclination angle (μ), the disk outer radius (R_d), the maximum grain size at the disk midplane (a_{maxb}), and the dust settling, assumed to be constant throughout the disk.

The composition of the disk consists of amorphous silicates (pyroxenes) with a mass fraction of 0.004 and carbonates in the form of graphite with a mass fraction of 0.0025 (all these mass fractions are relative to gas). The PACS fluxes did not show a strong dependence on H_2O abundance, so we kept this parameter fixed at 10^{-5} . The emission from the inner edge or wall of the dust disk is calculated from the stellar properties, the maximum grain size (a_{maxw}), and the temperature (T_{wall}), which is assumed to be the sublimation temperature of silicate grains (1400 K) for the diffuse ISM (Draine & Lee 1984; D’Alessio et al. 2006), with a dust composition formed entirely by pyroxenes.

To simulate the settling of dust, D’Alessio et al. (2006) considered the ideal case of two dust populations, which differ in grain size. Both populations follow a size distribution with a function of the form $n(a) \propto a^{-p}$, where a is the radius of the grain, whose minimum value is $a_{\text{min}} = 0.005 \mu\text{m}$, and p is an exponent equal to 3.5, resembling the size distribution found in the ISM. The first population corresponds to small grains with $a_{\text{max}} = 0.25 \mu\text{m}$ —characteristic of ISM dust—which is expected in unevolved disks. These grains are mostly located in the upper layers and are assumed to be well mixed with the gas throughout the disk. The second population consists of larger grains, $a_{\text{max}} = 1 \text{ mm}$, and lives in the disk midplane. As the settling process takes place on the disk, dust particles will leave the upper layer and leave behind a depleted population of small grains that has a dust-to-gas mass ratio, ζ_{small} , lower than the initial value, ζ_{std} . On the other hand, the population of big grains will have a dust-to-gas mass ratio, ζ_{big} , larger than the initial value, since small dust particles that settle from upper layers will add mass to this population. Therefore, a decrease in ζ_{small} automatically implies an increase (of the same proportion) in ζ_{big} . We parameterize settling with the parameter ϵ , referred to as the dust-to-gas mass ratio and defined as $\epsilon = \zeta_{\text{small}} / \zeta_{\text{std}}$, i.e., the mass fraction of the small grains relative to the standard value. Therefore, lower values of ϵ represent more settled disks.

5.2. Spectral Indices

Since evolutionary effects, like dust settling and grain growth, are more apparent at longer wavelengths, we made plots of spectral indices using the PACS photometry reported here and IRAC and MIPS fluxes from H07a, in order to determine the overall degree of dust settling in our disks.

The left panel of Figure 9 displays a diagram of $n_{4.5-24}$ versus n_{24-70} for σ Ori members (solid circles). We compare the observed spectral indices with theoretical indices calculated for a set of models with the following parameters: $M_* = 0.5 M_\odot$, $R_* = 2 R_\odot$, $T_{\text{eff}} = 4000 \text{ K}$ (all these parameters constitute mean values in the cluster as shown in Tables 2 and 3) and two values of mass accretion rate, $\dot{M} = 10^{-8} M_\odot \text{ yr}^{-1}$ (light blue symbols) and $\dot{M} = 10^{-9} M_\odot \text{ yr}^{-1}$ (red symbols), where the latter is a common value for σ Ori sources (Figure 8). We fixed the viscosity parameter α to a typical value of 0.01 (Hartmann et al. 1998). As we already said in Section 4.2, we used a distance to the σ Ori cluster of 385 pc. Predicted spectral indices are indicated by open circles for models with $R_d = 250 \text{ au}$, and plus signs for models with $R_d = 10 \text{ au}$, where the size of the symbol varies according to the degree of dust settling, with larger symbols representing more settled disks (lower values of ϵ). Squares and triangles account for TD/PTD disks and evolved disks, respectively. The scatter observed in each case represents the variety of properties such as maximum grain size at the disk midplane, a_{maxb} , the maximum grain size at the disk wall, a_{maxw} , disk inclination angle, μ , disk external radius, R_d , and ice abundances adopted in the models. A similar plot is shown in the right panel of Figure 9 for the spectral index n_{24-160} on the x axis. As shown, models with different degrees of settling populate different regions on this diagram, the more settled disks being bluer than the less settled ones. Note as well the dependence of mass accretion rate on the $n_{4.5-24}$ slope. Models with $\dot{M} = 10^{-9} M_\odot \text{ yr}^{-1}$ have $n_{4.5-24}$ spectral indices as low as -1.5 , while models with $\dot{M} = 10^{-8} M_\odot \text{ yr}^{-1}$ have indices higher than -1.0 . As can be inferred from these diagrams, the majority of our objects fall in regions of $\epsilon \leq 0.01$, indicating that most of the σ Ori disks have a significant degree of settling. In both cases (left and right panels of Figure 9) the indices n_{24-70} and n_{24-160} for a set of objects lie outside the region populated by the models. However, in Section 5.3 we modeled almost all of these outliers.

Figure 10 displays the $n_{4.5-24}$ versus n_{24-70} spectral indices of σ Ori sources (black dots) compared to disks in Taurus (1–3 Myr, diamonds) from Howard et al. (2013) and Luhman et al. (2010). Also shown are the medians and quartiles for the n_{24-70} (top) and $n_{4.5-24}$ (right) indices of each region for comparison. The σ Ori sample has spectral indices similar to the population of Taurus.

In order to inquire deeply into this subject as well as to understand the degree of dust settling in the sample, we compared in Figure 11 histograms of observed n_{24-70} and n_{24-160} indices for σ Ori (black) and Taurus (light blue) disks. The ranges of the spectral indices for the disk models shown in Figure 9 were plotted as bands on top of these figures for ϵ values of 1.0, 0.1, 0.01, 0.001, and 0.0001 from top to bottom. The Taurus histograms were made with MIPS $24 \mu\text{m}$ photometry from Luhman et al. (2010) while the PACS fluxes were taken from Howard et al. (2013), giving an overall average of 21 sources. As shown in the left panel, most of our objects have a considerable degree of dust settling, since the peak of the histogram, labeled as σ Ori, falls in the same range as models with $\epsilon \leq 0.01$. A similar situation happens for the n_{24-160} index, shown in the right panel. In this case, however, there is more overlap between ranges occupied by models with different degrees of settling. These results imply that disks in our sample have experienced some evolution over time. Note,

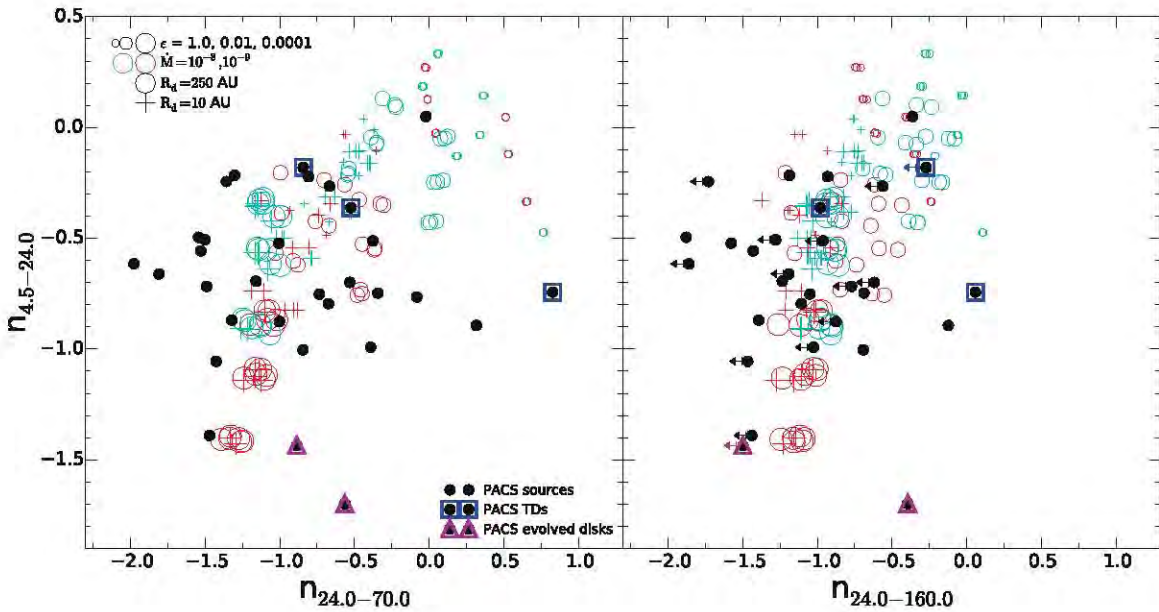


Figure 9. $n_{4.5-24}$ vs. n_{24-70} (left) and $n_{4.5-24}$ vs. n_{24-160} (right) for objects in the σ Ori cluster (solid circles) and disk models (open circles: models with $R_d = 250$ au; plus signs: models with $R_d = 10$ au). TDs are surrounded by blue squares and evolved disks by magenta triangles. The models use a star of $M_* = 0.5 M_\odot$, $R_* = 2 R_\odot$, $T_{\text{eff}} = 4000$ K, and two values of mass accretion rate, $\dot{M} = 10^{-8} M_\odot \text{ yr}^{-1}$ (light blue symbols) and $\dot{M} = 10^{-9} M_\odot \text{ yr}^{-1}$ (red symbols). Decreasing values of ϵ (more settled disks) are plotted with larger symbols ($\epsilon = 1.0, 0.01, \text{ and } 0.0001$). Error bars are included, but in most cases are smaller than the symbol. Arrows represent upper limits. Note the clear separation of the parameter ϵ on the x axis. The models are from D’Alessio et al. (2006). The σ Ori IRAC and MIPS photometry is taken from H07a.

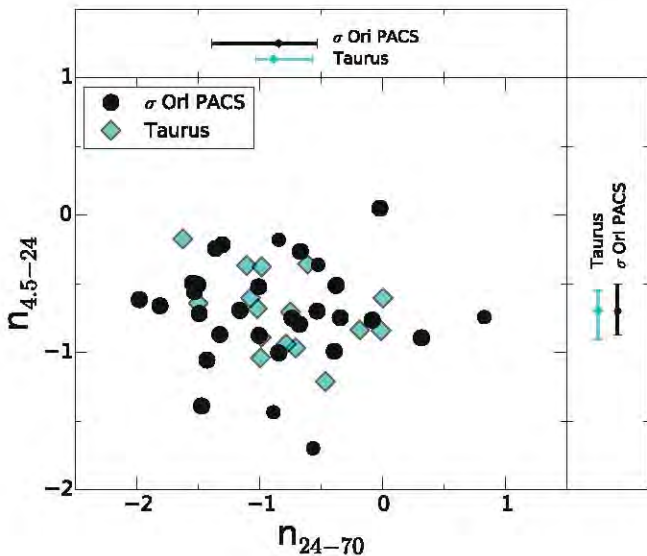


Figure 10. $n_{4.5-24}$ vs. n_{24-70} for objects in the σ Ori cluster (black dots). The Taurus star-forming region (light blue diamonds) is plotted for comparison, where the photometric data were taken from Howard et al. (2013) and Luhman et al. (2010). Also shown are the medians and quartiles for the n_{24-70} (top) and $n_{4.5-24}$ (right) indices of each region (error bars). Spectral indices for σ Ori are similar to those for Taurus.

as well, how disks in Taurus have a lower degree of dust settling, since the peaks of the Taurus histograms fall slightly to the right (bigger values of ϵ) compared to a significant number of σ Ori sources with $\epsilon \leq 0.01$ in the figures. This is consistent with previous studies of dust evolution where older disks are more settled and emit smaller IR excesses than young ones, which causes a decrease in the disk fraction as a function of age for a given stellar group (H07a). It is important to note that the fact that disks on Taurus already exhibit signs of dust settling

indicates that this process must happen at an early evolutionary stage.

5.3. Modeling of Individual Objects

To better constrain the dust content in our PACS disks classified as class II stars and EV disks (the TDs will be studied in a future paper), we modeled the SEDs of individual objects with irradiated accretion disk models, using as input the stellar properties and accretion rates reported in Table 2, assuming a viscosity parameter $\alpha = 0.01$ and a distance to σ Ori of 385 pc (Section 4.2). For each object we calculated a total of 1800 disk models, varying the outer radius (R_d), the degree of dust settling (ϵ), the cosine of the inclination angle (μ), and the maximum grain size at the disk midplane (a_{maxb}) and at the wall (a_{maxw}). Table 6 lists all the relevant parameters. We assumed a maximum grain size in the upper layer of the disk of $0.25 \mu\text{m}$. We selected as the best fit the model that yielded the minimum value of χ^2 . Upper limits in the observed fluxes were excluded from the calculation of the χ^2 value.

We modeled 18 sources out of 27 in the sample considered here (SO540 is taken as a TD, see Section 4.1): 17 class II stars and one EV disk. One of these objects, SO844, has millimeter detections taken with SCUBA-2 at $850 \mu\text{m}$, and the rest have only upper limits (Williams et al. 2013). Of the nine stars not modeled in this work, the source SO984 also has observations at $1300 \mu\text{m}$ taken with the Submillimeter Array (Williams et al. 2013). This object exhibits a MIPS $24 \mu\text{m}$ flux lower than that expected for class II stars (see Figure 3) and resembling that of PTDs, so it will be modeled, separately, in a future work. The rest are objects with significant uncertainties in their estimations of extinction and spectral type or objects without mass accretion rates (Section 4.2), so they were not modeled here.

Figure 12 shows the SEDs of our PACS disks (open circles) with the resulting fit (solid lines). Dashed lines indicate the σ

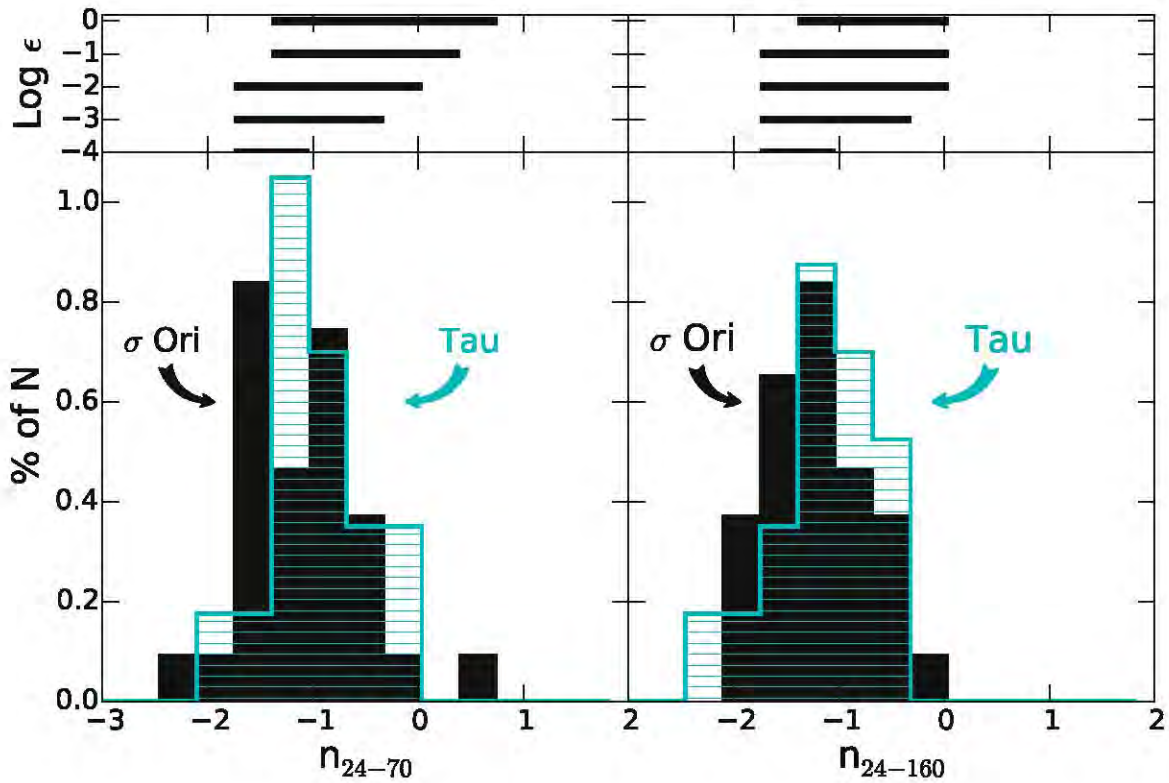


Figure 11. Bottom: histograms of n_{24-70} (left) and n_{24-160} (right) for objects in the σ Ori and Taurus regions. Top: n_{24-70} (left) and n_{24-160} (right) for models with different degrees of settling: $\epsilon = 1.0, 0.1, 0.01, 0.001,$ and 0.0001 from top to bottom. The models are from D’Alessio et al. (2006). The σ Ori MIPS photometry is from H07a. The Taurus PACS fluxes were taken from Howard et al. (2013), while the MIPS photometry was provided by Luhman et al. (2010). Note how disks in σ Ori have a higher degree of dust settling, since there is a significant number of PACS sources with lower values of ϵ compared to disks in Taurus.

Table 6
Model Parameters

Parameter	Value
R_d (au) ^a	10, 30, 50, 70, 100, 150, 200, 250, 300, 350
ϵ	1, 0.1, 0.01, 0.001, 0.0001
μ	0.3, 0.6, 0.9
$a_{\max b}$	100 μm , 1 mm, 10 cm
$a_{\max w}$	0.25 μm , 10 μm

Note.

^a The source SO697 needed a smaller R_d (Table 7).

Ori median (Table 4). Photospheric fluxes, using the colors of Kenyon & Hartmann (1995), are indicated by dotted lines. Table 7 gives the parameters of the best-fit model for each object with its corresponding reduced χ^2 value (χ^2_{red}) in the following order: target name, disk outer radius (R_d), confidence interval of disk outer radius ($R_d^- - R_d^+$), degree of dust settling (ϵ), cosine of the inclination angle (μ), maximum grain size at the disk midplane ($a_{\max b}$), maximum grain size at the wall ($a_{\max w}$), disk mass (M_d), and confidence interval of disk mass ($M_d^- - M_d^+$).

In order to calculate confidence intervals of the outer radius of the disks, we first estimated the likelihood function, \mathcal{L} , which is related to the χ^2 values through the expression $\mathcal{L} = \exp(-\chi^2/2)$. Since χ^2 is a multidimensional function, at every radius we have several values of χ^2 , one for each one of the calculated models. Thus, the likelihood \mathcal{L} is computed using the minimum χ^2 value at each radius. In Figure 13 we show plots of the normalized likelihood as a function of radius

for all the 18 sources that were successfully modeled. We have restrained the x axis around the maximum peak in each case in order to better visualize the likelihood function. As usual, the confidence intervals of R_d are given as those radii $R_{d,1}$ and $R_{d,2}$ at which the area below the likelihood curve is 95% of its total area (Sivia & Skilling 2012). These intervals are indicated by light blue shaded regions in each panel and are reported in column 3 of Table 7. For those cases where the best radius falls on one of the edges of the range of radii used in the models, we have considered these values as upper or lower limits, and they are indicated by parenthesis instead of square brackets in Table 7. On the other hand, since the mass of the disk is a parameter that correlates with size, the confidence intervals of the mass are given as the values of the mass given by the best-fit model at $R_{d,1}$ and $R_{d,2}$. These values are reported in column 9 of Table 7.

Some sources have peculiar SEDs: SO844 shows strong excess emission from the mid-IR to the far-IR, particularly in all four IRAC bands. This is probably due to variability. SO462, on the other hand, has a poor fit from H to IRAC 5.8 μm , which significantly increases the value of χ^2 ; it is worth noting that this source has the largest A_v ($=2.94$, see Table 2). Finally, SO697 needed a smaller radius than the other sources ($R_d = 7$ au). This is due to its low flux at 70 μm combined with one of the lowest 160 μm upper limits. Therefore, any disk model with an outer radius greater than 7 au will overestimate the flux at 70 μm and will produce a flux greater than the upper limit at 160 μm .

We point out that we used the values of χ^2 as a guide in order to obtain the model that provides the best fit to the photometry of each source. However, the values of χ^2 are

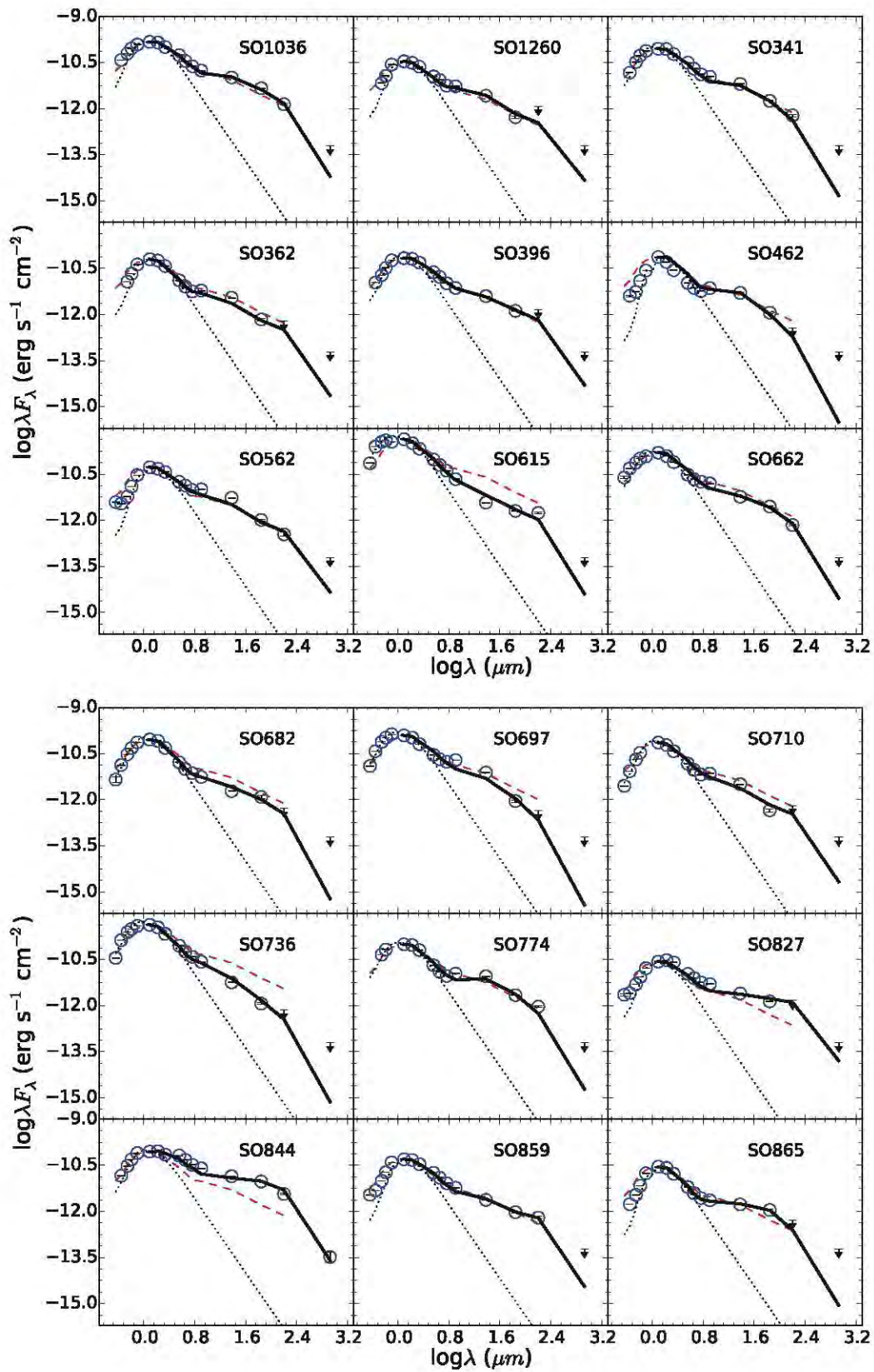


Figure 12. Spectral energy distributions for σ Ori sources including the millimeter photometry from Williams et al. (2013). As in Figure 3, photometry has been dereddened following the Mathis law (Mathis 1990, $R = 3.1$, open circles). Solid lines indicate the best-fit model. Dashed lines represent the median of σ Ori PACS sources (Table 4). Dotted lines correspond to the photosphere-like fluxes using the colors of Kenyon & Hartmann (1995). Error bars are included, but in most cases are smaller than the symbol. Downward arrows indicate upper limits.

Table 7
Estimated Disk Parameters

Target	R_d (au)	$R_d^- - R_d^+$ (au)	ϵ	μ	a_{maxb}	a_{maxw} (μm)	M_d ($10^{-3} M_\odot$)	$M_d^- - M_d^+$ ($10^{-3} M_\odot$)	χ^2_{red}
SO1036	70	[69–94]	0.01	0.3	10 cm	10	5.19	[4.78–6.10]	6.116
SO1260	250	[180–250]	0.0001	0.9	100 μm	10	3.11	[2.57–3.11]	14.33
SO341	200	[158–208]	0.01	0.6	10 cm	10	1.24	[1.05–1.34]	24.784
SO362	150	[126–156]	0.0001	0.9	100 μm	0.25	1.01	[0.91–1.11]	31.489
SO396	10	(10–29)	0.01	0.3	100 μm	10	1.15	(1.15–2.46)	2.040
SO462	10	(10–16)	0.01	0.9	10 cm	0.25	0.098	(0.09–0.14)	265.259
SO562	200	[142–229]	0.0001	0.9	100 μm	10	2.70	[2.24–3.26]	55.817
SO615	200	[100–238]	0.0001	0.9	100 μm	10	1.25	[0.68–1.49]	51.825
SO662	200	[79–250]	0.001	0.9	10 cm	10	2.44	[1.32–2.91]	52.388
SO682	10	(10–12)	0.01	0.6	1 mm	0.25	0.031	(0.028–0.035)	14.469
SO697	7	[6–11]	0.01	0.6	10 cm	10	0.11	[0.10–0.16]	110.766
SO710	100	[63–126]	0.0001	0.9	100 μm	10	0.69	[0.45–0.85]	44.761
SO736	10	(10–12)	0.001	0.3	10 cm	0.25	0.22	(0.22–0.27)	27.975
SO774	250	[203–250]	0.01	0.9	10 cm	10	1.68	[1.43–1.68]	47.192
SO827	250	[185–250]	0.01	0.6	100 μm	10	4.94	[3.90–4.60]	34.874
SO844 ^a	150	[149–158]	0.1	0.6	10 cm	10	39.40	[39.40–43.70]	48.159
SO859	30	[10–36]	0.01	0.3	100 μm	10	0.47	[0.23–0.57]	16.131
SO865	250	[237–250]	0.01	0.9	10 cm	0.25	0.85	[0.77–0.85]	3.450

Note. Column 1: ID following H07a; Column 2: disk outer radius; Column 3: confidence interval of disk outer radius; Column 4: degree of dust settling; Column 5: cosine of the inclination angle; Column 6: maximum grain size at the disk midplane; Column 7: maximum grain size at the disk wall; Column 8: disk mass; Column 9: confidence interval of disk mass; Column 10: χ^2_{red} value of the fit.

^a Object with SCUBA-2 850 μm photometry from Williams et al. (2013).

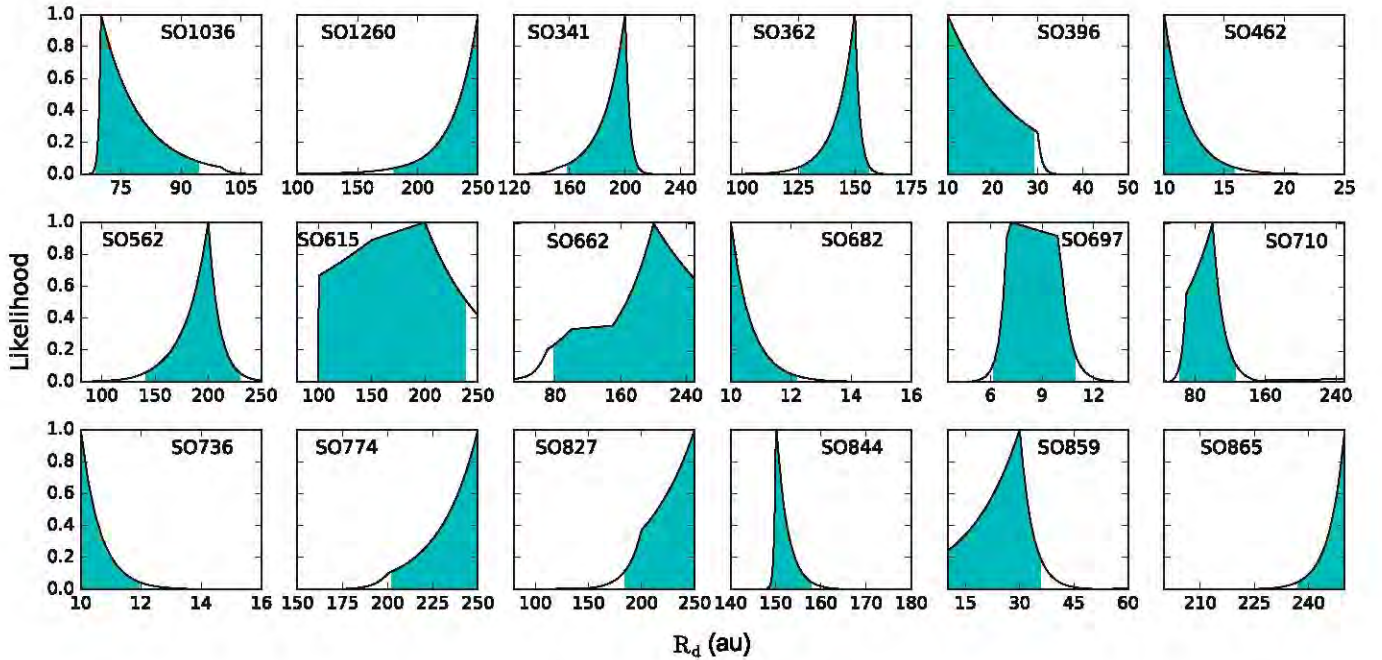


Figure 13. Likelihood function, \mathcal{L} , vs. disk radius, R_d , for each source. The x axis has been restrained around the maximum peak in each case in order to better visualize the likelihood function. Confidence intervals of R_d are shown as light blue shaded regions and are defined as the intervals that enclose 95% of the total area of \mathcal{L} .

expected to be large. One of the most problematic points to fit is the IRAC 8 μm band. In a real spectrum, this band contains a contribution from the 10 μm silicate feature. The total flux of this feature is highly dependent on the adopted composition of the silicates, as detailed modeling of IRS spectra has shown (see McClure et al. 2012, 2013b). However, we felt that one photometric point did not give enough constraints to justify having the silicate composition as an additional parameter. Another reason for the large values of χ^2 is that we are

including only the errors in the photometry, which are small, and not other sources of uncertainty such as the inherent uncertainties in the distance, luminosity, spectral types, and mass accretion rates. In a forthcoming paper we will model these sources including their IRS spectra, in order to characterize their silicate features, which will improve the current fit. Through this study we will characterize the inner parts of the disk in the sense of grain growth, dust processing, and types of silicates present in the disks.

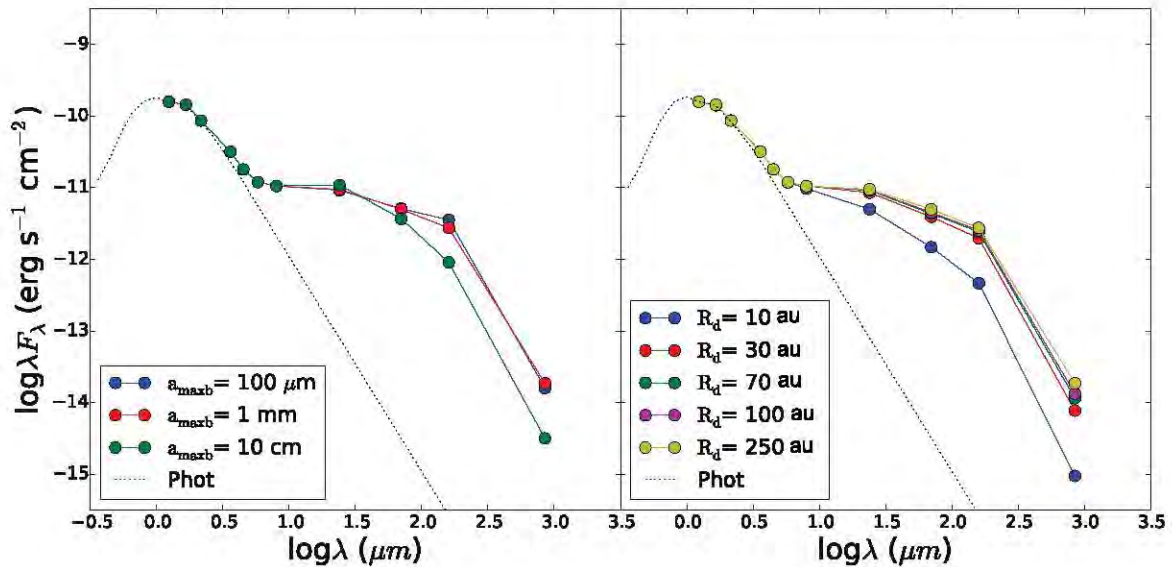


Figure 14. Left: theoretical SEDs with different values of a_{maxb} . Note how disks with $a_{\text{maxb}} = 10$ cm have far-IR fluxes substantially lower (by almost an order of magnitude) than disks with smaller a_{maxb} . However, changes in the SED for $a_{\text{maxb}} \leq 1$ mm are less than 10%, so we cannot discriminate them. Right: theoretical SEDs with different sizes. Note how small disks with $R_d = 10$ au exhibit lower fluxes in the mid- and far-IR than larger disks, the difference reaching almost an order of magnitude at $160 \mu\text{m}$. For the cases with $R_d \geq 70$ au changes between the SEDs at far-IR wavelengths are less than 10%, so we cannot discriminate them. Dotted lines correspond to the photosphere-like fluxes for one of the stars in our sample using the colors of Kenyon & Hartmann (1995). For these models we used an ϵ value of 0.01.

The flux in the mid-IR is mostly dictated by the mass accretion rate and the inclination, since for settled disks a large fraction of the flux arises in the innermost disk regions. For instance, 80% of the flux at $24 \mu\text{m}$ and shorter wavelengths arises inside ~ 2 au for a disk with $\epsilon = 0.001$, instead of ~ 20 au for a well mixed disk (D’Alessio et al. 2006; McClure et al. 2013a). In addition, as settling increases, the depleted upper layers become optically thin, exposing the disk midplane. Therefore, highly settled disks are colder and radiate less than disks with a low degree of settling (D’Alessio et al. 2006). We found that most of our objects (60%) can be explained by a significant degree of dust settling, $\epsilon = 0.01$, consistent with studies in young regions like Taurus and Ophiuchus (Furlan et al. 2006; McClure et al. 2010). We also found that some of our objects have an even higher degree of dust settling ($\epsilon = 0.0001$), which, in turn, is consistent with previous studies of disk fraction as a function of age in different young stellar populations (H07a).

The dependence of the flux on a_{maxb} has been discussed by D’Alessio et al. (2001). Even though we found nine sources to have $a_{\text{maxb}} = 100 \mu\text{m}$ (Table 7), the left panel of Figure 14 shows that models with $\epsilon = 0.01$ and $a_{\text{maxb}} \leq 1$ mm only differ by less than 10%, a factor that is even smaller for $\epsilon = 0.0001$, so we cannot discriminate sizes of $a_{\text{maxb}} \leq 1$ mm. The right panel, on the other hand, shows the effects of changing the disk radius on the SED. As expected, smaller disks produced steeper mid- and far-IR slopes and lower fluxes. Differences in disks radii are more apparent for $R_d < 70$ au. We found that 65% of our objects can be modeled with large sizes, $R_d \geq 100$ au. The rest have dust disk radii less than 80 au. Note how changes in R_d affect the SED from MIPS $24 \mu\text{m}$ to millimeter wavelengths while changes in a_{maxb} are apparent only beyond $24 \mu\text{m}$.

We found no correlation between the mass accretion rate and the degree of dust settling. The disks with highest and lowest mass accretion rate in our sample have $\epsilon = 0.01$. This seems to imply that the turbulence expected in the high accretors is not

influencing the vertical distribution of dust in disks, which is contrary to expectations.

6. DISCUSSION: DISK EVOLUTION IN THE σ Ori CLUSTER

6.1. Disk Properties

We have obtained detailed disk structures for 18 disks in the σ Ori cluster using irradiated accretion disk models (D’Alessio et al. 2006), constrained by mass accretion rates estimated independently from optical spectra. As a result of our modeling, we inferred disk masses and radii, assuming a gas-to-dust ratio close to that of the ISM. The masses of the best-fit models are given in Table 7; most of the masses are of the order of $\sim 10^{-3}$ to $10^{-4} M_\odot$. By analyzing possible degeneracies in SED fitting using a set of 1800 generic models with different parameters, we estimated that the uncertainty in the inferred disk masses is a factor of 3, if the mass accretion rates of the sources are known.

Our mass determinations are consistent with those inferred by Williams et al. (2013) from $850 \mu\text{m}$ SCUBA-2 observations. Williams et al. (2013) detected nine disks, but only five of these lie inside the FOV of our PACS observations. Four of these sources (SO540, SO844, SO984, and SO1153) were detected at 70 and $160 \mu\text{m}$. The only source not detected, SO609, is a class III star (H07a). Of the detections, SO1153 is a class I star, as seen in Figure 3, and it was not modeled here. Similarly, the source SO984 will be modeled in a future work together with other TDs such as SO540 (see Section 5.3). The SED and best-fit model for the source SO844 are shown in Figure 12 with inferred properties in Table 7. The disk mass for this object, $39 M_{\text{Jup}}$, is a factor of ~ 8 higher than the mass estimated by Williams et al. (2013). The reason for this is that our dust grain opacity (κ_ν) at $850 \mu\text{m}$ for this object is significantly lower than theirs. Unlike Williams et al. (2013), which assumed a dust opacity of $\kappa_\nu = 0.1(\nu/1200 \text{ GHz}) \text{ cm}^2 \text{ g}^{-1}$, we used a

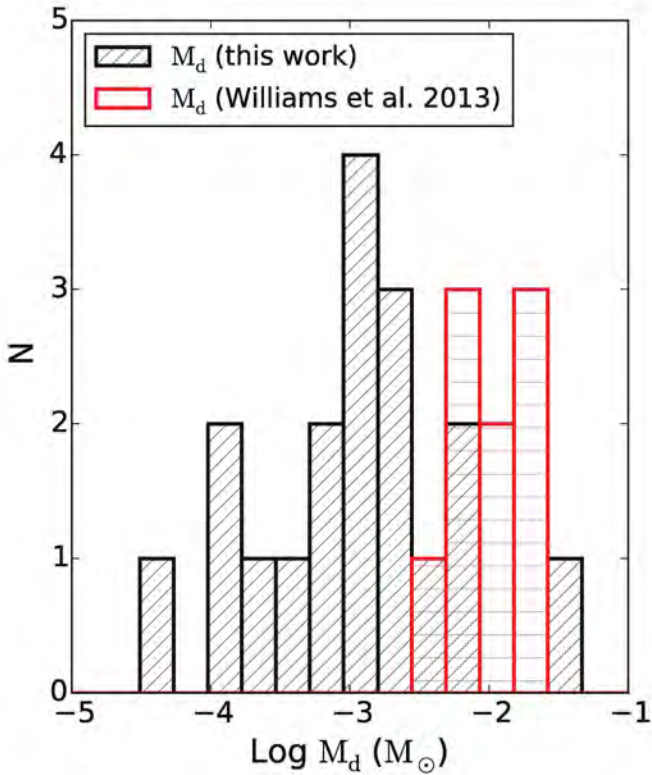


Figure 15. Disk mass (M_d) distribution for σ Ori members with PACS detections reported in Table 7 (black). The mass distribution found by Williams et al. (2013) is shown in red for comparison. All our disks except SO844 ($M_d = 39 M_{\text{Jup}}$) correspond to the lower end of the cluster mass distribution while those of Williams et al. are located at the high-mass end. This plot shows how PACS observations can be more suitable for detecting less massive small disks than millimeter observations.

consistent opacity law (estimated through detailed modeling of the SEDs) for each one of our objects. This opacity depends on the mix of materials assumed in our disk models (silicates, graphite, water, etc.), their abundances, and their grain size distributions. Therefore, each object has a distinct disk dust opacity. With our dust opacity we can reproduce not only the flux at $850 \mu\text{m}$ but the entire SED (see Figure 12).

Figure 15 shows the disk mass distribution for our σ Ori sources in black compared to the mass distribution found by Williams et al. (2013) in red. Our detections include significantly lower values than the survey of Williams et al. (2013). The fact that we have detected 24 more sources than Williams et al. (2013) inside the FOV of their observations indicates that the PACS photometry was more suitable for detecting even small young disks than the shallow submillimeter observations. However, since our longest wavelength is $160 \mu\text{m}$, we may be missing emission from the largest grains and underestimating our masses. Our models are consistent with the upper limits of the $850 \mu\text{m}$ SCUBA-2 observations (Figure 12), which suggests that the mass deficit is not large. Moreover, Williams et al. (2013) reported a 3σ limit of $4.3 \times 10^{-3} M_{\odot} \sim 4.5 M_{\text{Jup}}$, so their non-detections imply disk masses $< 5 M_{\text{Jup}}$, a value that is very similar to the upper limit of our disk masses for sources not detected with millimeter observations ($\sim 5.5 M_{\text{Jup}}$, source SO1036; see Table 7). This supports the fact that we are truly looking at disks with very low masses. More sensitive millimeter observations are still required to determine this mass deficit. In any event, the masses

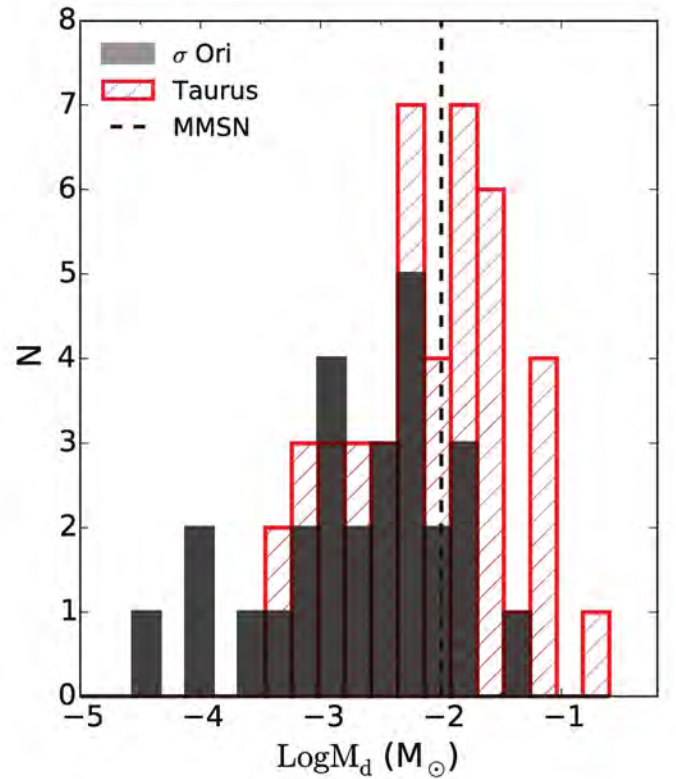


Figure 16. Histograms of disk mass (M_d) for disks in σ Ori (black) and Taurus members (red) reported in Andrews & Williams (2005). The disk mass distribution for σ Ori disks includes our sample (Table 7) and sources reported by Williams et al. (2013). Also shown is the minimum mass solar nebula of $10 M_{\text{Jup}}$ (dashed line). σ Ori disk masses range between 0.03 and $\sim 39 M_{\text{Jup}}$. Most objects have masses significantly lower than the disk masses in Taurus.

of the σ Ori disks apart from SO844 range between 0.03 and $\sim 6 M_{\text{Jup}}$, with 35% being lower than $1 M_{\text{Jup}}$. Like Williams et al. (2013), we conclude that Jupiter-scale giant planet formation must be complete in these objects, which indicates either that giant planets form in less than 3 Myr or that it is difficult to make them in clustered environments.

Figure 16 shows the disk mass distribution of σ Ori (our sample and Williams’) compared to that of Taurus. An overall decrease in disk mass is clearly seen. This behavior of disk mass with age is expected from viscous evolution (Hartmann et al. 1998). For instance, between 1 and 3 Myr, the ages of Taurus and σ Ori, the disk mass should decrease by a factor of 1.5. However, the disk sizes should correspondingly increase by a factor of 2.5, which we do not see (see next section and Table 7). One possibility is that these disks have been subject to radial drift, according to which the millimeter-size grains have drifted inward and have piled up into pressure bumps, resulting in an observationally smaller dust disk (Pinilla et al. 2012b; Birnstiel & Andrews 2014), an effect that may be at play in TW Hya (Andrews et al. 2012) and other disks (Panić et al. 2009; Laibe et al. 2012; Pinilla et al. 2012a; Rosenfeld et al. 2013; Zhang et al. 2014). Another possible explanation for the presence of small disks is due to interactions with stellar companions. This effect has been observed in Taurus for close binaries with separations < 40 au (Kraus & Hillenbrand 2012). Multiplicity in σ Ori has been reviewed by Caballero (2014), where he notes that outside the central arcminute, only 10 close binaries have been reported with angular separations between $0''.4$ and $3''.0$ (~ 150 – 1200 au). Of these, only two have been

Table 8
KS Test Between Histograms of Spectral Indices for the Taurus and σ Ori Samples

Index	D	p
n_{24-70}	0.27	0.35
n_{24-160}	0.19	0.77
n_{K-24}	0.14	0.96
n_{K-70}	0.24	0.37
n_{K-160}	0.29	0.19

imaged with adaptive optics. In short, more high-resolution imaging surveys of close binaries in σ Ori are needed in order to determine whether multiplicity is a major factor affecting the evolution of disks. Alternatively, these disks may have suffered the effects of photoevaporation, in which case both the dust and the gas have dissipated from the outer disk. We explore this possibility in the next section.

6.2. Disk Photoevaporation in σ Ori

The age of the σ Ori cluster is estimated to be ~ 3 Myr (H07a), which is older than Taurus (Kenyon & Hartmann 1995, $\sim 1-2$ Myr) or the ONC (Hillenbrand 1997, < 1 Myr). By applying Kolmogorov–Smirnov tests for the n_{24-70} and n_{24-160} spectral indices between disks in Taurus and σ Ori (see Figure 11), we found that the levels of significance p for these indices are not small enough (compared to the statistics D) to say that the distributions are intrinsically different (Table 8). However, testing differences in the inner parts of the disks between the two distributions (using n_{K-24} , n_{K-70} , and n_{K-160} spectral indices) shows that, as the wavelength increases, the distributions become substantially different, such that for the case of the last index, n_{K-160} , we can reject the null hypothesis that the samples are drawn from the same distribution ($D > p$, Table 8). This may imply that dissipation due to nearby massive stars dominates in the σ Ori cluster, photoevaporating the outer disks, in contrast to the inside-out dissipation in regions without massive stars, like Taurus.

Since disks in σ Ori are accretion disks, with substantial mass accretion rates (Section 4.2), viscous evolution must also be at play. Two alternatives are then possible: isolated viscous evolution or viscous evolution mediated by external photoevaporation. To consider the latter as a possibility, we must first consider its feasibility. To do so, we estimated the field intensity, G_0 , produced by the three brightest objects in the system, the σ Ori Aa, Ab (O9.5, B0.5) pair and σ Ori B ($\sim B0-B2$) with a total mass of $\sim 44 M_\odot$ (Caballero 2014; Simón-Díaz et al. 2015). Using the reported stellar luminosities for these stars, and assuming that most of the stellar radiation is in the form of FUV photons, we estimated the intensity of the incident radiation at a given distance r from the source:

$$G_0 = \frac{1}{F_0} \frac{L_{\text{FUV}}}{4\pi r^2}, \quad (5)$$

where F_0 is the typical interstellar flux level with a value of $1.6 \times 10^{-3} \text{ erg s}^{-1} \text{ cm}^{-2}$ (Habing 1968), L_{FUV} is the FUV luminosity of the σ Ori multiple system and r the true distance to the ionizing sources. We used Monte Carlo simulations to calculate the distribution of true distances to the center for a given impact parameter, and from this the expected distribution of G_0 , following Anderson et al. (2013).

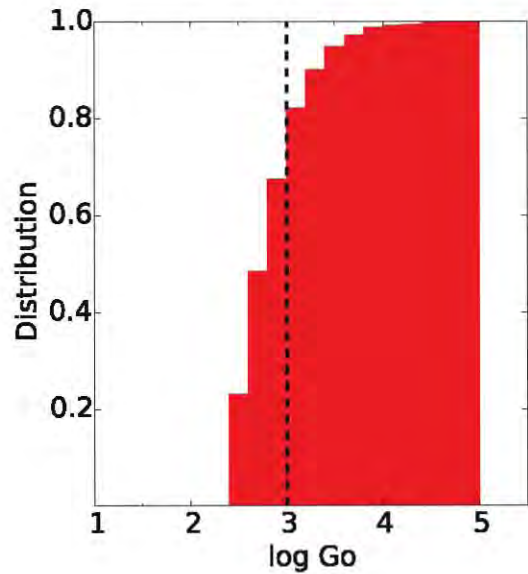


Figure 17. Cumulative distribution of expected FUV fluxes for a sample of 32 PACS disks in the σ Ori cluster. Nearly 80% of PACS disks are exposed to flux levels of $G_0 \lesssim 1000$ (dashed line).

We obtained that 80% of our disks are exposed to flux levels of $300 \lesssim G_0 \lesssim 1000$ (see Figure 17). Even though these are modest values of G_0 , Anderson et al. (2013) show that even with values of external FUV radiation fields as low as $G_0 = 300$, external photoevaporation can play a significant role by greatly reducing the lifetime of the disks, as well as by truncating their outer edges. This is consistent with the fact that a third of our disks have radii ≤ 30 au (see Table 7). As we showed in Section 5.3 small radii can reliably be determined from the SED. These radii refer to the extent of the dust disk since we lack resolved gas observations; nevertheless, this result indicates that a possible explanation for the presence of small disks in populated regions is due to external photoevaporation by massive OB stars.

Even though there is no correlation between disk radii and projected distance—a result also found in the ONC proplyds (Vicente & Alves 2005; Mann & Williams 2010; Mann et al. 2014)—our argument is reinforced by the fact that (a) two of our smallest disks, the sources SO697 ($R_d = 7$ au) and SO682 ($R_d = 10$ au), have the closest projected distances to the σ Ori multiple system (0.45 and 0.14 pc, respectively), (b) 81% of our largest disks (e.g., the sources SO774, SO865, and SO1260) are located at projected distances greater than 1 pc, and (c) most of the $850 \mu\text{m}$ SCUBA-2 detections of Williams et al. (2013) are *outside* the PACS field, at distances ≥ 2.23 pc from the central ionizing sources.

In Figure 18 we show our determinations of disk masses and radii in σ Ori compared to those of proplyds in the ONC. We have included in the figure the confidence intervals of M_d and R_d estimated in Section 5.3. The disk masses for the ONC are taken from Mann & Williams (2010) and radii from Vicente & Alves (2005). We also show the expected evolution of viscous disks subject to photoevaporation from Anderson et al. (2013). Unlike isolated viscous evolution, in which disks expand as the disk mass increases, viscous disks subject to external photoevaporation first expand until they reach the evaporation radius, where photoevaporation begins to act and to rip out the external disk regions. As a result, both the disk mass and radius

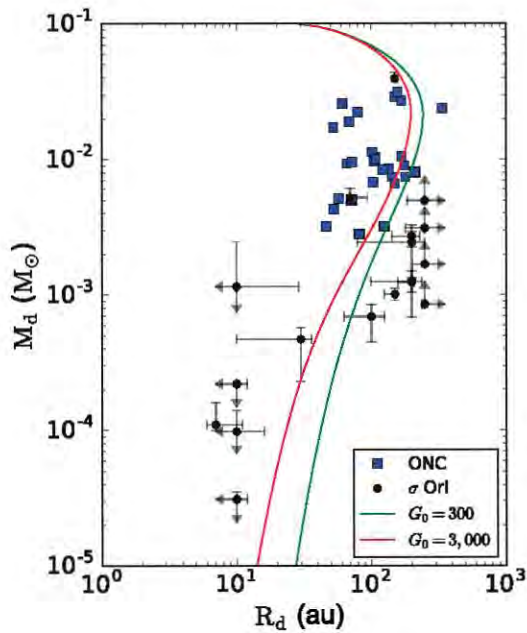


Figure 18. Disk mass (M_d) vs. disk radius (R_d) for σ Ori sources (black dots) and proplyds in the ONC (blue squares). We have included the confidence intervals of M_d and R_d estimated in Section 5.3. The disk masses for the ONC are taken from Mann & Williams (2010) and radii from Vicente & Alves (2005). Evolutionary tracks (solid curves) are taken from Anderson et al. (2013) for two values of G_0 , 3000 (red) and 300 (green), and a viscosity parameter $\alpha = 0.01$.

decrease with age (Anderson et al. 2013). The σ Ori disks fit this trend. Their masses are lower than those of the ONC disks, since they are older, while their radii are comparable or smaller. The two models shown in Figure 18 correspond to two values of G_0 , 300 and 3000, with the lower value corresponding to overall larger disk radii. This suggests that the shift between the ONC disks and the σ Ori disks may be due to the latter being subject to comparatively lower levels of FUV flux (which explains the slightly larger radii) for a longer period of time (which may explain the smaller radii). However, given that disk radii of proplyds were measured from *Hubble Space Telescope*/WFPC2 $H\alpha$ images, and hence these values are related to the gaseous disks, and we estimated disk radii from modeling the SEDs, which are associated with the dusty disks, there are likely systematic differences between the two measurements of disk radius made using very different methods. We need more sensitive millimeter observations of gas in these disks in order to make a more robust comparison.

The evolutionary models shown in Figure 18 assume a constant value of G_0 throughout the disk evolution. This is only an approximation since stars are not static—they orbit around the cluster center and therefore will experience different FUV flux levels during their lifetime. For very eccentric orbits the stars will stay longer in outer regions, where the FUV field is low, and retain their disk masses longer. Furthermore, these models assume a constant value of α ; adopting a non-uniform radial profile for the viscosity alters the disk structure (Kalyaan et al. 2015) and therefore the mass–radius evolutionary tracks. We adopted a viscosity parameter of $\alpha = 0.01$. With this viscosity the disks are depleted down to $10^{-5} M_\odot$ very quickly (< 1 Myr). Using a lower α will increase the lifetime of the disks but will not produce disks as large as observed. Note that the timescale for disk dispersal depends strongly on the

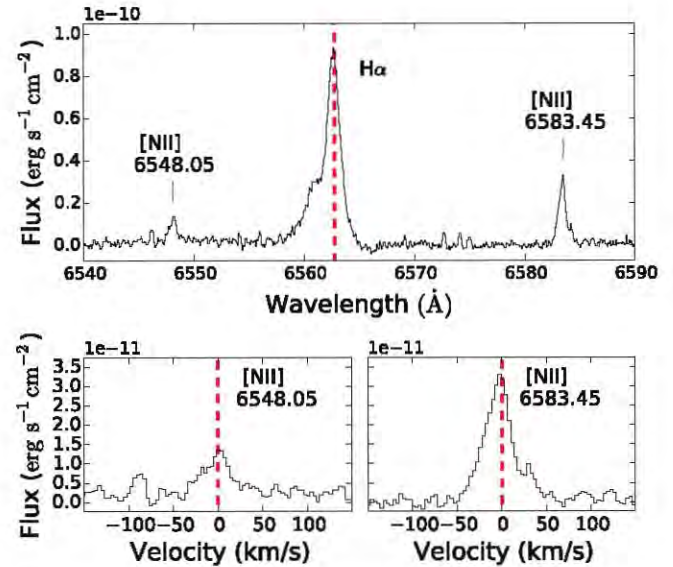


Figure 19. Top: Hectochoelle spectrum of SO662 (H14) showing the forbidden emission lines of [N II] along with the $H\alpha$ line characteristic of TTSs. Bottom: Lines of [N II] in velocity space. This object is located at $d_p = 0.60$ pc and has a disk size $R_d = 200$ au (Table 7). The presence of the forbidden lines of [N II] may be evidence of photoevaporation (Rigliaco et al. 2009).

assumed disk viscosity, and therefore a relatively small range of α can lead to a wide range in the disk mass and radius at a given time. The models also assume an initial disk radius of 30 au. In reality, disks will exhibit a wide range of radii depending on the initial conditions of the core where the stars are formed. However, Anderson et al. (2013) showed that varying the initial radius by a factor of two does not change the evolutionary tracks. Another approximation of the models is the assumption of a stellar mass of $M_* = 1 M_\odot$. Stars with smaller masses will produce shallower gravitational potential wells, allowing the unbound material to be located closer to the star, and possibly producing smaller disks. All these approximations may be responsible for the differences in radii observed between the models and disks in σ Ori. Finally, as mentioned above, the radial distribution of dust may differ from that of the gas. However, even with these simplifying assumptions, the models reproduce the observations of the ONC remarkably well and those of the σ Ori disks sample quite well.

Additional support for the photoevaporative hypothesis comes from the presence of forbidden lines in the optical spectra of the disk sources. These lines are expected to form in a photoevaporating wind (Hartigan et al. 1995; Acke et al. 2005; Pascucci & Sterzik 2009; Rigliaco et al. 2009, 2012, 2013; Gorti et al. 2011; Natta et al. 2014). Rigliaco et al. (2009) found forbidden lines of [S II] and [N II] in high-resolution spectra of SO587, located at $d_p = 0.35$ pc. They associated these emission lines with a photoevaporating wind estimated to give $\dot{M}_{\text{loss}} \sim 10^{-9} M_\odot \text{ yr}^{-1}$. Unfortunately, we did not model this object because it was not detected with PACS.

The survey of H14 includes high-resolution spectra of some of the PACS sources; these spectra cover the region around $H\alpha$ and include the [N II] $\lambda 6548.05$ and $\lambda 6583.45$ forbidden lines. The top panel of Figure 19 displays the spectrum of SO662 ($R_d = 200$ au, $M_d \sim 2 M_{\text{Jup}}$; Table 7), showing the $H\alpha$ line in emission, characteristic of TTSs, and the forbidden lines of [N II]. This object is located at $d_p = 0.6$ pc. In the bottom panel

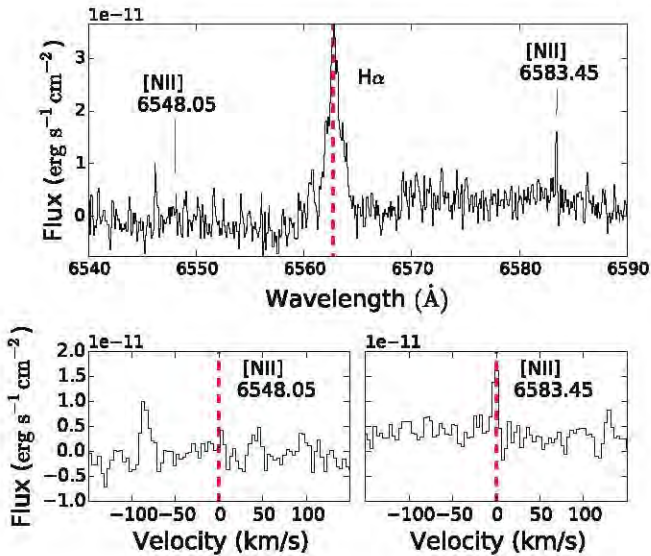


Figure 20. Top: Hectochelle spectrum of SO697 (H14) showing the $H\alpha$ line but no emission lines of [N II]. Bottom: spectrum in velocity space at the wavelengths of the [N II] emission lines. This object is the smallest disk in our sample with a disk size of $R_d = 7$ au and is located at $d_p = 0.45$ pc (Table 7). The absence of the forbidden lines of [N II] may be the result of the shrinking of the disk due to photoevaporation.

we also show the lines in velocity space. The blueshift of these lines, if any, is smaller than 3 km s^{-1} (our error in velocity determination), consistent with the lowest blueshifts found in TTSs for the [O I] line (Rigliaco et al. 2013; Natta et al. 2014). The low velocity value indicates that the forbidden line emission does not come from a jet, for which velocities reach hundreds of km s^{-1} (Hartigan et al. 1995). Figure 20, on the other hand, shows the spectrum of SO697, our smallest disk ($R_d = 7$ au, $M_d \sim 0.1 M_{\text{Jup}}$; Table 7) located at $d_p = 0.45$ pc. This object does not exhibit the [N II] forbidden line at 6548.05 \AA and has a very weak emission at 6583.45 \AA (bottom right panel). Similarly, none of our small disks with high-resolution spectra (SO396, SO462, and SO859) shows any emission lines of [N II].

Strong optical forbidden emission lines are expected to form in highly ionized regions, such as in the bright cusps characteristic of proplyds in the ONC, so the fact that within the first 0.6 pc from σ Ori, one of our largest disks exhibits these lines while none of our small disks has any features suggests that photoevaporation is in action in the cluster. If this is indeed the case, then SO662 is a photoevaporating disk in its initial phase while the small disks are those that moved close enough to the hot stars during the lifetime of the cluster to be stripped of their outermost regions and hence cannot produce the forbidden lines. We need a greater sample of disks with high-resolution spectra covering a range of projected distances from the central stars to confirm this hypothesis and characterize the region in the cluster that is affected by photoevaporation.

7. CONCLUSIONS

We analyzed the IR emission of 32 TTSs (mostly class II stars) with PACS detections belonging to the σ Ori cluster located in the Ori OB1b subassociation. We modeled 18 sources using the irradiated accretion disk models of D’Alessio et al. (2006). Our main conclusions are as follows:

1. PACS detections are consistent with stars surrounded by optically thick disks with high $24 \mu\text{m}$ excesses and spectral types between K2.0 and M5.0.
2. Detailed modeling indicates that most of our objects (60%) can be explained by $\epsilon = 0.01$, indicative of significant dust settling and possible grain growth. This is consistent with previous studies of other young star-forming regions (Furlan et al. 2009; McClure et al. 2010; Manoj et al. 2011).
3. 61% of our disks can be modeled with large sizes ($R_d \geq 100$ au). The rest have dust disk radii of less than 80 au. These disks may have been subject to photoevaporation. We estimated that 80% of our disks are exposed to FUV fluxes of $300 \lesssim G_0 \lesssim 1000$. These values may be high enough to photoevaporate the outer edges of the closer disks. Additionally, within the first 0.6 pc from the central ionizing sources we found forbidden emission lines of [N II] in SO662 ($R_d = 200$ au) while none of the small disks exhibits any features. This suggests that the region producing the lines is located in the outer disk. Therefore, SO662 may be a photoevaporative disk in its initial phase, while the small disks have already photoevaporated most of their material and hence cannot produce the [N II] lines.
4. The masses of our disks range between 0.03 and $\sim 39 M_{\text{Jup}}$, with 35% of the disks having masses lower than $0.001 M_{\odot}$, i.e., the mass of Jupiter. These low masses suggest that the formation of giant planets is probably over in the cluster. If this is the case, then timescales for giant planet formation should be less than 3 Myr, or giant planets are difficult to form in clustered environments.

This work was supported by UNAM-PAPIIT grant number IN110816 to J.B.P. Model calculations were performed in the supercomputer at DGTIC-UNAM. K.M. acknowledges a scholarship from CONACYT and financial support from CONACYT grant number 168251. J.H. acknowledges UNAM-DGAPA’s PREI program for visiting research at IRyA. We have made extensive use of the NASA-ADS database.

REFERENCES

- Acke, B., van den Ancker, M. E., & Dullemond, C. P. 2005, *A&A*, **436**, 209
- Adams, F. C., Hollenbach, D., Laughlin, G., & Gorti, U. 2004, *ApJ*, **611**, 360
- Alexander, R. D., Clarke, C. J., & Pringle, J. E. 2006, *MNRAS*, **369**, 229
- Anderson, K. R., Adams, F. C., & Calvet, N. 2013, *ApJ*, **774**, 9
- Andrews, S. M., & Williams, J. P. 2005, *ApJ*, **631**, 1134
- Andrews, S. M., Wilner, D. J., Hughes, A. M., et al. 2012, *ApJ*, **744**, 162
- Balog, Z., Müller, T., Nielbock, M., et al. 2014, *ExA*, **37**, 129
- Barrado y Navascués, D., Béjar, V. J. S., Mundt, R., et al. 2003, *A&A*, **404**, 171
- Birnstiel, T., & Andrews, S. M. 2014, *ApJ*, **780**, 153
- Briceño, C., Calvet, N., Anderson, K., et al. 2013, in *Protostars and Planets VI*, ed. H. Beuther et al. (Tucson, AZ: Univ. Arizona Press), poster **2B046**
- Caballero, J. A. 2008a, *MNRAS*, **383**, 375
- Caballero, J. A. 2008c, *MNRAS*, **383**, 750
- Caballero, J. A. 2014, *Obs*, **134**, 273
- Caballero, J. A., Cornide, M., & de Castro, E. 2010, *AN*, **331**, 257
- Caballero, J. A., Valdivielso, L., Martín, E. L., et al. 2008b, *A&A*, **491**, 515
- Calvet, N., D’Alessio, P., Hartmann, L., et al. 2002, *ApJ*, **568**, 1008
- Clarke, C. J. 2007, *MNRAS*, **376**, 1350
- Daemgen, S., Jayawardhana, R., Petr-Gotzens, M. G., & Meyer, E. 2015, arXiv:1506.05132.
- Dahm, S. E., & Carpenter, J. M. 2009, *AJ*, **137**, 4024
- D’Alessio, P., Calvet, N., & Hartmann, L. 2001, *ApJ*, **553**, 321

- D'Alessio, P., Calvet, N., Hartmann, L., Franco-Hernández, R., & Servín, H. 2006, *ApJ*, **638**, 314
- de Zeeuw, P. T., Hoogerwerf, R., de Bruijne, J. H. J., Brown, A. G. A., & Blaauw, A. 1999, *AJ*, **117**, 354
- Draine, B. T., & Lee, H. M. 1984, *ApJ*, **285**, 89
- Dullemond, C. P., Hollenbach, D., Kamp, I., & D'Alessio, P. 2007, in *Protostars and Planets V*, ed. B. Reipurth, D. Jewitt, & K. Keil, (Tuscon, AZ: Univ. Arizona Press), 555
- Eisner, J. A., Plambeck, R. L., Carpenter, J. M., et al. 2008, *ApJ*, **683**, 304
- Espaillat, C., Muzerolle, J., Najita, J., et al. 2014, in *Protostars and Planets VI*, ed. H. Beuther et al. (Tuscon, AZ: Univ. Arizona Press), 497
- Facchini, S., Clarke, C. J., & Bisbas, T. G. 2016, *MNRAS*, **457**, 3593
- Fischer, W. J., Megeath, S. T., Stutz, A. M., et al. 2013, *AN*, **334**, 53
- Furlan, E., Hartmann, L., Calvet, N., et al. 2006, *ApJS*, **165**, 568
- Furlan, E., Watson, D. M., McClure, M. K., et al. 2009, *ApJ*, **703**, 1964
- García-Arredondo, F., Henney, W. J., & Arthur, S. J. 2001, *ApJ*, **561**, 830
- Gatti, T., Natta, A., Randich, S., Testi, L., & Sacco, G. 2008, *A&A*, **481**, 423
- Gorti, U., Hollenbach, D., Najita, J., & Pascucci, I. 2011, *ApJ*, **735**, 90
- Guarcello, M. G., Drake, J. J., Wright, N. J., et al. 2016, arXiv:106.01773
- Guarcello, M. G., Drake, J. J., Wright, N. J., García-Alvarez, D., & Kraemer, K. E. 2014, *ApJ*, **793**, 56
- Guarcello, M. G., Micela, G., Peres, G., Prisinzano, L., & Sciortino, S. 2010, *A&A*, **521**, A61
- Habing, H. J. 1968, *BAN*, **19**, 421
- Hartigan, P., Edwards, S., & Ghandour, L. 1995, *ApJ*, **452**, 736
- Hartmann, L. 2009, *Accretion Processes in Star Formation* (2nd ed.; Cambridge: Cambridge Univ. Press)
- Hartmann, L., Calvet, N., Gullbring, E., & D'Alessio, P. 1998, *ApJ*, **495**, 385
- Hartmann, L., Megeath, S. T., Allen, L., et al. 2005, *ApJ*, **629**, 881
- Henney, W. J., & O'Dell, C. R. 1999, *AJ*, **118**, 2350
- Hernández, J., Calvet, N., Briceño, C., et al. 2007b, *ApJ*, **671**, 1784
- Hernández, J., Calvet, N., Perez, A., et al. 2014, *ApJ*, **794**, 36
- Hernández, J., Hartmann, L., Megeath, T., et al. 2007a, *ApJ*, **662**, 1067
- Hillenbrand, L. A. 1997, *AJ*, **113**, 1733
- Hodapp, K. W., Iserlohe, C., Stecklum, B., & Krabbe, A. 2009, *ApJL*, **701**, L100
- Hollenbach, D. J., Yorke, H. W., & Johnstone, D. 2000, in *Protostars and Planets IV*, ed. V. Manning, A. P. Boss, & S. S. Russell, (Tuscon, AZ: Univ. Arizona Press), 401
- Howard, C. D., Sandell, G., Vacca, W. D., et al. 2013, *ApJ*, **776**, 21
- Ihaka, R., & Gentleman, R. 1996, *J. Comput. Graphical Stat.*, **5**, 299
- Ingleby, L., Calvet, N., Herczeg, G., et al. 2013, *ApJ*, **767**, 112
- Johnstone, D., Hollenbach, D., & Bally, J. 1998, *ApJ*, **499**, 758
- Kalyaan, A., Desch, S. J., & Monga, N. 2015, *ApJ*, **815**, 112
- Kenyon, S. J., & Hartmann, L. 1995, *ApJS*, **101**, 117
- Kim, K. H., Watson, D. M., Manoj, P., et al. 2013, *ApJ*, **769**, 149
- Kraus, A. L., & Hillenbrand, L. A. 2012, *ApJ*, **757**, 141
- Lada, C. J. 1987, in *IAU Symp. 115, Star Forming Regions*, ed. M. Peimbert & J. Jugaku, (Dodrecht: Reidel), 1
- Lada, C. J., Muench, A. A., Luhman, K. L., et al. 2006, *AJ*, **131**, 1574
- Laibe, G., Gonzalez, J.-F., & Maddison, S. T. 2012, *A&A*, **537**, A61
- Luhman, K. L., Allen, P. R., Espaillat, C., Hartmann, L., & Calvet, N. 2010, *ApJS*, **186**, 111
- Luhman, K. L., & Mamajek, E. E. 2012, *ApJ*, **758**, 31
- Manara, C. F., Testi, L., Rigliaco, E., et al. 2013, *A&A*, **551**, A107
- Mann, R. K., Di Francesco, J., Johnstone, D., et al. 2014, *ApJ*, **784**, 82
- Mann, R. K., & Williams, J. P. 2010, *ApJ*, **725**, 430
- Manoj, P., Kim, K. H., Furlan, E., et al. 2011, *ApJS*, **193**, 11
- Mathews, G. S., Pinte, C., Duchêne, G., Williams, J. P., & Ménard, F. 2013, *A&A*, **558**, A66
- Mathis, J. S. 1990, *ARA&A*, **28**, 37
- McClure, M. K., Calvet, N., Espaillat, C., et al. 2013a, *ApJ*, **769**, 73
- McClure, M. K., D'Alessio, P., Calvet, N., et al. 2013b, *ApJ*, **775**, 114
- McClure, M. K., Furlan, E., Manoj, P., et al. 2010, *ApJS*, **188**, 75
- McClure, M. K., Manoj, P., Calvet, N., et al. 2012, *ApJL*, **759**, L10
- Muzerolle, J., Allen, L. E., Megeath, S. T., Hernández, J., & Gutermuth, R. A. 2010, *ApJ*, **708**, 1107
- Muzerolle, J., Hillenbrand, L., Calvet, N., Briceño, C., & Hartmann, L. 2003, *ApJ*, **592**, 266
- Muzerolle, J., Luhman, K. L., Briceño, C., Hartmann, L., & Calvet, N. 2005, *ApJ*, **625**, 906
- Natta, A., Testi, L., Alcalá, J. M., et al. 2014, *A&A*, **569**, A5
- Natta, A., Testi, L., Muzerolle, J., et al. 2004, *A&A*, **424**, 603
- O'dell, C. R., & Wen, Z. 1994, *ApJ*, **436**, 194
- Olofsson, J., Szűcs, L., Henning, T., et al. 2013, *A&A*, **560**, A100
- Ott, S. 2010, in *ASP Conf. Ser. 434, Astronomical Data Analysis Software and Systems XIX*, ed. Y. Mizumoto, K.-I. Morita, & M. Ohishi (San Francisco, CA: ASP), 139
- Panić, O., Hogerheijde, M. R., Wilner, D., & Qi, C. 2009, *A&A*, **501**, 269
- Pascucci, I., & Sterzik, M. 2009, *ApJ*, **702**, 724
- Pecaut, M. J., & Mamajek, E. E. 2013, *ApJS*, **208**, 9
- Pinilla, P., Benisty, M., & Birnstiel, T. 2012a, *A&A*, **545**, A81
- Pinilla, P., Birnstiel, T., Ricci, L., et al. 2012b, *A&A*, **538**, A114
- Rigliaco, E., Natta, A., Randich, S., & Sacco, G. 2009, *A&A*, **495**, L13
- Rigliaco, E., Natta, A., Randich, S., Testi, L., & Biazzo, K. 2011, *A&A*, **525**, A47
- Rigliaco, E., Natta, A., Testi, L., et al. 2012, *A&A*, **548**, AA56
- Rigliaco, E., Pascucci, I., Gorti, U., Edwards, S., & Hollenbach, D. 2013, *ApJ*, **772**, 60
- Riviere-Marichalar, P., Pinte, C., Barrado, D., et al. 2013, *A&A*, **555**, A67
- Rosenfeld, K. A., Andrews, S. M., Wilner, D. J., Kastner, J. H., & McClure, M. K. 2013, *ApJ*, **775**, 136
- Roussel, H. 2013, *PASP*, **125**, 1126
- Siess, L., Dufour, E., & Forestini, M. 2000, *A&A*, **358**, 593
- Simón-Díaz, S., Caballero, J. A., Lorenzo, J., et al. 2015, *ApJ*, **799**, 169
- Sivia, D. S., & Skilling, J. 2012, *Data Analysis a Bayesian Tutorial* (2nd ed.; Oxford: Oxford Univ. Press)
- Smith, N., Bally, J., Shuping, R. Y., Morris, M., & Kassisi, M. 2005, *AJ*, **130**, 1763
- Störzer, H., & Hollenbach, D. 1999, *ApJ*, **515**, 669
- Uchida, K. I., Calvet, N., Hartmann, L., et al. 2004, *ApJS*, **154**, 439
- van Loon, J. T., & Oliveira, J. M. 2003, *A&A*, **405**, L33
- Vicente, S. M., & Alves, J. 2005, *A&A*, **441**, 195
- Williams, J. P., Andrews, S. M., & Wilner, D. J. 2005, *ApJ*, **634**, 495
- Williams, J. P., Cieza, L. A., Andrews, S. M., et al. 2013, *MNRAS*, **435**, 1671
- Zhang, K., Isella, A., Carpenter, J. M., & Blake, G. A. 2014, *ApJ*, **791**, 42

5.2 Article 2

5.2.1 Abstract

Presentamos observaciones Herschel tomadas con el espectrómetro y fotómetro PACS de 8 estrellas clásicas T Tauri en las subasociaciones de Orión OB1a con $\sim 7 - 10$ Myr, y OB1b con $\sim 4 - 5$ Myr. Modelaje detallado de las distribuciones espectrales de energía, particularmente la fuerte emisión de silicatos a $10 \mu\text{m}$, muestra que estos objetos son discos (pre-)transicionales con una cierta cantidad de polvo ópticamente delgado dentro de sus cavidades, las cuales oscilan entre ~ 4 AU y ~ 9 AU en tamaño. Analizamos espectros tomados con el instrumento IRS en el telescopio espacial Spitzer de 2 objetos en la muestra: CVSO-107 y CVSO-109. El espectro IRS de CVSO-107 indica la presencia de material cristalizado dentro de la cavidad mientras que la banda de silicatos de CVSO-109 se caracteriza por tener un perfil “pristine” producido por silicatos amorfos; los mecanismos que generan el polvo ópticamente delgado parecen depender de condiciones locales en el disco. Usando fotometría milimétrica estimamos masas de polvo para CVSO-107 y CVSO-109 menores a la masa mínima de sólidos necesarios para formar los planetas en nuestro Sistema Solar, lo que sugiere que la formación de planetas gigantes debe haber finalizado en estos discos. Especulamos que la presencia y abastecimiento de material ópticamente grueso en las regiones internas de estos discos pre-transicionales puede deberse a la formación de planetas poco masivos.



Herschel PACS Observations of 4–10 Myr Old Classical T Tauri Stars in Orion OB1

Karina Maucó¹, César Briceño², Nuria Calvet³, Jesús Hernández⁴, Javier Ballesteros-Paredes¹, Omaira González¹, Catherine C. Espaillat⁵, Dan Li⁶, Charles M. Telesco⁷, Juan José Downes⁸, Enrique Macías⁵, Chunhua Qi⁹, Raúl Michel⁴, Paola D’Alessio^{1,11}, and Babar Ali¹⁰

¹ Instituto de Radioastronomía y Astrofísica, UNAM, Campus Morelia, Antigua Carretera a Pátzcuaro No. 8701, Col. Ex Hacienda San Jos de la Huerta, Morelia, Michoacán, C.P. 58089, México; k.mauco@irya.unam.mx

² Observatorio Interamericano Cerro Tololo, AURA/CTIO, Casilla 603, La Serena, Chile

³ Department of Astronomy, University of Michigan, 311 West Hall, 1085 South University Avenue, Ann Arbor, MI 48109, USA

⁴ Instituto de Astronomía, UNAM, Campus Ensenada, Carretera Tijuana-Ensenada km 103, 22860 Ensenada, B.C., México

⁵ Department of Astronomy, Boston University, 725 Commonwealth Avenue, Boston, MA 02215, USA

⁶ Department of Physics & Astronomy, University of Pennsylvania, Philadelphia, PA 19104, USA

⁷ Department of Astronomy, University of Florida, Gainesville, FL 3261-2055, USA

⁸ Centro de Investigaciones de Astronomía, CIDA, Av. Alberto Carnevalli, Sector “La Hechicera,” Mérida, Venezuela, Apartado Postal 264, Mérida 5101-A, Mérida—Venezuela

⁹ Harvard-Smithsonian Center for Astrophysics 60 Garden Street, Mail Stop 42, Cambridge, MA 02138, USA

¹⁰ Space Sciences Institute, 4750 Walnut Street, Suite 205, Boulder, CO, USA

Received 2017 December 25; revised 2018 April 11; accepted 2018 April 16; published 2018 May 16

Abstract

We present *Herschel* PACS observations of eight classical T Tauri Stars in the ~ 7 –10 Myr old OB1a and the ~ 4 –5 Myr old OB1b Orion subassociations. Detailed modeling of the broadband spectral energy distributions, particularly the strong silicate emission at $10\ \mu\text{m}$, shows that these objects are (pre-)transitional disks with some amount of small optically thin dust inside their cavities, ranging from ~ 4 to ~ 90 au in size. We analyzed *Spitzer* IRS spectra for two objects in the sample: CVSO-107 and CVSO-109. The IRS spectrum of CVSO-107 indicates the presence of crystalline material inside its gap, while the silicate feature of CVSO-109 is characterized by a pristine profile produced by amorphous silicates; the mechanisms creating the optically thin dust seem to depend on disk local conditions. Using millimeter photometry, we estimated dust disk masses for CVSO-107 and CVSO-109 lower than the minimum mass of solids needed to form the planets in our solar system, which suggests that giant planet formation should be over in these disks. We speculate that the presence and maintenance of optically thick material in the inner regions of these pre-transitional disks might point to low-mass planet formation.

Key words: infrared: stars – open clusters and associations: individual (Orion OB1 association) – protoplanetary disks – stars: formation – stars: pre-main sequence

1. Introduction

Understanding how solid material in protoplanetary disks evolves from conditions similar to those in the interstellar medium (ISM) to planetary embryos and beyond requires both theoretical developments and observational constraints. As many complex processes are at play, observations are essential to inform theory and set constraints on the multiple effects occurring in these disks.

Many studies have now revealed stars with inner disks devoid of optically thick material—the so-called transitional disks (TDs)—and with spectral energy distributions (SEDs) characterized by small or negligible near-infrared excesses but significant emission in the mid-infrared and beyond (Strom et al. 1989; Skrutskie et al. 1990; Calvet et al. 2002; Espaillat et al. 2007, 2008a, 2014). This morphology has been interpreted as cavities in the inner regions and has been confirmed through (sub)millimeter interferometric imaging and, recently, by spatially resolved images (e.g., Andrews et al. 2009, 2011a, 2011b; Brown et al. 2009; Hughes et al. 2009; Isella et al. 2010; van Dishoeck et al. 2015; Carrasco-González et al. 2016), especially those taken with the Very Large Telescope (VLT)/SPHERE and the Atacama Large Millimeter/submillimeter Array (ALMA; ALMA Partnership et al. 2015; Andrews et al. 2016; Nomura et al. 2016; Schwarz

et al. 2016; van Boekel et al. 2017). A subset of these disks, commonly called pre-transitional disks (PTDs), show similar features but with substantial near-infrared excesses over the stellar photosphere. This excess has been explained by an optically thick disk located close to the star, separated from the outer disk by a gap (Espaillat et al. 2008a, 2010, 2011).

TDs and PTDs are thought to be at an important phase of disk evolution. The distinct SEDs of these sources have puzzled researchers over the years. For instance, dust-clearing mechanisms in TDs/PTDs are still under debate. It is uncertain whether processes act simultaneously or a single process dominates the evolution. Observations made with the *Spitzer* Space Telescope (Werner et al. 2004) have been widely used to identify TDs/PTDs and to characterize their IR emission. Moreover, *Spitzer* IRS spectra have also provided unprecedented details regarding disk cavities and dust properties within them. Extensive modeling of several TDs/PTDs around T Tauri stars (TTs) has been made (Calvet et al. 2002, 2005; Uchida et al. 2004; D’Alessio et al. 2005; Espaillat et al. 2007, 2008b, 2010; McClure et al. 2010, 2012, 2013). Some mechanisms have been proposed to explain the substantial dust clearing observed on these disks, e.g., grain growth, photoevaporation, and interaction with embedded planets or stellar companions (Espaillat et al. 2014). Many researchers have proposed planet formation as the most likely mechanism, since models of planet–disk interaction have resulted in cleared disk regions (e.g., Paardekooper & Mellema 2004; Dodson-Robinson

¹¹ Author is deceased.

& Salyk 2011; Zhu et al. 2011; Dipierro & Laibe 2017; Dong et al. 2017). Additionally, thanks to new-generation high angular resolution instruments, observational evidence implying the presence of (proto)planets has increased over the years (e.g., Huélamo et al. 2011; Kraus et al. 2011; Follette et al. 2015; Pinilla et al. 2015; Sallum et al. 2015, 2016; Andrews et al. 2016; de Juan Ovelar et al. 2016).

Studies of disk frequencies as a function of age have set timescales for disk evolution of $\sim 5\text{--}7$ Myr for late-type (K to M) stars (e.g., Hernández et al. 2007a). However, most disk studies have concentrated on populations $\lesssim 2$ Myr old (i.e., Taurus, the Orion Nebula Cluster), and much less information exists for older populations, especially around 10 Myr. The main reason is that already at ages of ~ 4 Myr the parent molecular clouds have largely dissipated, such that these somewhat older stars are harder to identify among the general field population. It is not surprising that many of the $\sim 4\text{--}10$ Myr old groups have been discovered in the past ~ 20 yr. The TW Hya association (Webb et al. 1999) and the η Cha cluster (Mamajek et al. 1999) are among the nearest 10 Myr old groups but contain only around 20 stars. The Scorpius-Centaurus OB association, with ages $\sim 5\text{--}20$ Myr (e.g., Preibisch & Mamajek 2008; Pecaú & Mamajek 2016), is the closest OB association (~ 130 pc) and has been studied extensively as a source of older pre-main-sequence (PMS) disk-bearing stars. The Upper-Scorpius (US) region has ~ 800 members reported by Luhman & Mamajek (2012), though spectroscopic confirmation of many low-mass members is still ongoing (Pecaú & Mamajek 2016); the age is still debated, proposed to be in the range of 4–10 Myr (Preibisch & Mamajek 2008; Pecaú & Mamajek 2016). ALMA submillimeter studies in US have reported dust properties and disk sizes in samples of ~ 100 disk systems (Carpenter et al. 2006, 2009; Barenfeld et al. 2016, 2017).

As the closest region with active low- and high-mass star formation ($d \sim 400$ pc), the Orion OB1 association contains large samples of young stars, spanning ages from the protostellar stage up to “older” PMS stars, and sharing a common origin (Bally 2008; Briceño 2008). While Sco-Cen only hosts slightly more evolved stars ($\gtrsim 4$ Myr) and no recognizable star clusters, Orion has populous stellar aggregates at all ages up to ~ 10 Myr. These young, dense stellar groups provide an opportunity for exploring the evolution of protoplanetary disks in clustered environments. At the young end of optically visible PMS stars, the ~ 1 Myr old Trapezium cluster contains $\gtrsim 2000$ stars (Muench et al. 2008), and the ~ 3 Myr σ Ori cluster has over 300 confirmed members (Hernández et al. 2014). At the “old” end of the PMS age spectrum, the ~ 10 Myr old 25 Ori cluster (Briceño et al. 2007) has ~ 250 members, which have been characterized spectroscopically and photometrically by us in a consistent and uniform way. Here we present *Herschel Space Telescope* 70 and $160\ \mu\text{m}$ observations of four fields in the Orion OB1 association, targeting a limited subset of the stellar population in the 4–10 Myr age range, including the 25 Ori cluster.

Disk fluxes are strongly dependent on the stage of dust evolution at the wavelength range probed by *Herschel*. *Wide-field Infrared Survey Explorer* (WISE) covered wavelengths from 3.6 to $22\ \mu\text{m}$, and *Spitzer* was most sensitive from 3.6 to $24\ \mu\text{m}$, with limited sensitivity at $70\ \mu\text{m}$. Therefore, studies of dust depletion have mostly been limited to the inner disk regions. With *Herschel* we now have a window into longer

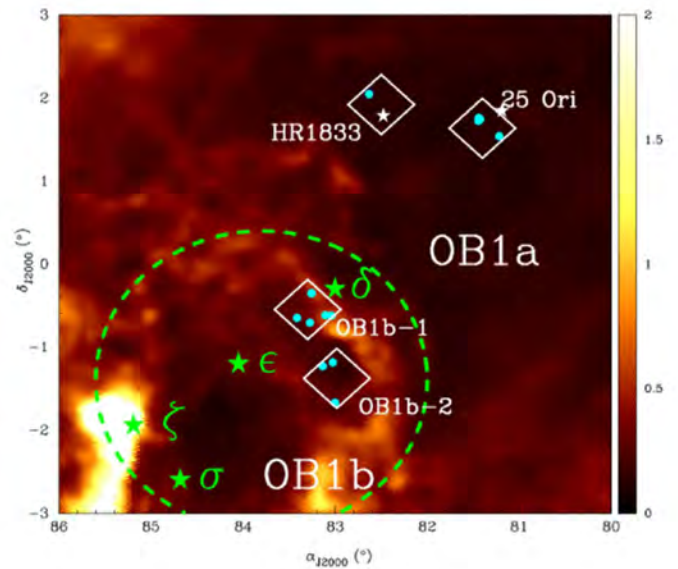


Figure 1. Location of the four *Herschel* PACS fields in the Orion OB1 association, overlaid on the extinction map from Schlegel et al. (1998). The Orion OB1b region encompasses the three Orion belt stars and is delimited by the large dashed circle (Briceño et al. 2005); the OB1a region is located west and north of OB1b and includes the 25 Ori cluster and the HR 1833 stellar aggregate. The TTSs detected at $70\ \mu\text{m}$ in the PACS fields are shown as cyan circles. Our *Herschel* fields are all in regions of low extinction with $A_V \lesssim 1$ mag.

wavelengths important for disk studies. Additionally, the smaller beam size and higher spatial resolution of PACS compared with *Spitzer*/MIPS result in a lower rate of confusion, with background sources making it easier for *Herschel* to detect faint sources. Combining the *Herschel* data with optical V , R , I , near-infrared J , H , K photometry and mid-IR data from *Spitzer*/WISE, we assemble SEDs for eight disk-bearing sources, which we then fit with detailed irradiated accretion disk models to infer the structure, characteristics, and evolutionary state of these disks. In Section 2 we discuss observations, sample selection, and data reduction; our analysis and results are shown in Section 3, where we present the observed SEDs of our objects (Section 3.1), the stellar parameters and mass accretion rate estimates (Section 3.2), a description of our disk models (Section 3.3), and the method we used to model the SEDs (Section 3.4); the main results are discussed in Section 4; and finally, our conclusions are listed in Section 5.

2. Observations

In this section we summarize the observational data sets obtained for our sample. Optical photometry was used to characterize the stellar properties, which are inputs in our models, and as an indicator of how variable these stars are, which was included as an additional uncertainty in the χ^2 estimate. Mid-IR data were used in the modeling of the silicate bands, particularly at $10\ \mu\text{m}$. PACS photometry allowed the characterization of the outer disk edge, while submillimeter data were used to estimate disk mass and to constrain the properties of the outer disk.

2.1. Sample

We targeted a set of 165 TTSs distributed in four fields (Figure 1), two in the ~ 4 –5 Myr old Orion OB1b subassociation and two in the ~ 7 –10 Myr old Orion OB1a region (Briceño et al. 2005). These stars have been confirmed as members of the OB association based on their K and M spectral types, H α emission, and the presence of Li I ($\lambda 6707$) in absorption (Briceño et al. 2005). For this sample, we also have multiband, multiepoch optical photometry from the CVSO (Briceño et al. 2005, 2018, in preparation) and from the Sloan Digital Sky Survey (SDSS);¹² near-infrared *J*, *H*, and *K_S* magnitudes from the Two Micron All Sky Survey (2MASS; Skrutskie et al. 2006); *Z*, *J*, *H*, and *K_S* photometry from the Visible and Infrared Survey Telescope for Astronomy Science Verification Survey of Orion OB1 (VISTA; Petr-Gotzens et al. 2011); and infrared photometry from the Infrared Array Camera (IRAC; Fazio et al. 2004) and the Multiband Imaging Photometer for *Spitzer* (MIPS; Rieke et al. 2004) at 3.6, 4.5, 5.8, 8.0, and 24.0 μm from our GO-13437 and GO-50360 programs (Hernández et al. 2007b; C. Briceño et al. 2018, in preparation) and at 3.6, 4.5, 6, 12, and 22 μm from *WISE* (Wright et al. 2010). The two fields in the Ori OB1a region are roughly centered on the 25 Ori cluster (Briceño et al. 2007) and the HR 1833 stellar aggregate (C. Briceño et al. 2018, in preparation), and combined they encompass 118 confirmed TTSs. The two Ori OB1b fields contain 47 confirmed TTSs. The spectral types for the young stars in both regions are similar and span the range K4–M5, which at the ages of our stars corresponds to masses $0.12 \lesssim M/M_{\odot} \lesssim 1.2$ (Baraffe et al. 1998).

2.2. *Herschel* PACS Photometry

Our *Herschel*/PACS imaging survey of the Orion OB1 fields was carried out with eight unique *Herschel* observations at 70 and 160 μm , obtained on 2012 March 16, 18, 28, and 29. We used the “scan map” observational template with medium scan speed (20"/s) to map a square field 30' per side. Each scan line was 30' long, and 134 overlapping scan lines with a step size of 15 arcsec were sufficient to reach the target size and sensitivity. Each field was observed twice at orthogonal scan directions. This technique is commonly used to mitigate the low-frequency drift of the bolometer time lines. With this configuration, we aimed at reaching a 1σ point source sensitivity of 2.6 and 6 mJy in the blue and red channels, respectively. Our *Herschel* program identifier is OT1_ncalvet_1.

We rely on the *Herschel* data processing pipelines (Ott 2010) for the initial data processing and begin further processing at the so-called Level 1 stage. All data discussed here are based on the “FM6” version of the PACS calibration (Nielbock et al. 2013) and processed with version 9 of the *Herschel* Interactive Processing Environment (HIPE Ott 2010) software.

We processed the Level 1 data with the Scanamorphos technique, a mapmaking software developed and described by Roussel (2012). Scanamorphos removes the $1/f$ noise¹³ by making use of the redundancy built in the observations. Readers are referred to Roussel (2012) for details about the processing steps. Scanamorphos preserves astrophysical emission on all spatial scales, ranging from point sources to extended structures with scales just below the map size;

¹² <http://www.sdss3.org/dr9/>

¹³ The term $1/f$ noise is used here to generically describe bolometer signal drifts that are inversely correlated with their Fourier frequency.

therefore, the maps produced are suitable for both spatially extended and point sources.

We performed source detection on the 70 μm images processed with Scanamorphos, using the *daofind* task in IRAF.¹⁴ We then proceeded to obtain aperture photometry on both 70 and 160 μm channels, using the IRAF *apphot* task. Following Fischer et al. (2013), for the 70 μm images we used an aperture radius of 9".6, inner sky annulus radius of 9".6, and sky annulus width of 9".6; for the 160 μm images we used an aperture radius of 12".8, inner sky annulus radius of 12".8, and a 12".8 sky annulus width. Because the pixel scale is 1"/pixel for the 70 μm images and 2"/pixel for the 160 μm images, these apertures correspond to 9.6 and 6.4 pixels, respectively. Though the relatively small apertures require large aperture corrections, 0.7331 for the blue channel (70 μm) and 0.6602 for the red channel (160 μm), they minimize uncertainties due to large variations in the sky background in regions with significant nebulosity, especially with the 160 μm images. Photometric errors were determined as the sum in quadrature of the measurement error and the calibration error.

Of the 165 TTSs located within the PACS fields, only 16 are classified as disk sources based on their $K_s - [4.5]$ excess, using the criterion in Figure 1 of Luhman & Mamajek (2012). The number of disk sources goes up to 25 if we use the excess emission at $K_s - [8.0]$ or $K_s - [24]$. We detected eight of these disk sources with PACS (33%–50% depending on the disk indicator), all classified as accreting classical TTSs (CTTSs)¹⁵ based on our optical spectra. These objects are also tagged as Class II stars based on the IRAC SED slopes in Hernández et al. (2007b). They are distributed as follows: two are located in the OB1a region, specifically in the 25 Ori cluster and the HR 1833 group (C. Briceño et al. 2018, in preparation), and six in the two OB1b PACS fields. We present *Herschel* PACS photometry at 70 and 160 μm for these objects. PACS photometry is shown in Table 1 in the following order: target CVSO ID, 2MASS ID, right ascension, declination, 70 μm flux, 160 μm flux, and the location of each source.

2.3. *CanariCam* Photometry

We observed five sources in the OB1 fields (two in OB1a: CVSO-35 and CVSO-1265; three in OB1b: CVSO-104, CVSO-114NE, and CVSO-121) in the Si2 (8.7 μm), Si4 (10.3 μm), Si5 (11.6 μm), and Si6 (12.5 μm) narrowband silicate filters on 2014 September 22 and 23 and October 3 and 5 with the *CanariCam*¹⁶ instrument (Telesco et al. 2003) on the Gran Telescopio de Canarias (GTC). The selection criterion was targets with *Spitzer*/IRAC and *Herschel*/PACS (70 and 160 μm) detections. *CanariCam* has a 26" \times 19" field of view with a detector plate scale of 0".08 per pixel. The reduction of the data was done using the *CanariCam* data reduction pipeline (RedCan). RedCan produces flux-calibrated images using the associated standard star images along with their theoretical spectra reported by Cohen et al. (1999). An extensive description of the RedCan pipeline can be found in González-Martín et al. (2013). Table 2 summarizes the *CanariCam* photometry. Column

¹⁴ IRAF is distributed by the National Optical Astronomy Observatory, which is operated by the Association of Universities for Research in Astronomy (AURA) under a cooperative agreement with the National Science Foundation.

¹⁵ CTTSs are T Tauri stars still actively accreting from a circumstellar disk; they are usually classified as such from low-resolution spectra showing a strong H α emission line, with an equivalent width above the value expected for chromospheric emission at the spectral type of the star (White & Basri 2003).

¹⁶ <http://www.gtc.iac.es/instruments/canaricam/canaricam.php>

Table 1
PACS Photometry for CTTs in the OB1a and OB1b Subassociations

CVSO ID	2MASS ID	R.A. (J2000.0) (hh:mm:ss)	Decl. (J2000.0) (hh:mm:ss)	F_{70} (mJy)	F_{160} (mJy)	Location
CVSO-35	05254589+0145500	05:25:45.90	+01:45:50.3	18.83 ± 1.19	12.77 ± 2.48	25 Ori
CVSO-104	05320638−0111000	05:32:06.45	−01:11:00.3	77.41 ± 2.35	56.28 ± 3.78	OB1b
CVSO-107	05322578−0036533	05:32:25.77	−00:36:53.2	105.34 ± 3.32	106.51 ± 8.34	OB1b
CVSO-109	05323265−0113461	05:32:32.66	−01:13:46.0	69.38 ± 2.69	38.97 ± 5.36	OB1b
CVSO-114NE	05330196−0020593	05:33:01.97	−00:20:59.3	30.67 ± 2.56	94.33 ± 12.12	OB1b
CVSO-121	05333982−0038541	05:33:39.82	−00:38:53.9	71.59 ± 2.26	47.29 ± 3.11	OB1b
CVSO-238	05320040−0140110	05:32:00.40	−01:40:11.0	8.126 ± 1.22	5.13 ± 2.92	OB1b
CVSO-1265	05303164+0203051	05:30:31.66	+02:03:05.2	35.32 ± 1.45	48.56 ± 2.95	HR 1833

(1) shows the CVSO ID following Briceño et al. (2005), while Columns (2)–(5) indicate the fluxes in the four narrowband silicate filters for each source. Errors are about 15% of the photometric value in each band (Alonso-Herrero et al. 2016).

2.4. Optical Photometry

We obtained new optical photometry of a subset of our stars for which there was no existing SDSS photometry, or stars with UV excesses, or those with strong photometric variability between the CVSO and the SDSS photometric bands. These observations were obtained at the 4.3 m Discovery Channel Telescope (DCT) at Lowell Observatory, Arizona, USA, and the 0.84 m telescope at the San Pedro Mártir National Astronomical Observatory in Baja California, México.

2.4.1. The Discovery Channel Telescope

We observed CVSO-107 and CVSO-109 in the $U, B, V, R,$ and I Johnson–Cousins filters on 2013 November 29 with the Large Monolithic Imager (LMI)¹⁷ on the DCT. The LMI has a $12'.5 \times 12'.5$ field of view, with an unbinned pixel size of $0''.12$; we utilized the 2×2 pixel binning mode, resulting in a pixel scale of $0''.24$ per pixel. We used IRAF to carry out bias and flat-field corrections, using twilight flats, and then to derive aperture photometry interactively. The optical photometry is listed in Table 3, where we show the CVSO ID following Briceño et al. (2005) in Column (1) and present the photometry of the $U, B, V, R_c,$ and I_c filters of our sample in Columns (2)–(6).

2.4.2. San Pedro Mártir

CVSO-35, CVSO-104, CVSO-114NE, and CVSO-121 were observed in the $UBV(RI)_c$ system, during an open cluster campaign, in 2016 December 4 and 5 at the San Pedro Martir (SPM) Observatory with the 0.84 m telescope and the *Marconi* 3 CCD detector (a deep depletion e2v CCD42-40 chip with gain of $1.83 e^-/\text{ADU}$ and readout noise of $4.7 e^-$).

The field of view was $7'.4 \times 7'.4$, and binning 2×2 was used during the observations. In order to properly measure both bright and dim stars, different exposure times were employed. We used 2, 20, and 200 s in both R and I filters; 4, 40, and 400 s for the V filter; 6, 60, and 600 s for the B filter; and 10, 100, and 1000 s for the U filter. Standard stars in Landolt fields were observed during the night in order to calibrate the photometry. The data reduction was done with IRAF, following the standard procedure for correcting bias and flat-field frames. Instrumental

Table 2
CanariCam Photometry of Five PACS Sources in the OB1a and OB1b Subassociations

CVSO ID	$F_{\text{Si}2}$ (Jy)	$F_{\text{Si}4}$ (Jy)	$F_{\text{Si}5}$ (Jy)	$F_{\text{Si}6}$ (Jy)
CVSO-35	68.86	106.96	120.58	121.09
CVSO-104	25.08	50.75	48.28	16.92
CVSO-114NE	29.01	23.97	24.39	25.48
CVSO-121	35.58	50.22	35.11	17.05
CVSO-1265	27.51	56.73	34.98	20.70

Note. Column (1): CVSO ID following Briceño et al. (2005). Column (2): Si2 flux. Column (3): Si4 flux. Column (4): Si5 flux. Column (5): Si6 flux. Errors are about 15% of the photometric value in each band.

magnitudes were derived using standard point-spread function photometry. Transformation equations, based on the observed standard stars, were then applied to convert the instrumental magnitudes to calibrated magnitudes. The resulting photometry is shown in Table 3.

2.5. Submillimeter Photometry

We observed CVSO-107 and CVSO-109 on 2010 January 1 with the Submillimeter Array (SMA) on top of Maunakea, Hawaii, using the compact array configuration (projected baselines of 9.8–81.2 m). The weather was excellent, with the 225 GHz opacity around 0.05 and a stable atmospheric phase. The double-sideband system temperatures were 72–156 K. Calibration of the visibility phases and amplitudes was achieved with observations of the quasar J0532+075, at intervals of about 30 minutes. The bandpass response was calibrated using 3C 454.3. Observations of Uranus provided the absolute scale for the flux density calibration, and the derived flux of J0532+075 was 0.71 Jy. The data were calibrated using the MIR software package.¹⁸ Continuum images were generated and CLEANed using standard techniques in the MIRIAD software package. Fluxes are listed in Column (2) of Table 4.

2.6. Spitzer IRS Spectra

CVSO-107 and CVSO-109 were observed by the *Spitzer* IRS instrument on 2006 March 18 (AORKEY: 14646016) with the short-wavelength, low-resolution (SL) module and the long-wavelength, low-resolution (LL) module of IRS. The observation was carried out in IRS Staring mode, covering

¹⁷ <http://www2.lowell.edu/rsch/LMI/specs.html>

¹⁸ <http://www.cfa.harvard.edu/~cqj/mircook.html>

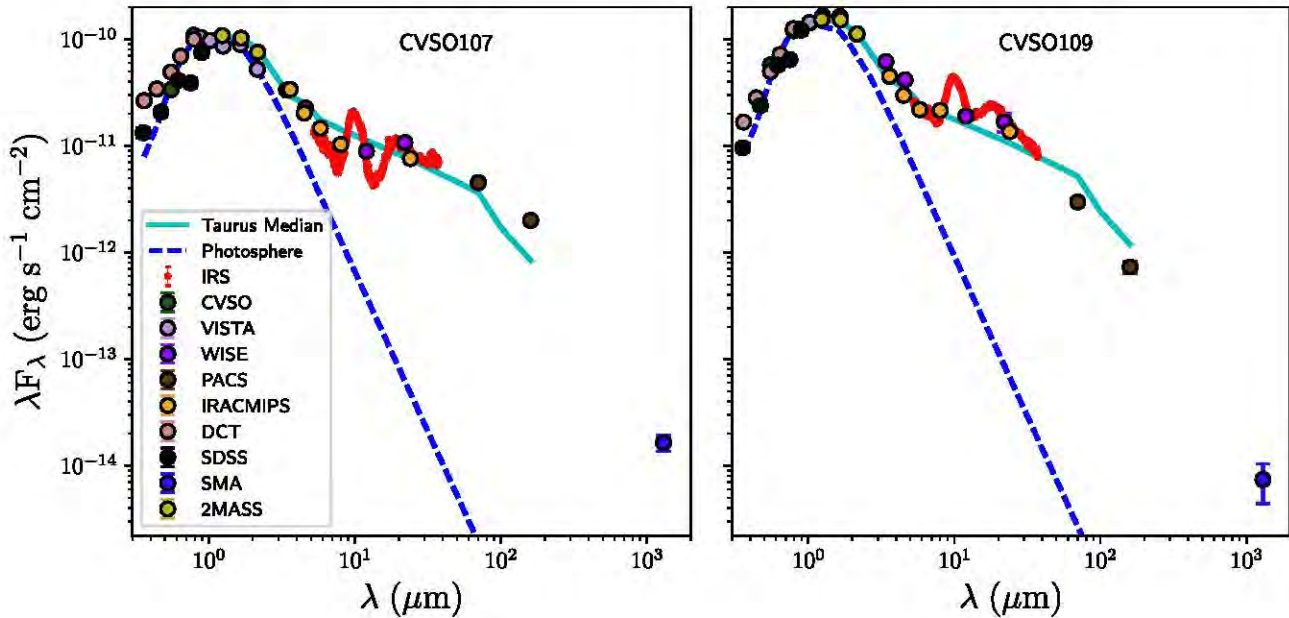


Figure 2. Dereddened SEDs of the two stars in our sample that have *Spitzer* IRS spectra. Optical data are from the CVSO (Briceño et al. 2005, 2007; C. Briceño et al. 2018, in preparation), the SDSS, and the DCT; the near-IR magnitudes at J , H , and K_S are from 2MASS (Skrutskie et al. 2006); and those at Z , Y , J , H , and K_S are from VISTA (Petr-Gotzens et al. 2011). The mid-IR measurements at 3.6, 4.5, 5.8, 8, and 24 μm are from our *Spitzer* GO-13437 and GO-50360 programs (Hernández et al. 2007b), and those at 3.4, 4.6, 12, and 22 μm are from the AllWISE Source Catalog (Wright et al. 2010). The IRS spectra are shown as solid red lines. The dashed-blue line is the stellar photosphere (normalized to the J band of each object) of the same spectral type (Kenyon & Hartmann 1995), and the light-blue solid line is the Taurus median from Maucó et al. (2016). Error bars are typically smaller than the symbols.

Table 3
Optical Photometry

CVSO ID	U	B	V	R_c	I_c
CVSO-35 ^a	16.744 ± 0.007	15.578 ± 0.002	14.059 ± 0.002	13.226 ± 0.002	12.388 ± 0.002
CVSO-104 ^a	15.973 ± 0.017	15.659 ± 0.015	15.026 ± 0.076	14.442 ± 0.034	13.319 ± 0.007
CVSO-107 ^b	15.287 ± 0.005	15.548 ± 0.004	14.628 ± 0.002	13.788 ± 0.004	12.831 ± 0.003
CVSO-109 ^b	14.897 ± 0.012	14.997 ± 0.005	14.044 ± 0.003	13.260 ± 0.006	12.219 ± 0.005
CVSO-114NE ^a	16.592 ± 0.005	16.984 ± 0.004	15.986 ± 0.010	15.086 ± 0.006	13.752 ± 0.007
CVSO-121 ^a	15.886 ± 0.004	15.598 ± 0.001	14.392 ± 0.006	13.528 ± 0.003	12.672 ± 0.002

Notes.

^a SPM photometry.

^b DCT photometry.

Table 4
Submillimeter Fluxes

CVSO ID	F_{1300} (mJy)
CVSO-107	7.1 ± 1.2
CVSO-109	3.2 ± 1.3

$\sim 5\text{--}40$ μm at a resolving power of $\lambda/\delta\lambda = 60\text{--}100$. We extracted and calibrated the spectrum using the Spectral Modeling, Analysis, and Reduction Tool (SMART) software package (IRS instrument team; Higdon et al. 2004). More details on the data reduction can be found in Furlan et al. (2006).

3. Analysis and Results

In this section we examine the emission of the disks detected by PACS in the Orion OB1a and OB1b associations by comparing the predictions of irradiated accretion disk models to their SEDs. We estimate the stellar properties of our sample and describe the

dust structure needed to explain the emission. For objects with submillimeter data, we also show our disk mass estimates.

3.1. Spectral Energy Distributions

In Figure 2 we show the dereddened SEDs of our PACS sample for sources with *Spitzer* IRS spectra. Figure 3 shows the SEDs for those sources for which we do not have IRS data. We adopted the Mathis reddening law (Mathis 1990, $R = 3.1$) with visual extinctions, A_v , from Briceño et al. (2005) and C. Briceño et al. (2018, in preparation). The dashed line indicates the stellar photosphere (normalized to the J band of each object) of the same spectral type following Kenyon & Hartmann (1995). The light-blue solid line is the Taurus median (estimated from photometric data only) for K and M, class II stars taken from Maucó et al. (2016). All our objects exhibit excesses over the photosphere from the near-IR to millimeter wavelengths consistent with the presence of a disk. Additionally, CVSO-35, CVSO-104, CVSO-121, and CVSO-1265 with CanariCam photometry and especially

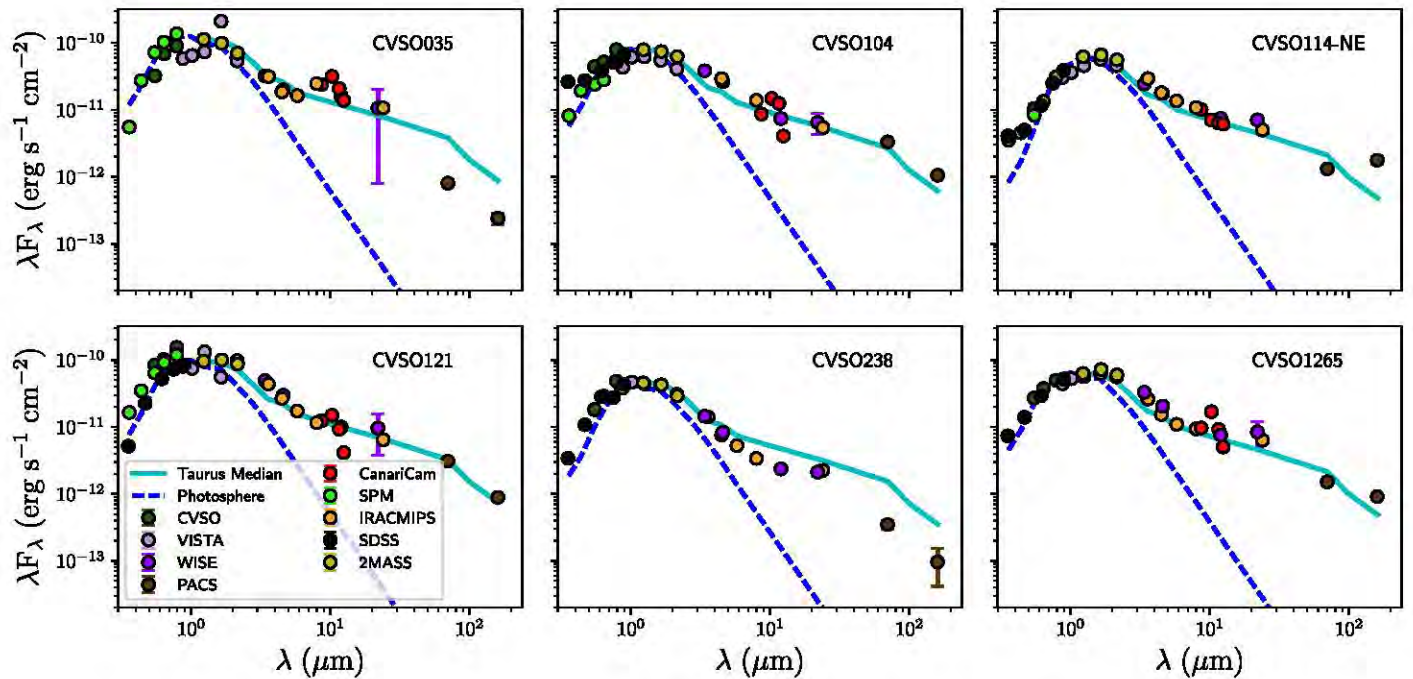


Figure 3. Dereddened SEDs of stars in our sample without IRS spectra. Optical data are from the CVSO (Briceño et al. 2005, 2007; C. Briceño et al. 2018, in preparation), SDSS, and SPM; the near-IR magnitudes at J , H , and K_S are from 2MASS (Skrutskie et al. 2006); and those at Z , Y , J , H , and K_S are from VISTA (Petr-Gotzens et al. 2011). The mid-IR measurements at 3.6, 4.5, 5.8, 8, and 24 μm are from our *Spitzer* GO-13437 and GO-50360 programs (Hernández et al. 2007b); those at 8.7, 10.3, 11.6, and 12.5 are from CanariCam; and those at 3.4, 4.6, 12, and 22 μm are from AllWISE Source Catalog (Wright et al. 2010). Symbols and line styles are the same as in Figure 2.

CVSO-107 and CVSO-109 with IRS spectra show strong 10 μm silicate emission.

CVSO-35, CVSO-104, CVSO-107, and CVSO-121 show significant variability in optical and near-IR as seen from the scatter in the V , R_c , I_c magnitudes, as well as in the J , H , and K_S bands taken at different epochs. Although most of our objects have typical full-disk excess emission beyond 20 μm , with SED comparable to the median of Taurus, objects like CVSO-107 and CVSO-238, and possibly CVSO-104 and CVSO-121, seem to have a flux deficit around 10–12 μm relative to the median, possibly the result of the first stages in the development of an inner disk gap; if so, these objects could be in the process of evolving to a TD, like CVSO-224 (see Espaillat et al. 2008b), which shows a deep emission deficit at wavelengths between ~ 8 and 22 μm , the telltale sign of an inner disk hole cleared of dust. In the case of CVSO-114NE PACS fluxes at wavelengths longer than 10 μm look flatter than in the rest of the sample. This star forms an apparent pair with the star CVSO-114SW, separated by $4''.9$ (Thanathibodee et al. 2018) Both components have been observed and resolved using far-UV, optical, and near-IR spectroscopy, as well as high angular resolution imaging; analysis of the accretion properties indicates that the northeast (NE) component, studied here, is a CTTS, while the southwest (SW) component is a weak TTS (Thanathibodee et al. 2018). The SW component is only brighter than the NE component in the optical, so it is unlikely to have a contribution in the PACS range.

3.2. Stellar and Accretion Properties

We estimated stellar and accretion properties of all the CTTSs detected by PACS in Orion OB1a and OB1b reported as members in Briceño et al. (2005, 2007), for which we have the necessary spectra and photometry. Table 5 lists the results as follows: target CVSO ID from Briceño et al. (2005), spectral

type, effective temperature (T_{eff}), visual extinction (A_v), stellar mass (M_*), stellar radius (R_*), stellar luminosity (L_*), accretion rate (\dot{M}), stellar age, and distance. To characterize the stellar properties of the sources, we located them in the H-R diagram. For this, we estimated the luminosity of our sample using 2MASS J photometry, visual extinctions, and spectral types from Briceño et al. (2005; C. Briceño et al. 2018, in preparation). We used bolometric corrections and effective temperatures from the standard table for 5–30 Myr old PMS stars from Pecaut & Mamajek (2013). Using these luminosities and effective temperatures, we estimated stellar radii. We used the PMS evolutionary tracks of Siess et al. (2000) to obtain stellar masses. We assumed a distance for the OB1b association of 440 pc and distances of 354 and 368 pc for the 25 Ori and HR 1833 stellar aggregates, respectively (Briceño et al. 2005; C. Briceño et al. 2018, in preparation). Since Pecaut & Mamajek (2013) only include three optical magnitudes (B , V , and I_c), we used the intrinsic colors from Kenyon & Hartmann (1995), which includes more optical magnitudes (U , B , V , R_c , and I_c), to represent the stellar photosphere.

Mass accretion rates (\dot{M}) were estimated from the $H\alpha$ line luminosity. The $H\alpha$ luminosity was estimated by approximating the flux of the line ($F_{H\alpha}$) as $\text{EW}(H\alpha) \times F_{\text{cont}}$, where F_{cont} and $\text{EW}(H\alpha)$ are the continuum flux around the line and the equivalent width, respectively. In turn, we calculated F_{cont} from the R_c magnitude of each source (Briceño et al. 2005) corrected by extinction and its equivalent width $\text{EW}(H\alpha)$ from low-resolution spectra (C. Briceño et al. 2018, in preparation). Finally, we used the relation between the $H\alpha$ luminosity and mass accretion rate from Ingleby et al. (2013). All the accretion parameters of PACS CTTSs are shown in Table 5.

Two of our sources, CVSO-107 and CVSO-109, have reported accretion rates in Ingleby et al. (2014). They estimated \dot{M} by fitting the excess in spectra taken with the Magellan

Table 5
Properties of PACS CTTS Sources in the OB1a and OB1b Subassociations

CVSO ID	SpT	T_{eff} (K)	A_v (mag)	M_* (M_{\odot})	R_* (R_{\odot})	L_* (L_{\odot})	\dot{M} ($10^{-9} M_{\odot} \text{ yr}^{-1}$)	Age (Myr)	d (pc)
CVSO-35	K6	4020	0.3	0.73	1.67	0.66	0.87	3.0	354
CVSO-104	K7	3970	0.1	0.67	1.77	0.67	5.62	2.6	440
CVSO-107	K7	3970	0.4	0.66	2.07	0.96	2.89 ^a	1.6	440
CVSO-109	M0	3770	0.0	0.50	2.66	1.28	6.71 ^a	0.6	440
CVSO-114NE	M1.5	3560	0.0	0.47	1.87	0.47	0.52 ^a	1.5	440
CVSO-121	K6	4020	0.4	0.73	1.92	0.86	2.32	2.4	440
CVSO-238	M0.6	3630	0.0	0.42	1.52	0.36	3.71	2.5	440
CVSO-1265	K7	3970	0.0	0.70	1.32	0.39	1.51	6.7	368

Note. Column (1): ID following Briceño et al. (2005). Column (2): spectral type. Column (3): effective temperature. Column (4): visual extinction. Column (5): stellar mass. Column (6): stellar radius. Column (7): stellar luminosity. Column (8): mass accretion rate. Column (9): age. Column (10): distance (Briceño et al. 2005; C. Briceño et al. 2018, in preparation).

^a \dot{M} estimated using R_c magnitude from DCT.

Echelle Spectrograph (MagE)¹⁹ using accretion shock models from Calvet & Gullbring (1998). Our estimate agrees with their results for CVSO-107 and is consistent within a factor of 2 for CVSO-109. Differences are mainly due to uncertainties in stellar mass, radius, and extinction.

3.3. Disk Models

We used the ‘‘D’Alessio Irradiated Accretion Disk’’ (DIAD) models from D’Alessio et al. (2006) in order to fit the SEDs of our sources. These models assume that the disk is heated by stellar irradiation and viscous dissipation. The viscosity is parameterized through α (Shakura & Sunyaev 1973) assuming steady accretion with constant \dot{M} . To simulate the settling of dust, D’Alessio et al. (2006) considered two populations of dust grains that follow a size distribution $\propto a^{-3.5}$, where a is the radius of the grain, between a_{min} and a_{max} (Mathis et al. 1977). We assumed that the grains are segregated spheres (Pollack et al. 1994). One population consists of small ($a_{\text{max}} = 0.25 \mu\text{m}$) grains dominant in the upper layers of the disk, while the other is described by larger grains in the disk midplane. The settling of dust is parameterized with the parameter ϵ , defined as $\epsilon = \zeta_{\text{small}}/\zeta_{\text{std}}$, where ζ_{small} is the dust-to-gas mass ratio of small grains and ζ_{std} is the sum of the assumed mass abundances of the different dust components relative to gas, i.e., ϵ describes the depletion (in mass) of small grains relative to the standard value. Therefore, lower values of ϵ represent more settled disks.

The main input parameters are the stellar properties (M_* , R_* , L_*); the mass accretion rate (\dot{M}); the viscosity parameter (α); the disk outer radius (R_d); the cosine of the inclination angle (μ); the maximum grain size at the disk midplane ($a_{\text{max,b}}$), at the disk inner edge or wall ($a_{\text{max,w}}$), and at the disk upper layers ($a_{\text{max,s}}$); and the dust settling parameter ϵ .

TDs are modeled with an optically thick outer disk with a sharp inner edge (‘‘wall’’). PTDs also have a truncated outer disk but require optically thick material near the star, and thus a gap exists between the inner and the outer thick material (Espaillat et al. 2007).

We assumed a composition for the optically thick disks of amorphous silicates (pyroxenes) with a mass fraction relative to gas of $\zeta_{\text{sil}} = 0.004$ and of carbonates in the form of graphite with $\zeta_{\text{graf}} = 0.0025$. We computed opacities for the silicates and graphite grains with Mie theory with optical constants from

Dorschner et al. (1995) and Draine & Lee (1984), respectively. We also included H_2O ice opacities, calculated with optical constants from Warren (1984) and with $\zeta_{\text{ice}} = 0.002$. We considered a case with no water ice (a mass fraction of 10^{-5}) in the outer disk also. We used a maximum grain size at the disk midplane of $a_{\text{max,b}} = 1 \text{ mm}$.

In PTDs, the inner disk has a sharp inner edge (‘‘inner wall’’) located at the dust destruction radius for silicate grains. The emission from the inner wall is calculated from the stellar properties, the maximum grain size ($a_{\text{max,w}}^i$), and the temperature (T_w^i), assumed to be the sublimation temperature of silicate grains (Muzerolle et al. 2003; D’Alessio et al. 2006; 1400 K), with a dust composition of pyroxenes and $\zeta_{\text{sil}} = 0.004$. The height of the inner wall (z_w^i) was fixed to 4 times the gas scale height. The stellar radiation impinges directly onto the wall, which we assume is vertical. We calculate the structure and emission of the wall atmosphere following the prescriptions of D’Alessio et al. (2004, 2005). We calculated the location and height of the inner edge of the outer disk (‘‘outer wall’’) by varying its radius R_w^o , or equivalently its temperature T_w^o (see D’Alessio et al. 2005; Espaillat et al. 2010) to achieve the best fit to the SEDs.

In both PTDs and TDs, the gap or hole sometimes contains a small amount of optically thin dust, which contributes to the $10 \mu\text{m}$ silicate emission feature. We calculated the emission from this optically thin dust region following Calvet et al. (2002). The optically thin dust inside the gaps/holes is composed of amorphous silicates (olivines), amorphous carbon, and organics. Troilites and crystalline silicates in the form of enstatite and forsterite were only included in modeling objects with *Spitzer*/IRS spectra. Opacities and optical constants for organics and troilite were adopted from Pollack et al. (1994) and Begemann et al. (1994), respectively. We added organics and troilite to the dust mixture following Espaillat et al. (2010) with $\zeta_{\text{org}} = 0.0041$ and $\zeta_{\text{troi}} = 0.000768$ and sublimation temperatures of $T_{\text{org}} = 425 \text{ K}$ and $T_{\text{troi}} = 680 \text{ K}$. For the amorphous carbon we use $\zeta_{\text{amc}} = 0.001$, and for silicates we use $\zeta_{\text{sil}} = 0.004$. The opacity for crystalline silicates is taken from Sargent et al. (2009). We did not include ice in the optically thin region since the temperatures here are high enough for it to be sublimated. Opacities were calculated using Mie theory, assuming spherical grains (Pollack et al. 1994). We note, however, that we do not aim to model the detailed composition of dust in this region, but rather to

¹⁹ <http://www.lco.cl/telescopes-information/magellan/instruments/instruments/mage>

Table 6
Model Parameters

Parameter	Value
Cosine of inclination angle, μ	0.3, 0.6, 0.9
Optically Thick Outer Disk	
α	0.01, 0.001
ϵ	0.01, 0.001
R_d^o (au)	200, 300
H ₂ O ice	1e-5, 0.002
Optically Thick Outer Wall	
amax_w^o (μm)	0.25, 10, 1000
T_w^o (K)	40, 80, 120, 160, 200
z_w^o (in units of H)	0.1-2.5, in steps of 0.1
H ₂ O ice	1e-5, 0.002
Optically Thick Inner Disk	
amax^i (μm)	0.25, 10
ϵ	0.1, 0.01
graf_{ab}	0.0025, 0.25
R_d^i (au)	0.1, 0.15, 0.2
Optically Thin Region	
$R_{i,\text{thin}}$ (au)	0.1, 0.5
$R_{o,\text{thin}}$ (au)	3, 5, 7, 10, 20, 30, 40, 50
p	0.0, 0.3, 0.6, 0.9
$\text{amax}_{\text{thin}}$ (μm)	0.25, 100

illustrate what typical dust compositions can reasonably describe the observed SEDs.

3.4. SED Modeling of (Pre-)transitional Disks

We have calculated detailed disk structures for eight CTTs detected in our PACS 70 and 160 μm survey in the Orion OB1a and OB1b subassociations. We used the DIAD models (D’Alessio et al. 2006), constrained by the mass accretion rates estimated independently from optical spectra (Section 3.2). As a result of our modeling, all our objects turned out to be PTDs/TDs, characterized by small deficits of mid-IR emission along with strong silicate features at 10 μm . We found that the emission of the silicate bands cannot be reproduced by the classical full-disk model; instead, we needed a dust distribution characteristic of PTDs/TDs with optically thin dust inside their gaps/holes. We inferred the properties of the edge or “wall” of the outer disk, the size of the cavity, the mass and composition of the optically thin dust inside the cavity, and, for those objects with millimeter photometry, we also estimated disk masses and radii.

We used as input for the models the stellar properties, accretion rates, and distances reported in Table 5. For each object we calculated a total of 2160 optically thick disk models and more than 1500 optically thin dust models. All the relevant parameters we varied are listed in Table 6. We selected as the best fit the model that yielded the minimum value of the reduced χ_{red}^2 . All our objects have PTD morphologies, except CVSO-35, which is a TD.

Since these are variable stars (see Figures 2 and 3) and we have multiepoch optical and mid-IR photometry at different bands with very similar wavelengths, we included stellar variability in the estimate of the χ_{red}^2 by considering the

weighted average between photometric bands taken at almost the same wavelength. The following pairs of photometric bands were averaged: SDSS(riz)–CVSO(VRI), 2MASS(*JHK*)–VISTA(*JHK*), and IRAC/MIPS(3.6,4.5,24)–WISE(W1,W2,W4). For objects without SDSS photometry or incomplete CVSO photometry, we used SPM and DCT data instead. When multiepoch photometry was available, we took the maximum difference between photometric values as the standard error used in the estimate of the χ_{red}^2 . However, since our main purpose is to model the emission from the disk rather than stellar variability, we assigned a 90% weight to data with wavelength larger than 2 μm and the remaining 10% to the optical data in the final χ_{red}^2 .

Figures 4 and 5 show the SEDs of our PACS disks (filled circles) with the resulting fit (solid lines). The contributions of the different model components are also shown. The CanariCam photometry around 10 μm and IRS spectra are highlighted (red). Tables 7 and 8 list the parameters of the best-fit model for each object; in Table 7 we show the outer disk properties, and in Table 8 we show the properties of the optically thin dust region.

As shown in Figures 4 and 5, PACS fluxes are almost completely dominated by the wall of the outer disk for most of our sources, so we cannot constrain the properties of the outer disks for objects without millimeter photometry. However, we did estimate confidence intervals for the location of the outer wall and its height. To set these intervals, we first estimated the likelihood function, \mathcal{L} , which is related to the χ_{red}^2 values through the expression $\mathcal{L} = \exp(-\chi_{\text{red}}^2/2)$. Since χ_{red}^2 is a multidimensional function, at every R_w^o or z_w^o we have several values of χ_{red}^2 , one for each one of the calculated models. Thus, the likelihood \mathcal{L} is computed using the minimum χ_{red}^2 value in each case. Figures 6 and 7 show the likelihood function for R_w^o and z_w^o , respectively. The confidence intervals are given as those extreme limits at which the area below the likelihood curve maximum is 63% (1σ) of its total area (Sivia & Skilling 2012). These intervals are indicated by light-blue shaded regions in each panel and are reported in Table 7. For those cases where the best parameter falls on one of the edges of the range of values used in the models, we have considered these values as upper or lower limits, and they are indicated by parentheses instead of square brackets in Table 7.

Even though we are including the errors in the photometry and a proxy of the star variability in the estimate of the χ_{red}^2 , there are other sources of uncertainty, such as the inherent uncertainties in the distance, spectral types, and mass accretion rates. Therefore, the χ_{red}^2 should be taken only as a guide in order to obtain the model that provides the best fit to the photometry for each source and not as an actual estimate of the goodness of the fit.

3.4.1. Inner Disk and Optically Thin Region

The inner parts of our PTDs consist of an optically thick dusty belt within the first ~ 0.2 au from the star and with grains that can reach 10 μm in size. The innermost edge of this ring of optically thick material is located at the dust destruction radius given by the sublimation temperature of silicate grains (1400 K).

All our objects needed the presence of a small amount of optically thin dust inside their cavities. Keeping the total mass fraction of silicates relative to gas constant, $\zeta_{\text{sil}} = 0.004$, we

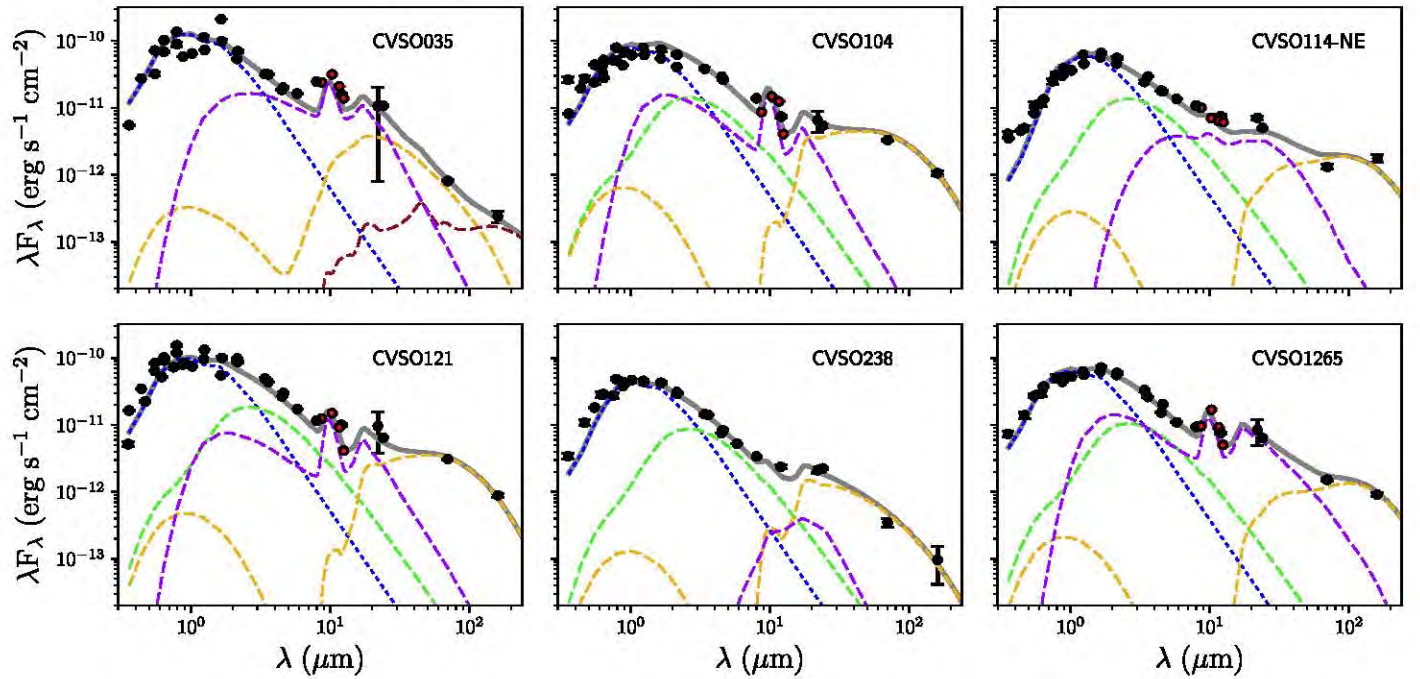


Figure 4. Best-fit model (solid line) of the SED of PACS OB1a and 1b sources without IRS spectra. As in Figures 2 and 3, photometry has been dereddened following the Mathis law (Mathis 1990; $R = 3.1$; filled circles). Dotted lines correspond to the photosphere-like fluxes using the colors of Kenyon & Hartmann (1995) (normalized to the J band of each object). Dashed lines represent the model components in the following way: inner wall+disk (green), optically thin dust region (purple), outer wall (yellow), and outer disk (brown). Error bars are included, but in most cases they are smaller than the symbol. The CanariCam photometry has been highlighted (red).

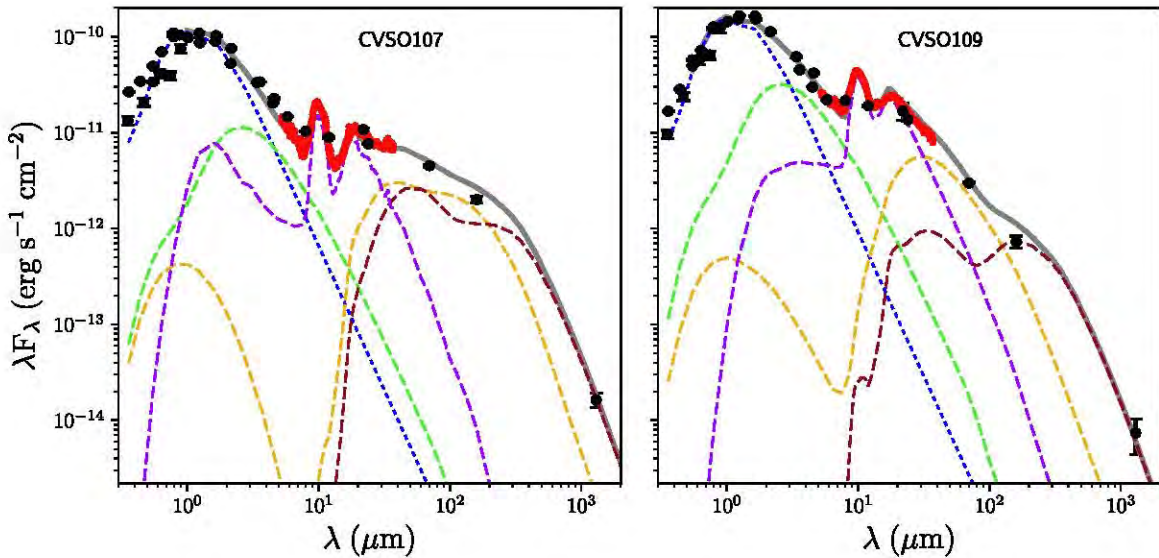


Figure 5. Best-fit model (solid line) of the SED of PACS OB1a and 1b sources with IRS spectra. As in Figures 2 and 3, photometry has been dereddened following the Mathis law (Mathis 1990; $R = 3.1$; solid circles). Line styles and colors are the same as in Figure 4. IRS spectra are indicated by red lines.

varied the fractional abundance of the different silicate species (see Section 3.3) inside the gaps/holes, the extension of the optically thin region ($R_{i,thin}$, $R_{o,thin}$), the maximum size of the dust grains ($a_{max,thin}$), and the exponent of the power law describing the dust distribution (p) in order to fit the silicate feature. The total emission of the optically thin region was scaled to the vertical optical depth at $10 \mu\text{m}$ (τ_{10}). Table 6 describes the parameter space we used in order to model the optically thin dust inside the cavities, while Table 8 lists its estimated properties.

The silicate emission feature of all our objects with CanariCam photometry except CVSO-114NE can be explained

with small submicron-sized grains. CVSO-114NE exhibits no $10 \mu\text{m}$ silicate feature, indicating a lack of small grains; in this case, we found that larger grains ($a_{max,thin} = 10 \mu\text{m}$) can describe the emission. Our modeling of the silicate features was more detailed for those objects with *Spitzer*/IRS spectra. The silicate feature of CVSO-109 resembles that of pristine spectra, e.g., with no signs of dust processing (Watson et al. 2009), and it is composed of dust made up entirely of amorphous silicates ($\sim 99\%$). CVSO-107, on the other hand, shows forsterite and enstatite features beyond $20 \mu\text{m}$ in its IRS spectra (e.g., the $33 \mu\text{m}$ forsterite feature). We found an optically thin dust composition consistent with $\sim 79\%$ amorphous silicates, $\sim 13\%$

Table 7
Outer Disk Properties

CVSO ID	μ	H ₂ O Ice	Optically Thick Outer Wall						Optically Thick Outer Disk					χ_{red}^2
			amax_w^o (μm)	T_w^o (K)	z_w^o	(z_w^{o-}, z_w^{o+}) (au)	R_w^o (au)	R_w^{o-}, R_w^{o+}	α (au)	R_d^o (M_\odot)	ϵ (M_\odot)	M_{dust}	M_{disk}	
CVSO-35	0.3	0.002	10	200	0.36	[0.25, 0.40]	4.3	(3.9, 4.9]	0.01	300	0.001	3.5	0.0016	26.77
CVSO-104	0.6	0.002	0.25	120	0.9	[0.32, 1.22]	26.5	[21.5, 168.7]	1.50
CVSO-107	0.9	1e-5	0.25	80	0.3	[0.15, 0.43]	86.2	[71.7, 92.6]	0.001	300	0.01	116.8	0.054	22.01
CVSO-109	0.6	1e-5	10	120	0.45	[0.35, 0.68]	18.9	(19.0, 20.6]	0.006	200	0.001	29.0	0.0134	10.06
CVSO-114NE	0.3	1e-5	0.25	80	0.3	(0.3, 0.43]	57.9	[51.4, 93.6]	0.47
CVSO-121	0.3	0.002	0.25	120	0.54	[0.37, 0.72]	27.8	[19.1, 159.1]	0.56
CVSO-238	0.9	0.002	0.25	160	0.6	[0.25, 0.88]	8.8	(2.9, 81.0]	1.03
CVSO-1265	0.3	1e-5	0.25	80	0.3	[0.24, 0.48]	57.0	[24.9, 129.0]	0.50

Note. Column (1): ID following Briceño et al. (2005). Column (2): cosine of inclination angle. Column (3): H₂O ice abundance. Column (4): maximum grain size of the outer wall. Column (5): outer wall temperature. Column (6): outer wall height (in units of the gas scale height H). Column (7): outer wall height confidence intervals (in units of the gas scale height H). Column (8): location of the outer wall. Column (9): confidence intervals of the location of the outer wall. Column (10): outer disk viscosity. Column (11): outer disk radius. Column (12): degree of dust settling of the outer disk. Column (13): outer disk dust mass. Column (14): outer disk total mass. Column (15): χ_{red}^2 . Total disk mass estimates are assuming a dust-to-gas mass ratio similar to that of the ISM.

Table 8
Inner Disk and Optically Thin Dust Region Properties

CVSO ID	Optically Thick Inner Disk			Optically Thin Dust Region											
	amax_w^i (μm)	R_w^i (au)	R_d^i (au)	$R_{\text{i,thin}}$ (au)	$R_{\text{o,thin}}$ (au)	$\text{amax}_{\text{thin}}$ (μm)	τ_0	p (%)	sil (%)	org (%)	amc (%)	troi (%)	fors (%)	enst ($10^{-9} M_\odot$)	$M_{\text{dust,thin}}$
CVSO-35	0.01	5.0	0.25	0.08	0.0	~57	~29	~14	0.0	<0.2	<0.2	0.37
CVSO-104	10	0.09	0.10	0.1	20.0	0.25	0.08	0.6	~85	0.0	~14	0.0	<0.2	<0.2	4.72
CVSO-107	10	0.1	...	0.1	50.0	0.25	0.04	0.2	~79	~9	0.0	0.0	~10	~3	14.46
CVSO-109	10	0.11	0.15	0.5	5.0	0.25	0.1	0.0	~99	0.0	0.0	0.0	<0.2	<0.2	1.65
CVSO-114NE	10	0.07	0.2	0.2	10	10	0.1	0.0	~23	~71	~6	0.0	<0.2	<0.2	2.86
CVSO-121	10	0.09	0.10	0.1	20	0.25	0.035	0.2	~85	0.0	~14	0.0	<0.2	<0.2	1.65
CVSO-238	10	0.06	0.15	0.5	3.0	0.25	0.03	0.9	~23	~71	~6	0.0	<0.2	<0.2	0.072
CVSO-1265	10	0.06	0.20	0.1	30	0.25	0.055	0.0	~72	0.0	~27	0.0	<0.2	<0.2	7.90

Note. Column (1): ID following Briceño et al. (2005). Column (2): maximum grain size in the inner wall. Column (3): dust destruction radius. Column (4): inner disk radius. Columns (5) and (6): extension of the optically thin dust region. Column (7): maximum grain size of optically thin dust. Column (8): vertical optical depth at 10 μm . Column (9): power-law exponent of the distribution of optically thin dust. Columns (10)–(15): percentages of dust species in the optically thin region. Column (16): optically thin dust mass.

forsterite and enstatite crystals, and ~9% organics. Figure 8 shows the fit to the IRS spectrum range for both sources.

The mass of optically thin dust populating the cavities (Table 8) ranges from $7.2 \times 10^{-11} M_\odot$ to $1.44 \times 10^{-8} M_\odot$. According to Table 8, the optically thin dust region extends to more than 50% the size of the disk gap for about half of the sample, and about 30% or less for the other half. These results should be taken as an approximation of how much dust is required within the gaps/holes to be able to explain the observed emission and not as a detailed prescription of the actual spatial distribution of dust. High-resolution IR interferometry is needed to probe the morphology of this component in detail.

3.4.2. Outer Disk

The disks in the sample have a wide range of gap/hole sizes, from ~4 au to almost 90 au in radius. Large confidence intervals obtained for some objects reflect the need for acquiring mid-IR spectra along with (sub)millimeter data to better constrain cavity sizes. We estimated outer disk properties

for CVSO-107 and CVSO-109, the only two sources with SMA detections in the sample. The disks required low values of the viscosity parameter (Table 7), similarly to other PTDs/TDs (Espaillat et al. 2007, 2008a, 2010), and a significant degree of dust settling, $\epsilon \leq 0.01$. CVSO-107 has a disk radius of $R_d = 300$ au, while CVSO-109 has a smaller disk with $R_d = 200$ au.

In CVSO-35, the only TD in the sample, the PACS emission is not entirely dominated by the outer wall, but seems to have a small contribution from a low-mass optically thick outer disk (see Figure 4). We found a disk with $\alpha = 0.01$, $\epsilon = 0.001$, and $R_d = 300$ au. However, these values should be taken as an approximation since we do not have (sub)millimeter data for this source.

3.4.3. Disk Masses

The dust masses of the best-fit models for objects in which we probe the outer disk are given in Table 7. The corresponding total disk mass, with a dust-to-gas mass ratio $\zeta = 0.0065$ (the sum of our assumed abundances), is also

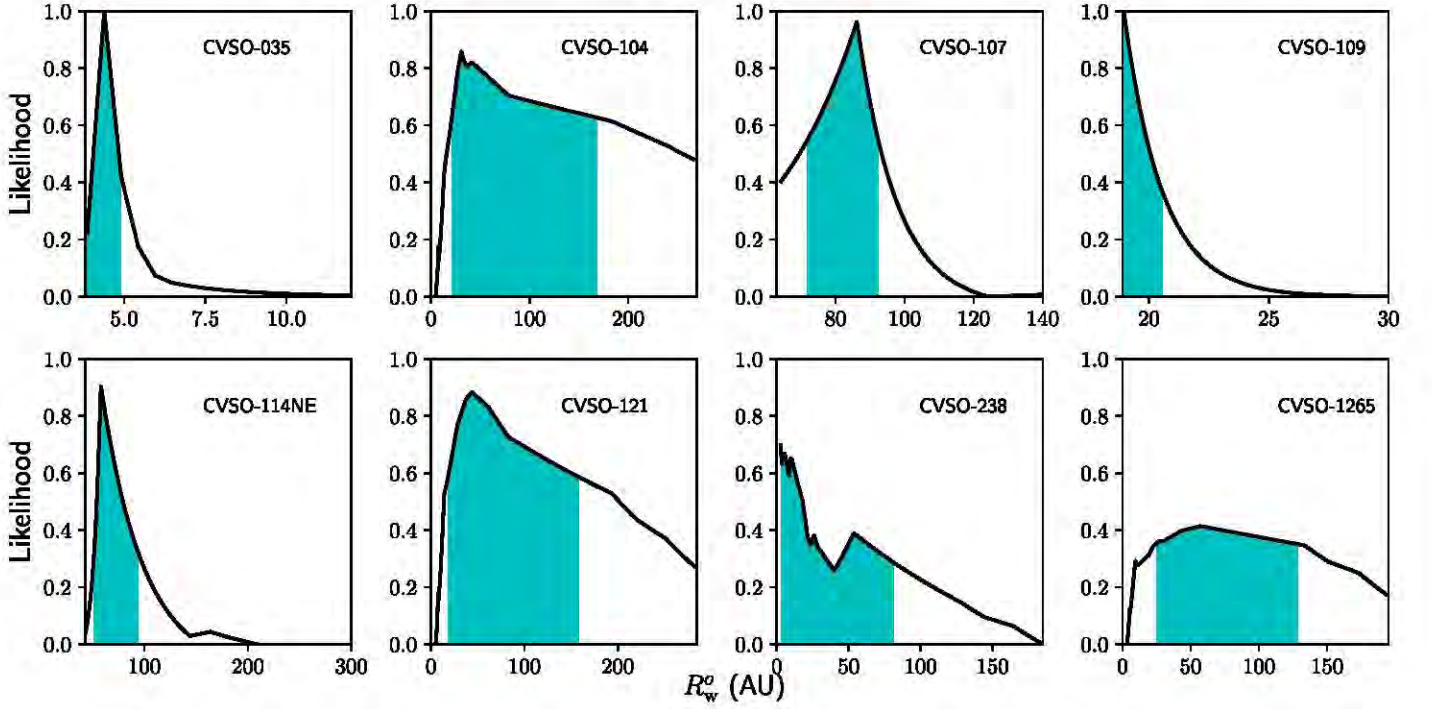


Figure 6. Likelihood function, \mathcal{L} , vs. outer wall location, R_w^o , for each source. The x -axis has been restrained around the maximum peak in each case in order to better visualize the likelihood function. Confidence intervals of R_w^o are shown as light-blue shaded regions and are defined as the intervals that enclose 63% (1σ) of the total area of \mathcal{L} . Confidence intervals are reported in Table 7.

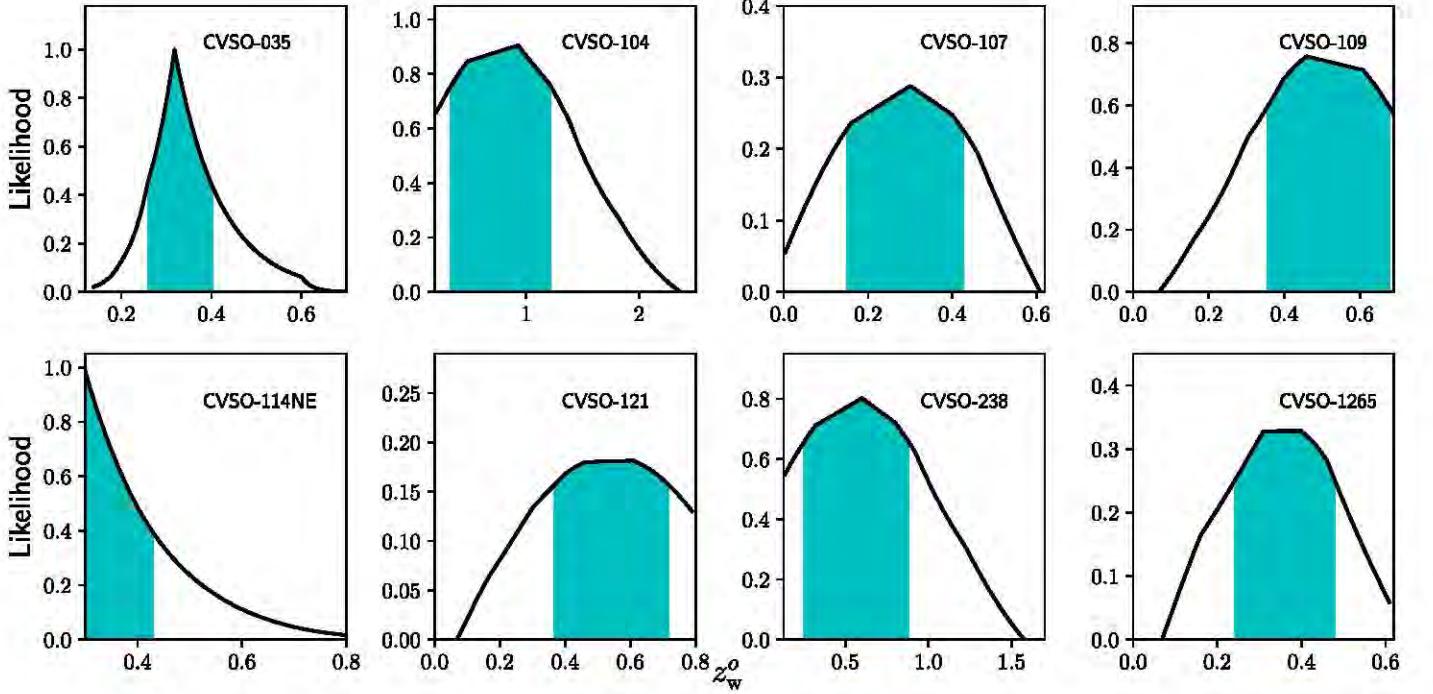


Figure 7. Likelihood function, \mathcal{L} , vs. outer wall height, z_w^o (in units of the gas scale height H), for each source. The x -axis has been restrained around the maximum peak in each case in order to better visualize the likelihood function. Confidence intervals of z_w^o are shown as light-blue shaded regions and are defined as the intervals that enclose 63% (1σ) of the total area of \mathcal{L} . Confidence intervals are reported in Table 7.

given. We note, however, that the disk mass for CVSO-35 should be taken with caution since we need (sub)millimeter data to properly constrain this parameter.

We compared the masses obtained through detailed modeling of the SEDs with disk masses estimated using the SMA fluxes at 1.3 mm of CVSO-107 and CVSO-109 and assuming

optically thin emission. Following Hildebrand (1983),

$$M_{\text{dust}} = \frac{F_\nu d^2}{\kappa_\nu B_\nu(T_{\text{dust}})}, \quad (1)$$

where F_ν is the submillimeter flux at 1.3 mm, d is the source distance, T_{dust} is a characteristic dust temperature assumed to

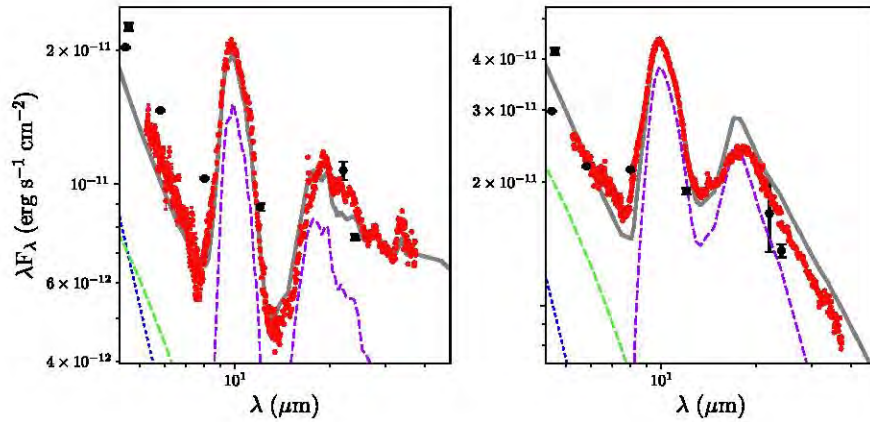


Figure 8. Best-fit model (solid line) to the IRS spectra (red circles) of CVSO-107 (left) and CVSO-109 (right). Dotted lines correspond to the photosphere-like fluxes using the colors of Kenyon & Hartmann (1995) (normalized to the J band of each object). Dashed lines represent the model components in the following way: inner wall+disk (green), optically thin dust region (purple). Error bars are included, but in most cases they are smaller than the symbol.

be the median for Taurus disks (Andrews & Williams 2005; $T = 20$ K), B_ν is the Planck function at T_{dust} , and κ_ν is the dust grain opacity taken as $0.1 \text{ cm}^2 \text{ g}^{-1}$ at 1000 GHz using an opacity power-law index of $\beta = 1$ (Beckwith et al. 1990). Using the above equation and a dust-to-gas mass ratio of 0.01, we computed M_{disk} of 0.0087 and $0.0039 M_\odot$ for CVSO-107 and CVSO-109, respectively. These masses are a factor of ~ 6 and ~ 3 lower than the masses obtained from detailed modeling (Table 7). The difference is due in part to the difference in opacities (our opacity is a factor of 2 lower than the κ_ν used in Equation (1) and dust-to-gas mass ratios, due to the assumption of constant temperature, and also due to the contribution from hotter, optically thick disk regions to the 1.3 mm flux, not included in Equation (1)). We stress that we used a consistent opacity law for each one of our objects, which depends on the mix of materials assumed in our disk models (silicates, graphite, water, etc.), their abundances, and their grain size distributions, rather than the simplified approach of a single grain opacity in an isothermal disk to estimate disk masses reported in Table 7.

4. Discussion

4.1. Why These Objects Fail to Be Described as Full Disks

In order to model our disk sample, we included both full and truncated disk models as priors, and the best fit was obtained with PTDs/TDs. We first note the small decrease of mid-IR emission in the SEDs of some of our objects compared to the median of CTTSs in Taurus (Figure 3, light-blue line). This points to a lack of optically thick material similar to those found in known PTDs (Espaillat et al. 2008a, 2010). More importantly, full-disk models do not appear to produce high enough IR emission at $10 \mu\text{m}$ to explain the observed silicate features, even in objects with IRS spectra as CVSO-107 and CVSO-109. Figures 9 and 10 show the best fit to the SEDs of CVSO-107 and CVSO-109, respectively, considering full-disk models. As shown, the model underestimates near- and mid-IR excesses, especially at the silicate bands at 10 and $20 \mu\text{m}$ (see figure insets). For CVSO-109 the model also overestimates the emission beyond $26 \mu\text{m}$. A viable way to generate high enough emission at the silicate bands and a small decrease in the mid-IR emission is by including optically thin dust inside gaps.

Even in the case of CVSO-238, which does not have photometry or spectra around $10 \mu\text{m}$, we were unable to model its PACS photometry along with its *WISE* $22 \mu\text{m}$ and IRAC/MIPS $24 \mu\text{m}$ photometry with a full disk.

Given the intermediate to advanced age of this region, it is not unreasonable to think that these objects may have experienced significant evolution over time. Based on our disk mass estimates for CVSO-107 and CVSO-109, we can assume that early on in their lives there was probably enough material to form multiple planets. If this is indeed the case, then these planets might be responsible for the radial structures—characteristic of disks with gaps and holes—observed here. However, there are other possible explanations. For instance, magnetized disks without planets (Flock et al. 2015), or fast pebble growth near condensation fronts (Zhang et al. 2015), may create structures in disks. In these cases, rings in disks can be the precursors of planets rather than the cause (e.g., Carrasco-González et al. 2016). The clear presence of near-IR excesses in the SEDs of all our stars, along with significant mass accretion rates, indicates that there is still gas and dust in the inner regions, and therefore these objects can be classified as PTDs/TDs based on the observational data currently available for these sources. We note, however, that high-resolution IR interferometric observations are still needed in order to confirm the morphology of these disks.

4.2. Implications for Dust Evolution

Investigating dust evolution in the outer disk requires far-IR observations of a significant sample of TTSs spanning the first several megayears in the lives of low-mass stars. Since by 5 Myr only about 20% of the stars still retain their inner disks (Hernández et al. 2007a), disk populations at intermediate ages are essential to link current disk properties with evolutionary processes.

As shown in Figure 4 and discussed in the previous section, the SED modeling of our sources indicates that these are PTDs/TDs. Moreover, while most PTD/TD studies have focused on young star-forming regions of less than 3 Myr, few have been done to address the physical mechanisms responsible for the existence of PTDs/TDs in older regions.

The intermediate to advanced age of our sources (~ 4 – 10 Myr) poses two possible evolutionary scenarios: (1) that these stars had full disks until recently and have now become PTDs/TDs, or (2) that the PTD/TD appearance is

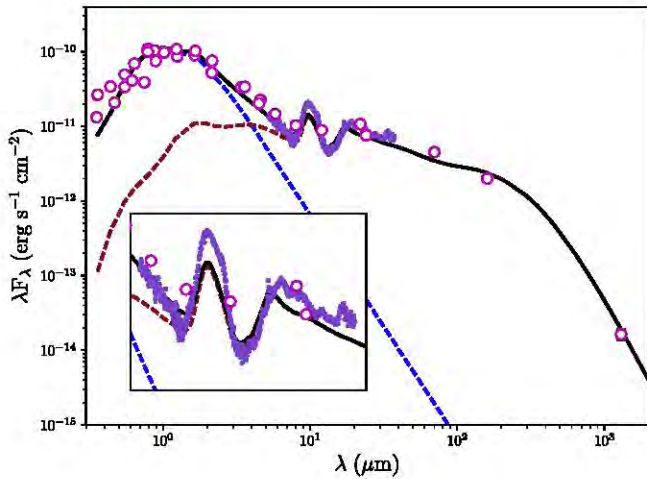


Figure 9. Best fit to the SED of CVSO-107 considering full-disk models. Magenta open circles indicate photometric data, while the IRS spectra are shown as purple circles. The solid black line represents the best fit. The model consists of a stellar photosphere (blue dashed line) and a disk (brown dashed line). Note how full disks are unable to generate enough near- and mid-IR emission especially at the silicate features at 10 and 20 μm .

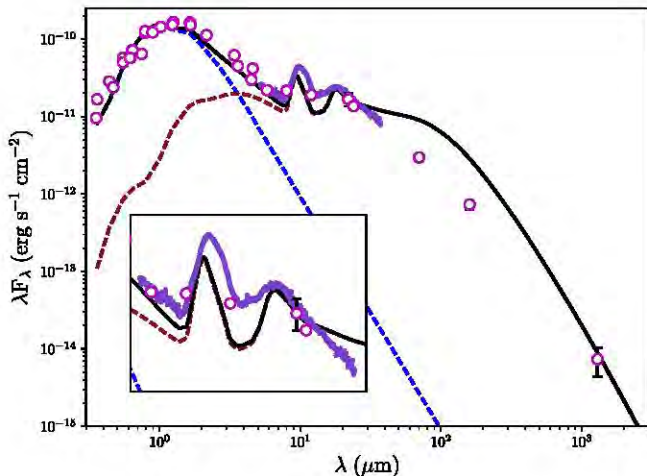


Figure 10. Best fit to the SED of CVSO-109 considering full-disk models. Magenta open circles indicate photometric data, while the IRS spectra are shown as purple circles. The solid black line represents the best fit. The model consists of a stellar photosphere (blue dashed line) and a disk (brown dashed line). Note how full disks are unable to generate enough near- and mid-IR emission especially at the silicate features at 10 and 20 μm . The model also overestimates the emission beyond 26 μm .

long-lasting, in which case we are actually looking at “mature” PTD/TD systems. The latter argument is reinforced by the fact that all our PACS detections turn out to be PTDs/TDs. This challenges the current understanding of disk evolution, where PTD morphology is thought to be a transient stage. Moreover, dust evolution models struggle to find viable ways to explain inner disk survival for long periods of time.

One possible mechanism that seems to explain PTD appearance is dust filtration induced by the presence of embedded planets (e.g., Paardekooper & Mellema 2006; Rice et al. 2006; Fouchet et al. 2007; Zhu et al. 2012; Espaillat et al. 2014; Pinilla et al. 2015). Since dust and gas in disks are not perfectly coupled, gas drag forces dust grains to drift toward a pressure maximum (Weidenschilling 1977; Johansen et al. 2014). This filtration process will lead to discontinuous grain populations in the radial direction, with small grains in

the inner disk and larger grains outward. Recently, Pinilla et al. (2016) studied partial filtration of dust particles to explain the survival of the inner disks in PTDs by combining hydrodynamical simulations of planet–disk interactions with dust evolution models. According to them, in systems forming low-mass planets ($< 1 M_{\text{jup}}$), the micron-sized particles ($\leq 1 \mu\text{m}$) are not perfectly trapped at the outer edge of the planet gap, but in constant movement through the gap via turbulent diffusion. This partial filtration of grains supports a constant replenishment of small dust from the outer to the inner disk. As a consequence, the near-IR excess can remain for up to 5 Myr of evolution, and the SED morphology remains almost identical. They concluded that the near-IR excess that characterizes PTDs is not necessarily an evolutionary effect, but depends on the type of planets sculpting the disks. Our sources are at the upper end of ages studied by Pinilla et al. (2016) (they only considered 1 and 5 Myr old disks); nonetheless, if this effect remains for older disks, which is possible since these disks are still accreting, then the results of Pinilla et al. (2016) suggest that the disks studied here could be forming low-mass planets.

Some of our targets exhibit strong silicate emission. The silicate feature at 10 μm carries vital information of the submicron grains left over inside the gaps and holes of PTDs/TDs. In particular, it carries information on dust processing in the inner disk through the presence of crystalline material. For the two sources with IRS spectra, we were able to estimate the general composition of dust grains producing the silicate characteristic emission. CVSO-109 has no signs of crystalline silicates, while CVSO-107 exhibits some degree of dust processing with small amounts of enstatite and forsterite crystals. This variety of dust properties for objects of the same region is hard to explain and might indicate some correlation between the processes that create the optically thin dust with disk local conditions, e.g., density and temperature, over time. The presence or absence of crystals inside disk cavities sets important constraints to the density and temperature profiles of the small dust (coupled to the gas) that will probably end up forming planets and thus setting their properties.

Total disk masses of the two targets with SMA fluxes are greater than $10 M_{\text{jup}}$, the minimum-mass solar nebula (Weidenschilling 1977). However, these masses are estimated assuming a dust-to-gas mass ratio of 0.0065. If one considers larger dust-to-gas mass ratios, which are expected in older star-forming regions, these values can easily drop below a few Jupiter masses. Moreover, dust disk masses for these objects are small and well below the minimum mass of solids needed to form the planets in our solar system (Weidenschilling 1977). This is consistent with previous studies in other star-forming regions indicating that disks older than 5 Myr lack sufficient dust to form giant planet cores and therefore that timescales for giant planet formation must be quite short (Carpenter et al. 2014; Barenfeld et al. 2016, 2017).

5. Summary and Conclusions

We present *Herschel* PACS fluxes at 70 and 160 μm and CanariCam 10 μm photometry of eight CTTs in the Orion OB1a and OB1b subassociations. We combined the *Herschel* data with optical *UBVRI*, near- and mid-IR, and submillimeter photometry and mid-IR spectra from *Spitzer*, when available, to construct the SEDs of these sources, which we modeled with irradiated accretion disk models (D’Alessio et al. 2006). Our main conclusions are as follows:

1. The best-fit models to the SEDs of the targets indicate that all are PTDs/TDs, with some amount of optically thin dust inside their cavities. PACS photometry was particularly useful to characterize the inner edge of the outer disks. Full-disk models cannot produce enough emission at $10\ \mu\text{m}$ to explain the CanariCam photometry or the *Spitzer* IRS spectra.
2. The IRS spectra of CVSO-107 and CVSO-109 can be explained with small grains mostly composed of amorphous silicates. The silicate feature of CVSO-109 resembles that of a pristine spectrum with no signs of dust grain processing. In contrast, the IRS spectrum of CVSO-107 is better described with the presence of enstatite and forsterite crystals in its optically thin dust mixture.
3. The presence of near-IR excess in the SEDs of our 4–10 Myr PTD sample may point to low-mass ($<1 M_{\text{jup}}$) planet formation. According to Pinilla et al. (2016), the survival and maintenance of the inner disk could be explained by partial filtration of dust, in which the micron-sized grains pass through the gap, supporting a constant replenishment of dust from the outer to the inner disk.
4. Our inferred dust disk masses, M_{dust} , are less than the minimum mass of solids needed to form the planets in our solar system. This is consistent with previous studies on disk populations older than 5 Myr, giving support to the scenario of short timescales for giant planet formation.

We thank the referee for the helpful comments that improved the content and presentation of this work. We also thank the observers who were involved in acquiring one or more sets of observations.

K.M. acknowledges a scholarship from CONACYT.

C.C.E. was supported by the National Science Foundation under grant no. AST-1455042.

These results made use of the Discovery Channel Telescope at Lowell Observatory, supported by Discovery Communications, Inc., Boston University, the University of Maryland, the University of Toledo, and Northern Arizona University. The Submillimeter Array is a joint project between the Smithsonian Astrophysical Observatory and the Academia Sinica Institute of Astronomy and Astrophysics and is funded by the Smithsonian Institution and the Academia Sinica. The authors wish to recognize and acknowledge the very significant cultural role and reverence that the summit of Maunakea has always had within the indigenous Hawaiian community. We are most fortunate to have the opportunity to conduct observations from this mountain.

Funding for SDSS-III has been provided by the Alfred P. Sloan Foundation, the Participating Institutions, the National Science Foundation, and the U.S. Department of Energy Office of Science. The SDSS-III website is <http://www.sdss3.org/>. SDSS-III is managed by the Astrophysical Research Consortium for the Participating Institutions of the SDSS-III Collaboration, including the University of Arizona, the Brazilian Participation Group, Brookhaven National Laboratory, Carnegie Mellon University, University of Florida, the French Participation Group, the German Participation Group, Harvard University, the Instituto de Astrofísica de Canarias, the Michigan State/Notre Dame/JINA Participation Group, Johns Hopkins University, Lawrence Berkeley National Laboratory, Max Planck Institute for Astrophysics, Max Planck Institute for

Extraterrestrial Physics, New Mexico State University, New York University, Ohio State University, Pennsylvania State University, University of Portsmouth, Princeton University, the Spanish Participation Group, University of Tokyo, University of Utah, Vanderbilt University, University of Virginia, University of Washington, and Yale University.

This research has made use of the NASA/IPAC Infrared Science Archive, which is operated by the Jet Propulsion Laboratory, California Institute of Technology, under contract with the National Aeronautics and Space Administration.

This publication makes use of data products from the Two Micron All Sky Survey, which is a joint project of the University of Massachusetts and the Infrared Processing and Analysis Center/California Institute of Technology, funded by the National Aeronautics and Space Administration and the National Science Foundation.

J.B.-P. acknowledges UNAM-PAPIIT grant no. IN110816 and UNAM's DGAPA-PASPA Sabbatical program.

J.H. acknowledges UNAM-PAPIIT grant no. IA103017.

The grid of accretion disk models used in the present work has been calculated using the supercomputers Miztli, at DGTIC, provided by UNAM, and Mouruka, at IRyA, provided by CONACyT grant number INFR-2015-01-252629.

Software: Astropy (Astropy Collaboration et al. 2013), Matplotlib (Barrett et al. 2005), HIPE (Ott 2010), RedCan (González-Martín et al. 2013), IRAF (Davis 1999), MIRIAD (<http://www.cfa.harvard.edu/cqi/mircook.html>), SMART (Higdon et al. 2004).

Facilities: Herschel(PACS), GTC(CanariCam), SMA, OANSPM:0.8 m, DCT(LMI), *Spitzer*(IRS), *WISE*, Sloan, CTIO:2MASS.

ORCID iDs

Karina Maucó <https://orcid.org/0000-0001-8284-4343>
 Jesús Hernández <https://orcid.org/0000-0001-9797-5661>
 Omaira González <https://orcid.org/0000-0002-2356-8358>
 Catherine C. Espaillat <https://orcid.org/0000-0001-9227-5949>
 Juan José Downes <https://orcid.org/0000-0001-6559-2578>
 Enrique Macías <https://orcid.org/0000-0003-1283-6262>
 Babar Ali <https://orcid.org/0000-0002-4659-4700>

References

- ALMA Partnership, Brogan, C. L., Pérez, L. M., et al. 2015, *ApJL*, **808**, L3
 Alonso-Herrero, A., Esquej, P., Roche, P. F., et al. 2016, *MNRAS*, **455**, 563
 Andrews, S. M., Rosenfeld, K. A., Wilner, D. J., & Bremer, M. 2011a, *ApJL*, **742**, L5
 Andrews, S. M., & Williams, J. P. 2005, *ApJ*, **631**, 1134
 Andrews, S. M., Wilner, D. J., Espaillat, C., et al. 2011b, *ApJ*, **732**, 42
 Andrews, S. M., Wilner, D. J., Hughes, A. M., Qi, C., & Dullemond, C. P. 2009, *ApJ*, **700**, 1502
 Andrews, S. M., Wilner, D. J., Zhu, Z., et al. 2016, *ApJL*, **820**, L40
 Astropy Collaboration, Robitaille, T. P., Tollerud, E. J., et al. 2013, *A&A*, **558**, A33
 Bally, J. 2008, in *Handbook of Star Forming Regions, Volume I: The Northern Sky ASP Monograph Publications*, ed. B. Reipurth (Vol. 4; San Francisco, CA: ASP), 459
 Baraffe, I., Chabrier, G., Allard, F., & Hauschildt, P. H. 1998, *A&A*, **337**, 403
 Barenfeld, S. A., Carpenter, J. M., Ricci, L., & Isella, A. 2016, *ApJ*, **827**, 142
 Barenfeld, S. A., Carpenter, J. M., Sargent, A. I., Isella, A., & Ricci, L. 2017, *ApJ*, **851**, 85
 Barrett, P., Hunter, J., Miller, J. T., Hsu, J.-C., & Greenfield, P. 2005, in *ASP Conf. Ser. 347, Astronomical Data Analysis Software and Systems XIV*, ed. P. Shopbell, M. Britton, & R. Ebert (San Francisco, CA: ASP), 91
 Beckwith, S. V. W., Sargent, A. I., Chini, R. S., & Guesten, R. 1990, *AJ*, **99**, 924

- Begemann, B., Dorschner, J., Henning, T., Mutschke, H., & Thamm, E. 1994, *ApJL*, **423**, L71
- Briceno, C. 2008, in *Handbook of Star Forming Regions, Volume I: The Northern Sky ASP Monograph Publications*, ed. B. Reipurth (Vol. 4; San Francisco, CA: ASP), 838
- Briceño, C., Calvet, N., Hernández, J., et al. 2005, *AJ*, **129**, 907
- Briceño, C., Hartmann, L., Hernández, J., et al. 2007, *ApJ*, **661**, 1119
- Brown, J. M., Blake, G. A., Qi, C., et al. 2009, *ApJ*, **704**, 496
- Calvet, N., D'Alessio, P., Hartmann, L., et al. 2002, *ApJ*, **568**, 1008
- Calvet, N., D'Alessio, P., Watson, D. M., et al. 2005, *ApJL*, **630**, L185
- Calvet, N., & Gullbring, E. 1998, *ApJ*, **509**, 802
- Carpenter, J. M., Mamajek, E. E., Hillenbrand, L. A., & Meyer, M. R. 2006, *ApJL*, **651**, L49
- Carpenter, J. M., Mamajek, E. E., Hillenbrand, L. A., & Meyer, M. R. 2009, *ApJ*, **705**, 1646
- Carpenter, J. M., Ricci, L., & Isella, A. 2014, *ApJ*, **787**, 42
- Carasco-González, C., Henning, T., Chandler, C. J., et al. 2016, *ApJL*, **821**, L16
- Cohen, M., Walker, R. G., Carter, B., et al. 1999, *AJ*, **117**, 1864
- D'Alessio, P., Calvet, N., Hartmann, L., Franco-Hernández, R., & Servín, H. 2006, *ApJ*, **638**, 314
- D'Alessio, P., Calvet, N., Hartmann, L., Muzerolle, J., & Sitko, M. 2004, in *IAU Symp. 221, Star Formation at High Angular Resolution*, ed. M. G. Burton, R. Jayawardhana, & T. L. Bourke (Cambridge: Cambridge Univ. Press), 403
- D'Alessio, P., Hartmann, L., Calvet, N., et al. 2005, *ApJ*, **621**, 461
- Davis, L. E. 1999, in *ASP Conf. Ser. 189, Precision CCD Photometry*, ed. E. R. Craine, D. L. Crawford, & R. A. Tucker (San Francisco, CA: ASP), 35
- de Juan Ovelar, M., Pinilla, P., Min, M., Dominik, C., & Birnstiel, T. 2016, *MNRAS*, **459**, L85
- Dipierro, G., & Laibe, G. 2017, *MNRAS*, **469**, 1932
- Dodson-Robinson, S. E., & Salyk, C. 2011, *ApJ*, **738**, 131
- Dong, R., Li, S., Chiang, E., & Li, H. 2017, *ApJ*, **843**, 127
- Dorschner, J., Begemann, B., Henning, T., Jaeger, C., & Mutschke, H. 1995, *A&A*, **300**, 503
- Draine, B. T., & Lee, H. M. 1984, *ApJ*, **285**, 89
- Espaillet, C., Calvet, N., D'Alessio, P., et al. 2007, *ApJL*, **670**, L135
- Espaillet, C., Calvet, N., Luhman, K. L., Muzerolle, J., & D'Alessio, P. 2008a, *ApJL*, **682**, L125
- Espaillet, C., D'Alessio, P., Hernández, J., et al. 2010, *ApJ*, **717**, 441
- Espaillet, C., Furlan, E., D'Alessio, P., et al. 2011, *ApJ*, **728**, 49
- Espaillet, C., Muzerolle, J., Hernández, J., et al. 2008b, *ApJL*, **689**, L145
- Espaillet, C., Muzerolle, J., Najita, J., et al. 2014, in *Protostars and Planets VI*, ed. H. Beuther et al. (Tucson, AZ: Univ. Arizona Press), 497
- Fazio, G. G., Hora, J. L., Allen, L. E., et al. 2004, *ApJS*, **154**, 10
- Fischer, W. J., Megeath, S. T., Stutz, A. M., et al. 2013, *AN*, **334**, 53
- Flock, M., Ruge, J. P., Dzyurkevich, N., et al. 2015, *A&A*, **574**, A68
- Follette, K., Close, L., Males, J., et al. 2015, *BAAS*, **47**, 6
- Fouchet, L., Maddison, S. T., Gonzalez, J.-F., & Murray, J. R. 2007, *A&A*, **474**, 1037
- Furlan, E., Hartmann, L., Calvet, N., et al. 2006, *ApJS*, **165**, 568
- González-Martín, O., Rodríguez-Espinosa, J. M., Díaz-Santos, T., et al. 2013, *A&A*, **553**, A35
- Hernández, J., Calvet, N., Briceño, C., et al. 2007a, *ApJ*, **671**, 1784
- Hernández, J., Calvet, N., Perez, A., et al. 2014, *ApJ*, **794**, 36
- Hernández, J., Hartmann, L., Megeath, T., et al. 2007b, *ApJ*, **662**, 1067
- Higdon, S. J. U., Devost, D., Higdon, J. L., et al. 2004, *PASP*, **116**, 975
- Hildebrand, R. H. 1983, *QJRAS*, **24**, 267
- Huélamo, N., Lacour, S., Tuthill, P., et al. 2011, *A&A*, **528**, L7
- Hughes, A. M., Andrews, S. M., Espaillat, C., et al. 2009, *ApJ*, **698**, 131
- Ingleby, L., Calvet, N., Herczeg, G., et al. 2013, *ApJ*, **767**, 112
- Ingleby, L., Calvet, N., Hernández, J., et al. 2014, *ApJ*, **790**, 47
- Isella, A., Natta, A., Wilner, D., Carpenter, J. M., & Testi, L. 2010, *ApJ*, **725**, 1735
- Johansen, A., Blum, J., Tanaka, H., et al. 2014, in *Protostars and Planets VI*, ed. H. Beuther et al. (Tucson, AZ: Univ. Arizona Press), 547
- Kenyon, S. J., & Hartmann, L. 1995, *ApJS*, **101**, 117
- Kraus, A. L., Ireland, M. J., Martinache, F., & Hillenbrand, L. A. 2011, *ApJ*, **731**, 8
- Luhman, K. L., & Mamajek, E. E. 2012, *ApJ*, **758**, 31
- Mamajek, E. E., Lawson, W. A., & Feigelson, E. D. 1999, *ApJL*, **516**, L77
- Mathis, J. S. 1990, *ARA&A*, **28**, 37
- Mathis, J. S., Rumpl, W., & Nordsieck, K. H. 1977, *ApJ*, **217**, 425
- Maucó, K., Hernández, J., Calvet, N., et al. 2016, *ApJ*, **829**, 38
- McClure, M. K., D'Alessio, P., Calvet, N., et al. 2013, *ApJ*, **775**, 114
- McClure, M. K., Furlan, E., Manoj, P., et al. 2010, *ApJS*, **188**, 75
- McClure, M. K., Manoj, P., Calvet, N., et al. 2012, *ApJL*, **759**, L10
- Muench, A., Getman, K., Hillenbrand, L., & Preibisch, T. 2008, in *Handbook of Star Forming Regions, Volume I: The Northern Sky ASP Monograph Publications*, ed. B. Reipurth (Vol. 4; San Francisco, CA: ASP), 483
- Muzerolle, J., Hillenbrand, L., Calvet, N., Briceño, C., & Hartmann, L. 2003, *ApJ*, **592**, 266
- Nielbock, M., Müller, T., Klaas, U., et al. 2013, *ExA*, **36**, 631
- Nomura, H., Tsukagoshi, T., Kawabe, R., et al. 2016, *ApJL*, **819**, L7
- Ott, S. 2010, in *ASP Conf. Ser. 434, Astronomical Data Analysis Software and Systems XIX*, ed. Y. Mizumoto, K.-I. Morita, & M. Ohishi (San Francisco, CA: ASP), 139
- Paardekooper, S. J., & Mellema, G. 2004, in *ASP Conf. Ser. 321, Extrasolar Planets: Today and Tomorrow*, ed. J. Beaulieu, A. Lecavelier Des Etangs, & C. Terquem (San Francisco, CA: ASP), 347
- Paardekooper, S.-J., & Mellema, G. 2006, *A&A*, **453**, 1129
- Pecaut, M. J., & Mamajek, E. E. 2013, *ApJS*, **208**, 9
- Pecaut, M. J., & Mamajek, E. E. 2016, *MNRAS*, **461**, 794
- Petr-Gotzens, M., Alcalá, J. M., Briceño, C., et al. 2011, *Msngr*, **145**, 29
- Pinilla, P., de Juan Ovelar, M., Ataiee, S., et al. 2015, *A&A*, **573**, A9
- Pinilla, P., Klarman, L., Birnstiel, T., et al. 2016, *A&A*, **585**, A35
- Pollack, J. B., Hollenbach, D., Beckwith, S., et al. 1994, *ApJ*, **421**, 615
- Preibisch, T., & Mamajek, E. 2008, in *Handbook of Star Forming Regions, Vol. 2: The Southern Sky*, ed. B. Reipurth (San Francisco, CA: ASP), 235
- Rice, W. K. M., Armitage, P. J., Wood, K., & Lodato, G. 2006, *MNRAS*, **373**, 1619
- Rieke, G. H., Young, E. T., Engelbracht, C. W., et al. 2004, *ApJS*, **154**, 25
- Roussel, H. 2012, *PASP*, **125**, 1126
- Sallum, S., Eisner, J., Close, L. M., et al. 2016, *Proc. SPIE*, **9907**, 99070D
- Sallum, S., Follette, K. B., Eisner, J. A., et al. 2015, *Natur*, **527**, 342
- Sargent, B. A., Forrest, W. J., Tayrien, C., et al. 2009, *ApJS*, **182**, 477
- Schlegel, D. J., Finkbeiner, D. P., & Davis, M. 1998, *ApJ*, **500**, 525
- Schwarz, K. R., Bergin, E. A., Cleeves, L. I., et al. 2016, *ApJ*, **823**, 91
- Shakura, N. I., & Sunyaev, R. A. 1973, in *IAU Symp. 55, X- and Gamma-Ray Astronomy*, ed. H. Bradt & R. Giacconi (Dordrecht: Reidel), 155
- Siess, L., Dufour, E., & Forestini, M. 2000, *A&A*, **358**, 593
- Sivia, D., & Skilling, J. 2012, *Data Analysis: A Bayesian Tutorial* (Oxford: Oxford Univ. Press), 246
- Skrutskie, M. F., Cutri, R. M., Stiening, R., et al. 2006, *AJ*, **131**, 1163
- Skrutskie, M. F., Dutkevitch, D., Strom, S. E., et al. 1990, *AJ*, **99**, 1187
- Strom, K. M., Strom, S. E., Edwards, S., Cabrit, S., & Skrutskie, M. F. 1989, *AJ*, **97**, 1451
- Telesco, C. M., Ciardi, D., French, J., et al. 2003, *Proc. SPIE*, **4841**, 913
- Thanathibodee, T., Calvet, N., Herczeg, G., et al. 2018, *ApJ*, submitted
- Uchida, K. I., Calvet, N., Hartmann, L., et al. 2004, *ApJS*, **154**, 439
- van Boekel, R., Henning, T., Menu, J., et al. 2017, *ApJ*, **837**, 132
- van Dishoeck, E. F., van der Marel, N., Bruderer, S., & Pinilla, P. 2015, in *ASP Conf. Ser. 499, Revolution in Astronomy with ALMA: The Third Year*, ed. D. Iono et al. (San Francisco, CA: ASP), 281
- Warren, S. G. 1984, *ApOpt*, **23**, 1206
- Watson, D. M., Leisenring, J. M., Furlan, E., et al. 2009, *ApJS*, **180**, 84
- Webb, R. A., Zuckerman, B., Platais, I., et al. 1999, *ApJL*, **512**, L63
- Weidenschilling, S. J. 1977, *Ap&SS*, **51**, 153
- Werner, M. W., Roellig, T. L., Low, F. J., et al. 2004, *ApJS*, **154**, 1
- White, R. J., & Basri, G. 2003, *ApJ*, **582**, 1109
- Wright, E., Eisenhardt, P., Mainzer, A., et al. 2010, *AJ*, **140**, 1868
- Zhang, K., Blake, G. A., & Bergin, E. A. 2015, *ApJL*, **806**, L7
- Zhu, Z., Nelson, R. P., Dong, R., Espaillat, C., & Hartmann, L. 2012, *ApJ*, **755**, 6
- Zhu, Z., Nelson, R. P., Hartmann, L., Espaillat, C., & Calvet, N. 2011, *ApJ*, **729**, 47

5.3 Article 3

5.3.1 Abstract

Presentamos un modelaje detallado de la distribución espectral de energía de la estrella de masa intermedia (IMTTS, por sus siglas en inglés) SO 411. Un análisis astrométrico y cinemático de la fuente muestra que puede estar asociada a la población dispersa ubicada en frente del cúmulo de σ Ori. Nuestro modelaje indica que SO 411 está rodeada por un disco en transición con polvo ópticamente delgado dentro de la cavidad de ~ 11 AU de tamaño, mientras que aún está acreutando masa a la estrella. A través del modelado detallado de las bandas de silicatos a $10 \mu\text{m}$ y $20 \mu\text{m}$ obtuvimos que la mitad de los silicatos presentes en el disco son amorfos (30% olivinos y 20% piroxenos) mientras que el resto está constituido por un 20% de forsterita, 5% de enstatita y 25% de silica. El espectro PAH de SO 411 es consistente con su estado intermedio entre las estrellas Herbig Ae calientes y luminosas y las estrellas T Tauri menos masivas y más frías. Análisis del rasgo PAH a $7.7 \mu\text{m}$ indica que todavía hay presencia de PAHs pequeños en el disco de SO 411.

A TRANSITIONAL DISK AROUND AN INTERMEDIATE MASS STAR IN THE SPARSE POPULATION OF THE ORION OB1 ASSOCIATION

ALICE PÉREZ-BLANCO,¹ KARINA MAUCÓ,² JESÚS HERNÁNDEZ,³ NURIA CALVET,⁴ CATHERINE ESPAILLAT,⁵ MELISSA MCCLURE,⁶ CESAR BRICEÑO,⁷ CONNOR ROBINSON,⁵ DANIEL FELDMAN,⁵ AND LUIS VILLARREAL⁸

¹*University of Leeds, School of Physics and Astronomy, LS29JT, Leeds, UK.*

²*Instituto de Radioastronomía y Astrofísica (IRyA), Universidad Nacional Autónoma de México, Morelia, Mexico*

³*Instituto de Astronomía, Universidad Nacional Autónoma de México, Ensenada, BC, Mexico*

⁴*Department of Astronomy, University of Michigan, 500 Church Street, Ann Arbor, MI 48109, USA*

⁵*Department of Astronomy, Boston University, 725 Commonwealth Avenue, Boston, MA 02215, USA*

⁶*Anton Pannekoek Institute for Astronomy, University of Amsterdam, Science Park 904, 1098 XH Amsterdam, The Netherlands*

⁷*Cerro Tololo Interamerican Observatory, Casilla 603, la Serena, Chile*

⁸*Postgrado de Física Fundamental, Universidad de Los Andes, Mérida, Venezuela*

(Received 2018; Revised 2018; Accepted)

ABSTRACT

We present a detailed irradiated disk model for the spectral energy distribution of the intermediate mass T Taur star SO 411. An astrometric and kinematic analysis indicates that SO 411 could be associated with a sparse stellar population located in front of the σ Orionis cluster. Our modeling indicates that SO 411 is surrounded by a transitional disk with optically thin dust inside a dust cavity of radius ~ 11 AU, while still accreting mass onto the star. Detailed modeling of the 10 and 20 μm silicate features indicates that half of the silicates are amorphous (30% of olivine and 20% of pyroxene) while the remaining are 20% forsterite, 5% enstatite and 25% silica. The PAH spectrum of SO 411 is consistent with his intermediate state between the hot and luminous Herbig Ae and the less massive and cooler T Tauri stars. Analysis of the 7.7 μm PAH feature indicates that small PAHs still remain in the SO 411 disk.

Keywords: open clusters and associations: individual σ Orionis — stars:pre-main sequence — accretion disks

1. INTRODUCTION

Circumstellar disks, a natural byproduct of the star forming process, exhibit a variety of characteristics that have been attributed to different evolutionary stages. Starting with optically thick flared disks, they evolve into dusty second generation debris disks and eventually go on to form planetary systems (e.g. Calvet & D’Alessio 2011; Williams & Cieza 2011; Testi et al. 2014; Alexander et al. 2014). A crucial phase is represented by stars with transitional disks (TD; Strom et al. 1989; Calvet et al. 2005) or pre-transitional disks (PTD; Espaillat et al. 2007a,b). TD are observationally characterized as having little or no excess above the photosphere in the near infrared (NIR; $\lesssim 10\mu\text{m}$) and excesses consistent with primordial disks at longer wavelengths (D’Alessio 2009; Espaillat et al. 2014), while PTD still show some flux excess at the shorter NIR wavelengths. The presence of large holes (in TD) or wide gaps (in PTD) in the inner dust distribution of protoplanetary disks, which explains the deficit of NIR excesses in the spectral energy distribution (SED), is been supported by millimeter interferometric observations showing a dust-depleted region in the inner part of the disk (Andrews et al. 2011; Casassus 2016). These holes and gaps have been interpreted as footprints of a dynamical clearing mechanism in which the disk interacts with planets or companions (Zhu et al. 2011, 2012; Espaillat et al. 2014; Owen 2016; Ruíz-Rodríguez et al. 2016). However, other non-dynamical clearing mechanisms such as photoevaporation, viscous evolution, dust grain growth and dead zones have been invoked to explain these dust discontinuities in protoplanetary disks (e.g. Alexander et al. 2014; Chiang & Murray-Clay 2007; Dullemond & Dominik 2005; Birnstiel et al. 2012; Pinilla et al. 2016).

Intermediate Mass T Tauri Stars (IMTTS; Calvet et al. 2004), showing emission lines and spectral types ranging from late F to early K, represent the link between Herbig Ae/Be stars (HAeBe; with spectral types B, A or early F) and Classical T Tauri stars (CTTS; with spectral types K or M). Since IMTTS evolve along radiative tracks, they will eventually become HAeBe stars, Vega type stars, or hybrid disks around A type stars such as those reported by Péricaud et al. (2017). This last class of objects, which have gas to dust ratio enhanced by two or three orders of magnitudes compared to primordial disks, could represent the last bridge between the final stages of the primordial component in the disks and the beginning of the debris disk phase (Péricaud et al. 2017; Espaillat et al. 2017).

The TD/PTD phase in CTTS represents one of the evolutionary pathways from primordial to second generation disks (e.g. Currie et al. 2009; Hernández et al. 2010; Cieza et al. 2013). The number ratio of transitional disks to primordial disks around T Tauri stars suggests a timescale of transitional disks clearing of 10%-20% of the lifetime of primordial disks

(Muzerolle et al. 2010; Luhman et al. 2010). Moreover, the disk dispersal mechanisms are more efficient at higher stellar masses (Hernández et al. 2007, 2009; Lada et al. 2006; Sung et al. 2009; Ribas et al. 2015). Thus, it is not surprising that less than 10% of the known TD/PTD are in the IMTTS regime and only $\sim 2\%$ are associated to late F type stars (Espaillat et al. 2014; van der Marel et al. 2016). An alternative evolutionary pathway is represented by evolved disks (Hernández et al. 2010; Muzerolle et al. 2010; Ercolano & Pascucci 2017), which exhibit overall weaker infrared excesses than the median SED of Taurus (Furlan et al. 2006).

Meeus et al. (2001) classified the SEDs of HAeBe stars into group I and group II, in which group I shows stronger mid and far infrared excesses compared with those of group II. Dullemond & Dominik (2004) suggest an evolutionary scheme from group I (flared disks) to group II (flat disks). In support of this suggestion, using on Herschel/PACS photometry, Pascual et al. (2016) propose that a higher amount of small dust grains in group I can explain the Meuss’s classification supporting an evolution from group I to group II. However, Maaskant et al. (2013) propose that group I of HAeBe stars may have a dust depleted inner region similar to that observed in PTD/TD, and thus, it is unlikely that group I (with inner holes) can evolve to group II (without inner holes). On the other hand, the recent discovery of cavities in large grains in the disks of group II sources (Zhang et al. 2016; Rubinstein et al. 2018) adds another uncertainty to these alternatives. Therefore, additional studies are necessary to reveal whether group I and group II form an evolutionary sequence or if these two groups follow different evolutionary pathways as those suggested for the CTTS mass range. Since IMTTS represent a bridge in mass between CTTS and HAeBe stars, detailed studies of TD/PTD around IMTTS could improve the understanding of the evolutionary process connecting the two ranges of stellar masses.

SO 411 (also named HD 294268, BD-02 1321, PDS 119) is a F type IMTTS believed until now to belong to the σ Orionis cluster (Torres et al. 1995; Caballero 2008; Hernández et al. 2014). However, the general region of the σ Orionis cluster can include stars from a foreground pre-main sequence stellar population kinematically separated by $\sim 7 \text{ km s}^{-1}$ in radial velocity (Jeffries et al. 2006; Maxted et al. 2008; Hernández et al. 2014). This foreground stellar population could have a median age and distance similar to older stellar groups associated with the sparser Orion OB1a subassociation (Briceño et al. 2007, 2018). Here, we present a spatial and kinematical analysis based on GAIA data that indicates that SO 411 most likely belongs to this foreground population.

The SED constructed from Spitzer photometry (IRAC and MIPS) indicates that SO 411 is surrounded by a TD/PTD disk (Hernández et al. 2007). The width of H α at 10% of the line peak ($\sim 294 \text{ km/s}$; Hernández et al. 2014) indicates that the

Table 1. DCT optical photometry

Object	U	B	V	R	I
	mag	mag	mag	mag	mag
SO 411	11.07	10.96	10.50	10.08	9.84

SO 411 disk is accreting mass onto the star (White & Basri 2003). Finally, its location in the region of PAH emission-dominated sources in IRAC color-color diagrams (Hernández et al. 2007; Gutermuth et al. 2009) suggests that SO 411 has PAH emission features. Visual inspection of the Spitzer IRS spectrum confirms the presence of PAH emission features and also shows silicate emission at $10\mu\text{m}$ indicating the presence of sub- μm grains close to the star (Sargent et al. 2009b). Thus, SO 411 represents an unique opportunity to study in detail an accreting TD/PTD around an IMTTS that shows evidence of small dust close to the star.

We present a detailed modeling of SO 411 using irradiated disks models (D’Alessio et al. 1998, 1999, 2001, 2006; Espaillat et al. 2010), which allows us to study the dust structure and mineralogy of its disk. This paper is organized as follows: Section §2 describes the observational data. Based on the second release of GAIA’s data (GAIA-DR2; Gaia Collaboration et al. 2018), we present the astrometric and kinematic properties of SO 411 and the σ Orionis cluster in §3.2. Additional properties of the target are analyzed in §3.3, a near infrared excess study in §3.5, and the disk modeling in §3.6. We then discuss the implications of the dust composition in §4.1 and the presence of PAH features in §4.2. Finally, in Section §5 we present our summary and conclusions.

2. OBSERVATIONS

2.1. Photometric data

We obtained optical photometry of SO 411 on February 2016 using the Large Monolithic Imager on the 4.3 meter Discovery Channel Telescope (DCT) at the Lowell Observatory (Arizona - USA). The images were reduced following the standard IRAF procedure to perform bias subtraction and sky-flat field correction. The photometry was obtained and calibrated following the procedure in Massey & Davis (1992) using the Landolt standard field SA 98 (Landolt 2009) observed at the same airmass as the target field (~ 1.35). Table 1 shows the optical photometric data of SO 411. The photometric uncertainties are below 0.02 magnitudes.

2.2. IRS Spectra

SO 411 was observed with the Infrared Spectrograph (IRS) on board the Spitzer Space Telescope (Houck et al. 2004) on

2007 October 11 as part of the program P30381 (Oliveira et al. 2006). Observations were obtained in staring mode using the short-low (SL) resolution module which spans wavelengths from 5 to $14\mu\text{m}$ and the high resolution modules (SH and LH) which span wavelengths from 10 to $37\mu\text{m}$. The SL spectrum was obtained from the Cornell Atlas of Spitzer/IRS Sources (CASSIS; Leboutteiller et al. 2011). The reduction and extraction of the LH & SH data was performed with optimal point source extraction option in the Spectral Modeling, Analysis and Reduction Tool (SMART; Higdon et al. 2004), which is an IDL-based processing and analysis tool for the IRS instrument.

2.3. SpeX Spectra

We obtained NIR spectra of SO 411 on 2015, February 6 using the micron medium-resolution spectrograph SpeX on the 3 meter NASA Infrared Telescope Facility (IRTF) at Mauna Kea Observatory. The spectra were obtained using the LXD long mode with a $0.5\times 15''$ slit and a wavelength coverage of $1.9\text{--}4.6\mu\text{m}$, giving a spectral resolution of $R\approx 1500$, and using the lower resolution prism mode with a $3.0\times 15''$ slit with wavelength coverage of $0.8\text{--}2.5\mu\text{m}$, with $R\approx 75$. The spectra were collected using the AB dither mode, in which the source is offset between two locations on the slit between the A and B exposure in order to subtract out sky emission and dark current for each AB spectra pair.

We reduced the observation using the 2014 version of the SpexTool, an IDL-based reduction package built specifically for the cross-dispersed spectra produced by SpeX (Cushing et al. 2004). The reduction process consisted of flat-fielding, sky corrections and wavelength calibration using calibration frames taken during observations. Each order for every observation was extracted, stacked, corrected for telluric absorption features using the measured spectra of a standard A0V star and then stitched together to form a complete spectrum. Regions of low signal-to-noise were removed from the final spectra. A more complete description of the SpexTool reduction process is described in Cushing et al. (2004). HD 34317 was the telluric A0V star used for the reduction of the SpeX spectra.

3. ANALYSIS

3.1. Spectral Type

Here we revisited the optical spectrum from Hernández et al. (2014) to improve the spectral type of SO 411 obtained using the SPTCLASS tool, an IRAF/IDL code based on the methods described by Hernández et al. (2004). The low resolution optical spectrum was obtained with the Boller & Chivens spectrograph mounted on the 2.1 meter telescope at the San Pedro Martir Observatory. We used a 400 lines mm^{-1} dispersion grating along with a $2''$ slit width, giving a spec-

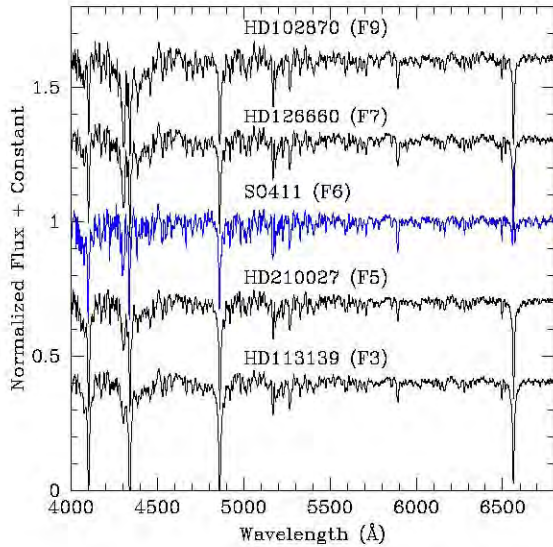


Figure 1. Spectra of SO 411 compared to spectral type standards. Visual inspection and measured spectroscopic features indicate an spectral type of $F6 \pm 1$.

tral resolution of $\sim 6\text{\AA}$ centered at $\sim 5500\text{\AA}$ (for additional details, see [Hernández et al. 2014](#)).

Figure 1 shows a comparison between the SO 411 spectrum and a group of standard spectra with similar resolution and spectral coverage obtained with the FAST spectrograph ([Fabricant et al. 1998](#)) mounted on the 1.5 meter telescope of the Fred Lawrence Whipple Observatory and used to calibrate the SPTCLASS tool. In a previous effort we had estimated the spectral type of SO 411 as $F7.5 \pm 2.5$ ([Hernández et al. 2014](#)). In order to reduce the uncertainty, we estimate a new spectral type using only the strongest spectral features that appear in IMTTS, such as the G-band ($\lambda 4300\text{\AA}$), Mn I+Fe I ($\lambda 4458\text{\AA}$), Fe I ($\lambda 5329\text{\AA}$), Ca I ($\lambda 5589\text{\AA}$), and Mn I ($\lambda 6015\text{\AA}$). The improved spectral type of $F6 \pm 1$ is in agreement with the previous estimate within the uncertainties.

3.2. Space-velocity analysis of SO 411

Here we study the astrometric and kinematic properties of SO 411 and the σ Orionis cluster. For a sample of known young stars defined in [Hernández et al. \(2014\)](#), we combined the parallaxes and proper motions from the GAIA-DR2 ([Gaia Collaboration et al. 2018](#)) with radial velocities (RVs) from [Maxted et al. \(2008\)](#), [Sacco et al. \(2008\)](#) and [Hernández et al. \(2014\)](#). For those stars with more than one measurements of RVs, we used a weighted mean to estimate the combined RV of the star. We selected stars with uncertainties in parallaxes better than 20%. For stars with uncertainties larger than this value, we cannot apply the inverse relation between parallaxes and distances and the estimation of distances becomes an inference problem in which the use of prior assumptions is necessary ([Bailer-Jones 2015](#)). Additionally, we selected

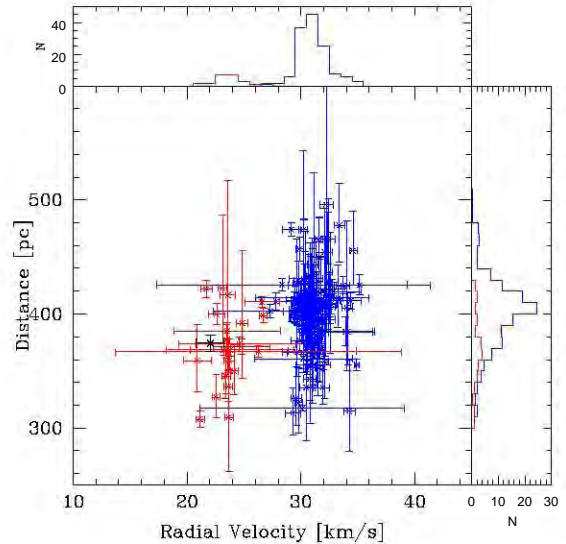


Figure 2. Distance vs. radial velocity for stars in the σ Orionis population (blue dots) and the sparse population (red dots). The black dot indicates the location of the star SO 411. The upper panel and right panel show the RVs distribution and the distance distribution, respectively

stars with distances between 300 pc and 500 pc. About 96% (162/169) of the sample of known young stars with radial velocity measurements fulfill this criterion.

Following [Jeffries et al. \(2006\)](#), we split the sample into two groups. One group (hereafter the σ Orionis population) has radial velocities between 27 km/s and 35 km/s and is consistent with the radial velocity of the central system (29.5 km/s; [Kharchenko et al. 2007](#)). The other group (hereafter the sparse population) has radial velocities between 20 km/s and 27 km/s and could be older and closer than the first population ([Jeffries et al. 2006](#); [Maxted et al. 2008](#); [Hernández et al. 2014](#)).

Figure 2 shows distances versus radial velocities (RVs) for the σ Orionis cluster and the sparse populations in the direction of the cluster. Using weighted means, distances and RVs were estimated for each population. The σ Orionis population has a distance of 401^{+33}_{-28} pc and a RV of 31.1 ± 1.3 km/s. The sparse population has a distance of 382^{+27}_{-23} pc and a RV of 23.6 ± 1.4 km/s. It is apparent that the distance (374 ± 7 pc) and the RV (22.0 ± 1.2 km/s) of SO 411 is in better agreement with the sparse population, which is slightly closer than the σ Orionis population.

Figure 3 shows the vector point diagram for the σ Orionis and the sparse populations. Using weighted mean we estimate the proper motions for the σ Orionis population ($\mu_\alpha = 1.0 \pm 1.8$ and $\mu_\delta = -0.7 \pm 1.8$) and for the sparse population ($\mu_\alpha = 1.1 \pm 1.5$ and $\mu_\delta = -2.1 \pm 3.7$). The proper motions of SO 411 ($\mu_\alpha = 2.0 \pm 0.1$ and $\mu_\delta = -1.6 \pm 0.1$) locate this object in the border of the overdensity of the σ Orionis population. Finally, [Caballero \(2008\)](#) analyzed the spatial distribution of

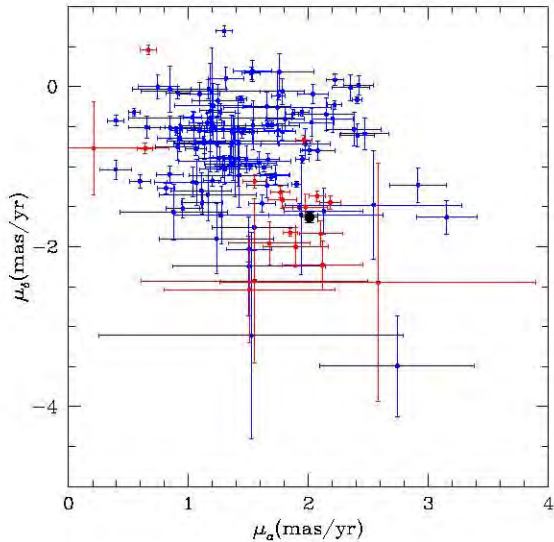


Figure 3. Vector point diagram for the σ Orionis population (blue dots) and for the sparse population (red dots). The black dot indicates the position of SO 411

possible members of the σ Orionis cluster and suggests that this cluster has two components: a dense core that extends from the center to a radius of $20'$, in which most members are located, and a rarefied halo at larger separations. SO 411 is located at $21.4'$ from the center, slightly beyond the dense core limit.

In brief, the astrometric and kinematic properties of SO 411 suggest that this star does not belong to the σ Orionis cluster and it is most likely associated with an older and sparser population located in front of the cluster.

3.3. Stellar properties and mass accretion rate

The effective temperature (T_{eff}), intrinsic colors and the bolometric correction of SO 411 were obtained by interpolating its spectral type in the table of Pecaut & Mamajek (2013) for pre-main sequence stars. Following the method described in Hernández et al. (2014) and using the colors V- I_C and V-J, we calculated an extinction of 0.2 magnitudes in the visual band. Using this value and the reddening law from Mathis (1990, $R_V=3.1$), the observational data described in §2 were corrected for extinction.

Assuming a distance of 374 ± 7 pc (Gaia Collaboration et al. 2018), we found a stellar luminosity (L_*) of $9.1 \pm 0.5 L_\odot$. The uncertainty in L_* is calculated only from the visual photometric error. The stellar mass (M_*) and stellar radius (R_*) were estimated by interpolating the T_{eff} and the L_* in the evolutionary tracks from Siess et al. (2000).

We estimated the accretion luminosity (L_{acc}) from several indicators. Table 2 shows the different values of \dot{M} we obtained. One indicator is the U-band excess, which measures the emission shock at the stellar surface. We used the correlation of this excess with L_{acc} from (Gullbring et al. 1998), and

obtained the mass accretion rate (\dot{M}) using the stellar mass and radius.

The luminosity of the $H\alpha$ line ($L_{H\alpha}$) can also be used as an accretion proxy (e.g. Ingleby et al. 2013; Alcalá et al. 2014; Fairlamb et al. 2017). We estimated this luminosity from the $H\alpha$ equivalent width ($\text{EW}[H\alpha]$), which are obtained by measuring the decrease in flux due to line absorption from the continuum that is expected when interpolating between two adjacent bands (Hernández et al. 2004). The intrinsic value for SO 411 ($\text{EW}[H\alpha]_{\text{std}}$) is obtained by interpolating its spectral type in the values of $\text{EW}[H\alpha]$ obtained for the standard sequence in Figure 1. Assuming no veiling at the continuum of $H\alpha$, the corrected value of SO 411 is obtained by $\text{EW}[H\alpha]_{\text{cor}} = \text{EW}[H\alpha] - \text{EW}[H\alpha]_{\text{std}}$. The flux of $H\alpha$ is calculated by $F_{H\alpha} = \text{EW}[H\alpha]_{\text{cor}} \times F_{\text{cont}}$, where F_{cont} is the continuum flux at 6563\AA obtained by interpolating between the fluxes measured in the filters R_C and I_C . The luminosity of $H\alpha$ follows from the assumed distance. Several correlations between L_{acc} and $L_{H\alpha}$ have been presented in the literature. The correlations by Ingleby et al. (2013) and Alcalá et al. (2014) were based on samples of CTTS, while the correlation by Fairlamb et al. (2017) were based on a sample of Herbig Ae/Be stars. The values of \dot{M} obtained with the different correlations are shown in Table 2. The Herbig Ae/Be correlation results in a higher estimate of \dot{M} than the CTTS correlations, a fact already noted by Fairlamb et al. (2017). The luminosity of $H\alpha$ in SO 411 is $\sim 3.7 \times 10^{-3} L_\odot$, which puts the object in between the lower $L_{H\alpha}$ values of the CTTS and the higher values of the Herbig Ae/Be, so it is not clear which of the two correlations between L_{acc} and $L_{H\alpha}$ is appropriate for SO 411. Given this uncertainty, we adopted as the mass accretion the mean of the values obtained from the two correlations, $\dot{M} \sim 5 \times 10^{-9} M_\odot \text{yr}^{-1}$, which is consistent with the mass accretion rates found in other transitional disks (Espaillat et al. 2014).

3.4. Spectral Energy Distribution

We constructed the spectral energy distribution of SO 411, shown in Figure 4. We used the data described in §2, and magnitudes and fluxes collected from the literature: 2MASS photometry from Cutri et al. (J, H and K bands; 2003), IRAC (3.6, 4.5, 5.8 and $8.0\mu\text{m}$) and MIPS ($24\mu\text{m}$) Spitzer's photometry from Hernández et al. (2007), WISE photometry (3.4, 4.6, 12 and $22\mu\text{m}$) from Cutri et al. (2013), AKARI's fluxes at 9 and $18\mu\text{m}$ from Ishihara et al. (2010) and AKARI's flux at $90\mu\text{m}$ from Yamamura et al. (2010). To cover the millimeter range, we included fluxes at $850\mu\text{m}$ and $1300\mu\text{m}$ obtained with the Submillimeter Common User Bolometer Array (SCUBA-2) camera on the 15-m James Clerk Maxwell Telescope (Williams et al. 2013) and the $1330\mu\text{m}$ continuum flux with the Atacama Large Millimeter-sub-millimeter Array (ALMA; Ansdell et al. 2017). For

Table 2. Stellar Properties

Parameter	Value	Comments
Spectral Type	$F6.0 \pm 1.0$...
A_V	0.2 ± 0.1	...
T_* (K)	6250	using Pecaut & Mamajek (2013)
L_* (L_\odot)	9.1 ± 0.5	...
M_* (M_\odot)	1.6	using Siess et al. (2000)
R_* (R_\odot)	2.0	using Siess et al. (2000)
\dot{M} ($M_\odot \text{yr}^{-1}$)	1.4×10^{-9}	from U-band excess (Gullbring et al. 1998)
\dot{M} ($M_\odot \text{yr}^{-1}$)	1.3×10^{-9}	from $H\alpha$ and the relation of Alcalá et al. (2014)
\dot{M} ($M_\odot \text{yr}^{-1}$)	1.6×10^{-9}	from $H\alpha$ and the relation of Ingleby et al. (2013)
\dot{M} ($M_\odot \text{yr}^{-1}$)	9.8×10^{-9}	from $H\alpha$ and the relation of Fairlamb et al. (2017)

comparison, Figure 4 also shows the stellar photosphere, calculated using the intrinsic colors for a F6 main sequence star from [Kenyon & Hartmann \(1995\)](#), normalized to the dereddened J band flux. Since [Pecaut & Mamajek \(2013\)](#) only include 3 optical magnitudes (B, V and I_C) we used the intrinsic colors from [Kenyon & Hartmann \(1995\)](#) which include more optical magnitudes (U, B, V, R_C and I_C) to represent the stellar photosphere. The differences between these two standard values are less than 4% in the optical bands. We also included in Figure 4 the Taurus median from [Maucó et al. \(2016\)](#), scaled at H.

The SED of SO 411 shows a clear flux deficit relative to the median of Taurus in the near-IR and flux excesses relative to the photosphere comparable to the median of Taurus at long wavelengths, indicating that the disk of SO 411 is a transitional disk, in agreement with the classification of TD/PTD based on photometry ([Hernández et al. 2007](#)). The outer optically thick disk is therefore truncated at some distance from the star ([Espaillat et al. 2011](#)). There still is some small flux excess over the photosphere in the near-IR, which could come from either optically thin dust in the inner cavity or from an optically thick inner disk remaining close to the star. In the last case, the disk would be a pre-transitional disk ([Espaillat et al. 2007a, 2011](#)).

3.5. Veiling and NIR excess continuum

To elucidate the nature of the material remaining inside the cavity in the disk of SO 411, we use the SpeX data to extract the spectrum of the material emitting in the near-IR. Following the methods in [Muzerolle et al. \(2003\)](#) and [Espaillat et al. \(2010\)](#), we extracted the NIR excess continuum over the photosphere in the SpeX spectrum.

We estimated the NIR excess continuum subtracting the spectroscopic template HD11443 from the SPEX spectrum

of SO 411. The spectrum of HD11443 (F6IV) taken from the IRTF Spectral Library¹ ([Cushing et al. 2005](#); [Rayner et al. 2009](#)) was used as template. Before the subtraction, the target was corrected by veiling and both the target and the template spectra were normalized to the K band. A veiling of $r \sim 0.1$ was estimated comparing the equivalent width of $Br\gamma$ measured for SO 411 with that of the template. Since $Br\gamma$ could have a non resolved emission contribution from the accretion shocks, the estimated veiling should be considered as an upper limit. Unfortunately, the SpeX spectrum was too noisy to estimate veiling from other spectroscopic lines not affected by accretion.

Figure 5 shows the NIR excess continuum for SO 411; for comparison, we also show the spectra of the pre-transitional disk LkCa 15 and of the transitional disk GM Aur ([Espaillat et al. 2010](#)). Similarly to GM Aur, the NIR excess continuum of SO 411 is small and it is too broad to be fitted by a single blackbody, unlike the spectrum of LkCa 15. This evidence suggests that the near-IR in SO 411 does not arise in optically thick emission near the star but most likely in optically thin dust inside the cavity, indicating that SO 411 is not a pre-transitional disk. Figure 5 also shows the presence of the PAH feature at $3.3\mu\text{m}$. Unfortunately this feature falls between two orders of the SpeX spectrum (§4.2).

3.6. Disk Model

We calculated the structure and emission of the disk surrounding SO 411 using the D’Alessio Irradiated Accretion Disks model (DIAD; [D’Alessio et al. 1998, 1999, 2001, 2005, 2006](#)), following the methods described in [Espaillat et al. \(2010\)](#), that apply the DIAD model to stars surrounded

¹ http://irtfweb.ifa.hawaii.edu/spex/IRTF_Spectral_Library/

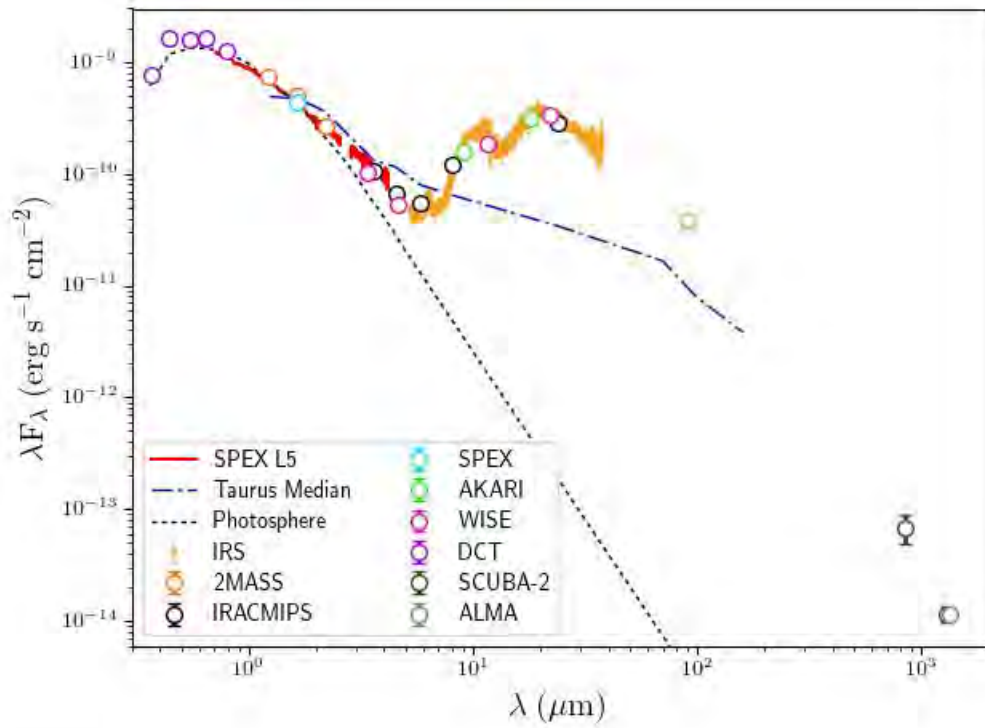


Figure 4. Spectral energy distribution of SO 411. As reference, we show the photosphere (black dotted line) and the median SED of Taurus (blue dot-dashed line) from [Maucó et al. \(2016\)](#), scaled at H. The sources for the photometry and spectroscopy are indicated in the legend.

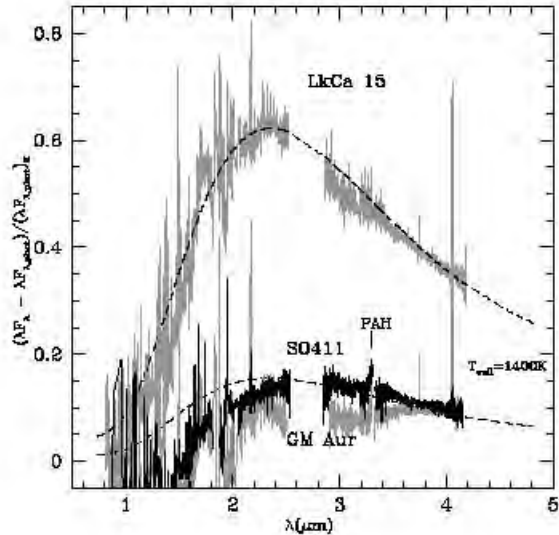


Figure 5. NIR excess continuum. Here we compare the NIR excess continuum of SO 411 with that estimated for the stars LkCa15 and GM Aur ([Espaillat et al. 2010](#)). SO 411 and GM Aur exhibit an IR excess continuum relatively small and flat which suggest that these stars are surrounded by a TD with optically thin dust inside the cavity. On the other hand, the PTD LkCa15 exhibits a relatively strong IR excess continuum that can be modeled as a single blackbody with temperature of 1400 K. The PAH feature at $3.3\mu\text{m}$ falls between two SpeX orders (see §4.2).

by TD or PTD. Based on the analysis in §3.5 we modeled the disk around SO 411 as a TD, that is, a truncated optically thick disk, allowing for optically thin dust inside the cavity. The input parameters that we held constant for the DIAD model were the accretion rate (\dot{M}) and the stellar properties (Table 2). Other parameters related to the disk structure and to the dust mixtures in the different parts of the disk were varied to achieve the best fit model to the observed SED. We assumed a value of 60° as the inclination of the system.

We assumed that the dust is thermally coupled to the gas and the dust size distributions are proportional to $a^{-3.5}$, where a is the radius of spherical grains, between a_{min} (fixed at $0.005\mu\text{m}$) and a_{max} ([Mathis et al. 1977](#)). In the optically thick disk the dust consists of silicates with mass fraction relative to gas of $\zeta_{sil}=0.004$ and graphite with mass fraction of $\zeta_{acm}=0.0025$ ($\zeta_{std}=0.0065$; [McClure et al. 2013](#)). The silicate grains are composed of amorphous silicates (pyroxene stoichiometry and olivine stoichiometry) and crystalline silicates (fosterite, and enstatite). The opacities for the amorphous silicates and graphite were computed using MIE theory with optical constants from [Dorschner et al. \(1995\)](#) and [Draine & Lee \(1984\)](#), respectively. The opacities for the crystalline silicates were taken from [Sargent et al. \(2009b\)](#). We did not include water ice.

The parameters of each disk component were adjusted simultaneously to fit the observed SED. The components of the

disk model that contribute to the synthetic SED include the optically thick disk, the inner edge of this disk (“the wall”, located at R_w), and the optically thin region between the star and the wall. We ran a grid of more than 3000 models, varying the input parameters in the ranges shown in Table 3, and calculated the χ^2 comparing the synthetic SED with the observations. The parameters of the model that yielded the best fit are shown in Table 4 and the theoretical SED is compared to the observations in Figure 6. Details for each component are given below.

Outer disk edge: We represent the inner edge of the optically thick disk by an optically thick “wall”, assumed to be vertical with evenly distributed dust. We calculated the structure and emission of this wall following D’Alessio et al. (2004). The dust mixture, the temperature of the wall, T_w , the radius of wall, R_w , and the height of the wall, z_w , in units of the gas scale height (H) are varied to obtain the best model.

The best fit parameters are given in Table 4, including the relative abundances of the silicate mixture. We found that the emission from the wall atmosphere is the main contributor to the silicate bands observed in the IRS spectra (cf. Figure 6).

Optically thick outer disk: The emission of the optically thick disk was calculated using the prescription in D’Alessio et al. (2006). The disk is heated by stellar irradiation and viscous dissipation and the disk structure and temperature distribution are calculated self-consistently for each radii. To simulate grain growth and settling, we assume that the disk is composed of two grain size distributions. In the upper disk layers, the grains have small sizes (with $a_{max} < 5\mu\text{m}$) and in the disk midplane the maximum grain size is given by a_{maxb} , which we adopt as a parameter. The viscosity is written in terms of the parameter α (Shakura & Sunyaev 1973; D’Alessio et al. 1998, 1999). Dust settling is parametrized with the quantity $\epsilon = \zeta_{small} / \zeta_{std}$, where ζ_{small} is the dust-to-gas mass ratio of the small grain population and ζ_{std} represents the sum of the mass fraction of the different dust components relative to gas. The dust composition was the same as in the outer disk edge. The radius of the disk, R_d , α , ϵ and a_{maxb} are varied to achieve the best fit to the observed SED. The best fit parameters are given in Table 4.

The mass of the disk, M_{disk} , is calculated by integrating the surface density up to the disk radius; it is also given in Table 4. Our M_{disk} , which is calculated based on dust emission and assuming a dust-to-gas mass ratio of 0.0065, is greater (by a factor of ~ 10) than the upper limit reported by Ansdell et al. (2017) from CO observations. They stated, however, that their gas mass estimate has several caveats since it depends on the uncertain $[\text{CO}]/[\text{H}_2]$ and $[\text{CO}]/[^{13}\text{CO}]$ ratios assumed in their models. If we, on the other hand, compare their dust mass estimate (from continuum observations at 1.33 mm) with ours, we found that our dust mass is only 3.5 greater than theirs. This difference is expected since they

used the simplified approach of a single grain opacity in an isothermal disk, which tends to overestimate the grain opacity and hence, underestimates the mass. With our dust grain opacity, however, we can reproduce not only the flux at 1.33 mm but the entire SED.

Optically thin inner region: The emission from dust inside the cavity was calculated by integrating the specific intensity emerging from optically thin annuli, in which all of the dust grains are heated by stellar radiation (Calvet et al. 2002; Espaillat et al. 2010). The maximum grain size ($a_{maxthin}$), the mass of the optically thin dust ($M_{thindust}$), the size of the region ($R_{i,thin}, R_{o,thin}$) and the fractional abundances of the silicates in the dust mixtures are varied to obtain the best model. The optically thin dust is composed by ~ 0.03 lunar masses distributed between 0.3 AU and 9.0 AU with a maximum grain size of $5\mu\text{m}$. Following Calvet et al. (2005); Espaillat et al. (2007a,b) we add organic ($\zeta_{org}=0.001$), troilite ($\zeta_{troi}=0.000768$) and amorphous carbon ($\zeta_{acm}=0.001$) to the dust mixture for comparison with other works in the literature. The opacities for organics, amorphous carbon and troilite are adopted from Pollack et al. (1994) and Begemann et al. (1994). For the silicates we used $\zeta_{sil}=0.004$. The parameters of the bestfit model are shown in Table 4. We stress that this is a proxy of the composition and spatial distribution of the optically thin dust since we need high resolution, near infrared interferometry to trace this component in detail.

4. DISCUSSION

4.1. Implications of dust mineralogy on disk evolution

Mid-infrared spectra of young stars can be well reproduced by a mixture of five main dust species: amorphous silicates with olivine and pyroxene stoichiometry, crystalline forsterite, enstatite and silica. Since the interstellar medium (ISM) is characterized by amorphous silicates, the crystalline grains found in Herbig Ae/Be and TTS systems must have been produced in the disk. Crystalline silicates such as forsterite and enstatite require formation temperatures above 1100 K (e.g., Fabian et al. 2000). These temperature are naturally reached near the central star, where one expects a large fraction of crystalline silicates. This has been confirmed by interferometric observations of Herbig Ae/Be disks showing highly crystalline inner disks (van Boekel et al. 2004). However, Spitzer IRS spectra also indicate the presence of large amounts of warm $\sim 400\text{--}500$ K crystalline silicates (enstatite or forsterite) at temperatures lower than the glass temperature of silicates. This can be explained through transport of grains and radial mixing of material from hotter inner disk regions toward the cooler outer regions at larger radii from the central star (e.g., Gail 2001). However, Bouwman et al. (2008) showed that the chemical gradients observed in circumstellar disks are difficult to explain in this scenario. Therefore, sili-

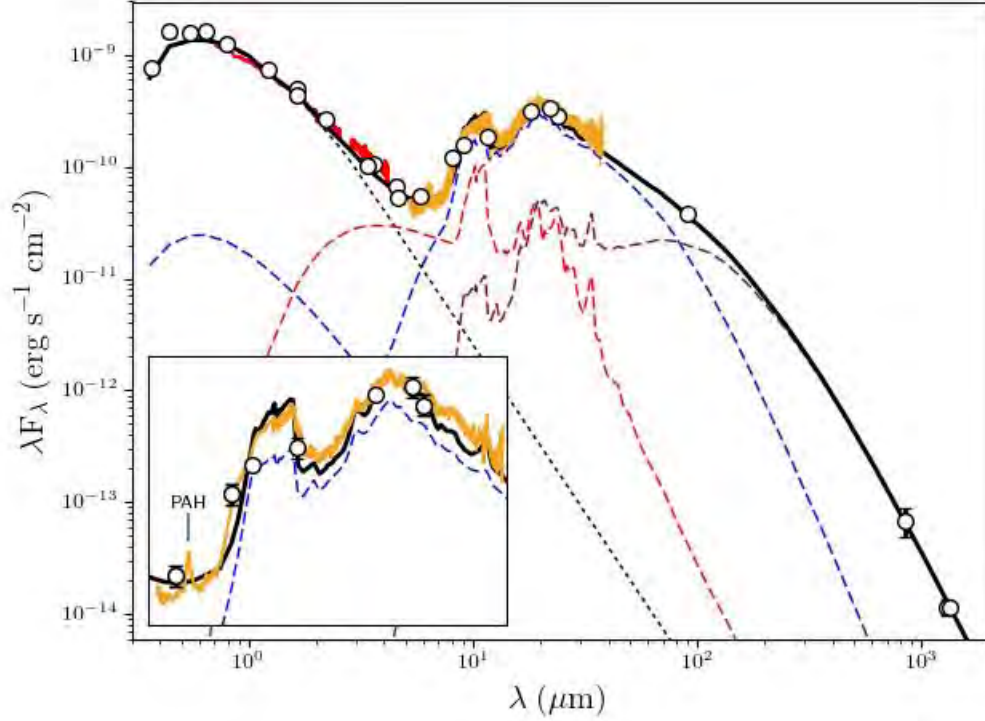


Figure 6. The observed SED of SO 411 and the best fit model. The synthetic SED (black solid line) includes the photosphere (black dotted line), the optically thin dust (red dashed line), the wall (blue dashed line) and the disk (brown dashed line). We also show in the figure inset the SED at the IRS wavelength range.

Table 3. Parameters explored

Parameter	Values
Optically Thick Disk	
ϵ	from 1 to 1e-5, step $\Delta\log(\epsilon)=1$
α	from 1 to 1e-4, step $\Delta\log(\alpha)=1$ ^a
$a_{max}(\mu m)$	from 0.1 to 1e4, step $\Delta\log(a_{max})=1$ ^e
R_{disk} (AU)	from 50 to 300, step=50 ^b
Optically Thick Wall	
T_{wall} (K)	from 100 to 1400, step=100 ^c
z_{wall} (AU)	from 1.0 to 5.5, step=0.1
$a_{maxw}(\mu m)$	from 0.1 to 1e4, step $\Delta\log(a_{maxw})=1$ ^e

^a We refine our best fit exploration including α of 0.003, 0.0006 and 0.0008

^b We refine our best fit exploration including steps of 10 AU.

^c We refine our best fit exploration including steps of 10 K.

^e We refine our best fit exploration including values of 0.25, 0.5, 0.75, 1.5, 2, 3, 4 and 5 μm

cate crystals must have formed locally in the disk, i.e. where they are presently observed.

In the case of SO 411, sharp bands of crystalline silicates can be observed in its IRS spectra indicating that thermal processing of dust has already taken place in the inner edge of the truncated disk, which dominates the IRS emission (see Figure 6). The inset of Figure 6 shows the IRS spectral range of SO 411 with the best fit model (solid line). As noted above, half the silicates of SO 411 are not amorphous, indicating some level of dust processing in its disk. Additionally, a modest contribution from the optically thin dust and from the thick disk can be observed in the silicate features at $10\mu\text{m}$ and $20\mu\text{m}$, respectively.

We found that forsterite is the most abundant silicate crystal (see Table 3), with a forsterite-to-enstatite ratio of 4. Similarly, olivine (amorphous precursor of forsterite) is slightly more abundant than pyroxene (amorphous precursor of enstatite). Infrared observations of the upper layers of protoplanetary disks around HAeBe and TTS show a different trend, i.e., enstatite is seen to be more concentrated towards the inner disk ($\lambda \sim 10 \mu\text{m}$, $T \sim 500 \text{ K}$), while forsterite is more abundant in the outer disk ($\lambda \sim 30 \mu\text{m}$, $T \sim 120 \text{ K}$) regions (Kessler-Silacci et al. 2006; Bouwman et al. 2008; Meeus et al. 2009; Juhász et al. 2010). According to Juhász et al. (2010), under chemical equilibrium the crystal population is dominated by enstatite, assuming solar abundances. Our finding contradicts this prediction, suggesting that the crystals we see in the spectra of SO 411 were formed under non-equilibrium conditions.

In order to produce in situ formation of crystalline silicates at a few AU from the star, one needs to consider an alternative heating mechanism beside irradiation; since at these distances the stellar radiation field cannot heat the dust at high enough temperatures for crystallization to occur. Given the TD morphology of SO 411, models of local heating of dust and gas by shock waves driven by tidal interactions of a giant planet with the disk has been proposed (Desch et al. 2005; Bouwman et al. 2010; Juhász et al. 2010; Mulders et al. 2011). A remarkable case is the HAeBe star HD 100546. This star also possesses a TD with forsterite grains in a disk wall located at $\sim 13 \text{ AU}$ (Mulders et al. 2011), and exhibits complex radial structures with appearance of spiral arms as well as detections of multiple companions in IR and sub-mm observations (e.g., Boccaletti et al. 2013; Mulders et al. 2013; Currie et al. 2014, 2015; Walsh et al. 2014; Quanz et al. 2015; Pinilla et al. 2015; Wright et al. 2015; Garufi et al. 2016; Follette et al. 2017). Another forsterite source is RECX 5 a M4 TTS also surrounded by a TD in the $\eta \text{ Cha}$ cluster (Bouwman et al. 2010).

As stated in Juhász et al. (2010), if the crystals are formed by shock heating in the outer disk, amorphous dust grains are then heated above the annealing temperature for a very

short time, favoring crystallization (Harker & Desch 2002). Over such a short timescale chemical equilibrium cannot be achieved and the resulting crystal product will be forsterite, independently of the starting stoichiometry of the amorphous particles. This can explain the observed dominance of forsterite in the outer disk of SO 411. Therefore, we conclude, as in Mulders et al. (2011), that the high forsterite abundance in the disk wall of SO 411 is somewhat connected to the presence of a hole, and hence, to giant planet formation. Additionally, studies on annealing of amorphous grains found that amorphous enstatite is converted to crystalline forsterite at $T \leq 1000 \text{ K}$ (Fabian et al. 2000; Roskosz et al. 2011). These studies concluded that the mineralogy of silicate dust of solar composition should naturally be dominated by olivine for $T \leq 1000 \text{ K}$, while above this temperature pyroxenes should dominate. Our result then suggests an upper limit for the annealing temperature of silicate crystals of 1000 K in the disk around SO 411.

The forsterite features of SO 411 are strikingly similar to those observed in the ISO spectrum of Comet Hale-Bopp (Crovisier et al. 2000) (see Figure 7). This provides a natural link to the composition of the solar nebula indicating that by $\sim 10 \text{ Myr}$ (the age of OB1a, Briceño et al. 2007), the local dust composition of the proto-solar nebula must have already resembled that of SO 411. It also raises the possibility that the disk around SO 411 contains a significant amount of comets, something already proposed for HD 100546 (Malfait et al. 1998). This locates the formation of Hale-Bopp-like objects near the outer giant planets in protoplanetary disks, as in the case of HD 100546.

In contrast with HD 100546 and RECX 5 (also shown in Figure 7, note the resembling of SO 411 with HD 100546), SO 411 also exhibits significant amounts of silica in its dust mixture. Laboratory annealing experiments of amorphous silicates also show that during the formation of forsterite, silica can be produced (e.g., Fabian et al. 2000). In fact, silica has been found in the spectrum of young stars both in amorphous and in crystalline form (e.g., Bouwman et al. 2001; van Boekel et al. 2005; Sargent et al. 2009a). As noted in Bouwman et al. (2008), the crystallization of forsterite from an amorphous enstatite precursor leads to a silica by-product. Therefore, the amount of silica should then be commensurate with the amount of forsterite produced from the enstatite component. This is exactly what we observed in SO 411. The reason why SO 411 does show silica content while others forsterite sources, such as HD 100546 and RECX 5 (and similarly, comet Hale-Bopp) do not, is unknown and a matter for future discussion.

4.2. PAH features

The detection of PAH emission is an indicator that carbonaceous material subsists in protoplanetary disks (Henning

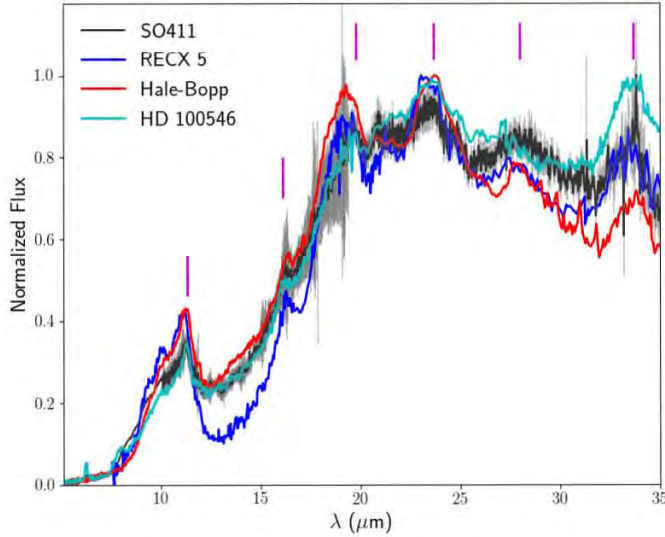


Figure 7. Spitzer IRS spectra of SO 411 (black line). Also plotted are the ISO spectrum of comet Hale-Bopp (red line) and HD 100546 (light-blue line) as well as the IRS spectra of RECX 5 (blue line) for comparison. All the spectra have been normalized. The main forsterite features are also indicated (magenta vertical lines).

& Meeus 2011). More than half of the HAeBe stars exhibit PAH features at 3.3, 6.2, 7.7, 8.6, 11.3 and 12.7 μm (Acke et al. 2010; Henning & Meeus 2011; Seok & Li 2017). On the other hand, PAH detections around T Tauri stars are more scarce; as far as we know, there are only three stars with spectral type K5 or later with reliable detection of PAH features: T54 (K5; Espaillat et al. 2017), EC 82 (K7) and IC348 LRL110 (M0; Seok & Li 2017)². This suggests that a stellar UV radiation field is necessary to excite the PAH molecules (Geers et al. 2006; Acke et al. 2010). On the other hand, the few PAH detections in T Tauri stars suggest that visible and NIR radiation may be capable of exciting PAH molecules (Li & Draine 2002; Mattioda et al. 2005). If UV radiation is not necessary to excite PAH molecules, the lack of PAH detection could be explained if the continuum and the 10 μm silicate emission feature hide the PAH features (Espaillat et al. 2017).

PAH features are seen in the IRS spectrum of SO 411 (Figure 6). The 3.3 μm PAH feature is also hinted in the SpeX spectra (Figure 5), but unfortunately part of the feature fell between two SpeX orders so we will not discuss it further. Although a feature at 6.2 μm is clearly seen in the IRS spectrum, the features at longer wavelength need to be extracted from the strong silicate features (Figure 6). The strong contribution of crystalline silicates makes this task even more difficult, specially at wavelengths longer than 10 μm , so we

² the stars IC348 LRL190(M3) and J1829070+003838(K7) listed in (Seok & Li 2017) have marginal detections

Table 4. Disk Parameters

Parameter	value
Optically Thick Outer Disk	
\dot{M} ($M_{\odot}\text{yr}^{-1}$).....	5×10^{-9}
α	0.003
ϵ	0.1
R_d (au)	50
a_{max} (μm)	0.25
a_{maxb} (μm)	1000
oliv _{ab} (%).....	30
py _{ab} (%).....	20
forst _{ab} (%).....	20
enst _{ab} (%).....	5
silica _{ab} (%)	25
M_{disk} (M_{\odot}).....	0.039
Optically Thick Outer Wall	
amax _w (μm)	1.0
T_w (K)	260
R_w (au)	11
z_w (in units of H)	4.4
oliv _{ab} (%).....	30
py _{ab} (%).....	20
forst _{ab} (%).....	20
enst _{ab} (%).....	5
silica _{ab} (%)	25
Optically Thin Region	
$R_{i,\text{thin}}$ (au)	0.3
$R_{o,\text{thin}}$ (au)	9.0
amax _{thin} (μm)	5.0
oliv _{ab} (%)	99
enst _{ab} (%).....	0.2
forst _{ab} (%).....	0.8
M_{thindust} (lunar masses).....	0.03

confine our analysis to the features at 6.2 and 7.7 μm , due to the CC stretch modes, and the 8.6 μm feature arising in the CH bending mode. We extracted the features following the procedure of Seok & Li (2017); namely, we fitted the “continuum” with a cubic spline going through the same anchor points as in that paper, and then subtracted this con-

tinuum from the observed spectrum. The resultant “normalized” spectrum is shown in Figure 8. We decided to follow this procedure, instead of subtracting the model spectrum, because we wanted to compare properties of the extracted PAH spectra of SO 411 to those of the extended set of Herbig Ae/Be and T Tauri stars in Sloan et al. (2005), Acke et al. (2010) and Seok & Li (2017), extracted with the same procedure.

In the selected wavelength range, besides the $6.2 \mu\text{m}$ feature, we detect a wide feature around $\sim 8.3 \mu\text{m}$, which we identify with the 7.7 and $8.6 \mu\text{m}$ features (Figure 8). Redshifted 6.2 and $7.7 \mu\text{m}$ PAH features have been observed in young stellar objects and the shifts give clues about the properties of the PAH emitters (e.g., Sloan et al. 2005; Acke et al. 2010; Seok & Li 2017). To estimate the location of the peaks, we fitted the features with Gaussian profiles, as shown in Figure 8. We found that the $6.2 \mu\text{m}$ feature is shifted to $\lambda_{6.2} = 6.27 \mu\text{m}$ and the $7.7 \mu\text{m}$ feature to $\lambda_{7.7} = 8.14 \mu\text{m}$. These shifts are consistent with the trend observed for the set of 53 Herbig Ae stars in Acke et al. (2010), who find that the $6.2 \mu\text{m}$ feature can be shifted to a maximum value of $\sim 6.275 \mu\text{m}$; for this maximum value, the corresponding shift in the $7.7 \mu\text{m}$ feature ranges between 7.82 to $8.1 \mu\text{m}$, in agreement with the shifts observed in SO 411. The shift of the $7.7 \mu\text{m}$ peak is consistent with the trend of position versus effective temperature found by Acke et al. (2010) for a sample of Herbig Ae and T Tauri stars; they find that the position of the peak is $< 8.1 \mu\text{m}$ for Herbig Ae, while it is $> 8.21 \mu\text{m}$ for TTS, so the observed shift of $8.14 \mu\text{m}$ in SO 411 is completely consistent with its intermediate nature between these two sets of stars.

Seok & Li (2017) explain the decrease of $\lambda_{7.7}$ between TTS and Herbig Ae as the result of a decrease of the size of the PAHs as the effective temperature and luminosity of the star increase. In turn, the loss of small grains in the Herbig Ae could be explained in terms of a higher photodissociation rate for small PAH when the number of energetic UV photons increases as the star gets hotter and more luminous (Seok & Li 2017). To estimate the PAH size in SO 411 we follow Seok & Li (2017), who characterize the grain size by the parameter a_p , which is the size that corresponds to the maximum of the log size distribution weighted by mass. Using the fits to the observed correlations of $\langle a_p \rangle$ with effective temperature and luminosity to mass ratio, we get $\langle a_p \rangle = 5.1$ and 4.6 \AA for the values of T_{eff} and L_*/M_* of SO 411 (Table 2), respectively. Moreover, the value of $\langle a_p \rangle$ predicted from the location of the $7.7 \mu\text{m}$ is 4.3 \AA (Seok & Li 2017). Given the large scatter in the calibrations and the uncertainties in the location of the continuum, we consider that these values are consistent with each other. A value of $\langle a_p \rangle$ between 4.5 and 5 \AA is smaller than in the ISM but in the upper end of the TTS distribution in the sample analyzed in Seok &

Li (2017), and indicates that small PAHs still remain in the disk of SO 411. Therefore, the PAH spectrum of SO 411 is consistent with its intermediate state between the hot and luminous Herbig Ae and the less massive and cooler T Tauri stars.

Acke et al. (2010) find that the mass fraction of small silica grains in cold dust decreases as the FWHM of the $6.2 \mu\text{m}$ feature increases in their sample of Herbig Ae. Our measurement for the FWHM of this feature is 0.182 \AA , which would imply a negligible silica mass fraction, according to this correlation. In contrast, we find a silica fraction of 25% of all silicates (§4.1). Herbig Ae stars do not seem to have abundances of silica as high as that found in SO 411, but they do occur in T Tauri stars (Sargent et al. 2009b). As Acke et al. (2010) state, the correlation between the FWHM of the $6.2 \mu\text{m}$ and the silica abundance is unexpected. Our finding that the correlation does not hold for less energetic environments may give an additional clue to its origin.

5. SUMMARY AND CONCLUSIONS

We present a detailed irradiated disk model for the intermediate mass T Tauri star SO 411 ($1.6 M_\odot$, spectral type F6). Our findings are as follows:

1. Combining data from the GAIA-DR2 and available radial velocities, we find that SO 411 is not associated with the σ Orionis cluster, but it is more likely related to an older and sparser population located in front of the cluster.
2. The star is surrounded by a primordial disk with mass $0.039 M_\odot$, with a gap extending to 11 AU from the star. Except at the midplane and at the wall, the disk is

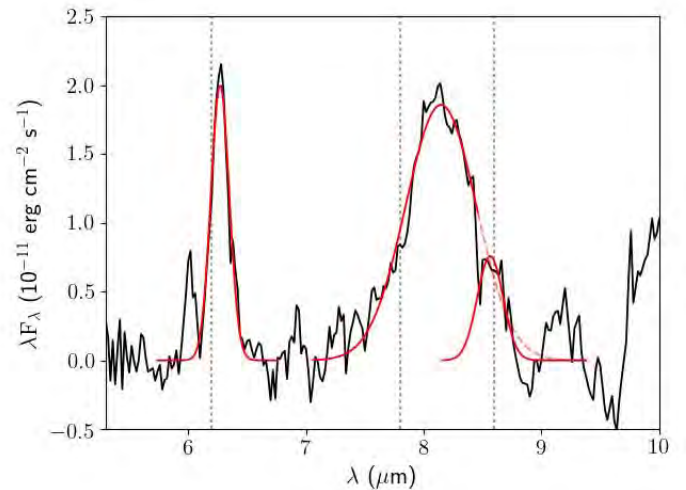


Figure 8. Continuum-subtracted PAH spectrum for SO 411 (black solid line). Dotted vertical lines indicate the PAH features at $6.2 \mu\text{m}$, $7.7 \mu\text{m}$ and $8.6 \mu\text{m}$. Red lines indicate the Gaussian fit we used for each PAH features.

populated by ISM grains with a depletion of only 10% relative to the standard dust-to-gas mass ratio.

3. We find evidence that the star is still accreting, with a mass accretion rate of $\dot{M} \sim 5 \times 10^{-9} M_{\odot} \text{yr}^{-1}$. Given the disk mass and mass accretion rate, the most likely cause for the inner disk clearing is the interaction with a forming planet (cf. [Espaillat et al. 2014](#)).
4. The SED shows a small near-IR excess arising from optically thin emission over a range of temperatures. With this, we show that SO 411 is not surrounded by a pre-transitional disk. The optically thin emission comes from a small amount of micron size grains of 0.03 lunar masses located between 0.3 and 9 AU from the star.
5. Analysis of the $10\mu\text{m}$ silicate feature profile indicates an approximately equal amount of crystalline and amorphous material, with forsterite as the most abundant silicate crystal. The crystalline material is found on the wall of the outer disk, which is the main contributor to the silicate features. Shock waves induced by giant planets can locally heat the material in the wall of the disk to produce crystals. The forsterite abundance found in SO 411 points to crystal formation in non-equilibrium conditions.
6. PAH features are detected in the IRS spectrum of SO 411. Analysis of the 6.2 and $7.7\mu\text{m}$ features indicates that small PAHs remain in the disk of SO 411. The PAH spectrum of SO 411 is consistent with its intermediate state between the hot and luminous Herbig Ae and the less massive and cooler T Tauri stars.

Acknowledgments. We are grateful to Jacques Crovisier for sending spectra of comet Hale-Bopp. The authors acknowledge support from programs UNAM-DGAPA-PAPIIT IN103017, Mexico. This paper utilizes the [D’Alessio et al. \(1998, 1999, 2001, 2005, 2006\)](#) Irradiated Accretion Disk

code. We wish to recognize the work of Paola D’Alessio, who passed away in 2013. Her legacy and pioneering works live on through her substantial contributions to the field. We thank the institutions and personnel that support data acquisition at the Observatorio Astronómico Nacional at San Pedro Martir, the Lowell Observatory and the Mauna Kea Observatory. This work is based on observations made with the Spitzer Space Telescope, which is operated by the Jet Propulsion Laboratory, under a contract with NASA. We used the Infrared Telescope Facility, which is operated by the University of Hawaii under contract NNH14CK55B with the NASA. These results made use of the Discovery Channel Telescope at Lowell Observatory, supported by Discovery Communications, Inc., Boston University, the University of Maryland, the University of Toledo and Northern Arizona University. This publication makes use of data products from the Two Micron All Sky Survey, which is a joint project of the University of Massachusetts and the Infrared Processing and Analysis Center/California Institute of Technology, funded by the National Aeronautics and Space Administration and the National Science Foundation. We also make use of data products from the Wide-field Infrared Survey Explorer, which is a joint project of the University of California, Los Angeles, and the Jet Propulsion Laboratory/California Institute of Technology, funded by the National Aeronautics and Space Administration. This work is based on observations with AKARI, a JAXA project with the participation of ESA. The grid of accretion disk models used in the present work has been calculated using the supercomputer Mouruka, at IRyA, provided by CONACyT grant number INFR-2015-01-252629.

Software: Astropy ([Astropy Collaboration et al. 2013](#)), Matplotlib ([Barrett et al. 2005](#)), IRAF ([Davis 1999](#)), SMART ([Higdon et al. 2004](#)), SpexTool ([Cushing et al. 2004](#))

Facilities: DCT(LMI), Spitzer(IRS,IRAC,MIPS), WISE, CTIO, 2MASS, IRTF, Akari, ALMA, JCMT(SCUBA-2), SPM(2m-B&C)

REFERENCES

- Acke, B., & van den Ancker, M. E. 2004, *A&A*, 426, 151
- Acke, B., Bouwman, J., Juhász, A., et al. 2010, *ApJ*, 718, 558
- Alcalá, J. M., Natta, A., Manara, C. F., et al. 2014, *A&A*, 561, A2
- Alexander, R., Pascucci, I., Andrews, S., Armitage, P., & Cieza, L. 2014, *Protostars and Planets VI*, 475
- Ansdell, M., Williams, J. P., Manara, C. F., et al. 2017, *AJ*, 153, 240
- Andrews, S. M., Wilner, D. J., Espaillat, C., et al. 2011, *ApJ*, 732, 42
- Astropy Collaboration, Robitaille, T. P., Tollerud, E. J., et al. 2013, *A&A*, 558, A33
- Bailer-Jones, C. A. L. 2015, *PASP*, 127, 994
- Begemann, B., Dorschner, J., Henning, T., Mutschke, H., & Thamm, E. 1994, *ApJL*, 423, L71
- Birnstiel, T., Andrews, S. M., & Ercolano, B. 2012, *A&A*, 544, A79
- Boccaletti, A., Pantin, E., Lagrange, A.-M., et al. 2013, *A&A*, 560, A20

- Bouwman, J., Lawson, W. A., Juhász, A., et al. 2010, *ApJL*, 723, L243
- Bouwman, J., Henning, T., Hillenbrand, L. A., et al. 2008, *ApJ*, 683, 479-498
- Bouwman, J., Meeus, G., de Koter, A., et al. 2001, *A&A*, 375, 950
- Brown, J. M., Blake, G. A., Dullemond, C. P., et al. 2007, *ApJL*, 664, L107
- Briceño, C., Hartmann, L., Hernández, J., et al. 2007, *ApJ*, 661, 1119
- Briceno, C., Calvet, N., Hernandez, J., et al. 2018, arXiv:1805.01008
- Caballero, J. A. 2008, *A&A*, 478, 667
- Caballero, J. A. 2008b, *MNRAS*, 383, 375
- Calvet, N., D'Alessio, P., Hartmann, L., et al. 2002, *ApJ*, 568, 1008
- Calvet, N., Muzerolle, J., Briceño, C., et al. 2004, *AJ*, 128, 1294
- Calvet, N., D'Alessio, P., Watson, D. M., et al. 2005, *ApJL*, 630, L185
- Calvet, N., & D'Alessio, P. 2011, *Physical Processes in Circumstellar Disks around Young Stars*, 14
- Casassus, S. 2016, *PASA*, 33, e013
- Chiang, E., & Murray-Clay, R. 2007, *Nature Physics*, 3, 604
- Cieza, L. A., Olofsson, J., Harvey, P. M., et al. 2013, *ApJ*, 762, 100
- Crovisier, J., Brooke, T. Y., Leech, K., et al. 2000, *Thermal Emission Spectroscopy and Analysis of Dust, Disks, and Regoliths*, 196, 109
- Currie, T., Cloutier, R., Brittain, S., et al. 2015, *ApJL*, 814, L27
- Currie, T., Muto, T., Kudo, T., et al. 2014, *ApJL*, 796, L30
- Cushing, M. C., Vacca, W. D., & Rayner, J. T. 2004, *PASP*, 116, 362
- Cushing, M. C., Rayner, J. T., & Vacca, W. D. 2005, *ApJ*, 623, 1115
- Cutri, R. M., Skrutskie, M. F., van Dyk, S., et al. 2003, *VizieR Online Data Catalog*, 2246
- Cutri, R. M., et al. 2013, *VizieR Online Data Catalog*, 2328,
- Currie, T., Lada, C. J., Plavchan, P., et al. 2009, *ApJ*, 698, 1
- D'Alessio, P., Cantó, J., Calvet, N., & Lizano, S. 1998, *ApJ*, 500, 411
- D'Alessio, P., Calvet, N., Hartmann, L., Lizano, S., & Cantó, J. 1999, *ApJ*, 527, 893
- D'Alessio, P., Calvet, N., & Hartmann, L. 2001, *ApJ*, 553, 321
- D'Alessio, P., Calvet, N., Hartmann, L., Muzerolle, J., & Sitko, M. 2004, *Star Formation at High Angular Resolution*, 221, 403
- D'Alessio, P., Hartmann, L., Calvet, N., et al. 2005, *ApJ*, 621, 461
- D'Alessio, P., Calvet, N., Hartmann, L., Franco-Hernández, R., & Servín, H. 2006, *ApJ*, 638, 314
- D'Alessio, P. 2009, *Revista Mexicana de Astronomía y Astrofísica Conference Series*, 35, 33
- Desch, S. J., Ciesla, F. J., Hood, L. L., & Nakamoto, T. 2005, *Chondrites and the Protoplanetary Disk*, 341, 849
- Dong, R., & Fung, J. 2017, *ApJ*, 835, 146
- Dorschner, J., Begemann, B., Henning, T., Jaeger, C., & Mutschke, H. 1995, *A&A*, 300, 503
- Draine, B. T., & Lee, H. M. 1984, *ApJ*, 285, 89
- Dullemond, C. P., & Dominik, C. 2004, *A&A*, 421, 1075
- Dullemond, C. P., & Dominik, C. 2005, *A&A*, 434, 971
- Españolat, C., Calvet, N., D'Alessio, P., et al. 2007, *ApJL*, 664, L111
- Españolat, C., Calvet, N., D'Alessio, P., et al. 2007, *ApJL*, 670, L135
- Españolat, C., D'Alessio, P., Hernández, J., et al. 2010, *ApJ*, 717, 441
- Españolat, C., Muzerolle, J., Najita, J., et al. 2014, *Protostars and Planets VI*, 497
- Españolat, C. C., Ribas, Á., McClure, M. K., et al. 2017, *ApJ*, 844, 60
- Españolat, C., Muzerolle, J., Hernández, J., et al. 2008, *ApJL*, 689, L145
- Españolat, C., Furlan, E., D'Alessio, P., et al. 2011, *ApJ*, 728, 49
- Españolat, C., Ingleby, L., Hernández, J., et al. 2012, *ApJ*, 747, 103
- Ercolano, B., & Pascucci, I. 2017, *Royal Society Open Science*, 4, 170114
- Fabian, D., Jäger, C., Henning, T., Dorschner, J., & Mutschke, H. 2000, *A&A*, 364, 282
- Fabricant, D., Cheimets, P., Caldwell, N., & Geary, J. 1998, *PASP*, 110, 79
- Fairlamb, J. R., Oudmaijer, R. D., Mendigutia, I., Ilee, J. D., & van den Ancker, M. E. 2017, *MNRAS*, 464, 4721
- Follette, K. B., Rameau, J., Dong, R., et al. 2017, *AJ*, 153, 264
- Furlan, E., Hartmann, L., Calvet, N., et al. 2006, *ApJS*, 165, 568
- Furlan, E., Luhman, K. L., Españolat, C., et al. 2011, *ApJS*, 195, 3
- Gaia Collaboration, Brown, A. G. A., Vallenari, A., et al. 2018, arXiv:1804.09365
- Gail, H.-P. 2001, *A&A*, 378, 192
- Garrison, R. F. 1967, *PASP*, 79, 433
- Garufí, A., Quanz, S. P., Schmid, H. M., et al. 2016, *A&A*, 588, A8
- Geers, V. C., Augereau, J.-C., Pontoppidan, K. M., et al. 2006, *A&A*, 459, 545
- Gullbring, E., Hartmann, L., Briceño, C., & Calvet, N. 1998, *ApJ*, 492, 323
- Gutermuth, R. A., Megeath, S. T., Myers, P. C., et al. 2009, *ApJS*, 184, 18
- Habart, E., Natta, A., & Krügel, E. 2004, *A&A*, 427, 179
- Harker, D. E., & Desch, S. J. 2002, *ApJL*, 565, L109
- Henning, T., & Meeus, G. 2011, *Physical Processes in Circumstellar Disks around Young Stars*, 114
- Hernández, J., Calvet, N., Briceño, C., Hartmann, L., & Berlind, P. 2004, *AJ*, 127, 1682
- Hernández, J., Hartmann, L., Megeath, T., et al. 2007, *ApJ*, 662, 1067
- Hernández, J., Calvet, N., Hartmann, L., et al. 2009, *ApJ*, 707, 705

- Hernández, J., Morales-Calderon, M., Calvet, N., et al. 2010, *ApJ*, 722, 1226
- Hernández, J., Calvet, N., Perez, A., et al. 2014, *ApJ*, 794, 36
- Higdon, S. J. U., Devost, D., Higdon, J. L., et al. 2004, *PASP*, 116, 975
- Houck, J. R., Roellig, T. L., van Cleve, J., et al. 2004, *ApJS*, 154, 18
- Ingleby, L., Calvet, N., Herczeg, G., et al. 2013, *ApJ*, 767, 112
- Davis, L. E. 1999, *Precision CCD Photometry*, 189, 35
- Ishihara, D., Onaka, T., Kataza, H., et al. 2010, *A&A*, 514, A1
- Jeffries, R. D., Maxted, P. F. L., Oliveira, J. M., & Naylor, T. 2006, *MNRAS*, 371, L6
- Juhász, A., Bouwman, J., Henning, T., et al. 2010, *ApJ*, 721, 431
- Kamp, I. 2011, *EAS Publications Series*, 46, 271
- Keller, L. D., Sloan, G. C., Forrest, W. J., et al. 2008, *ApJ*, 684, 411-429
- Kenyon, S. J., & Hartmann, L. 1995, *ApJS*, 101, 117
- Kessler-Silacci, J., Augereau, J.-C., Dullemond, C. P., et al. 2006, *ApJ*, 639, 275
- Kharchenko, N. V., Scholz, R.-D., Piskunov, A. E., Röser, S., & Schilbach, E. 2007, *Astronomische Nachrichten*, 328, 889
- Lada, C. J., Muench, A. A., Luhman, K. L., et al. 2006, *AJ*, 131, 1574
- Landolt, A. U. 2009, *AJ*, 137, 4186
- Lebouteiller, V., Bernard-Salas, J., Sloan, G. C., & Barry, D. J. 2010, *PASP*, 122, 231
- Lebouteiller, V., Barry, D. J., Spoon, H. W. W., et al. 2011, *ApJS*, 196, 8
- Li, A., & Draine, B. T. 2002, *ApJ*, 572, 232
- Luhman, K. L., Allen, P. R., Espaillat, C., Hartmann, L., & Calvet, N. 2010, *ApJS*, 186, 111
- Maaskant, K. M., Honda, M., Waters, L. B. F. M., et al. 2013, *A&A*, 555, A64
- Malfait, K., Waelkens, C., Waters, L. B. F. M., et al. 1998, *A&A*, 332, L25
- Massey, P., & Davis, L. E. 1992, *A user's guide to stellar CCD photometry with IRAF, NOAO*
- Mathis, J. S., Rumpl, W., & Nordsieck, K. H. 1977, *ApJ*, 217, 425
- Mathis, J. S. 1990, *ARA&A*, 28, 37
- Barrett, P., Hunter, J., Miller, J. T., Hsu, J.-C., & Greenfield, P. 2005, *Astronomical Data Analysis Software and Systems XIV*, 347, 91
- Mattioda, A. L., Allamandola, L. J., & Hudgins, D. M. 2005, *ApJ*, 629, 1183
- Maucó, K., Hernández, J., Calvet, N., et al. 2016, *ApJ*, 829, 38
- Maxted, P. F. L., Jeffries, R. D., Oliveira, J. M., Naylor, T., & Jackson, R. J. 2008, *MNRAS*, 385, 2210
- McClure, M. K., D'Alessio, P., Calvet, N., et al. 2013, *ApJ*, 775, 114
- McClure, M. K., Furlan, E., Manoj, P., et al. 2010, *ApJS*, 188, 75
- McClure, M. K., Manoj, P., Calvet, N., et al. 2012, *ApJL*, 759, L10
- Meeus, G., Juhász, A., Henning, T., et al. 2009, *A&A*, 497, 379
- Meeus, G., Waters, L. B. F. M., Bouwman, J., et al. 2001, *A&A*, 365, 476
- Mulders, G. D., Paardekooper, S.-J., Panić, O., et al. 2013, *A&A*, 557, A68
- Mulders, G. D., Waters, L. B. F. M., Dominik, C., et al. 2011, *A&A*, 531, A93
- Muzerolle, J., Calvet, N., Hartmann, L., & D'Alessio, P. 2003, *ApJL*, 597, L149
- Muzerolle, J., Allen, L. E., Megeath, S. T., Hernández, J., & Gutermuth, R. A. 2010, *ApJ*, 708, 1107
- Oliveira, J., Bouwman, J., Jeffries, R., van Loon, J., & van den Ancker, M. 2006, *Spitzer Proposal*, 30381
- Olofsson, J., Augereau, J.-C., van Dishoeck, E. F., et al. 2009, *A&A*, 507, 327
- Owen, J. E. 2016, *PASA*, 33, e005
- Pascual, N., Montesinos, B., Meeus, G., et al. 2016, *A&A*, 586, A6
- Pecaut, M. J., & Mamajek, E. E. 2013, *ApJS*, 208, 9
- Péicaud, J., Di Folco, E., Dutrey, A., Guilloteau, S., & Piétu, V. 2017, *A&A*, 600, A62
- Pinilla, P., Flock, M., Ovelar, M. d. J., & Birnstiel, T. 2016, *A&A*, 596, A81
- Pinilla, P., Birnstiel, T., & Walsh, C. 2015, *A&A*, 580, A105
- Pollack, J. B., Hollenbach, D., Beckwith, S., et al. 1994, *ApJ*, 421, 615
- Quanz, S. P., Amara, A., Meyer, M. R., et al. 2015, *ApJ*, 807, 64
- Rayner, J. T., Cushing, M. C., & Vacca, W. D. 2009, *ApJS*, 185, 289
- Ribas, Á., Bouy, H., & Merín, B. 2015, *A&A*, 576, A52
- Roskosz, M., Gillot, J., Capet, F., Roussel, P., & Leroux, H. 2011, *A&A*, 529, A111
- Rubinstein, A. E., Macias, E., Espaillat, C. C., et al. 2018, *arXiv:1804.07343*
- Ruíz-Rodríguez, D., Ireland, M., Cieza, L., & Kraus, A. 2016, *MNRAS*, 463, 3829
- Sacco, G. G., Franciosini, E., Randich, S., & Pallavicini, R. 2008, *A&A*, 488, 167
- Sargent, B. A., Forrest, W. J., Tayrien, C., et al. 2009, *ApJ*, 690, 1193
- Sargent, B. A., Forrest, W. J., Tayrien, C., et al. 2009, *ApJS*, 182, 477
- Sartori, M. J., Gregorio-Hetem, J., Rodrigues, C. V., Hetem, A., Jr., & Batalha, C. 2010, *AJ*, 139, 27-38
- Schaefer, G. H. 2013, *EAS Publications Series*, 64, 181
- Seok, J. Y., & Li, A. 2017, *ApJ*, 835, 291
- Shakura, N. I., & Sunyaev, R. A. 1973, *X- and Gamma-Ray Astronomy*, 55, 155
- Siess, L., Dufour, E., & Forestini, M. 2000, *A&A*, 358, 593

- Simón-Díaz, S., Caballero, J. A., Lorenzo, J., et al. 2015, *ApJ*, 799, 169
- Sloan, G. C., Keller, L. D., Forrest, W. J., et al. 2005, *ApJ*, 632, 956
- Strom, K. M., Strom, S. E., Edwards, S., Cabrit, S., & Skrutskie, M. F. 1989, *AJ*, 97, 1451
- Sung, H., Stauffer, J. R., & Bessell, M. S. 2009, *AJ*, 138, 1116
- Testi, L., Birnstiel, T., Ricci, L., et al. 2014, *Protostars and Planets VI*, 339
- Torres, C. A. O., Quast, G., de La Reza, R., Gregorio-Hetem, J., & Lepine, J. R. D. 1995, *AJ*, 109, 2146
- van Boekel, R., Min, M., Waters, L. B. F. M., et al. 2005, *A&A*, 437, 189
- van Boekel, R., Waters, L. B. F. M., Dominik, C., et al. 2004, *A&A*, 418, 177
- van der Marel, N., Verhaar, B. W., van Terwisga, S., et al. 2016, *A&A*, 592, A126
- Visser, R., Geers, V. C., Dullemond, C. P., et al. 2007, *A&A*, 466, 229
- Walsh, C., Juhász, A., Pinilla, P., et al. 2014, *ApJL*, 791, L6
- Watson, D. M., Leisenring, J. M., Furlan, E., et al. 2009, *ApJS*, 180, 84
- White, R. J., & Basri, G. 2003, *ApJ*, 582, 1109
- Williams, J.P., & Cieza, L. A. 2011, *ARA&A*, 49, 67
- Williams, J. P., Cieza, L. A., Andrews, S. M., et al. 2013, *MNRAS*, 435, 1671
- Wright, C. M., Maddison, S. T., Wilner, D. J., et al. 2015, *MNRAS*, 453, 414
- Yamamura, I., Makiuti, S., Ikeda, N., et al. 2010, *VizieR Online Data Catalog*, 2298
- Zhang, K., Bergin, E. A., Blake, G. A., et al. 2016, *ApJL*, 818, L16
- Zhu, Z., Nelson, R. P., Hartmann, L., Espaillat, C., & Calvet, N. 2011, *ApJ*, 729, 47
- Zhu, Z., Nelson, R. P., Dong, R., Espaillat, C., & Hartmann, L. 2012, *ApJ*, 755, 6

Chapter 6

Conclusions

The present work has focused on the study of the physical properties of protoplanetary disks around young stars located in the Orion complex. We used optical U, V, R, I, near-IR J, H, K photometry, mid-IR data from Spitzer/WISE/CanariCam and far-IR Herschel PACS observations at 70 and 160 μm , which we reported for the first time, to construct SEDs that we then fit with theoretical models of irradiated accretion disks, whose emission is calculated in a self-consistent way and including dust settling, in order to characterize disks around CTTS.

The main propose of this study was to bring new insights about the main issues concerning disk evolution, planet formation and disk dissipation. Previous studies of dust in disks in other star forming regions made with Spitzer and WISE have mostly been limited to the inner 10 AU from the central star. With Herschel we were able to probe parts of the disk that emit at longer wavelengths, important for disk evolutionary studies, particularly to constrain dust settling. Herschel data also allowed the characterization of the outer parts of the upper layer of the disk and was more suitable for detecting even small young disks than submm surveys. PACS photometry played a crucial role characterizing (pre-)transitional disks since enabled us to constrain the properties of the inner edge of the outer disks.

Many current issues in star and planet formation can only be tested with large sets of pre-main sequence (PMS) stars with ages $\sim 3 - 10$ Myr, a time when disks dissipate (Calvet et al., 2005; Hernández et al., 2007b), and giant planets are expected to form (Podosek et al., 1996). For this reason we analyzed the IR emission of a sample of 40 TTS with PACS detections in the Orion OB1 association spanning this age range. Through detail modeling of the spectral energy distributions of a set of these objects using the irradiated

accretion disk models of (D’Alessio et al., 1998, 2004, 2006a), we inferred the structure, characteristics and evolutionary state of our sample.

We first, estimated stellar parameters of all our sources and characterized accretion processes using high and low resolution spectra by analyzing the H α line profiles. We obtained that PACS detections are consistent with stars surrounded by optically thick disks with high 24 μm excesses, spectral types between K2 and M5 (except for SO 411 which is an F6 star) and mass accretion rates of $10^{-11} - 10^{-9} M_{\odot}/\text{yr}$. We then modeled a total of 18 class II CTTS and one TD (SO 411) with PACS detections in the young (~ 3 Myr) σ Ori cluster and another 8 CTTS, also with PACS detections, in the older Orion OB1b ($\sim 5 - 7$ Myr) and OB1a ($\sim 7 - 10$ Myr) subassociations.

For class II stars in the σ Ori cluster, we found that most of our objects have significant dust settling and possible grain growth consistent with previous studies of other young star-forming regions (Furlan et al., 2009; McClure et al., 2010; Manoj et al., 2011). We found a subset of objects with large disk sizes as well as systems with disks radii as small as 10 AU. In order to inquire about the possible mechanisms acting on these sources that may result in small disks sizes, we estimated the field intensity, G_0 , produced by the three brightest objects in the center of the cluster to test how feasible it was that the radiation from these stars externally illuminated the disks producing the dissipation of the disk material. We found strong evidence of external photoevaporation of the disks due to the energy fields of the multiple massive OB system in σ Ori. We obtained that 80% of our disks were exposed to significant flux levels high enough to truncate the outer edge of the disks and to reduce their lifetime. We also analyzed forbidden optical emission lines in high-resolution spectra for some of our sources, obtained with the multi-fiber spectrograph hectochelle, and looked for low velocity, blue shifted line profiles, like the [N II] line at 6548/6583 \AA , which are related to photoevaporating winds. We compared our results of disks masses and radii with models of viscous evolution including external photoevaporation of Anderson et al. (2013), and found that our objects follow the trend dictated by externally illuminated disks models. This constitutes one of the first evidence of photoevaporating disks in the σ Ori cluster showing the existence of these type of disks in star-forming regions of intermediate age.

A worth mentioning case is the source SO 411, a TD with spectral type F6. This source was thought to belong to the σ Ori cluster until now. Combining data from the GAIA-DR2 and available radial velocities, we find that this source is not associated with the σ Ori cluster, but it is more likely related to an older and sparser population located in front of the cluster associated with OB1a. Through detailed modeling of the SED including its

IRS spectra we found that the star is surrounded by a primordial disk with mass of $0.039 M_{\odot}$, truncated at a distance of ~ 11 AU from the star. Inside the cavity we found a small amount of optically thin dust consistent of $\sim 5 \mu\text{m}$ grains composed of amorphous silicates and, surprisingly, a significant amount of forsterite crystal with a fractional abundance of 20% over only 5% of enstatite. This dominance of forsterite is explained by non-equilibrium annealing processes. Given the TD morphology of SO 411 the best explanation is in situ crystal formation driven by shock heating waves created by the interaction of a giant planet with the disk material. SO 411 resembles remarkably well the ISO spectrum of Comet-Hale Bopp (Crovisier et al., 2000) and HD 100546 (Bouwman et al., 2010). This may imply the presence of a swarm of comets in the disk of SO 411, which are probably formed near the outer giant planets in protoplanetary disks. One peculiar aspect of SO 411, not found in other forsterite sources as HD 100546 and RECX 5, is the presence of substantial silica component. According to Bouwman et al. (2008), the crystallization of forsterite from an amorphous enstatite precursor leads to a silica by-product and therefore, the amount of silica should then be commensurate with the amount of forsterite produced from the enstatite precursor. This is exactly what we observed in SO 411. The reason why SO 411 does show silica content while others forsterite sources, as HD 100546 and RECX 5 do not, is unknown and a matter for future discussion. Finally, this source also exhibits PAH detections in its IRS spectra at 6.2, 7.7, and 8.6 μm . The PAH spectrum of SO 411 is consistent with its intermediate state between the hot and luminous Herbig Ae and the less massive and cooler T Tauri stars.

For objects in the Orion OB1a and OB1b subassociations we found that all PACS detections are (pre-)transitional disks with some amount of optically thin dust inside their gaps/holes, according to their mid-IR emission especially at 10 μm . Full disk models failed to reproduce the silicate bands probed by the CanariCam photometry or the *Spitzer* IRS spectra. PACS data was particularly suitable to characterize the inner edge of the outer disk, where grain evolution is expected to occur at evolutionary stages well beyond the protostellar phase. Two of these sources, CVSO-107 and CVSO-109, also have *Spitzer* IRS spectra. We found that the 10 and 20 μm silicate features can be explained with small grains mostly composed of amorphous silicates. The silicate feature of CVSO-109 resembles that of a pristine spectrum with no signs of dust grain processing, characteristic of sub-micron ISM-like dust. In contrast, the IRS spectrum of CVSO-107 is better described with some amounts of enstatite and forsterite crystals in its optically thin dust mixture.

The intermediate-advanced age of our sources ($\sim 4 - 10$ Myr) poses two possible evolutionary scenarios for the presence of (pre-)transitional disks. The first one is that these stars had full disks until recently, and have now become (pre-)transitional disks. In contrast, the second scenario suggests that the pre-transitional disk appearance is long-lasting, in which case we are actually looking at “mature” pre-transitional disk systems. This last argument is reinforced by the fact that all our PACS detections turn out to be (pre-)transitional disks. Assuming this last picture, we speculated that the presence of near-IR excess in the SEDs of our sources may point to low-mass ($< 1 M_{\text{jup}}$) planet formation, where, according to Pinilla et al. (2016), the survival and maintenance of the inner disk could be explained by partial filtration of dust, in which the micron-sized grains pass through the gap, supporting a constant replenishment of dust from the outer to the inner disk. This has important implications for disk evolution since suggests that the near-IR excess that characterizes pre-transitional disks is not necessarily an evolutionary effect, but depends on the type of planets sculpting the disks.

In general, the masses of our disk sample range between 0.03 and $\sim 54 M_{\text{jup}}$, with 26% of the disks having masses lower than $0.001 M_{\odot}$. These low masses suggest that the formation of giant planets is probably over in these regions. If this is indeed the case, then timescales for giant planet formation should be less than 3 Myr, or giant planets are difficult to form in clustered environments. This is consistent with previous studies on disk populations older than 3 Myr, giving support to the scenario of short timescales for giant planet formation (e.g., Carpenter et al., 2014; Barenfeld et al., 2016, 2017).

To study in more detail the size of the photoevaporated region in σ Ori and to determine, for the first time, the dependence of the photoevaporating wind with mass accretion rate in the disk, we plan to work with high-resolution spectroscopic data taken with the Magellan Inamori Kyocera Echelle (MIKE) spectrograph and with the Magellan Echellette Spectrograph (MagE) mounted on the Magellan 6.5 m telescope at Las Campanas Observatory. We are looking for forbidden optical emission lines, like [O I], [S II], [N II], in disks at different projected distances from the center and with different properties. We will be able to study the accretion signatures in the spectra, such as the broad $H\alpha$, other Balmer emission lines, the IR triplet and H and K lines of CaII with wind properties as well. Additionally, we have VLA continuum observations of the cluster at X (3 cm) and C (6 cm) bands. The main goal is to search for free-free emission, which is related to photoevaporating winds, to probe the scope of external photoevaporation in the cluster and how this process affects disk evolution.

Bibliography

- Abergel, A., D. Teyssier, J. P. Bernard, F. Boulanger, A. Coulais, D. Fosse, E. Falgarone, M. Gerin, M. Perault, J.-L. Puget, L. Nordh, G. Olofsson, M. Hultgren, A. A. Kaas, P. André, S. Bontemps, M. M. Casali, C. J. Cesarsky, E. Copet, J. Davies, T. Montmerle, P. Persi, and F. Sibille
2003. ISOCAM and molecular observations of the edge of the Horsehead nebula. , 410:577–585.
- Acke, B. and M. E. van den Ancker
2004. ISO spectroscopy of disks around Herbig Ae/Be stars. , 426:151–170.
- Adams, F. C., D. Hollenbach, G. Laughlin, and U. Gorti
2004. Photoevaporation of Circumstellar Disks Due to External Far-Ultraviolet Radiation in Stellar Aggregates. , 611:360–379.
- Adams, F. C., F. H. Shu, and C. J. Lada
1987. The Disks of T Tauri Stars with Flat Infrared Spectra. In *Bulletin of the American Astronomical Society*, volume 19 of , P. 1096.
- Akeson, R. L., A. F. Boden, J. D. Monnier, R. Millan-Gabet, C. Beichman, J. Beletic, N. Calvet, L. Hartmann, L. Hillenbrand, C. Koresko, A. Sargent, and A. Tannirkulam
2005. Keck Interferometer Observations of Classical and Weak-line T Tauri Stars. , 635:1173–1181.
- Alexander, R., I. Pascucci, S. Andrews, P. Armitage, and L. Cieza
2014. The Dispersal of Protoplanetary Disks. *Protostars and Planets VI*, Pp. 475–496.
- Alexander, R. D. and P. J. Armitage
2007. Dust dynamics during protoplanetary disc clearing. , 375:500–512.

- Alexander, R. D., C. J. Clarke, and J. E. Pringle
2006a. Photoevaporation of protoplanetary discs - II. Evolutionary models and observable properties. , 369:229–239.
- Alexander, R. D., C. J. Clarke, and J. E. Pringle
2006b. Photoevaporation of protoplanetary discs - II. Evolutionary models and observable properties. , 369:229–239.
- Allen, L. E., N. Calvet, P. D’Alessio, B. Merin, L. Hartmann, S. T. Megeath, R. A. Gutermuth, J. Muzerolle, J. L. Pipher, P. C. Myers, and G. G. Fazio
2004. Infrared Array Camera (IRAC) Colors of Young Stellar Objects. , 154:363–366.
- ALMA Partnership, C. L. Brogan, L. M. Pérez, T. R. Hunter, W. R. F. Dent, A. S. Hales, R. E. Hills, S. Corder, E. B. Fomalont, C. Vlahakis, Y. Asaki, D. Barkats, A. Hirota, J. A. Hodge, C. M. V. Impellizzeri, R. Kneissl, E. Liuzzo, R. Lucas, N. Marcelino, S. Matsushita, K. Nakanishi, N. Phillips, A. M. S. Richards, I. Toledo, R. Aladro, D. Broguiere, J. R. Cortes, P. C. Cortes, D. Espada, F. Galarza, D. Garcia-Appadoo, L. Guzman-Ramirez, E. M. Humphreys, T. Jung, S. Kamenno, R. A. Laing, S. Leon, G. Marconi, A. Mignano, B. Nikolic, L.-A. Nyman, M. Radiczcz, A. Remijan, J. A. Rodón, T. Sawada, S. Takahashi, R. P. J. Tilanus, B. Vila Vilaro, L. C. Watson, T. Wiklind, E. Akiyama, E. Chapillon, I. de Gregorio-Monsalvo, J. Di Francesco, F. Gueth, A. Kawamura, C.-F. Lee, Q. Nguyen Luong, J. Mangum, V. Pietu, P. Sanhueza, K. Saigo, S. Takakuwa, C. Ubach, T. van Kempen, A. Wootten, A. Castro-Carrizo, H. Francke, J. Gallardo, J. Garcia, S. Gonzalez, T. Hill, T. Kaminski, Y. Kuroono, H.-Y. Liu, C. Lopez, F. Morales, K. Plarre, G. Schieven, L. Testi, L. Videla, E. Villard, P. Andreani, J. E. Hibbard, and K. Tatematsu
2015. The 2014 ALMA Long Baseline Campaign: First Results from High Angular Resolution Observations toward the HL Tau Region. , 808:L3.
- Anderson, K. R., F. C. Adams, and N. Calvet
2013. Viscous Evolution and Photoevaporation of Circumstellar Disks Due to External Far Ultraviolet Radiation Fields. , 774:9.
- Andre, P., D. Ward-Thompson, and M. Barsony
2000. From Prestellar Cores to Protostars: the Initial Conditions of Star Formation. *Protostars and Planets IV*, P. 59.

- Andrews, S. M., K. A. Rosenfeld, D. J. Wilner, and M. Bremer
2011a. A Closer Look at the LkCa 15 Protoplanetary Disk. , 742:L5.
- Andrews, S. M. and J. P. Williams
2005. Circumstellar Dust Disks in Taurus-Auriga: The Submillimeter Perspective. , 631:1134–1160.
- Andrews, S. M., D. J. Wilner, C. Espaillat, A. M. Hughes, C. P. Dullemond, M. K. McClure, C. Qi, and J. M. Brown
2011b. Resolved Images of Large Cavities in Protoplanetary Transition Disks. , 732:42.
- Andrews, S. M., D. J. Wilner, A. M. Hughes, C. Qi, and C. P. Dullemond
2009. Protoplanetary Disk Structures in Ophiuchus. , 700:1502–1523.
- Andrews, S. M., D. J. Wilner, Z. Zhu, T. Birnstiel, J. M. Carpenter, L. M. Pérez, X.-N. Bai, K. I. Öberg, A. M. Hughes, A. Isella, and L. Ricci
2016. Ringed Substructure and a Gap at 1 au in the Nearest Protoplanetary Disk. , 820:L40.
- Ansdell, M., J. P. Williams, C. F. Manara, A. Miotello, S. Facchini, N. van der Marel, L. Testi, and E. F. van Dishoeck
2017. An ALMA Survey of Protoplanetary Disks in the σ Orionis Cluster. , 153:240.
- Ansdell, M., J. P. Williams, N. van der Marel, J. M. Carpenter, G. Guidi, M. Hogerheijde, G. S. Mathews, C. F. Manara, A. Miotello, A. Natta, I. Oliveira, M. Tazzari, L. Testi, E. F. van Dishoeck, and S. E. van Terwisga
2016. ALMA Survey of Lupus Protoplanetary Disks. I. Dust and Gas Masses. , 828:46.
- Bally, J.
2008. *Overview of the Orion Complex*, P. 459.
- Baraffe, I., G. Chabrier, F. Allard, and P. H. Hauschildt
1998. Evolutionary models for solar metallicity low-mass stars: mass-magnitude relationships and color-magnitude diagrams. , 337:403–412.
- Barenfeld, S. A., J. M. Carpenter, L. Ricci, and A. Isella
2016. ALMA Observations of Circumstellar Disks in the Upper Scorpius OB Association. , 827:142.

- Barenfeld, S. A., J. M. Carpenter, A. I. Sargent, A. Isella, and L. Ricci
2017. Measurement of Circumstellar Disk Sizes in the Upper Scorpius OB Association with ALMA. , 851:85.
- Bockelée-Morvan, D., D. Gautier, F. Hersant, J.-M. Huré, and F. Robert
2002. Turbulent radial mixing in the solar nebula as the source of crystalline silicates in comets. , 384:1107–1118.
- Bouwman, J., T. Henning, L. A. Hillenbrand, M. R. Meyer, I. Pascucci, J. Carpenter, D. Hines, J. S. Kim, M. D. Silverstone, D. Hollenbach, and S. Wolf
2008. The Formation and Evolution of Planetary Systems: Grain Growth and Chemical Processing of Dust in T Tauri Systems. , 683:479–498.
- Bouwman, J., W. A. Lawson, A. Juhász, C. Dominik, E. D. Feigelson, T. Henning, A. G. G. M. Tielens, and L. B. F. M. Waters
2010. The Protoplanetary Disk Around the M4 Star RECX 5: Witnessing the Influence of Planet Formation? , 723:L243–L247.
- Bouwman, J., G. Meeus, A. de Koter, S. Hony, C. Dominik, and L. B. F. M. Waters
2001. Processing of silicate dust grains in Herbig Ae/Be systems. , 375:950–962.
- Briceño, C., N. Calvet, J. Hernández, A. K. Vivas, L. Hartmann, J. J. Downes, and P. Berlind
2005. The cida variability survey of orion ob1. i. the low-mass population of ori ob1a and 1b. , 129:907–926.
- Briceño, C., N. Calvet, J. Hernandez, A. K. Vivas, C. Mateu, J. J. Downes, J. Loerincs, A. Perez-Blanco, P. Berlind, C. Espaillat, L. Allen, L. Hartmann, M. Mateo, and J. Bailey, III
2018. The CIDA Variability Survey of Orion OB1 II: demographics of the young, low-mass stellar populations. *ArXiv e-prints*.
- Briceño, C., T. Preibisch, W. H. Sherry, E. A. Mamajek, R. D. Mathieu, F. M. Walter, and H. Zinnecker
2007. *The Low-Mass Populations in OB Associations*, Pp. 345–360. University of Arizona Press.

- Briceño, C., A. K. Vivas, N. Calvet, L. Hartmann, R. Pacheco, D. Herrera, L. Romero, P. Berlind, G. Sánchez, J. A. Snyder, and P. Andrews
2001. The cida-quest large-scale survey of orion ob1: Evidence for rapid disk dissipation in a dispersed stellar population. *Science*, 291:93–97.
- Briceño, C.
2008. *The Dispersed Young Population in Orion*, volume Volume I: The Northern Sky of *Astronomical Society of the Pacific Monograph Series*, Pp. 838–854. Astronomical Society of the Pacific.
- Briceño, C., L. Hartmann, J. Hernández, N. Calvet, A. K. Vivas, G. Furesz, and A. Szentgyorgyi
2007. 25 orionis: A kinematically distinct 10 myr old group in orion OB1a. *The Astrophysical Journal*, 661:1119.
- Brown, A. G. A., E. J. de Geus, and P. T. de Zeeuw
1994. The Orion OB1 association. 1: Stellar content. , 289:101–120.
- Brown, J. M., G. A. Blake, C. Qi, C. P. Dullemond, D. J. Wilner, and J. P. Williams
2009. Evidence for Dust Clearing Through Resolved Submillimeter Imaging. , 704:496–502.
- Caballero, J. A.
2008. Dynamical parallax of σ Ori AB: mass, distance and age. .
- Caballero, J. A.
2014. Stellar multiplicity in the sigma Orionis cluster: a review. *The Observatory*, 134:273–287.
- Calvet, N. and P. D’Alessio
2011. *Protoplanetary Disk Structure and Evolution*, Pp. 14–54.
- Calvet, N., P. D’Alessio, L. Hartmann, D. Wilner, A. Walsh, and M. Sitko
2002. Evidence for a Developing Gap in a 10 Myr Old Protoplanetary Disk. , 568:1008–1016.
- Calvet, N., P. D’Alessio, D. M. Watson, R. Franco-Hernández, E. Furlan, J. Green, P. M. Sutter, W. J. Forrest, L. Hartmann, K. I. Uchida, L. D. Keller, B. Sargent, J. Najita, T. L. Herter, D. J. Barry, and P. Hall
2005. Disks in Transition in the Taurus Population: Spitzer IRS Spectra of GM Aurigae and DM Tauri. , 630:L185–L188.

- Calvet, N., G. C. Magris, A. Patino, and P. D'Alessio
1992. Irradiation of Accretion Disks around Young Objects. II. Continuum Energy Distribution. , 24.
- Calvet, N., A. Patino, G. C. Magris, and P. D'Alessio
1991. Irradiation of accretion disks around young objects. I - Near-infrared CO bands. , 380:617–630.
- Carpenter, J. M., E. E. Mamajek, L. A. Hillenbrand, and M. R. Meyer
2006. Evidence for Mass-dependent Circumstellar Disk Evolution in the 5 Myr Old Upper Scorpius OB Association. , 651:L49–L52.
- Carpenter, J. M., E. E. Mamajek, L. A. Hillenbrand, and M. R. Meyer
2009. Debris Disks in the Upper Scorpius OB Association. , 705:1646–1671.
- Carpenter, J. M., L. Ricci, and A. Isella
2014. An ALMA Continuum Survey of Circumstellar Disks in the Upper Scorpius OB Association. , 787:42.
- Carr, J. S.
1995. Infrared CO Emission and Disks around Young Stars. , 224:25–28.
- Carr, J. S., R. D. Mathieu, and J. R. Najita
2001. Evidence for Residual Material in Accretion Disk Gaps: CO Fundamental Emission from the T Tauri Spectroscopic Binary DQ Tauri. , 551:454–460.
- Carrasco-González, C., R. Galván-Madrid, G. Anglada, M. Osorio, P. D'Alessio, P. Hofner, L. F. Rodríguez, H. Linz, and E. D. Araya
2012a. Resolving the Circumstellar Disk around the Massive Protostar Driving the HH 80-81 Jet. , 752:L29.
- Carrasco-Gonzalez, C., J. F. Gomez, J. M. Torrelles, G. Anglada, L. F. Rodriguez, and J. Marti
2011. Mapping the Magnetic Field in Massive Protostellar Jets. ATNF Proposal.
- Carrasco-González, C., T. Henning, C. J. Chandler, H. Linz, L. Pérez, L. F. Rodríguez, R. Galván-Madrid, G. Anglada, T. Birnstiel, R. van Boekel, M. Flock, H. Klahr, E. Macias, K. Menten, M. Osorio, L. Testi, J. M. Torrelles, and Z. Zhu
2016. The VLA View of the HL Tau Disk: Disk Mass, Grain Evolution, and Early Planet Formation. , 821:L16.

- Carrasco-González, C., M. Osorio, G. Anglada, P. D'Alessio, L. F. Rodríguez, J. F. Gómez, and J. M. Torrelles
2012b. Multiplicity, Disks, and Jets in the NGC 2071 Star-forming Region. , 746:71.
- Carrasco-González, C., L. F. Rodríguez, G. Anglada, J. Martí, J. M. Torrelles, and M. Osorio
2010. A Magnetized Jet from a Massive Protostar. *Science*, 330:1209.
- Carrasco-González, C., L. F. Rodríguez, G. Anglada, J. Martí, J. M. Torrelles, and M. Osorio
2013. Discovery of synchrotron emission from a YSO jet. In *European Physical Journal Web of Conferences*, volume 61 of *European Physical Journal Web of Conferences*, P. 03003.
- Carrasco-González, C., L. F. Rodríguez, M. Osorio, G. Anglada, J. Martí, J. M. Torrelles, R. Galván-Madrid, and P. D'Alessio
2011. New results on the HH 80-81 jet. In *Revista Mexicana de Astronomía y Astrofísica Conference Series*, volume 40 of *Revista Mexicana de Astronomía y Astrofísica*, vol. 27, Pp. 229–230.
- Clarke, C. J.
2007. The photoevaporation of discs around young stars in massive clusters. , 376:1350–1356.
- Clarke, C. J., A. Gendrin, and M. Sotomayor
2001. The dispersal of circumstellar discs: the role of the ultraviolet switch. , 328:485–491.
- Clarke, C. J. and J. E. Pringle
1993. Accretion disc response to a stellar fly-by. , 261:190–202.
- Crovisier, J., T. Y. Brooke, K. Leech, D. Bockelée-Morvan, E. Lellouch, M. S. Hanner, B. Altieri, H. U. Keller, T. Lim, S. Encrenaz, M. Griffin, T. de Graauw, E. van Dishoeck, and R. F. Knacke
2000. The Thermal Infrared Spectra of Comets Hale-Bopp and 103P/Hartley 2 Observed with the Infrared Space Observatory. *Thermal Emission Spectroscopy and Analysis of Dust, Disks, and Regoliths*, 196:109–117.
- Crovisier, J., K. Leech, D. Bockelee-Morvan, T. Y. Brooke, M. S. Hanner, B. Altieri, H. U. Keller, and E. Lellouch
1997. The spectrum of Comet Hale-Bopp (C/1995 01) observed with the

Infrared Space Observatory at 2.9 AU from the Sun. *Science*, 275:1904–1907.

Dahm, S. E. and J. M. Carpenter

2009. Spitzer Spectroscopy of Circumstellar Disks in the 5 Myr Old Upper Scorpius OB Association. , 137:4024–4045.

D’Alessio, P., N. Calvet, and L. Hartmann

2001. Accretion Disks around Young Objects. III. Grain Growth. , 553:321–334.

D’Alessio, P., N. Calvet, L. Hartmann, R. Franco-Hernández, and H. Servín

2006a. Effects of Dust Growth and Settling in T Tauri Disks. , 638:314–335.

D’Alessio, P., N. Calvet, L. Hartmann, R. Franco-Hernández, and H. Servín

2006b. Effects of Dust Growth and Settling in T Tauri Disks. , 638:314–335.

D’Alessio, P., N. Calvet, L. Hartmann, J. Muzerolle, and M. Sitko

2004. Models of Accretion Disks Around Young Stars. In *Star Formation at High Angular Resolution*, M. G. Burton, R. Jayawardhana, and T. L. Bourke, eds., volume 221 of *IAU Symposium*, P. 403.

D’Alessio, P., J. Cantö, N. Calvet, and S. Lizano

1998. Accretion Disks around Young Objects. I. The Detailed Vertical Structure. , 500:411–427.

D’Alessio, P., L. Hartmann, N. Calvet, R. Franco-Hernández, W. J. Forrest, B. Sargent, E. Furlan, K. Uchida, J. D. Green, D. M. Watson, C. H. Chen, F. Kemper, G. C. Sloan, and J. Najita

2005. The Truncated Disk of CoKu Tau/4. , 621:461–472.

de Juan Ovelar, M., P. Pinilla, M. Min, C. Dominik, and T. Birnstiel

2016. Constraining turbulence mixing strength in transitional discs with planets using SPHERE and ALMA. , 459:L85–L89.

de Zeeuw, P. T., R. Hoogerwerf, J. H. J. de Bruijne, A. G. A. Brown, and A. Blaauw

1999. A HIPPARCOS Census of the Nearby OB Associations. , 117:354–399.

- Dipierro, G. and G. Laibe
2017. An opening criterion for dust gaps in protoplanetary discs. , 469:1932–1948.
- Dodson-Robinson, S. E. and C. Salyk
2011. Transitional Disks as Signposts of Young, Multiplanet Systems. , 738:131.
- Dong, R., S. Li, E. Chiang, and H. Li
2017. Multiple Disk Gaps and Rings Generated by a Single Super-Earth. , 843:127.
- Dorschner, J., B. Begemann, T. Henning, C. Jaeger, and H. Mutschke
1995. Steps toward interstellar silicate mineralogy. II. Study of Mg-Fe-silicate glasses of variable composition. , 300:503.
- Downes, J. J., C. Briceño, C. Mateu, J. Hernández, N. Calvet, and L. Hartmann
2011. The formation and early evolution of brown dwarfs viewed through the Orion dispersed populations. In *Revista Mexicana de Astronomía y Astrofísica Conference Series*, volume 40 of *Revista Mexicana de Astronomía y Astrofísica*, vol. 27, Pp. 217–220.
- Downes, J. J., C. Briceño, C. Mateu, J. Hernández, A. K. Vivas, N. Calvet, L. Hartmann, M. G. Petr-Gotzens, and L. Allen
2014. The low-mass star and sub-stellar populations of the 25 Orionis group. , 444:1793–1811.
- Downes, J. J., C. Román-Zúñiga, J. Ballesteros-Paredes, C. Mateu, C. Briceño, J. Hernández, M. G. Petr-Gotzens, N. Calvet, L. Hartmann, and K. Mauco
2015. The number fraction of discs around brown dwarfs in Orion OB1a and the 25 Orionis group. , 450:3490–3502.
- Draine, B. T.
2006. On the Submillimeter Opacity of Protoplanetary Disks. , 636:1114–1120.
- Dullemond, C. P., D. Hollenbach, I. Kamp, and P. D’Alessio
2007. Models of the Structure and Evolution of Protoplanetary Disks. *Protostars and Planets V*, Pp. 555–572.

- Eisner, J. A., R. L. Plambeck, J. M. Carpenter, S. A. Corder, C. Qi, and D. Wilner
2008. Proplyds and Massive Disks in the Orion Nebula Cluster Imaged with CARMA and SMA. , 683:304–320.
- Espaillet, C., N. Calvet, P. D’Alessio, J. Hernández, C. Qi, L. Hartmann, E. Furlan, and D. M. Watson
2007. On the Diversity of the Taurus Transitional Disks: UX Tauri A and LkCa 15. , 670:L135–L138.
- Espaillet, C., N. Calvet, K. L. Luhman, J. Muzerolle, and P. D’Alessio
2008a. Confirmation of a Gapped Primordial Disk around LkCa 15. , 682:L125.
- Espaillet, C., P. D’Alessio, J. Hernández, E. Nagel, K. L. Luhman, D. M. Watson, N. Calvet, J. Muzerolle, and M. McClure
2010. Unveiling the Structure of Pre-transitional Disks. , 717:441–457.
- Espaillet, C., E. Furlan, P. D’Alessio, B. Sargent, E. Nagel, N. Calvet, D. M. Watson, and J. Muzerolle
2011. A Spitzer IRS Study of Infrared Variability in Transitional and Pre-transitional Disks Around T Tauri Stars. , 728:49.
- Espaillet, C., J. Muzerolle, J. Hernández, C. Briceño, N. Calvet, P. D’Alessio, M. McClure, D. M. Watson, L. Hartmann, and B. Sargent
2008b. A Slowly Accreting ~10 Myr-old Transitional Disk in Orion OB1a. , 689:L145.
- Espaillet, C., J. Muzerolle, J. Najita, S. Andrews, Z. Zhu, N. Calvet, S. Kraus, J. Hashimoto, A. Kraus, and P. D’Alessio
2014. An Observational Perspective of Transitional Disks. *Protostars and Planets VI*, Pp. 497–520.
- Fabian, D., T. Henning, C. Jäger, H. Mutschke, J. Dorschner, and O. Wehrhan
2001. Steps toward interstellar silicate mineralogy. VI. Dependence of crystalline olivine IR spectra on iron content and particle shape. , 378:228–238.
- Facchini, S., C. J. Clarke, and T. G. Bisbas
2016. External photoevaporation of protoplanetary discs in sparse stellar groups: the impact of dust growth. , 457:3593–3610.

- Follette, K., L. Close, J. Males, B. Macintosh, S. Sallum, J. Eisner, K. M. Kratter, K. Morzinski, P. Hinz, A. Weinberger, T. J. Rodigas, A. Skemer, V. Bailey, A. Vaz, D. Defrere, e. spalding, and P. Tuthill
2015. An Accreting Protoplanet: Confirmation and Characterization of LkCa15b. In *AAS/Division for Extreme Solar Systems Abstracts*, volume 3 of *AAS/Division for Extreme Solar Systems Abstracts*, P. 203.01.
- Forrest, W. J., B. Sargent, E. Furlan, P. D'Alessio, N. Calvet, L. Hartmann, K. I. Uchida, J. D. Green, D. M. Watson, C. H. Chen, F. Kemper, L. D. Keller, G. C. Sloan, T. L. Herter, B. R. Brandl, J. R. Houck, D. J. Barry, P. Hall, P. W. Morris, J. Najita, and P. C. Myers
2004. Mid-infrared Spectroscopy of Disks around Classical T Tauri Stars. , 154:443–447.
- Furlan, E., L. Hartmann, N. Calvet, P. D'Alessio, R. Franco-Hernández, W. J. Forrest, D. M. Watson, K. I. Uchida, B. Sargent, J. D. Green, L. D. Keller, and T. L. Herter
2006. A Survey and Analysis of Spitzer Infrared Spectrograph Spectra of T Tauri Stars in Taurus. , 165:568–605.
- Furlan, E., D. M. Watson, M. K. McClure, P. Manoj, C. Espaillat, P. D'Alessio, N. Calvet, K. H. Kim, B. A. Sargent, W. J. Forrest, and L. Hartmann
2009. Disk Evolution in the Three Nearby Star-forming Regions of Taurus, Chamaeleon, and Ophiuchus. , 703:1964–1983.
- Gail, H.-P.
2001. Radial mixing in protoplanetary accretion disks. I. Stationary disc models with annealing and carbon combustion. , 378:192–213.
- Gail, H.-P.
2002. Radial mixing in protoplanetary accretion disks. III. Carbon dust oxidation and abundance of hydrocarbons in comets. , 390:253–265.
- Galván-Madrid, R., L. F. Rodríguez, H. B. Liu, G. Costigan, C. Carrasco-González, C. F. Manara, J. Forbrich, and S. Ramsay
2017. Testing the Jet-Accretion Connection in Young Stellar Objects in the Time Domain. In *Revista Mexicana de Astronomía y Astrofísica Conference Series*, volume 49 of *Revista Mexicana de Astronomía y Astrofísica*, vol. 27, Pp. 170–170.
- García-Arredondo, F., W. J. Henney, and S. J. Arthur
2001. Hydrodynamic Simulations of Proplyd Bow Shocks. , 561:830–842.

- Geers, V. C., J.-C. Augereau, K. M. Pontoppidan, C. P. Dullemond, R. Visser, J. E. Kessler-Silacci, N. J. Evans, II, E. F. van Dishoeck, G. A. Blake, A. C. A. Boogert, J. M. Brown, F. Lahuis, and B. Merín
2006. C2D Spitzer-IRS spectra of disks around T Tauri stars. II. PAH emission features. , 459:545–556.
- Habart, E., A. Abergel, C. M. Walmsley, D. Teyssier, and J. Pety
2005. Density structure of the Horsehead nebula photo-dissociation region. , 437:177–188.
- Habart, E., A. Natta, and E. Krügel
2004. PAHs in circumstellar disks around Herbig Ae/Be stars. , 427:179–192.
- Habart, E., A. Natta, L. Testi, and M. Carillet
2006. Spatially resolved PAH emission in the inner disks of Herbig Ae/Be stars. , 449:1067–1075.
- Harker, D. E. and S. J. Desch
2002. Annealing of Silicate Dust by Nebular Shocks at 10 AU. , 565:L109–L112.
- Hartigan, P., S. Edwards, and L. Ghandour
1995. Disk Accretion and Mass Loss from Young Stars. , 452:736.
- Hartmann, L.
1998. *Accretion Processes in Star Formation*.
- Hartmann, L.
2009a. *Accretion Processes in Star Formation: Second Edition*. Cambridge University Press.
- Hartmann, L.
2009b. *Accretion Processes in Star Formation: Second Edition*. Cambridge University Press.
- Hartmann, L., S. T. Megeath, L. Allen, K. Luhman, N. Calvet, P. D’Alessio, R. Franco-Hernandez, and G. Fazio
2005. IRAC Observations of Taurus Pre-Main-Sequence Stars. , 629:881–896.
- Henney, W. J. and C. R. O’Dell
1999. A Keck High-Resolution Spectroscopic Study of the Orion Nebula Proplyds. , 118:2350–2368.

- Henning, T. and G. Meeus
2011. *Dust Processing and Mineralogy in Protoplanetary Accretion Disks*, Pp. 114–148.
- Herbig, G. H.
1962. The properties and problems of t tauri stars and related objects. *Advances in Astronomy and Astrophysics*, 1:47–103.
- Hernández, J., N. Calvet, C. Briceño, L. Hartmann, A. K. Vivas, J. Muzerolle, J. Downes, L. Allen, and R. Gutermuth
2007a. Spitzer Observations of the Orion OB1 Association: Disk Census in the Low-Mass Stars. , 671:1784–1799.
- Hernández, J., N. Calvet, L. Hartmann, C. Briceño, A. Sicilia-Aguilar, and P. Berlind
2005. Herbig Ae/Be Stars in nearby OB Associations. , 129:856–871.
- Hernández, J., N. Calvet, A. Perez, C. Briceño, L. Olguin, M. E. Contreras, L. Hartmann, L. Allen, C. Espaillat, and R. Hernan
2014. A Spectroscopic Census in Young Stellar Regions: The σ Orionis Cluster. , 794:36.
- Hernández, J., L. Hartmann, T. Megeath, R. Gutermuth, J. Muzerolle, N. Calvet, A. K. Vivas, C. Briceño, L. Allen, J. Stauffer, E. Young, and G. Fazio
2007b. A Spitzer Space Telescope Study of Disks in the Young σ Orionis Cluster. , 662:1067–1081.
- Hollenbach, D. J., H. W. Yorke, and D. Johnstone
2000. Disk Dispersal around Young Stars. *Protostars and Planets IV*, P. 401.
- Howard, C. D., G. Sandell, W. D. Vacca, G. Duchêne, G. Mathews, J.-C. Augereau, D. Barrado, W. R. F. Dent, C. Eiroa, C. Grady, I. Kamp, G. Meeus, F. Ménard, C. Pinte, L. Podio, P. Riviere-Marichalar, A. Roberge, W.-F. Thi, S. Vicente, and J. P. Williams
2013. Herschel/PACS Survey of Protoplanetary Disks in Taurus/Auriga Observations of [O I] and [C II], and Far-infrared Continuum. , 776:21.
- Huélamo, N., S. Lacour, P. Tuthill, M. Ireland, A. Kraus, and G. Chauvin
2011. A companion candidate in the gap of the T Chamaeleontis transitional disk. , 528:L7.

- Hughes, A. M., S. M. Andrews, C. Espaillat, D. J. Wilner, N. Calvet, P. D'Alessio, C. Qi, J. P. Williams, and M. R. Hogerheijde
2009. A Spatially Resolved Inner Hole in the Disk Around GM Aurigae. , 698:131–142.
- Isella, A., A. Natta, D. Wilner, J. M. Carpenter, and L. Testi
2010. Millimeter Imaging of MWC 758: Probing the Disk Structure and Kinematics. , 725:1735–1741.
- Jaeger, C., F. J. Molster, J. Dorschner, T. Henning, H. Mutschke, and L. B. F. M. Waters
1998. Steps toward interstellar silicate mineralogy. IV. The crystalline revolution. , 339:904–916.
- Johnstone, D., D. Hollenbach, and J. Bally
1998. Photoevaporation of Disks and Clumps by Nearby Massive Stars: Application to Disk Destruction in the Orion Nebula. , 499:758–776.
- Juhász, A., J. Bouwman, T. Henning, B. Acke, M. E. van den Ancker, G. Meeus, C. Dominik, M. Min, A. G. G. M. Tielens, and L. B. F. M. Waters
2010. Dust Evolution in Protoplanetary Disks Around Herbig Ae/Be Stars the Spitzer View. , 721:431–455.
- Kalyaan, A., S. J. Desch, and N. Monga
2015. External Photoevaporation of the Solar Nebula. II. Effects on Disk Structure and Evolution with Non-uniform Turbulent Viscosity due to the Magnetorotational Instability. , 815:112.
- Kemper, F., W. J. Vriend, and A. G. G. M. Tielens
2004. The Absence of Crystalline Silicates in the Diffuse Interstellar Medium. , 609:826–837.
- Kenyon, S. J. and L. Hartmann
1987. Spectral energy distributions of T Tauri stars - Disk flaring and limits on accretion. , 323:714–733.
- Kenyon, S. J. and L. Hartmann
1995. Pre-main-sequence evolution in the taurus-auriga molecular cloud. , 101:117.
- Kessler-Silacci, J., J.-C. Augereau, C. P. Dullemond, V. Geers, F. Lahuis, N. J. Evans, II, E. F. van Dishoeck, G. A. Blake, A. C. A. Boogert,

- J. Brown, J. K. Jørgensen, C. Knez, and K. M. Pontoppidan
2006. c2d Spitzer IRS Spectra of Disks around T Tauri Stars. I. Silicate Emission and Grain Growth. , 639:275–291.
- Kraus, A. L., M. J. Ireland, F. Martinache, and L. A. Hillenbrand
2011. Mapping the Shores of the Brown Dwarf Desert. II. Multiple Star Formation in Taurus-Auriga. , 731:8.
- Lada, C. J. and F. C. Adams
1992. Interpreting infrared color-color diagrams - Circumstellar disks around low- and intermediate-mass young stellar objects. , 393:278–288.
- Lada, C. J., A. A. Muench, K. L. Luhman, L. Allen, L. Hartmann, T. Megeath, P. Myers, G. Fazio, K. Wood, J. Muzerolle, G. Rieke, N. Siegler, and E. Young
2006. Spitzer Observations of IC 348: The Disk Population at 2-3 Million Years. , 131:1574–1607.
- Lagage, P.-O., C. Doucet, E. Pantin, E. Habart, G. Duchêne, F. Ménard, C. Pinte, S. Charnoz, and J.-W. Pel
2006. Anatomy of a Flaring Proto-Planetary Disk Around a Young Intermediate-Mass Star. *Science*, 314:621–623.
- Luhman, K. L., P. R. Allen, C. Espaillat, L. Hartmann, and N. Calvet
2010. The Disk Population of the Taurus Star-Forming Region. , 186:111–174.
- Luhman, K. L. and E. E. Mamajek
2012. The Disk Population of the Upper Scorpius Association. , 758:31.
- Maaskant, K. M., M. Min, L. B. F. M. Waters, and A. G. G. M. Tielens
2014. Polycyclic aromatic hydrocarbon ionization as a tracer of gas flows through protoplanetary disk gaps. , 563:A78.
- Malfait, K., C. Waelkens, L. B. F. M. Waters, B. Vandenbussche, E. Huygen, and M. S. de Graauw
1998. The spectrum of the young star HD 100546 observed with the Infrared Space Observatory. , 332:L25–L28.
- Mamajek, E. E., W. A. Lawson, and E. D. Feigelson
1999. The eta chamaeleontis cluster: A remarkable new nearby young open cluster. *The Astrophysical Journal Letters*, 516:L77L80.

- Manara, C. F., G. Rosotti, L. Testi, A. Natta, J. M. Alcalá, J. P. Williams, M. Ansdell, A. Miotello, N. van der Marel, M. Tazzari, J. Carpenter, G. Guidi, G. S. Mathews, I. Oliveira, T. Prusti, and E. F. van Dishoeck
2016. Evidence for a correlation between mass accretion rates onto young stars and the mass of their protoplanetary disks. , 591:L3.
- Mann, R. K., J. Di Francesco, D. Johnstone, S. M. Andrews, J. P. Williams, J. Bally, L. Ricci, A. M. Hughes, and B. C. Matthews
2014. ALMA Observations of the Orion Proplyds. , 784:82.
- Manoj, P., K. H. Kim, E. Furlan, M. K. McClure, K. L. Luhman, D. M. Watson, C. Espaillat, N. Calvet, J. R. Najita, P. D'Alessio, L. Adame, B. A. Sargent, W. J. Forrest, C. Bohac, J. D. Green, and L. A. Arnold
2011. Spitzer Infrared Spectrograph Survey of Young Stars in the Chamaeleon I Star-Forming Region. , 193:11.
- Manoj, P., D. M. Watson, D. A. Neufeld, S. T. Megeath, R. Vavrek, V. Yu, R. Visser, E. A. Bergin, W. J. Fischer, J. J. Tobin, A. M. Stutz, B. Ali, T. L. Wilson, J. Di Francesco, M. Osorio, S. Maret, and C. A. Poteet
2013. Herschel/PACS Spectroscopic Survey of Protostars in Orion: The Origin of Far-infrared CO Emission. , 763:83.
- Mathews, G. S., C. Pinte, G. Duchêne, J. P. Williams, and F. Ménard
2013. A Herschel PACS survey of the dust and gas in Upper Scorpius disks. , 558:A66.
- Maucó, K., C. Briceño, N. Calvet, J. Hernández, J. Ballesteros-Paredes, O. González, C. C. Espaillat, D. Li, C. M. Telesco, J. José Downes, E. Macías, C. Qi, R. Michel, P. DAlessio, and B. Ali
2018. Herschel PACS Observations of 410 Myr Old Classical T Tauri Stars in Orion OB1. , 859:1.
- McClure, M. K., P. D'Alessio, N. Calvet, C. Espaillat, L. Hartmann, B. Sargent, D. M. Watson, L. Ingleby, and J. Hernández
2013. Curved Walls: Grain Growth, Settling, and Composition Patterns in T Tauri Disk Dust Sublimation Fronts. , 775:114.
- McClure, M. K., E. Furlan, P. Manoj, K. L. Luhman, D. M. Watson, W. J. Forrest, C. Espaillat, N. Calvet, P. D'Alessio, B. Sargent, J. J. Tobin, and H.-F. Chiang
2010. The Evolutionary State of the Pre-main Sequence Population in Ophiuchus: A Large Infrared Spectrograph Survey. , 188:75–122.

- McClure, M. K., P. Manoj, N. Calvet, L. Adame, C. Espaillat, D. M. Watson, B. Sargent, W. J. Forrest, and P. D'Alessio
2012. Probing Dynamical Processes in the Planet-forming Region with Dust Mineralogy. , 759:L10.
- Meaburn, J., J. A. O'connor, J. A. López, M. Bryce, M. P. Redman, and A. Noriega-Crespo
2000. The ejecta from the luminous blue variable star P Cygni. , 318:561–572.
- Meyer, M. R., N. Calvet, and L. A. Hillenbrand
1997. Intrinsic Near-Infrared Excesses of T Tauri Stars: Understanding the Classical T Tauri Star Locus. , 114:288–300.
- Muench, A., K. Getman, L. Hillenbrand, and T. Preibisch
2008. *Star Formation in the Orion Nebula I: Stellar Content*, P. 483.
- Muench, A. A., C. J. Lada, K. L. Luhman, J. Muzerolle, and E. Young
2007. A Spitzer Census of the IC 348 Nebula. , 134:411–444.
- Mulders, G. D., L. B. F. M. Waters, C. Dominik, B. Sturm, J. Bouwman, M. Min, A. P. Verhoeff, B. Acke, J. C. Augereau, N. J. Evans, T. Henning, G. Meeus, and J. Olofsson
2011. Low abundance, strong features: window-dressing crystalline forsterite in the disk wall of HD 100546. , 531:A93.
- Najita, J., J. S. Carr, and R. D. Mathieu
2003. Gas in the Terrestrial Planet Region of Disks: CO Fundamental Emission from T Tauri Stars. , 589:931–952.
- Najita, J. R., N. Crockett, and J. S. Carr
2008. CO Fundamental Emission from V836 Tauri. , 687:1168–1179.
- Natta, A., L. Testi, J. M. Alcalá, E. Rigliaco, E. Covino, B. Stelzer, and V. D'Elia
2014. X-shooter spectroscopy of young stellar objects. V. Slow winds in T Tauri stars. , 569:A5.
- Natta, A., L. Testi, J. Muzerolle, S. Randich, F. Comerón, and P. Persi
2004. Accretion in brown dwarfs: An infrared view. , 424:603–612.

- Nomura, H., T. Tsukagoshi, R. Kawabe, D. Ishimoto, S. Okuzumi, T. Muto, K. D. Kanagawa, S. Ida, C. Walsh, T. J. Millar, and X.-N. Bai
2016. ALMA Observations of a Gap and a Ring in the Protoplanetary Disk around TW Hya. , 819:L7.
- Nuth, J. A., F. J. M. Rietmeijer, S. L. Hallenbeck, P. A. Withey, and F. Ferguson
2000. Nucleation, Growth, Annealing and Coagulation of Refractory Oxides and Metals: Recent Experimental Progress and Applications to Astrophysical Systems. *Thermal Emission Spectroscopy and Analysis of Dust, Disks, and Regoliths*, 196:313–332.
- O’dell, C. R. and Z. Wen
1994. Postrefurbishment mission Hubble Space Telescope images of the core of the Orion Nebula: Proplyds, Herbig-Haro objects, and measurements of a circumstellar disk. , 436:194–202.
- Olofsson, J., L. Szűcs, T. Henning, H. Linz, I. Pascucci, and V. Joergens
2013. The Herschel/PACS view of disks around low-mass stars in Chamaleon-I. , 560:A100.
- Paardekooper, S. J. and G. Mellema
2004. Planets in Disks: A New Method for Hydrodynamic Disk Simulations. In *Extrasolar Planets: Today and Tomorrow*, J. Beaulieu, A. Lecavelier Des Etangs, and C. Terquem, eds., volume 321 of *Astronomical Society of the Pacific Conference Series*, P. 347.
- Pascucci, I. and M. Sterzik
2009. Evidence for Disk Photoevaporation Driven by the Central Star. , 702:724–732.
- Pascucci, I., L. Testi, G. J. Herczeg, F. Long, C. F. Manara, N. Hendler, G. D. Mulders, S. Krijt, F. Ciesla, T. Henning, S. Mohanty, E. Drabek-Maunder, D. Apai, L. Szűcs, G. Sacco, and J. Olofsson
2016. A Steeper than Linear Disk Mass-Stellar Mass Scaling Relation. , 831:125.
- Pecaut, M. J. and E. E. Mamajek
2016. The star formation history and accretion-disc fraction among the k-type members of the scorpius???centaurus ob association. *Monthly Notices of the Royal Astronomical Society*, 461(1):794–815.

- Pérez, L. M., J. M. Carpenter, C. J. Chandler, A. Isella, S. M. Andrews, L. Ricci, N. Calvet, S. A. Corder, A. T. Deller, C. P. Dullemond, J. S. Greaves, R. J. Harris, T. Henning, W. Kwon, J. Lazio, H. Linz, L. G. Mundy, A. I. Sargent, S. Storm, L. Testi, and D. J. Wilner
2012. Constraints on the Radial Variation of Grain Growth in the AS 209 Circumstellar Disk. , 760:L17.
- Pinilla, P., M. de Juan Ovelar, S. Ataiee, M. Benisty, T. Birnstiel, E. F. van Dishoeck, and M. Min
2015. Gas and dust structures in protoplanetary disks hosting multiple planets. , 573:A9.
- Pinilla, P., L. Klarmann, T. Birnstiel, M. Benisty, C. Dominik, and C. P. Dullemond
2016. A tunnel and a traffic jam: How transition disks maintain a detectable warm dust component despite the presence of a large planet-carved gap. , 585:A35.
- Pinte, C., W. R. F. Dent, F. Ménard, A. Hales, T. Hill, P. Cortes, and I. de Gregorio-Monsalvo
2016. Dust and Gas in the Disk of HL Tauri: Surface Density, Dust Settling, and Dust-to-gas Ratio. , 816:25.
- Podosek, F. A., X. Gao, R. H. Nichols, U. Ott, S. Specht, J. C. Brannon, and T. J. Bernatowicz
1996. Thoroughly Anomalous CR in Carbonaceous Chondrites. *Meteoritics and Planetary Science Supplement*, 31.
- Preibisch, T. and E. Mamajek
2008. *The Nearest OB Association: Scorpius-Centaurus (Sco OB2)*, P. 235.
- Ressler, M. E. and M. Barsony
2003. Structure of the Mid-Infrared-emitting Disk around WL 16. , 584:832–842.
- Rieke, G. H. and M. J. Lebofsky
1985. The interstellar extinction law from 1 to 13 microns. , 288:618–621.
- Rigliaco, E., A. Natta, S. Randich, and G. Sacco
2009. Discovery of an old photoevaporating disk in σ Orionis. , 495:L13–L16.

- Rigliaco, E., I. Pascucci, U. Gorti, S. Edwards, and D. Hollenbach
2013. Understanding the Origin of the [O I] Low-velocity Component from T Tauri Stars. , 772:60.
- Riviere-Marichalar, P., C. Pinte, D. Barrado, W. F. Thi, C. Eiroa, I. Kamp, B. Montesinos, J. Donaldson, J. C. Augereau, N. Huélamo, A. Roberge, D. Ardila, G. Sandell, J. P. Williams, W. R. F. Dent, F. Menard, J. Lillo-Box, and G. Duchêne
2013. Gas and dust in the TW Hydrae association as seen by the Herschel Space Observatory. , 555:A67.
- Rodríguez, L. F.
2011. Radio observations of jets from massive young stars. In *Jets at All Scales*, G. E. Romero, R. A. Sunyaev, and T. Belloni, eds., volume 275 of *IAU Symposium*, Pp. 367–373.
- Rodríguez, L. F., R. F. González, A. C. Raga, J. Cantó, A. Riera, L. Loinard, S. A. Dzib, and L. A. Zapata
2012. Radio continuum emission from knots in the DG Tauri jet. , 537:A123.
- Rodríguez, L. F., J. M. Moran, R. Franco-Hernández, G. Garay, K. J. Brooks, and D. Mardones
2008. The Collimated Jet Source in IRAS 16547-4247: Time Variation, Possible Precession, and Upper Limits to the Proper Motions Along the Jet Axis. , 135:2370–2379.
- Rodríguez, L. F., B. Reipurth, and H.-F. Chiang
2014. Radio Continuum Sources associated with the HH 92 and HH 34 Jets. , 50:285–291.
- Rodríguez, L. F., J. O. Yam, C. Carrasco-González, G. Anglada, and A. Trejo
2016. The Radio Jet Associated with the Multiple V380 Ori System. , 152:101.
- Sallum, S., J. Eisner, L. M. Close, P. M. Hinz, K. B. Follette, K. Kratter, A. J. Skemer, V. P. Bailey, R. Briguglio, D. Defrere, B. A. Macintosh, J. R. Males, K. M. Morzinski, A. T. Puglisi, T. J. Rodigas, E. Spalding, P. G. Tuthill, A. Vaz, A. Weinberger, and M. Xomperio
2016. Imaging protoplanets: observing transition disks with non-redundant masking. In *Optical and Infrared Interferometry and Imaging V*, volume 9907 of , P. 99070D.

- Sallum, S., K. B. Follette, J. A. Eisner, L. M. Close, P. Hinz, K. Kratter, J. Males, A. Skemer, B. Macintosh, P. Tuthill, V. Bailey, D. Defrère, K. Morzinski, T. Rodigas, E. Spalding, A. Vaz, and A. J. Weinberger
2015. Accreting protoplanets in the LkCa 15 transition disk. , 527:342–344.
- Sargent, B. A., W. J. Forrest, C. Tayrien, M. K. McClure, D. M. Watson, G. C. Sloan, A. Li, P. Manoj, C. J. Bohac, E. Furlan, K. H. Kim, and J. D. Green
2009. Dust Processing and Grain Growth in Protoplanetary Disks in the Taurus-Auriga Star-Forming Region. .
- Schlegel, D. J., D. P. Finkbeiner, and M. Davis
1998. Maps of dust infrared emission for use in estimation of reddening and cosmic microwave background radiation foregrounds. , 500:525.
- Schwarz, K. R., E. A. Bergin, L. I. Cleaves, G. A. Blake, K. Zhang, K. I. Öberg, E. F. van Dishoeck, and C. Qi
2016. The Radial Distribution of H₂ and CO in TW Hya as Revealed by Resolved ALMA Observations of CO Isotopologues. , 823:91.
- Sicilia-Aguilar, A., L. W. Hartmann, D. Watson, C. Bohac, T. Henning, and J. Bouwman
2007. Silicate Dust in Evolved Protoplanetary Disks: Growth, Sedimentation, and Accretion. , 659:1637–1660.
- Simón-Díaz, S., J. A. Caballero, J. Lorenzo, J. Maíz Apellániz, F. R. N. Schneider, I. Negueruela, R. H. Barbá, R. Dorda, A. Marco, D. Montes, A. Pellerin, J. Sanchez-Bermudez, Á. Sódor, and A. Sota
2015. Orbital and Physical Properties of the σ Ori Aa, Ab, B Triple System. , 799:169.
- Skrutskie, M. F., D. Dutkevitch, S. E. Strom, S. Edwards, K. M. Strom, and M. A. Shure
1990. A sensitive 10-micron search for emission arising from circumstellar dust associated with solar-type pre-main-sequence stars. , 99:1187–1195.
- Smith, N., J. Bally, R. Y. Shuping, M. Morris, and M. Kassiss
2005. Thermal Dust Emission from Proplyds, Unresolved Disks, and Shocks in the Orion Nebula. , 130:1763–1777.

- Störzer, H. and D. Hollenbach
1999. Photodissociation Region Models of Photoevaporating Circumstellar Disks and Application to the Proplyds in Orion. , 515:669–684.
- Strom, K. M., S. E. Strom, S. Edwards, S. Cabrit, and M. F. Skrutskie
1989. Circumstellar material associated with solar-type pre-main-sequence stars - A possible constraint on the timescale for planet building. , 97:1451–1470.
- Suárez, G., J. J. Downes, C. Román-Zúñiga, K. R. Covey, M. Tapia, J. Hernández, M. G. Petr-Gotzens, K. G. Stassun, and C. Briceño
2017. New Low-mass Stars in the 25 Orionis Stellar Group and Orion OB1a Sub-association from SDSS-III/BOSS Spectroscopy. , 154:14.
- Testi, L., T. Birnstiel, L. Ricci, S. Andrews, J. Blum, J. Carpenter, C. Dominik, A. Isella, A. Natta, J. P. Williams, and D. J. Wilner
2014. Dust Evolution in Protoplanetary Disks. *Protostars and Planets VI*, Pp. 339–361.
- Testi, L., A. Natta, D. S. Shepherd, and D. J. Wilner
2003. Large grains in the disk of CQ Tau. , 403:323–328.
- Thi, W.-F., G. Mathews, F. Ménard, P. Woitke, G. Meeus, P. Riviere-Marichalar, C. Pinte, C. D. Howard, A. Roberge, G. Sandell, I. Pascucci, B. Riaz, C. A. Grady, W. R. F. Dent, I. Kamp, G. Duchêne, J.-C. Augereau, E. Pantin, B. Vandenbussche, I. Tilling, J. P. Williams, C. Eiroa, D. Barrado, J. M. Alacid, S. Andrews, D. R. Ardila, G. Aresu, S. Brittain, D. R. Ciardi, W. Danchi, D. Fedele, I. de Gregorio-Monsalvo, A. Heras, N. Huelamo, A. Krivov, J. Lebreton, R. Liseau, C. Martin-Zaidi, I. Mendigutía, B. Montesinos, A. Mora, M. Morales-Calderon, H. Nomura, N. Phillips, L. Podio, D. R. Poelman, S. Ramsay, K. Rice, E. Solano, H. Walker, G. J. White, and G. Wright
2010. Herschel-PACS observation of the 10 Myr old T Tauri disk TW Hya. Constraining the disk gas mass. , 518:L125.
- Tsukagoshi, T., H. Nomura, T. Muto, R. Kawabe, D. Ishimoto, K. D. Kanagawa, S. Okuzumi, S. Ida, C. Walsh, and T. J. Millar
2016. A Gap with a Deficit of Large Grains in the Protoplanetary Disk around TW Hya. , 829:L35.
- Uchida, K. I., N. Calvet, L. Hartmann, F. Kemper, W. J. Forrest, D. M. Watson, P. D’Alessio, C. H. Chen, E. Furlan, B. Sargent, B. R. Brandl,

- T. L. Herter, P. Morris, P. C. Myers, J. Najita, G. C. Sloan, D. J. Barry, J. Green, L. D. Keller, and P. Hall
2004. The State of Protoplanetary Material 10 Million years after Stellar Formation: Circumstellar Disks in the TW Hydrae Association. , 154:439–442.
- van Boekel, R., T. Henning, J. Menu, J. de Boer, M. Langlois, A. Müller, H. Avenhaus, A. Boccaletti, H. M. Schmid, C. Thalmann, M. Benisty, C. Dominik, C. Ginski, J. H. Girard, D. Gisler, A. Lobo Gomes, F. Menard, M. Min, A. Pavlov, A. Pohl, S. P. Quanz, P. Rabou, R. Roelfsema, J.-F. Sauvage, R. Teague, F. Wildi, and A. Zurlo
2017. Three Radial Gaps in the Disk of TW Hydrae Imaged with SPHERE. , 837:132.
- van Boekel, R., M. Min, L. B. F. M. Waters, A. de Koter, C. Dominik, M. E. van den Ancker, and J. Bouwman
2005. A 10 μm spectroscopic survey of Herbig Ae star disks: Grain growth and crystallization. , 437:189–208.
- van Dishoeck, E. F., N. van der Marel, S. Bruderer, and P. Pinilla
2015. Quantifying the Gas Inside Dust Cavities in Transitional Disks: Implications for Young Planets. In *Revolution in Astronomy with ALMA: The Third Year*, D. Iono, K. Tatematsu, A. Wootten, and L. Testi, eds., volume 499 of *Astronomical Society of the Pacific Conference Series*, P. 281.
- Walter, F. M., S. J. Wolk, M. Freyberg, and J. H. M. M. Schmitt
1997. Discovery of the σ Orionis Cluster. , 68:1081.
- Ward-Thompson, D., L. Hartmann, and D. J. Nutter
2005. Turbulence in Class 0 and I protostellar envelopes. , 357:687–690.
- Warren, Jr., W. H. and J. E. Hesser
1978. A photometric study of the Orion OB 1 association. III - Subgroup analyses. , 36:497–572.
- Waters, L. B. F. M.
2015. Dust in protoplanetary disks: observations. In *European Physical Journal Web of Conferences*, volume 102 of *European Physical Journal Web of Conferences*, P. 00003.
- Watson, D. M., J. M. Leisenring, E. Furlan, C. J. Bohac, B. Sargent, W. J. Forrest, N. Calvet, L. Hartmann, J. T. Nordhaus, J. D. Green, K. H.

- Kim, G. C. Sloan, C. H. Chen, L. D. Keller, P. d'Alessio, J. Najita, K. I. Uchida, and J. R. Houck
2009. Crystalline Silicates and Dust Processing in the Protoplanetary Disks of the Taurus Young Cluster. , 180:84–101.
- Webb, R. A., B. Zuckerman, I. Platais, J. Patience, R. J. White, M. J. Schwartz, and C. McCarthy
1999. Discovery of Seven T Tauri Stars and a Brown Dwarf Candidate in the Nearby TW Hydrae Association. , 512:L63–L67.
- Wenrich, M. L. and P. R. Christensen
1996. Optical constants of minerals derived from emission spectroscopy: Application to quartz. , 101:15921–15931.
- Werner, M. W., T. L. Roellig, F. J. Low, G. H. Rieke, M. Rieke, W. F. Hoffmann, E. Young, J. R. Houck, B. Brandl, G. G. Fazio, J. L. Hora, R. D. Gehrz, G. Helou, B. T. Soifer, J. Stauffer, J. Keene, P. Eisenhardt, D. Gallagher, T. N. Gautier, W. Irace, C. R. Lawrence, L. Simmons, J. E. Van Cleve, M. Jura, E. L. Wright, and D. P. Cruikshank
2004. The Spitzer Space Telescope Mission. , 154:1–9.
- Williams, J. P., S. M. Andrews, and D. J. Wilner
2005. The Masses of the Orion Proplyds from Submillimeter Dust Emission. , 634:495–500.
- Williams, J. P. and L. A. Cieza
2011. Protoplanetary Disks and Their Evolution. , 49:67–117.
- Wright, E., P. Eisenhardt, A. Mainzer, M. Ressler, R. Cutri, T. Jarrett, J. Kirkpatrick, D. Padgett, R. McMillan, M. Skrutskie, et al.
2010. The wide-field infrared survey explorer (wise): mission description and initial on-orbit performance. *The Astronomical Journal*, 140:1868.
- Zhu, Z., R. P. Nelson, L. Hartmann, C. Espaillat, and N. Calvet
2011. Transitional and pre-transitional disks: Gap opening by multiple planets? *The Astrophysical Journal*, 729:47.